Inner shell ionization effects on molecules of biological interest in an aqueous medium

Lucie Huart

Sorbonne Université

École doctorale n°397: Physique et Chimie des Matériaux

Réalisée à l'Institut de Minéralogie, de Physique des Matériaux et de Cosmochimie (Sorbonne Université), au Laboratoire de Nanosciences et Innovation pour les Matériaux, la Biomédecine et l'Énergie (CEA Saclay) et au Synchrotron SOLEIL.

Effets d'ionisation en couche interne sur des molécules d'intérêt biologique en milieu aqueux.

Par Lucie HUART

Thèse de doctorat de Physique Chimie

Dirigée par Marie-Anne Hervé du PENHOAT, Jean-Philippe RENAULT et Christophe NICOLAS.

Présentée et soutenue publiquement le 17/01/2022

Devant un jury composé de :

Eckart RÜHL	Professeur (Freie Universität Berlin)	Rapporteur
Jean-Luc RAVANAT	Directeur de recherche, HDR (CEA Grenoble)	Rapporteur
François ROCHET	Professeur, HDR (Sorbonne Université)	Membre du jury
Sandrine LACOMBE	Professeure, HDR (Université Paris-Saclay)	Membre du jury
Sylwia PTASINSKA	Professeure associée (University of Notre Dame)	Membre du jury
M.-A.HERVE DU PENHOAT	Maîtresse de conférence, HDR (Sorbonne Université)	Directrice de thèse
Jean-Philippe RENAULT	Chercheur CEA, HDR (CEA Saclay)	Encadrant (invité)
Christophe NICOLAS	Scientifique de ligne (Synchrotron SOLEIL)	Encadrant (invité)

Résumé de la thèse

Cette thèse s'intéresse à l'étude des dommages radio-induits par les rayonnements ionisants. Elle s'intègre dans le cadre du projet ANR HighEneCh (ANR-17-CE30-0017) qui regroupe un consortium de spécialistes couvrant la spectroscopie électronique et l'instrumentation des grandes installations (SOLEIL, UPMC-LCPMR), la chimie des rayonnements (CEA-NIMBE), les systèmes microfluidiques (CEA-NIMBE) et les dispositifs d'irradiation par les rayons X-mous et les simulations de dynamique moléculaire *ab initio* (UPMC - IMPMC), dans le but d'apporter des connaissances fondamentales sur les différents mécanismes impliqués dans la chimie déclenchée, en milieu aqueux, par des photons de haute énergie dans les domaines des rayons X mous et durs. Bien que très largement étudiée, la description de l'interaction rayonnement matière reste en effet encore incomplète, car il s'agit d'un problème complexe tant sur le plan spatial que temporel. Si l'interaction rayonnement matière a lieu dans un intervalle de temps très court (de l'ordre de 10^{-15} s), elle induit des modifications chimiques et biologiques qui impactent le système sur plusieurs heures. Par ailleurs, dans un environnement biologique, les molécules d'eau étant majoritairement présentes, elles demeurent la cible privilégiée des ionisations[1], [2]. La radiolyse de l'eau et les effets indirects induits aux biomolécules par les radicaux de l'eau sont donc d'un intérêt particulier[3].

Cette étude se concentre sur le cas particulier des rayons X de basse énergie (200 eV-2 keV), dits X mous, dans les liquides. Ces rayonnements, bien que très peu utilisés en radiothérapie, constituent en effet un système modèle pour la compréhension des évènements fortement ionisants que sont les ionisations en couche internes. Plus spécifiquement, lorsque des photons interagissent avec un système chimique, ils transfèrent une partie de leur énergie créant ainsi des excitations et ionisations dans la matière. Du fait de leur basse énergie, les rayons X-mous interagissent préférentiellement avec les électrons de la couche interne des atomes qui constituent la matière biologique, comme le carbone, l'azote ou l'oxygène, dès lors que l'énergie du photon incidente est supérieure à l'énergie de liaison de l'électron de cœur. Ce dernier est alors éjecté (Figure 1.(a)). Il s'agit d'une manière plus générale de l'effet photo-électrique, expliqué par Einstein (Prix Nobel 1921). Dans le cas d'atomes légers, tels que le carbone, l'azote ou l'oxygène, la lacune en

couche interne est ensuite préférentiellement comblée par un électron de la couche externe, conduisant à l'émission d'un électron Auger[4], comme l'illustre la Figure 1.(b).

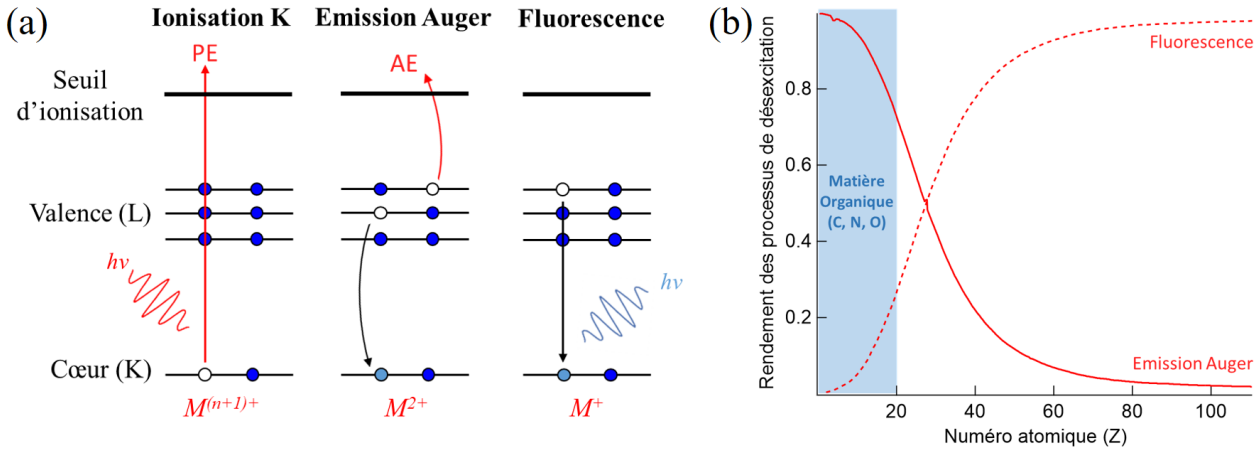

Figure 1: Schéma du processus de photo-ionisation en couche interne (a) effet photo-électrique puis désexcitation par effet Auger (émission d'électron Auger) ou fluorescence (émission de photon). (b) Probabilité des deux processus de désexcitations, et mise en lumière de la désexcitation préférentielle par voie non radiative (effet Auger) dans le cas d'échantillons biologiques (matière organique).

L'ionisation en couche interne conduit donc à l'émission d'électrons de basse énergie (<1 keV), très ionisants. Ces électrons sont en effet des particules à haut transfert d'énergie linéique (TEL), qui déposent toute leur énergie dans des volumes nanométriques, conduisant à la formation de « clusters » d'ionisation[5]. Ainsi, même si les ionisations en couche internes restent des évènements rares pour les rayonnements de haute énergie (tels que les rayonnements en radiothérapie), ils n'en restent pas moins d'une importance capitale en raison de leur grande efficacité radio-biologique[6], [7]. Des études pionnières conduites par l'équipe de D.T. Goodhead à la fin du 20ème siècle ont par exemple démontré que les rayons X-mous étaient plus efficaces que les rayons X de plus haute énergie, à dose équivalente, pour conduire à l'inactivation de cellules biologiques[8]. Ce phénomène a rapidement été mis en lien avec la structure de trace, c'est-à-dire la répartition des ionisations dans la matière[9]. Plus précisément, ces études ont mis en évidence l'importance des électrons de basse énergie dans les effets létaux des particules de bas TEL[10], [11]. Pour autant, l'étude des rayons X-mous dans un milieu condensé, tel que l'eau liquide, est rendue difficile en raison de la faible pénétration de ces rayonnements (quelques microns pour des photons de 1 keV).

L'un des principaux objectifs de cette thèse est d'étudier la production d'espèces radiolytiques dans les échantillons aqueux, afin de comprendre les mécanismes physico-chimiques impliqués lors de l'irradiation d'un soluté par des photons X-mous. En particulier, elle s'est attaché à la compréhension des conséquences radiochimiques d'une ionisation en couche interne autour des seuils K d'atomes spécifiques (C, N, O ou sels métalliques), généralement présents en grande abondance dans les échantillons biologiques. Enfin, cette thèse apporte également une description de ces évènements d'ionisation en couche interne à des temps ultra-courts (femto seconde) par le biais d'études de spectroscopie d'électrons. En outre, cette approche permet de sonder les évènements initiateurs de la chaîne complexe des phénomènes physico-chimique pouvant mener à des dommages sur des biomolécules, tels que l'émission d'électrons Auger.

I. Chimie initiée dans les liquides par l'exposition aux rayons X-mous

Afin d'étudier les processus de radiolyse de l'eau dans les liquides, nous avons décidé de quantifier la production des radicaux de l'eau, tel que le radical hydroxyle ($HO^{\cdot}$). La forte réactivité de ce radical empêche sa quantification directe. Une stratégie est donc de mettre en place un système de sonde chimique basée sur la quantification de produits stables, formés par réaction de la sonde avec les radicaux produits dans la solution[12]. Dans la littérature, les expériences de radiolyse de l'eau sont bien souvent réalisées pour des énergies de photon supérieures à 1.5 keV en utilisant le dosimètre de Fricke (oxydation du sulfate de fer)[13]. Certaines études ont néanmoins été conduites plus récemment[14], [15] pour les rayons X de plus basse énergie. Elles ont montré que le rendement des radicaux $HO^{\cdot}$, mesuré quelques microsecondes après le dépôt d'énergie, présentaient un minimum de production autour de 1.5 keV. Une telle diminution est généralement attribuée à de fortes densités d'ionisation, qui s'accompagnent de réactions précoces des radicaux au sein des traces[9]. Plusieurs études théoriques modélisant le parcours des électrons[16], [17] ou des photons[18], [19] dans l'eau liquide, ont par ailleurs reproduit ce minimum. Pour autant, les données expérimentales de la littérature ne permettent pas de rendre compte de la structure spatiale du dépôt d'énergie dans la trace, caractéristique du TEL de la particule. Le but de cette partie est donc d'optimiser à la fois les techniques

d'irradiation et les techniques de détection des dommages/radicaux produits, afin de permette l'étude des effets de ces rayons X-mous peu pénétrants.

Dans le cadre de cette thèse, nous avons choisi d'utiliser un système de détection par fluorescence, basé sur le piégeage chimique des radicaux $HO^{\cdot}$ par des ions benzoate (principe détaillé dans la Figure 2). Cette molécule aromatique réagit spécifiquement avec les radicaux hydroxyles, conduisant à la production d'une molécule fluorescente: le 2-hydroxybenzoate (2-HOBz)[20]. Grâce à l'extrême sensibilité de la technique de fluorescence (seuil de détection ~10^{-6} mol/L) et la stabilité chimique du système[21], il est possible de suivre la production des radicaux plusieurs heures après l'irradiation. Grâce à l'évolution linéaire du signal de fluorescence en fonction de la dose, il est possible de remonter directement au rendement de production des radicaux G($HO^{\cdot}$).

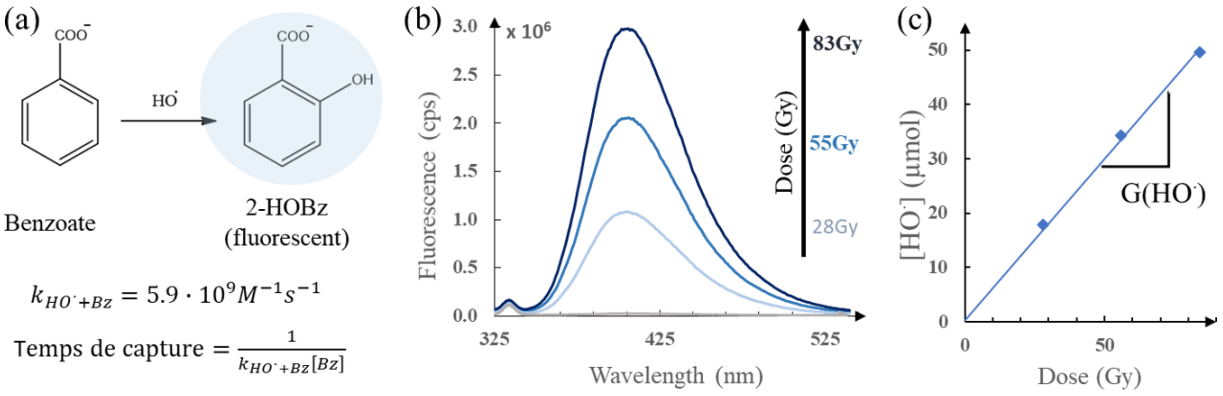

Figure 2: Principe de la méthode de piégeage des radicaux hydroxyles: (a) Réaction d'hydroxylation du benzoate et vitesse de réaction, (b) Détection du signal de fluorescence des échantillon irradiés, (c) Évolution de la concentration des radicaux hydroxyles en fonction de la dose et détermination du rendement de production (G($HO^{\cdot}$)).

Des irradiations ont été initialement conduites dans une cuve statique contenant 1 mL d'échantillon (profondeur 1 cm), sur la ligne METROLOGIE du synchrotron SOLEIL. Cela a été rendu possible grâce à l'utilisation d'un système d'extraction du faisceau synchrotron à l'air (dispositif IRAD[22], [23]). Nous avons ainsi mesuré l'évolution du rendement de production du radical hydroxyle en fonction de l'énergie des photons, qui présente un minimum vers 1.28 keV (Figure 3.(a)). Ce minimum, en bon accord avec les données de la littérature, semble caractéristique des « clusters » d'ionisations.

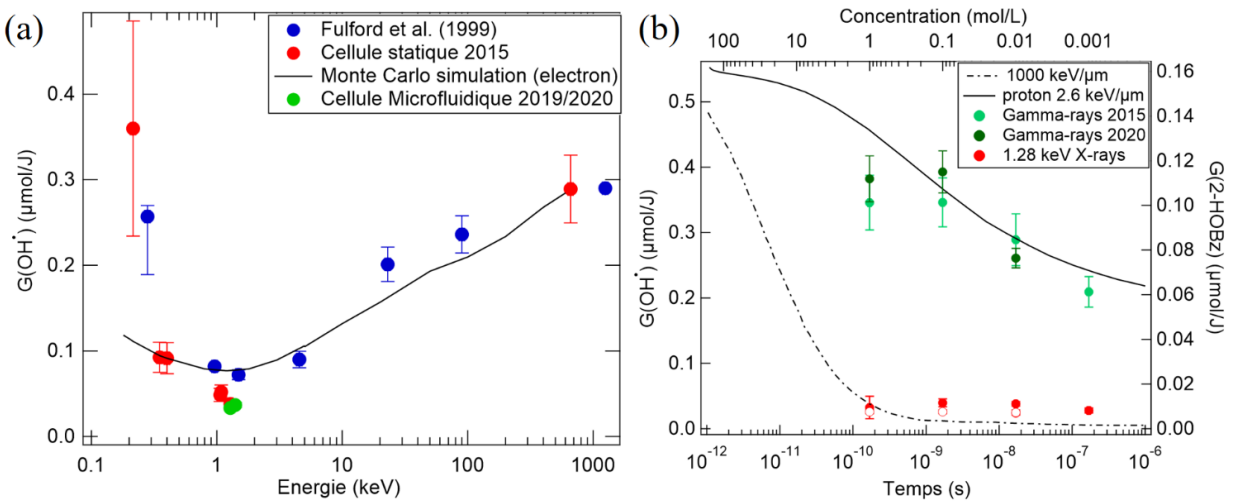

Figure 3: Production de radicaux hydroxyles dans des solutions de benzoate irradiées par des rayons X-mous : (a) Rendement G($HO^{\bullet}$) en fonction de l'énergie de photon, (b) Évolution temporelle du rendement. Les mesures en cuve statique (symboles pleins) et en cellule microfluidique (symboles vides) sont comparées aux mesures de Fulford et al [14], et à des simulations

Par ailleurs, en augmentant la concentration de la sonde dans le milieu, il est également possible d'avoir des informations sur la répartition spatiale des espèces produites à des temps plus courts . En irradiant des solutions de benzoate de sodium de concentration croissantes (1 mM à 1 M), il a ainsi été possible de mesurer les rendements de production dans une gamme de temps allant de 170 ns à 170 ps. Ces mesures, couplées à des simulations de Monte-Carlo conduites par Benoit Gervais (GANIL, Caen), ont permis de démontrer que les rayons X se comportaient comme des particules de haut TEL. Ces données ont fait l'objet d'un premier papier[24].

En raison de la faible pénétration des rayons X-mous, la dose déposée est beaucoup plus importante en surface et conduit à un dépôt très inhomogène de l'énergie. Afin d'optimiser l'irradiation, une cellule microfluidique, initialement développée pour des mesure de microscopie X (STXM [25]), a été adaptée pour les expériences d'irradiations sous rayons X-mous. Cette cellule microfluidique (présentée en Figure 4.(a)), constituée de deux membranes de silicium, placées en sandwich et maintenue par un un système de serrage, permet la circulation du fluide dans un canal de 5 µm d'épaisseur. La cellule microfluidique comprend une fenêtre ultrafine de nitrure de silicium (0.3 mm x 1mm, 150 nm d'épaisseur), choisie pour sa très bonne transmission du faisceau X-mous. Afin d'optimiser la robustesse du système, les premières irradiations ont été conduites sur un

système comportant une seule fenêtre à l'avant de la cellule (fenêtre d'irradiation). Il a donc fallu penser à un système d'alignement sur ligne synchrotron.

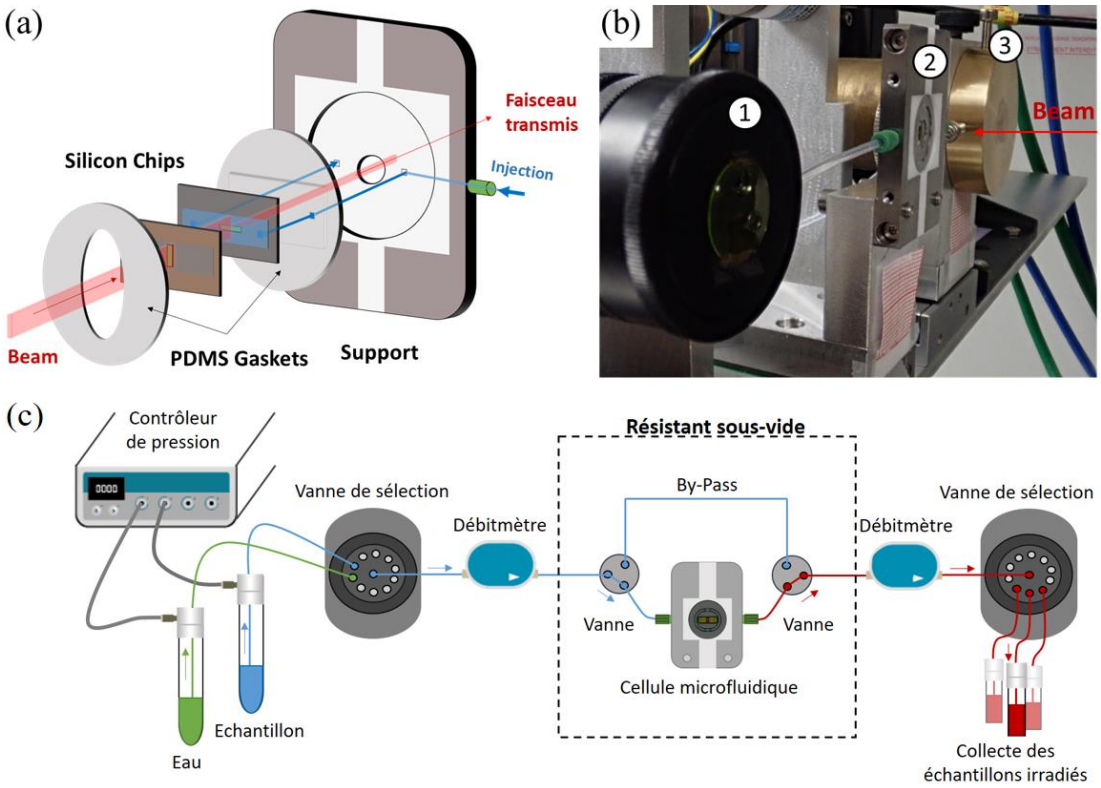

Figure 4: Cellule microfluidique pour irradiation sur ligne synchrotron: (a) Schéma du dispositif, (b) Photographie de l'installation sur la ligne METROLOGIE : ① Scintillateur + Caméra, ② Cellule microfluidique, ③ Photodiode avec un masque en laiton, (c) Schéma du circuit microfluidique permettant l'injection et la collection des échantillons.

Le premier système ① permet d'ajuster la géométrie du faisceau synchrotron à celle de la cellule, grâce à une cible aux dimensions de la cellule gravée sur le YAG:Ce. La photodiode ②, quant à elle, permet de déterminer la dose déposée dans les échantillons. Un masque en laiton couvre la surface de détection, afin de ne laisser qu'une ouverture aux dimensions de la fenêtre d'irradiation. Cela permet à la fois d'aligner la cellule, en utilisant les positions relatives connues de chacun des éléments, mais également de mesurer précisément la dose déposée.

La cellule est intégrée dans un circuit microfluidique alimenté par un contrôleur en pression (Figure 4.(c)). Des vannes permettent de sélectionner les chemins de circulation du fluide et des débitmètres, placés en amont et en aval de la cellule permettent de mesurer précisément le débit. Ce dernier point est très important puisqu'il permet de déterminer

le temps d'exposition du fluide qui circule dans la cellule. Une fois irradié, l'échantillon est collecté et analysé par la suite par fluorimétrie.

Le développement de cette cellule, couplé à l'utilisation du benzoate comme dosimètre chimique, a démontré une grande sensibilité et une grande stabilité. Les résultats obtenus sont en bon accord avec les données obtenues en cellule statique, comme l'illustre la Figure 3. Ce développement technique a par ailleurs fait l'objet de la publication d'un deuxième article[26].

Par la suite, afin d'optimiser les irradiations et d'accéder à des énergies de photons plus basses (seuil K du carbone par exemple), de nombreux développements ont été effectués. Une première étape a été l'intégration de la cellule dans une chambre sous vide. Ce dispositif a été testé sur la ligne PLEIADES du synchrotron SOLEIL. Afin de permettre l'alignement dans cette espace réduit et inaccessible une fois monté, une seconde fenêtre a été ajoutée à l'arrière de la cellule microfluidique pour permettre de travailler en transmission. Un dispositif, utilisant des cellules de silicium photomultiplicatrices, a été installé à l'arrière de la cellule microfluidique afin de détecter le faisceau transmis. Ce système a grandement facilité l'alignement de la cellule sur les lignes synchrotron. Enfin, des optimisations ont été faites visant à limiter le temps d'expérience. Cela a été possible grâce à l'automatisation des irradiations *via* la programmation du système microfluidique (débits, collecte). D'un point de vue analytique, des développements sont en cours pour permettre une analyse du fluide directement à la sortie de la cellule microfluidique (UV-visible, spectrométrie de masse). Ces dispositifs d'analyse «en ligne» permettent d'éviter la collecte des échantillons et constituent ainsi un gain de temps évident. D'ors et déjà, grâce au développement de ce système microfluidique, l'irradiation des échantillons aqueux est trois à quatre fois moins coûteuse en temps. Cela a notamment permis d'étudier différents seuils d'ionisation. En particulier, nous nous sommes intéressés aux seuils K des ions métalliques. Des études théoriques suggèrent en effet que l'ionisation en couche interne d'éléments comme le magnésium conduit à des transferts d'énergie localisés dans la première sphère de solvation de l'ion. Pour autant, nous n'avons pu détecter aucun effet de l'ionisation en couche interne de ces ions sur les rendements de production des radicaux hydroxyles. Pour autant, nous avons noté des différences de rendement en présence ou

absence de sels lors de l'irradiation par des rayons X de basse énergie. Ces phénomènes semblent pourtant ne pas intervenir pour des particules de plus bas LET (rayons gamma).

Afin d'apporter une description globale des processus d'excitation ou ionisation en couche interne et tenter de comprendre les transfert d'énergie solvant/solutés intervenant aux temps ultra-courts, une deuxième partie du projet s'est attachée à l'étude spectroscopique de solutions aqueuses.

II. Études des évènements précurseurs : l'ionisation en couche interne

Les processus de photo-ionisation (effet photo-électrique et effet Auger) interviennent dans des temps ultra-courts (femto-seconde). Pour autant, ces processus constituent l'élément déclencheur d'une cascade d'évènements conduisant bien souvent à l'inactivation complète des cellules irradiées[23], [27], [28]. Il est donc nécessaire de comprendre les changements électroniques initiés au sein des molécules afin d'apporter une description complète du processus de dépôt d'énergie. Dans ce domaine, la spectroscopie de photoélectrons (PES ou XPS en anglais) est très largement développée. Cette technique, basée sur l'effet photo-électrique, consiste à analyser l'énergie cinétique des électrons arrachés à la matière sous l'irradiation d'un faisceau X. L'énergie cinétique des électrons (E_k) est directement reliée à l'énergie des photons ($E = h\nu$): $E_k = E - E_B$[1]. Il est donc possible d'identifier les éléments constituant l'échantillon en remontant à leur énergie de liaison (E_B). En analyse XPS, le signal mesuré dépend non seulement de la concentration atomique mais également de l'environnement chimique de ces atomes. Il s'agit donc d'obtenir des informations sur la structure même de l'échantillon. Afin de limiter les collisions des électrons éjectés avec les molécules de gaz (freinage), les mesures XPS sont classiquement effectuées sous ultra-vide ($<10^{-6}$ mbar) et donc particulièrement utilisées pour l'analyse des surfaces d'échantillons solides[29]. Néanmoins, de nouveaux systèmes de jet liquide sous vide ont vu le jour afin de permettre l'analyse de liquides hautement volatils, tels que les solutions aqueuses[30]. Ces dispositifs, illustrés en Figure 5, consistent à injecter à forte pression (plusieurs bars) une solution à travers un capillaire en verre, le « nozzle ». Il en résulte un jet (Ø40 µm à 60 µm) stable sur quelques centimètres.

[1] h est la constante de Planck, et ν est la fréquence du rayonnement incident.

L'injection d'un fluide hautement volatile dans un environnement ultravide conduit à son évaporation et donc une augmentation locale de pression. Un système de pompage différentiel est donc nécessaire pour assurer la stabilité de l'expérience. D'autre part, il est important d'optimiser l'alignement du jet avec le faisceau synchrotron afin de pouvoir détecter les électrons de la phase liquide. Les électrons arrachés sont ensuite collectés par l'analyseur pour permettre leur détection. Afin de déterminer leur énergie cinétique, des analyseurs de type hémisphériques sont classiquement utilisés.

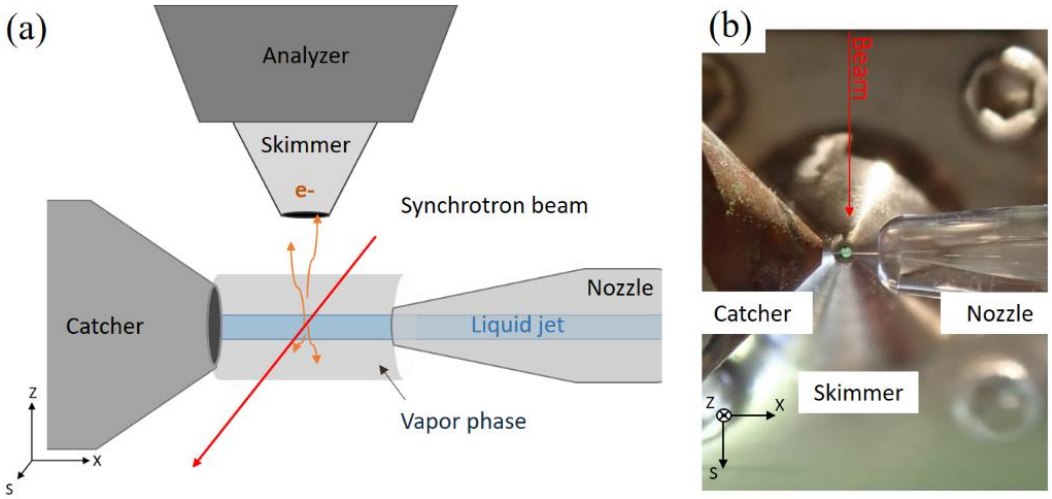

Figure 5: Dispositif d'analyse XPS sur micro-jet liquide sous vide: (a) schéma de principe, (b) photographie du montage.

Le dispositif de jet liquide sous vide développé à PLEIADES, présenté en Figure 5, utilise un système de «catcher» chauffé, qui permet de collecter le fluide étudié par XPS, afin de l'analyser par d'autre méthodes. Une première étape a été de démontrer les performances d'un tel dispositif pour l'étude de molécules solvatées, allant de la petite molécule chimique jusqu'aux grandes biomolécules, telles que des protéines. En outre, une étude complète a été réalisée sur le benzoate pour connaître en détail sa structure électronique, la manière dont il se répartit dans le jet liquide et les effets de concentration de la solution sur cette répartition.

Il était également important de vérifier que le passage de biomolécules fragiles dans le dispositif de jet liquide sous vide, et particulièrement leur récupération *via* le catcher chauffé, ne modifiait pas les propriétés de ces molécules (fragmentation, dénaturation, *etc*). Ces tests ont été conduits sur l'albumine de sérum bovin (BSA), une protéine bien connue et pouvant être utilisée à haute concentration (~0.5 mM – 40 g/L) [31]. Grâce à ce système,

des spectres de la BSA en phase liquide ont été enregistrés pour la première fois avec des mesures XPS haute résolution. Grâce à différentes techniques de caractérisation (UV-vis, électrophorèse sur gel, dichroïsme circulaire), il a été démontré que la protéine avait conservé sa conformation naturelle après son passage dans le jet liquide. Par comparaison des résultats en phase liquide et solide (analyse XPS en laboratoire), il a été possible de mettre en évidence les effets du solvant sur les propriétés électroniques du soluté. Plus précisément, les diagrammes des différentes bandes électroniques de la BSA (solvatée ou non) ont pu être déterminées.

Dans le cadre du projet HighEneCh, le micro-jet liquide a également été couplé à un spectromètre en temps de vol de type bouteille magnétique, pour permettre des mesures uniques de coïncidence électron-électron. Ce système consiste à former des lignes de champ magnétique, à l'aide d'un aimant, pour renvoyer vers le détecteur tous les électrons produits au niveau de l'interaction échantillon/faisceau X. L'énergie cinétique des électrons est ensuite déterminée en mesurant leur temps de vol (temps pour atteindre le détecteur). Grâce à la structure temporelle pulsée du synchrotron, et le fait que ce système collecte quasiment tous les électrons, il est possible de corréler chaque photoélectron avec les électrons Auger associés à son émission. Les mesures XPS (photoélectrons) apportent des informations sur l'énergie des électrons émis et sur la dissipation d'énergie due à la présence du solvant. Les processus de désexcitation coulombienne (ICD) et de transfert d'électrons (ETMD)[2], qui surviennent en phase condensée, ont été décrits pour la première fois par Cederbaum *et al.*[32]–[34]. Lorsque ces dernières sont mises en corrélation avec l'émission d'électrons Auger, elles permettent de fournir des informations sur les différentes voies de relaxation des biomolécules en milieu aqueux. Plus précisément, les mesures en coïncidences permettent de filtrer tous les évènements, pour lesquels un, ou deux électrons, ont été détectés (photoélectron et Auger électrons), en fonction de l'énergie cinétique des photoélectrons. Nous avons ainsi pu obtenir les spectres Auger issus de l'ionisation spécifique d'une fonction chimiques dans différentes molécules solvatées comportant un cycle aromatique. Les différences observées dans les spectres Auger corrélés aux photoélectrons issus de différents types de carbone montrent que différent états finaux

[2] *Interatomic/Intermolecular Coulombic Decay (ICD et Electron-Transfer-Mediated Decay (ETMD) respectivement.*

sont peuplés. Ils nous informent donc sur la structure électronique des dications formés et l'énergie des différents électrons émis dans le milieu. Ces informations sont essentielles pour les calculs théoriques, qui pourront ainsi permettre de simuler les processus initiaux conduisant à la dégradation ou fragmentation de la molécule.

Conclusion

Cette thèse, à l'interface chimie-physique, présente deux approches complémentaires pour l'étude des irradiations par des rayons X-mous. Prenant pour point de départ la description de la radiolyse de l'eau dans le cas particulier de ces rayonnements, elle cherche ensuite à remonter aux processus initiaux, à savoir la photo-ionisation. Toutes ces études ne pourraient être rendue possibles sans les développements techniques associés à l'étude de ces radiations peu pénétrantes. En particulier, ce projet décrit la mise en place et le développement d'une cellule microfluidique utilisée avec succès sur des lignes synchrotron. Ce dispositif, par ses caractéristiques (dimensions, résistance chimique, couplage analytique), offre une grande adaptabilité. En outre, si ce projet s'est focalisé sur l'analyse des radicaux de l'eau, les échantillons utilisés ont toutefois été très divers, allant de la petite molécule chimique (benzoate de sodium) à des systèmes beaucoup plus complexes comme des protéines (Cytc).

Les résultats présentés dans cette thèse sont un premier pas vers la compréhension des dommages induits par les électrons de basse énergie. Les différentes expériences d'irradiations ont toutefois mis en évidence la difficulté d'observer les processus d'ionisation en couche interne. En particulier, les effets de seuils prédit théoriquement sont complexes à observer expérimentalement. Les études spectroscopiques en phase liquide semblent cependant très prometteuses pour étayer la description des effets des électrons de basse énergie produits lors de la photoionisation. L'analyse des résultats en coïncidence est par ailleurs toujours en cours. Enfin, il faut soulever l'étroite collaboration avec des théoriciens venant soutenir les résultats de ce manuscrit. Il faut à ce sens noter que, de manière analogue, de nombreux résultats expérimentaux viennent eux aussi compléter les données d'entrée des simulations, en particulier pour les calculs de type Monte-Carlo.

Références

[1] S. Le Caër, "Water radiolysis: Influence of oxide surfaces on H2 production under ionizing radiation," *Water (Switzerland)*, vol. 3, no. 1, pp. 235–253, 2011.

[2] C. Ferradini and J.-P. Jay-Gerin, "La radiolyse de l'eau et des solutions aqueuses : historique et actualité," *Can. J. Chem.*, vol. 77, no. 9, pp. 1542–1575, 1999.

[3] G. V. Buxton, *Radiation Chemistry - Present Status and Future Trends*, vol. 4, no. 3. 2001.

[4] R. W. Howell, "Auger processes in the 21st century," *Int. J. Radiat. Biol.*, vol. 84, no. 12, pp. 959–975, 2008.

[5] D. T. Goodhead, "Energy deposition stochastics and track structure: What about the target?," *Radiat. Prot. Dosimetry*, vol. 122, no. 1–4, pp. 3–15, 2006.

[6] A. Chetioui, I. Despiney, L. Guiraud, L. Adoui, L. Sabatier, and B. Dutrillaux, "Possible Role of Inner-shell Ionization Phenomena in Cell Inactivation by Heavy Ions," *Int. J. Radiat. Biol.*, vol. 65, no. 5, pp. 511–522, Jan. 1994.

[7] A. Boissière *et al.*, "DNA core ionization and cell inactivation," *Radiat. Res.*, vol. 167, no. 4, pp. 493–500, 2007.

[8] M. N. Cornforth *et al.*, "Radiobiology of ultrasoft X rays. III. Normal human fibroblasts and the significance of terminal track structure in cell inactivation," *Radiat. Res.*, vol. 119, no. 3, pp. 511–522, 1989.

[9] H. Nikjoo and D. T. Goodhead, "Track structure analysis illustrating the prominent role of low-energy electrons in radiobiological effects of low-LET radiations," *Phys. Med. Biol.*, vol. 36, no. 2, pp. 229–238, 1991.

[10] H. Nikjoo, P. ONeill, D. Goodhead, and M. Terrissol, "Computational modelling of low-energy electron-induced DNA damage by early physical and chemical events," *Int. J. Radiat. Biol.*, vol. 71, no. 5, pp. 467–483, 1988.

[11] H. Nikjoo and L. Lindborg, "RBE of low energy electrons and photons," *Phys. Med. Biol.*, vol. 55, no. 10, 2010.

[12] S. M. Pimblott, J. A. Laverne, D. M. Barteis, and C. D. Jonah, "Reconciliation of transient absorption and chemically scavenged yields of the hydrated electron in radiolysis," *J. Phys. Chem.*, vol. 100, no. 22, pp. 9412–9415, 1996.

[13] R. Watanabe, N. Usami, and K. Kobayashi, "Oxidation yield of the ferrous ion in a fricke solution irradiated with monochromatic synchrotron soft x-rays in the 1.8-10 kev region," *Int. J. Radiat. Biol.*, vol. 68, no. 2, pp. 113–120, 1995.

[14] J. Fulford, P. Bonner, D. T. Goodhead, M. A. Hill, and P. O'Neill, "Experimental determination of the dependence of OH radical yield on photon energy: A comparison with theoretical simulations," *J. Phys. Chem. A*, vol. 103, no. 51, pp. 11345–11349, 1999.

[15] L. Vyšín *et al.*, "Chemical Dosimetry in the 'Water Window': Ferric Ions and Hydroxyl Radicals Produced by Intense Soft X Rays.," *Radiat. Res.*, vol. 000, 2020.

[16] J. L. Magee and A. Chatterjee, "Theory of the chemical effects of high-energy electrons," *J. Phys. Chem.*, vol. 82, no. 20, pp. 2219–2226, Oct. 1978.

[17] M. A. Hill and F. A. Smith, "Calculation of initial and primary yields in the radiolysis of water," *Radiat. Phys. Chem.*, vol. 43, no. 3, pp. 265–280, 1994.

[18] H. Yamaguchi, "A prescribed diffusion model of a many-radical system considering electron track structure in water," *Int. J. Radiat. Appl. Instrumentation. Part*, vol. 30, no. 4, pp. 279–284, 1987.

[19] H. Yamaguchi, "A spur diffusion model applied to estimate yields of species in water irradiated by monoenergetic photons of 50 eV-2 MeV," *Int. J. Radiat. Appl.*

Instrumentation. Part, vol. 34, no. 5, pp. 801–807, 1989.

[20] W. A. Armstrong and D. W. Grant, "The Aqueous Benzoate System as a Sensitive Dosimeter for Ionizing Radiations," *Can. J. Chem.*, vol. 38, no. 6, pp. 845–850, 1960.

[21] R. Musat, S. Moreau, F. Poidevin, M. H. Mathon, S. Pommeret, and J. P. Renault, "Radiolysis of water in nanoporous gold," *Phys. Chem. Chem. Phys.*, vol. 12, no. 39, pp. 12868–12874, 2010.

[22] M. A. Herve Du Penhoat *et al.*, "Lethal effect of carbon K-shell photoionizations in Chinese hamster V79 cell nuclei: Experimental method and theoretical analysis," *Radiat. Res.*, vol. 151, no. 6, pp. 649–658, 1999.

[23] B. Fayard *et al.*, "Cell Inactivation and Double-Strand Breaks: The Role of Core Ionizations, as Probed by Ultrasoft X Rays," *Radiat. Res.*, vol. 157, no. 2, pp. 128–140, 2002.

[24] L. Huart *et al.*, "Soft X-ray Radiation and Monte Carlo Simulations: Good Tools to Describe the Radiation Chemistry of Sub-keV Electrons," *J. Phys. Chem. A*, vol. 124, no. 10, pp. 1896–1902, 2020.

[25] C. Gosse, S. Stanescu, J. Frederick, and S. Lefrançois, "A flow cell for soft X-ray spectromicroscopy in liquid media Charlie," *J. Mater. Chem. B*, vol. 6, no. 35, pp. 7634–7639, 2020.

[26] L. Huart *et al.*, "A microfluidic dosimetry cell to irradiate solutions with poorly penetrating radiations: a step towards online dosimetry for synchrotron beamlines," *J. Synchrotron Radiat.*, vol. 28, no. 3, pp. 778–789, 2021.

[27] K. Kobayashi, K. Hieda, H. Maezawa, Y. Furusawa, M. Suzuki, and T. Ito, "Effects of k-shell x-ray absorption of intracellular phosphorus on yeast cells," *Int. J. Radiat. Biol.*, vol. 59, no. 3, pp. 643–650, 1991.

[28] S. Saigusa, Y. Ejima, K. Kobayashi, and M. S. Sasaki, "Induction of chromosome aberrations by monochromatic x-rays with resonance energy of phosphorus k-shell absorption edge," *Int. J. Radiat. Biol.*, vol. 61, no. 6, pp. 785–790, 1992.

[29] S. Hofmann, *Auger- and X-Ray Photoelectron Spectroscopy in Materials Science: A User-Oriented Guide*. 2013.

[30] M. Faubel, B. Steiner, and J. P. Toennies, "Photoelectron spectroscopy of liquid water, some alcohols, and pure nonane in free micro jets," *J. Chem. Phys.*, vol. 106, no. 22, pp. 9013–9031, 1997.

[31] T. Peters, *All About Albumin*. Elsevier, 1995.

[32] L. S. Cederbaum, J. Zobeley, and F. Tarantelli, "Giant intermolecular decay and fragmentation of clusters," *Phys. Rev. Lett.*, vol. 79, no. 24, pp. 4778–4781, 1997.

[33] R. Santra, J. Zobeley, and L. S. Cederbaum, "Electronic decay of valence holes in clusters and condensed matter," *Phys. Rev. B - Condens. Matter Mater. Phys.*, vol. 64, no. 24, pp. 1–10, 2001.

[34] T. Jahnke, "Interatomic and intermolecular Coulombic decay: The coming of age story," *J. Phys. B At. Mol. Opt. Phys.*, vol. 48, no. 8, 2015.

Sorbonne Université

Doctoral School n°397: Physique et Chimie des Matériaux

Conducted at the Institut de Minéralogie, de Physique des Matériaux et de Cosmochimie (Sorbonne Université), at the Laboratoire de Nanosciences et Innovation pour les Matériaux, la Biomédecine et l'Énergie (CEA Saclay) and at the SOLEIL Synchrotron.

Inner shell ionization effects on molecules of biological interest in an aqueous medium.

---

by Lucie HUART

PhD thesis in Physics and Chemistry

Directed by Marie-Anne Hervé du PENHOAT, Jean-Philippe RENAULT and Christophe NICOLAS.

Presented and defended on 17/01/2022

In front of a jury composed of :

Eckart RÜHL	Professor (Freie Universität Berlin)	Referee
Jean-Luc RAVANAT	Research Director, HDR (CEA Grenoble)	Referee
François ROCHET	Professor, HDR (Sorbonne Université)	Jury member
Sylwia PTASINSKA	Associate Professor (University of Notre Dame)	Jury member
Sandrine LACOMBE	Professor, HDR (Université Paris-Saclay)	Jury member
M.-A.HERVE DU PENHOAT	Associate Professor, HDR (Sorbonne Université)	PhD director
Jean-Philippe RENAULT	CEA Researcher, HDR (CEA Saclay)	Supervisor (invited)
Christophe NICOLAS	Beamline Scientist (Synchrotron SOLEIL)	Supervisor (invited)

"Chacun de nous, dans sa vie, a sa propre montagne à gravir"

Mike Horn

Acknowledgments

Voilà un nouveau chapitre qui se tourne. Je souhaiterai profiter de ces quelques page pour remercier tous ceux qui m'ont accompagné, de près ou de loin dans cette belle aventure. Je vous remercie sincèrement pour ces trois années qui représentent pour moi une expérience extrêmement riche sur tous les niveaux et dont je garderai un très bon souvenir.

En ce sens je commencerai par remercier **SORBONNE UNIVERSITÉ** ainsi que l'ensemble des membres du jury pour l'intérêt porté à mon travail et leurs commentaires constructifs. Je les remercie pour avoir examiné mon travail avec cette grande expertise, ainsi que pour leurs encouragements et leurs éloges qui me vont droit au cœur. Merci à **François ROCHET** d'avoir accepté la tâche de présider mon jury de thèse, et pour les remarques fort utiles qu'ils m'a adressées. Je remercie très sincèrement **Eckart RÜHL** et **Jean-Luc RAVANAT** qui ont accordé un temps précieux à la revue de ce manuscrit. Je leur sais gré de leurs commentaires positifs et de leurs remarques qui ont permis d'améliorer la qualité finale de ce mémoire. J'exprime également tous mes remerciements à **Sylwia PTASINSKA** ainsi que **Sandrine LACOMBE** pour avoir accepté d'apporter leur jugement sur la qualité de mon travail lors de la soutenance.

Je tiens ensuite à remercier les personnes sans qui ce projet n'aurait pas pu avoir eu lieu à savoir ma directrices et mes encadrants de thèse.

Tout d'abord **Marie-Anne**, ma directrice de thèse. Merci de m'avoir fait confiance en me permettant de rejoindre ce projet. Merci d'avoir été un modèle de rigueur scientifique pour ton suivi attentif de toutes les expériences qui filaient en tout sens ! Merci de m'avoir accompagnée tout au long de cette thèse et de m'avoir laissé la liberté de développer le projet à mon goût.

Je remercie **Jean-Philippe**, mon co-encadrant. Un grand merci à toi pour ton encadrement, et ta confiance au quotident. Merci de m'avoir accompagnée, soutenue et conseillée pendant ces trois années de thèse. Merci pour ces nombreux échanges scientifiques etpour toutes tes idées florissantes qui ont rendu ce projet de plus en plus intéressant. Enfin merci pour ta confiance dans mes capacités et en mon raisonnement scientifique.

Christophe, merci pour ta bonne humeur. Grâce à toi j'ai découvert le monde incroyable du synchrotron. J'ai pris beaucoup de plaisir pendant ces runs, pas toujours simple mais toujours très enrichissants ! Merci pour ton partage, ta patience et ta compréhension. Merci pour avoir su te dupliquer ou tripliquer et ainsi t'être rendu disponible pour répondre à mes questions, m'expliquer la spectroscopie, corriger le manuscrit et faire des blagues pour remonter le moral des troupes. Merci pour ton enthousiasme, ta joie de vivre communicative et ton positivisme. Merci pour nos petites discussions (sociétales, cuisine, musique, famille) qui font que chaque jour j'étais contente de venir travailler.

Enfin merci à **Jérôme**. J'ai été très chanceuse de participer au beau projet de la bouteille magnétique mais plus encore de croiser ton chemin. J'ai beaucoup apprécié travailler avec toi et te remercie pour ton écoute et présence au quotidien. Je garderai en mémoire le

binôme de choc que vous formez avec Christophe avec qui faire des manips lorsque rien ne marche correctement reste pour autant un vrai bonheur !

Pour conclure, je n'aurais pas pu rêver meilleur encadrement que vous quatre réunis. Votre investissement, vos savoirs/compétences complémentaires et vos qualités humaines confèrent toute sa force au projet. Je m'estime extrêmement chanceuse d'avoir pu réaliser ma thèse dans cet environnement pluridisciplinaire des plus enrichissants tant scientifiquement qu'humainement. Pour cela, je ne vous remercierai jamais assez !

Les collaborations scientifiques n'ont pas manquées dans ce travail et j'aimerais remercier les nombreuses personnes qui m'ont ouvert les portes de leur labo ou tout simplement pris le temps de m'aider quand j'en ai eu besoin.

Je remercie tout particulièrement **Corinne CHEVALLARD** pour de m'avoir formée à la microfluidique mais également pour tout ton apport scientifique lors des discussions des résultats et stratégies abordées. Que ce soit au cours des temps de faisceau ou autour d'un café, tu as toujours su trouver le conseil avisé qui me permettait de continuer dans la bonne direction. Je remercie **Charlie GOSSE** également pour son aide dans le projet microfluidique et son apport scientifique lors de la rédaction des articles. Dans le même temps, j'en profite pour remercier **Stéphane LEFRANÇOIS** et **Stefan STANESCU** pour m'avoir permis de rejoindre le projet de la cellule microfluidique et de contribuer à son développement.

Merci à **Jocelyne LEROY** pour les mesures XPS sur échantillons solides réalisées au CEA.

Je remercie **Benoit GERVAIS** pour les simulations effectuées au CIMAP à Caen et son apport scientifique dans les articles.

Merci à **l'équipe du LCPMR** pour m'avoir accueillie et intégrée au sein du projet de la bouteille magnétique et au cours des temps de faisceau sur PLEIADES.

Je remercie également le Pr. **Nobuhiro KOSUGI** pour ses calculs théoriques des données XPS.

Je tiens à remercier également **Alexandre GIULIANI** de la ligne DESIRS pour son aide lors de l'analyse des échantillons irradiés. Merci de m'avoir permis d'utiliser le spectromètre de masse de la ligne ainsi que pour ton aide sur le projet de couplage avec la cellule.

Je remercie **Stéphane LORCY** de la ligne ANTARES pour m'avoir permis de réaliser des mesures MEB sur IPANEMA.

Je remercie enfin les laboratoires de Chimie, Biologie et surface de SOLEIL pour leur collaboration et leur disponibilité. Je remercie tout particulièrement **Stéphane KUBSKY** et **Blandine PINEAU** pour leur aide précieuse lors de mes mesures. Je remercie également **l'équipe de la ligne LUCIA** et **la ligne HERMES** pour leur accueil et soutien scientifique lors des temps de faisceaux. Je remercie également toute **l'équipe de METROLOGIE**, merci à **Pascal MERCERE** pour ces conseils et sa disponibilité. Merci **à Paulo DASILVA** pour son aide sur l'installation de nos expériences sur METRO mais également pour m'avoir initiée à l'apiculture !

Je remercie chaleureusement **Marine FOURNIER** et **Aashini RAJPAL** que j'ai eu la chance de superviser pendant leur stage. Merci pour votre implication. J'ai vraiment

apprécié travailler avec vous, et j'espère vous avoir apporté autant que vous m'avez apporté, à moi et au sujet ! C'est vous qui avez les rênes en main à présent et je suis très confiante quant à la réussite de vos projets respectifs !

Je remercie **l'équipe BIBIP** pour son accueil au sein de l'IMPMC. Merci pour vos conseils et votre écoute au cours des différentes réunions de laboratoire. Mais également pour les petits échanges du quotidien détour d'un couloir.

Je tiens à remercier chaleureusement toute l'équipe de la meilleure ligne de lumière de SOLEIL : **PLEIADES** ! Merci à **Aleksandar, Emmanuel** et **John** pour leur accueil, leurs conseils et leur aide pendant ces trois années. J'ai découvert tout un nouveau monde en arrivant à SOLEIL et il fut très enrichissant grâce à vous !

Je remercie bien entendu **l'équipe du LIONS** pour son accueil. Je n'oublierai pas les footings, les pauses cafés et le festival international de la fondue ! Je vous dis un peu moins merci pour les kilos superflus dus aux gâteaux en tout genre mais ça les valaient !

Il me reste à remercier l'ensemble des personnes que j'ai rencontrées, et qui font le quotidien de la thèse que ce soit au CEA, à Jussieu ou au Synchrotron. Ce sont autant de discussions que de raisons de garder un bon souvenir de mon passage chez vous. Je ne me risque pas à préciser les nom de peur de ne pas être exhaustive, mais vous vous reconnaitrez parmi ces groupes: **les triplettes, le thésarium, la team du 508, le groupe apiculture, les licornes atomiques et les coachs, la team "A table".** Merci à tous pour votre bonne humeur et votre présence au quotidien. Même si le Covid a un peu perturbé le quotidien, j'ai passé de super moments avec vous et aujourd'hui je ne remercie pas seulement des collègues mais de véritables amis. La place me manque pour pour pouvoir exprimer la pensée toute particulière que j'ai pour chacun d'entre vous mais il n'y a pas une seule fois où je suis venue à reculons au labo, et ça, je vous le dois certainement !

Je voudrais enfin remercier toutes les personnes extérieures au CEA qui m'ont entourée durant ces trois années.

Merci à **mes amis,** pour leurs encouragements constants et leur écoute. Merci pour votre curiosité même si ce monde de la recherche vous paraît parfois bien loin. Merci pour les soirées, dîners, skype, week-ends et j'en passe, qui m'ont permis de garder la tête aérée et les pieds sur terre !

Un grand merci aussi à **ma famille, à mes parents, mon frère et ma sœur** pour leur soutien indéfectible. Merci pour votre patience et votre curiosité. Merci de m'avoir encouragée, d'avoir toujours cru en moi et de m'avoir donné les moyens d'arriver jusqu'ici.

Contents

Introduction

Life on Earth is a life full of radiation. We are indeed constantly exposed to natural radiation, either electromagnetic (solar radiation, terrestrial external radiation) or corpuscular (cosmic radiation and natural radioactivity). The study of radiation-matter interactions is therefore fundamental to the interpretation of the evolution of our surrounding world. Motivated by the understanding of the damage mechanisms of ionizing radiation, the vast field of light-matter interaction is constantly enriched by developing new experimental techniques and theoretical methods.

When radiation penetrates matter, it interacts with it and transfers energy to it. The radiation is characterized as ionizing if the energy deposited is high enough to detach an electron from matter, i.e., energy superior to the electron's binding energy (BE). The amount of transferred energy is then characterized by the dose absorbed by the material, commonly expressed in gray (Gy) (equivalent to one joule absorbed per kilogram)[1]. Since the beginning of the twentieth century, scientists have attempted to understand the deleterious effects of ionizing radiations, such as X-rays and Gamma-rays (γ-rays), whose properties are widely used in the scientific field and the industry. Biological effects could result from a long series of multi-scales processes initiated by the deposition of energy by the incident ionizing radiation in the medium. If the interactions start at the atomic level (atto- to femtosecond time scales) and impact the molecular level (femto- to pico-second time scales), they can ultimately affect the behavior of a cell for hours or days and eventually lead to the death of a living organism after months to years. In order to improve therapeutic applications and radioprotection, the effects of primary radiations and secondary particles generated in matter (photons, electrons, ions) and their consequences at different levels must be described. Today, radiotherapy represents on average 50% of cancer treatments, complementing and sometimes even replacing surgical and chemical treatments[2]. The proper functioning of cells and their regeneration depends on the structural integrity of each deoxyribonucleic acid molecule (DNA) present in the nucleus of cells. It contains and regulates all the genetic information of the organism. The efficiency of radiotherapy treatments relies on the ability of high-energy ionizing radiation to induce critical lesions on such biomolecules (DNA strand breaks, genetic mutations, chromosomal

aberrations…)[3]. In living cells, biomolecules are often surrounded by water molecules that also interact with radiation. The decomposition of water through exposure, namely water radiolysis, leads to the production of highly reactive oxygen species (ROS)[4], [5]. The alterations of biomolecules induced by ROS are commonly referred to as indirect damage (indirect effect), as opposed to damage caused by the direct ionization of biomolecules (direct effect).

In the context of radiobiology, the effects of ionizing radiation have been investigated for many years to identify energy transfer mechanisms, degradation processes, and repair mechanisms of living cells[6], [7]. Experiments conducted on cellular inactivation demonstrated that low energy X-rays, namely soft X-rays (0.1-2 keV energy range), were more efficient at inducing lethal effects than higher energy photons for the same amount of absorbed dose[8]–[11]. They evidenced that biological effects can no longer be described by macroscopic concepts such as the dose, as they depend on many other factors (type and energy of radiation, type of biological system)[8], [10]. In the light of these studies, Goodhead and his co-workers highlighted the importance of bringing a detailed description of the energy deposition at the molecular scale[12], [13]. They thus investigated the repartition of ionizations and excitations generated along the path of the primary particle and secondary electrons, commonly defined as the "track"[14]. Thanks to combined experimental and theoretical studies, Goodhead and his colleagues established a correlation between intense and localized energy deposits at the nanometric scale (typically in the order of DNA lateral dimensions) and the lethal effects generated in cells. This model of ionization clusters established thanks to the use of soft X-rays, ascribes the lethal effect of high energy photons to ionization clusters produced at the end of low-energy electrons tracks[15], [16].

Subsequently, a second model presented by Chetioui *et al.*[17] suggested that initial events of cell killing could occur at the atomic scale itself. The authors first showed that cellular inactivation cross-sections were correlated to the ones of inner-shell ionizations (K-ionization) of DNA atoms, in the case of heavy ions. A later study, conducted on γ-rays and 100 keV electrons, evaluated that DNA core-ionization events could be responsible for 75% of cells' inactivation[18]. With the advent of synchrotron radiation and its large tunability in photon energies, X-rays were used to probe core-ionization events on

biological samples. Early experiments were conducted on biological samples at atmospheric pressure by comparing the effect of equal doses of radiation below and above the Phosphorus-K edge (2153 eV). Even for a minor elemental constituent of DNA such as phosphorus, results evidenced the lethal and mutagenic effectiveness of core ionizations[19]–[21]. Later, a dedicated set-up was developed to investigate the biological effect of carbon and oxygen atoms' core ionizations[22]–[25]. Unfortunately, given the high attenuation of soft X-rays in condensed matter (only a few microns in liquid water), the irradiation studies on liquid samples remain scarce in this range of energy. Many studies have thus been carried out on dry films of DNA components, such as 2-deoxy-D-ribose or plasmid DNA[26], [27]. However, the absence of an aqueous environment highly modifies irradiation processes, both in terms of direct and indirect effects. Water molecules are indeed known to play a significant role in the intrinsic properties of biomolecules (electronic and three-dimensional structure, interactions with molecular environment, charge transfer).

Spectroscopic techniques, in particular in the soft X-ray energy range, are particularly well adapted to determine such properties. Similarly, essential contributions in biology are brought by X-ray and electron-based techniques such as TEM (Transmission Electron Microscopy), STXM (Scanning Transmission X-ray Microscopy), STM (Scanning Tunneling Microscopy), for instance. The development of such techniques for the study of biomolecules raises the question of beam-induced radiation damages. Sample evolution under beam irradiation indeed remains one of the significant problems when using an ionizing radiation beam. It is all the more accurate with the arrival of the new fourth-generation synchrotrons, which produce a more intense and focalized photons beam.

The objective of this thesis is to propose a way to study core-ionization effects on solvated biomolecules. The driving issues are:

- What are the critical events that cause the biological effects of ionizing radiation?
- What is the role of core-ionization?

Two approaches are combined to bring a precise idea of the different physico-chemical processes that may occur during soft X-rays irradiation. The first one consists of a physico-chemical study of the radiobiological effects induced by soft X-rays irradiation. The second

one proposes a spectroscopic approach to investigate initial processes of dose deposition at the atomic scale: the photoionization.

This thesis is part of the ANR-17-CE30-0017 HighEneCh project, which brings , ther a consortium of specialists in electronic spectroscopy and instrumentation of large facilities (SOLEIL, Sorbonne University-LCPMR), radiation chemistry, and microfluidic systems (CEA–NIMBE) and *ab initio* simulations of molecular dynamics, soft X-ray irradiation setups and associated dosimetry (Sorbonne University-IMPMC), with the aim of providing fundamental knowledge on the different mechanisms involved in the chemistry triggered, in aqueous media, by high energy photons in the soft X-ray domains.

This manuscript is divided into five chapters.

- **Chapter I** introduces the literature of interest for the thesis. It thus brings a general description of the interactions between soft X-rays and condensed matter. It presents a ”state of the art” of studies on the effects of ionizing radiation on biomolecules. Then it presents the interest of soft X-rays for spectroscopic measurements and how they can bring crucial information on solvated biomolecules. It ends with the description of the new electron spectrometer specially developed in the framework of the HighEneCh project and this thesis.
- **Chapter II** presents the physical and chemical methods required to answer the two driving issues and the experimental devices used.
- **Chapter III** describes the technical development of a microfluidic cell dedicated to soft X-rays irradiation on a synchrotron beamline. It highlights the main difficulties and strategies achieved to work with such a low penetration beam. It also presents ongoing developments and possible improvements for the use of this device.
- **Chapter IV** focuses on the radiochemistry initiated in aqueous solutions exposed to soft X-rays. The first part is dedicated to investigating water radiolysis and, more precisely, the hydroxyl radicals formed along the secondary electrons track. After implementing the microfluidic cell, dosimetric experiments highlight the advantages of this cell, which allows the irradiation of a flowing sample. This chapter also describes the early K-edge irradiation experiments conducted on liquid samples, looking for K-edge threshold effects and following the production of water radicals. Finally, it reviews the limit of the set-up in the case of high dose-rate irradiations.
- **Chapter V** presents the investigation of initial physical features of core-ionization in liquid samples. The first part is dedicated to a complete spectroscopic study of small solvated molecules (benzoate salts), presenting an under-vacuum liquid-jet setup's proof of concept and performance. To bring further the comprehension and the limits of the setup, experiments were conducted on a complex and fragile biomolecule: a protein. Finally, this chapter presents the latest improvement in terms of Auger electrons analysis, with the recent coincidence measurement conducted for the first time, at the PLEIADES beamline, on molecules solvated in liquid water.

References

[1] M. Tubiana, J. Dutreix, and A. Wambersie, *An Introduction to Radiobiology*. Taylor & Francis, 1990.

[2] National Cancer Institute (NCI), "Radiation therapy to treat cancer." [Online]. Available: https://www.cancer.gov/about-cancer/treatment/types/radiation-therapy.

[3] E. M. Zeman, "The Biological Basis of Radiation Oncology," in *Clinical Radiation Oncology*, Fourth Edi., Elsevier, 2016, pp. 2-40.e5.

[4] C. Ferradini and J.-P. Jay-Gerin, "La radiolyse de l'eau et des solutions aqueuses : historique et actualité," *Can. J. Chem.*, vol. 77, no. 9, pp. 1542–1575, 1999.

[5] F. Giesel, "Ueber Radium und radioactive Stoffe," *Berichte der Dtsch. Chem. Gesellschaft*, vol. 35, no. 3, pp. 3608–3611, 1902.

[6] S. Lacombe and C. Le Sech, "Advances in radiation biology: Radiosensitization in DNA and living cells," *Surf. Sci.*, vol. 603, no. 10–12, pp. 1953–1960, Jun. 2009.

[7] T. Helleday, E. Petermann, C. Lundin, B. Hodgson, and R. A. Sharma, "DNA repair pathways as targets for cancer therapy," *Nat. Rev. Cancer*, vol. 8, no. 3, pp. 193–204, 2008.

[8] R. Cox, J. Thacker, D. T. Goodhead, W. K. Masson, and R. E. Wilkinson, "Inactivation and mutation of cultured mammalian cells by aluminium characteristic ultrasoft x-rays: II. Dose-responses of chinese hamster and human diploid cells to aluminium x-rays and radiations of different LET," *Int. J. Radiat. Biol.*, vol. 31, no. 6, pp. 561–576, 1977.

[9] M. R. Raju *et al.*, "Radiobiology of ultrasoft X rays. I. Cultured hamster cells (V79)," *Radiat. Res.*, vol. 110, no. 3, pp. 396–412, Jun. 1987.

[10] D. T. Goodhead and J. Thacker, "Inactivation and Mutation of Cultured Mammalian Cells by improCharacteristic Ultrasoft X-rays," *Int. J. Radiat. Biol. Relat. Stud. Physics, Chem. Med.*, vol. 31, no. 6, pp. 541–559, Jan. 1977.

[11] R. W. G. Wyckoff, "The killing of certain bacteria by x-rays," *J. Exp. Med.*, vol. 52, no. 3, pp. 435–446, Sep. 1930.

[12] D. T. Goodhead and H. Nikjoo, "Track structure analysis of ultrasoft x-rays compared to high- and low-LET radiations," *Int. J. Radiat. Biol.*, vol. 55, no. 4, pp. 513–529, 1989.

[13] D. Goodhead and H. Nikjoo, "Current Status of Ultrasoft X Rays and Track Structure Analysis as Tools for Testing and Developing Biophysical Models of Radiation Action," *Radiat. Prot. Dosimetry*, vol. 31, no. 1–4, pp. 343–350, Jun. 1990.

[14] D. T. Goodhead, "Initial Events in the Cellular Effects of Ionizing Radiations: Clustered Damage in DNA," *Int. J. Radiat. Biol.*, vol. 65, no. 1, pp. 7–17, Jan. 1994.

[15] H. Nikjoo, D. Emfietzoglou, T. Liamsuwan, R. Taleei, D. Liljequist, and S. Uehara, "Radiation track, DNA damage and response - A review," *Reports Prog. Phys.*, vol. 79, no. 11, 2016.

[16] H. Nikjoo and D. T. Goodhead, "Track structure analysis illustrating the prominent role of low-energy electrons in radiobiological effects of low-LET radiations," *Phys. Med. Biol.*, vol. 36, no. 2, pp. 229–238, 1991.

[17] A. Chetioui, I. Despiney, L. Guiraud, L. Adoui, L. Sabatier, and B. Dutrillaux, "Possible Role of Inner-shell Ionization Phenomena in Cell Inactivation by Heavy Ions," *Int. J. Radiat. Biol.*, vol. 65, no. 5, pp. 511–522, Jan. 1994.

[18] A. Boissière *et al.*, "DNA core ionization and cell inactivation," *Radiat. Res.*, vol. 167, no. 4, pp. 493–500, 2007.

[19] K. Kobayashi, K. Hieda, H. Maezawa, Y. Furusawa, M. Suzuki, and T. Ito, "Effects of k-shell x-ray absorption of intracellular phosphorus on yeast cells," *Int. J. Radiat. Biol.*, vol.

59, no. 3, pp. 643–650, 1991.

[20] S. Saigusa, Y. Ejima, K. Kobayashi, and M. S. Sasaki, "Induction of chromosome aberrations by monochromatic x-rays with resonance energy of phosphorus k-shell absorption edge," *Int. J. Radiat. Biol.*, vol. 61, no. 6, pp. 785–790, 1992.

[21] R. Watanabe, N. Usami, M. Tomita, K. Kobayashi, A. Yokoya, and M. Maeda, "Enhancement of DNA double-strand break induction and cell killing by K-shell absorption of phosphorus in human cell lines," *Int. J. Radiat. Biol.*, vol. 92, no. 11, pp. 724–732, 2016.

[22] F. N. Gobert *et al.*, "Chromosome aberrations and cell inactivation induced in mammalian cells by ultrasoft X-rays: Correlation with the core ionizations in DNA," *Int. J. Radiat. Biol.*, vol. 80, no. 2, pp. 135–145, 2004.

[23] B. Fayard *et al.*, "Cell Inactivation and Double-Strand Breaks: The Role of Core Ionizations, as Probed by Ultrasoft X Rays," *Radiat. Res.*, vol. 157, no. 2, pp. 128–140, 2002.

[24] M. A. Herve Du Penhoat *et al.*, "Lethal effect of carbon K-shell photoionizations in Chinese hamster V79 cell nuclei: Experimental method and theoretical analysis," *Radiat. Res.*, vol. 151, no. 6, pp. 649–658, 1999.

[25] M. A. Hervé Du Penhoat *et al.*, "Double-strand break induction and repair in V79-4 hamster cells: The role of core ionisations, as probed by ultrasoft X-rays," *Int. J. Radiat. Biol.*, vol. 86, no. 3, pp. 205–219, 2010.

[26] K. Fujii, K. Akamatsu, and A. Yokoya, "Decomposition of 2-deoxy-D-ribose by irradiation with 0.6 keV electrons and by 0.5 keV ultrasoft X-rays," *Int. J. Radiat. Biol.*, vol. 80, no. 11–12, pp. 909–914, 2004.

[27] T. Shiina *et al.*, "Induction of DNA damage, including abasic sites, in plasmid DNA by carbon ion and X-ray irradiation," *Radiat. Environ. Biophys.*, vol. 52, no. 1, pp. 99–112, 2013.

Chapter I. Context

Contents Chapter I

Chapter I. Context

I.1. Light-matter interactions in the condensed phase

I.1.1. General Principle

The field of radiobiology studies the effect of ionizing radiations on biological systems[1]. Regarding the electromagnetic spectrum, ionizing radiations begin with the Vacuum Ultraviolet-light (VUV) until the Extrem UV radiation (6-100 eV). Then we find X-rays, divided into soft X-rays (100 eV-2 keV) and hard X-rays (energies above 2 keV). High energies are also achieved by γ-rays[3]. This chapter will focus mainly on the processes induced in biological samples by photons with energies lower than 50 keV. The nature of photons' interaction with matter depends on the incident photon's energy and the atomic number (Z) of the target atom. For organic matter, mainly constituted with light atoms ($Z < 20$), photons of energy below 50 keV interact mainly by the photo-electric effect. In this case, the energy of the incident photon (E) is entirely transferred to the medium, leading to the emission of an electron, called photo-electron (PE). This photoionization process, first observed by Heinrich Hertz in 1887, was later described by Einstein (Nobel Prize in 1921). It constitutes the triggering event of a cascade of processes taking place on very different time scales. The sequential chronology of the events is generally described through three temporal stages[2] (see Figure I-1).

- The creation of biological damage begins with the physical stage corresponding to energy deposition in the medium. The primary ionization and excitation processes are extremely fast and typically occur in 10^{-19} to 10^{-15} s. Energy can be deposited directly into the solutes, creating excited and ionized states of solvated molecules. The corresponding processes are called direct effects. However, water, which is often the most abundant molecule in the medium, absorbs much of the deposited energy, initiating indirect effects.

- The physico-chemical stage then takes place (10^{-15} s $< t < 10^{-12}$ s). During this stage, molecules dissociate and recombine with close species. It leads to the formation

[3] *Gamma-rays are identical to X-rays in their physical properties. The classification only depend on the origin of the electromagnetic radiation (nucleus for γ-rays and charged particles emission for X-rays).*

of reactive species such as free radicals or solvated electrons. At the end of this stage, the various products of the irradiated matter are thermalized, but their spatial distribution in the medium is heterogeneous.

- The chemical stage occurs in the 10^{-12} s < t < 10^{-6} s timescale. During this timescale, the created species diffuse, recombine and react with each other leading to the formation of molecular products. At about 10^{-6} s, the species' distribution can be considered homogeneous, and they start to react more efficiently with the species present initially in the medium than with other radiolytic species.

- To these stages, biochemical and biological stages can be added. The biochemical stage begins when the radical species produced in water react chemically with the biomolecules present in the surrounding environment. The resulting damages are referred to as "indirect effect". In living systems, the biological stage also includes the activity of the organism repair systems. This stage can last several hours and results in long-term effects (complex cellular lesions).

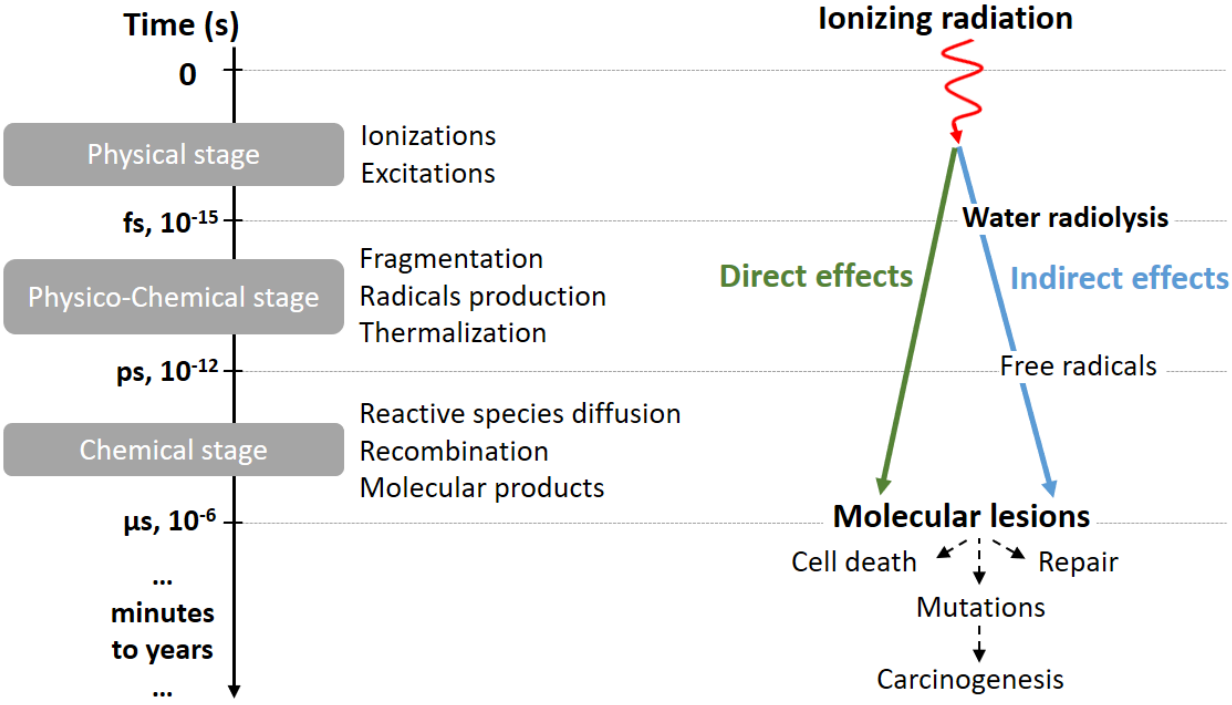

Figure I-1: Formal description of the radiolytic events occurring during a biomolecule irradiation and biological consequences.

I.1.2. Case of soft X-rays

I.1.2.i. Core ionization

The photoelectric effect is a threshold process that initiates the physical stage. It only occurs if the photon's energy is greater than the binding energy of the ejected electron. The closer the photon's energy is to the binding energy, the higher the probability of interaction. For soft X-rays, the energy of the photons (100 eV – 2 keV) is close to the binding energy of the K-shell electrons of organic matter (C, O, N, see Figure I-2). If the photon energy is above the one of the K-shell electrons of the targeted atoms, the photoionization thus occurs predominantly in the core layer.

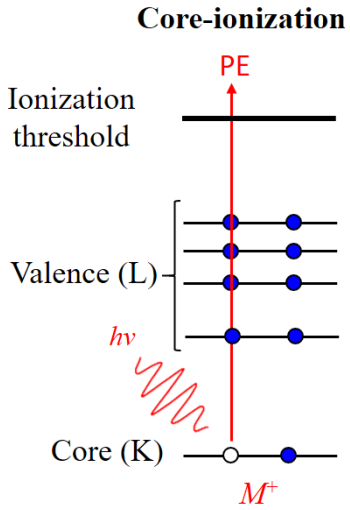

Atoms	C	N	O	Na	Mg
K-shell ionization threshold (eV)	284.2	409.9	543.1	1070.8	1303.0

Figure I-2: Core-ionization process and emission of a photoelectron. Values of K-shell ionization threshold for atoms found in organic matter are also presented (data from [1]).

Following the absorption of the incident photon of energy E, a PE is emitted. The following relation gives the energy of the PE:

$$E_k = E - E_B = h\nu - E_B \qquad (\text{I-1})$$

With E_k, the PE kinetic energy, h Planck's constant, and ν the frequency of the incident radiation. The ejection of a K-shell electron results in the formation of a singly charged ion (M^+) in a highly electronic excited state. Therefore, the electronic configuration undergoes successive rearrangements from the valence to the core layer to fill the core hole.

I.1.2.ii. Auger desexcitation processes

The energetic relaxation following core-ionization results in a release of energy that can be either radiative (fluorescence) or non-radiative (Auger decay). The fluorescence radiation and Auger electron (AE) energy characteristics and their emission probabilities are specific to each atom. In the case of biological samples, the Auger relaxation largely predominates, as illustrated in Figure I-3.(a)[3]. During the Auger decay (illustrated in Figure I-3.(b)), the core-hole filling is followed by the emission of a second electron[4]. The energy of this so-called AE is characteristic of the electronic transition. It is given by the energy difference between the initial and final states of the transition.

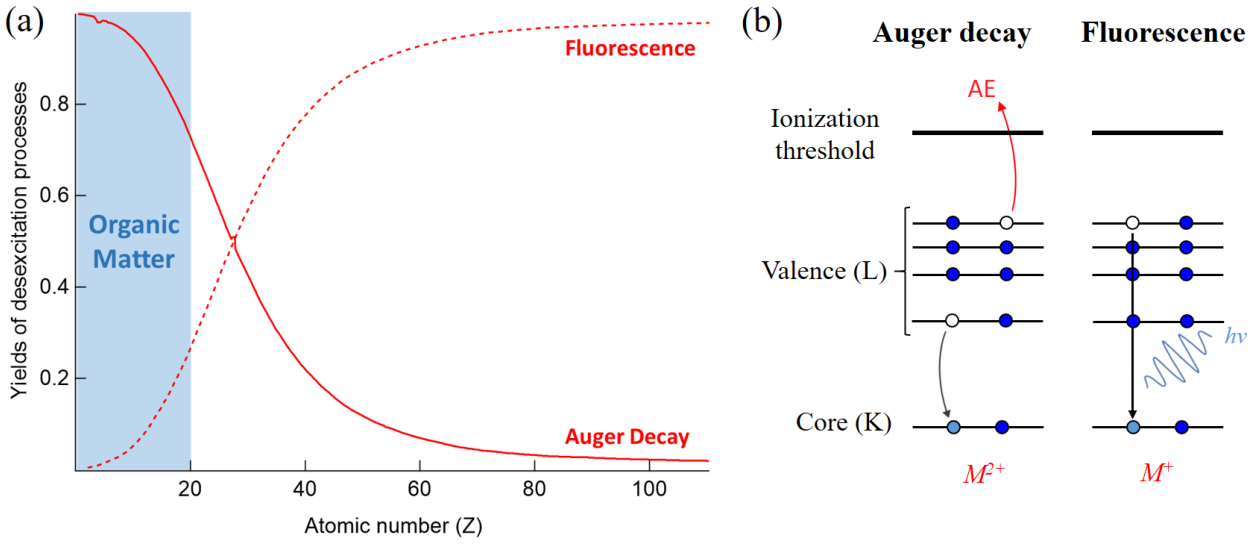

Figure I-3: Auger decay and fluorescence desexcitation processes following K ionization: (a) Competition of the two processes as a function of atomic number (data from [3]), (b) Scheme of the electronic rearrangements occurring during these two processes.

Core-ionization (or K-shell ionization) and its following Auger decay result in the emission of several electrons with energies that can reach a few hundred eV (depending on the binding energy of the core electron)[4]. Non-radiative mechanisms of deexcitation processes following K-shell ionization typically occur on the femtosecond timescale (physical stage)[5], [6]. More importantly, Auger decay leaves the atom at least in a double ionization state. The deexcitation pathways involve reorganization of the molecular structure, which almost always leads to fragmentations and radical production in the gas phase. Auger decay is thus also part of the physicochemical stage (Figure I-1). However,

[4] *Multiple AE can be emitted if the rearrangement of the electron cloud remains more energetically favourable.*

it can initiate a new cascade of events at the physical stage through the emission of sub-keV electrons. In addition to this local deexcitation, new types of non-local deexcitation pathways have been recently evidenced, as detailed in the following sub-section.

I.1.2.iii. Non-local deexcitation processes

A decade ago, the theoretical work of Cederbaum and co-workers predicted that new decay mechanisms could occur in the weakly bonded matter (van der Waals forces or hydrogen bonds)[7]. Such multiple interatomic electronic processes, involving species other than the initially ionized monomer, could turn out to be important for solvated molecules in the liquid phase[8], [9].

Calculations first evidenced energy transfer between neighboring species through Interatomic/Intermolecular Coulombic Decay (ICD)[10], [11]. In the case of ICD, the core-hole of the ionized atom is filled by a valence electron of the ionized species. The energy released is transferred to a neighboring molecule, which uses this excess energy to eject a valence electron (see Figure I-4). Cederbaum *et al.* conducted further theoretical studies and evidenced that deexcitation processes could involve electron transfer instead of energy transfer[12].

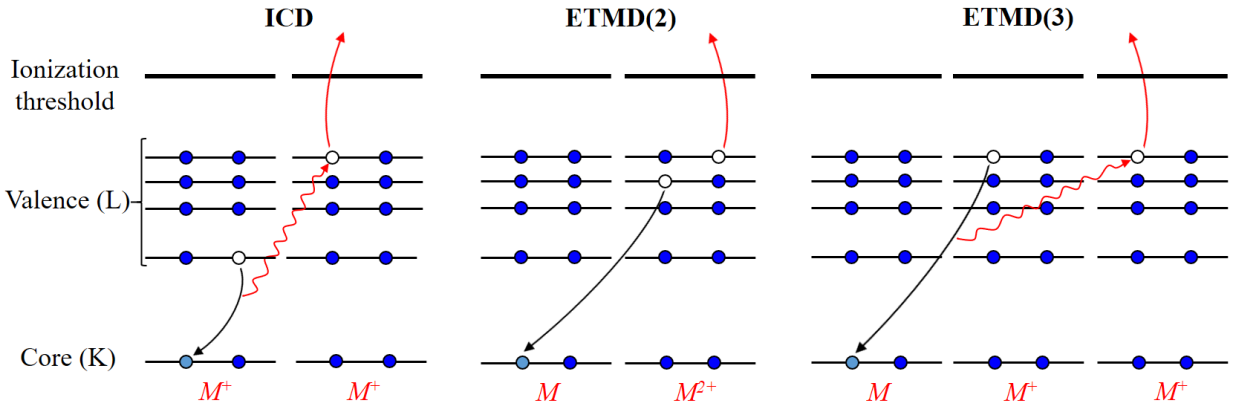

Figure I-4: Desexcitation processes sketches: Left: Inter-Coulombic Decay (ICD), Center and Right: Electron-Transfer-Mediated Decay (ETMD). The number in parenthesis refers to the number of species involved in the process.

In these electron-transfer-mediated decay (ETMD), the core-hole is this time filled by an electron from a neighboring atomic or molecular species. The energy released is used to ionize either the same electron-donating species (a process referred to as ETMD(2)), or

it is used to ionize a third neighboring molecule (namely ETMD(3) process)[7] (see Figure I-4). As for Auger decay, ICD and ETMD lead to energy and charge redistribution on the ionized molecules, leading to highly localized and highly concentrated production of oxidizing radicals if the neighboring molecules are water molecules. Moreover, it leads to the emission of low-kinetic energy electrons (<20 eV), which can induce irreparable damage in a biological sample[13] through dissociative attachments.

I.1.3. Energy transfer and track structure

Soft X-ray photons are directly ionizing through the photoelectric effect. However, they can also be considered an indirect ionizing radiation source since the PE and AE are sufficiently energetic to interact with the medium and thus produce further ionization events along their path[14]. The spatial distribution of the energy absorbed along the path is expressed by the notion of Linear Energy Transfer (LET):

$$LET \sim {}^{dE}/_{dx} \qquad \text{(I-2)}$$

The LET value represents the average energy locally deposited in matter (dE) per unit of path length (dx). It is usually expressed in keV/µm or J/m. It depends on the radiation (type and energy) and on the properties of the material irradiated[15], [16]. For electromagnetic radiations, the average LET is calculated from the LET of all the secondary electrons. In the case of soft X-rays, secondary electrons are electrons ejected during the photoionization events and the following deexcitation processes previously described. In radiobiology, the LET-value and the dose are usually used to evaluate the effectiveness of a particular radiation to induce radio-biological damages. Nevertheless, the LET value alone does not allow to explain the differences in biological effectiveness between different radiations[17]. For that purpose, it is necessary to bring an accurate description of the tracks' structure.

The transfer of energy by ionizing particles is discrete. The track consists of a stochastic discontinuous sequence of affected and unaffected domains[18]. A suitable parameter to characterize tracks is the average distance between two successive energy deposits along the primary particle's path. It depends on the LET of the particle. A particle, such as a PE or an AE, follows a deterministic trajectory for a short period of time. Then, it

undergoes a collision that makes its velocity $\overrightarrow{v_i}$ decrease (with possible creation of other particles). The trajectory of the particle has a stochastic character. Monte-Carlo simulation methods are perfectly adapted to reproduce such events as multiple collisions and the generation of secondary particles[19]. Following the calculations of Mozumder and co-workers, energy deposition events occurring in the track were categorized into four types of events: (1) spurs (spherical entities and an energy deposit up to 100 eV), generally corresponding to one isolated ionization event; (2) blobs (spherical or ellipsoidal entities and an energy deposit between 100–500 eV); (3) short tracks (cylindrical column and an energy deposit between 500–5000 eV) and (4) branch tracks (energy deposit higher than 5 keV)[20]. Figure I-5 schematizes the distribution of the energy deposit (represented by red points[5]) observed on track structures of low and high LET radiations.

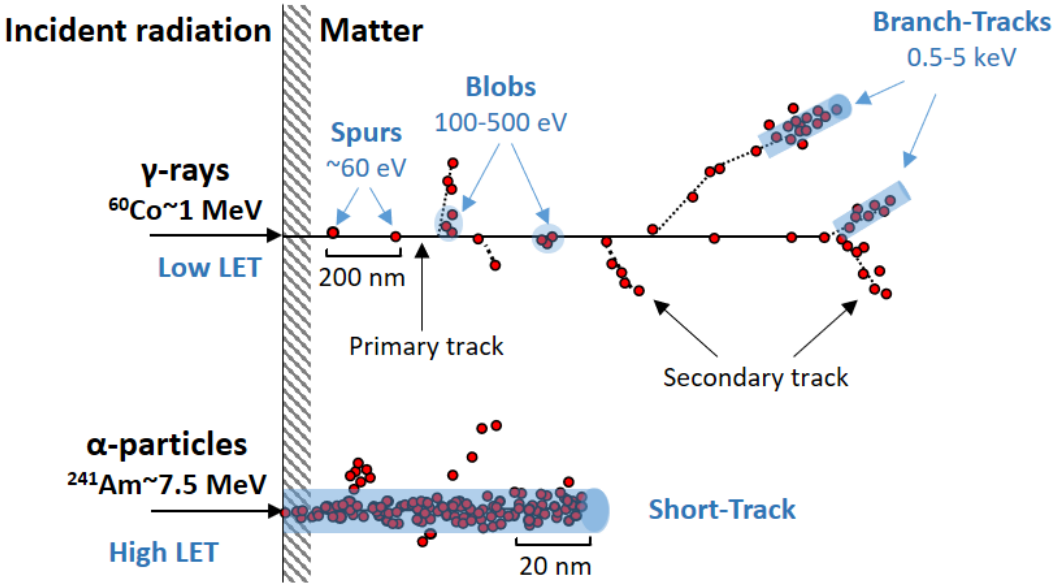

Figure I-5: Schematic representation of ionization along the particle track (inspired by [20]).

For γ-rays of ^{60}Co (LET = 0.23 keV/µm), the average distance between energy deposits is of the order of 200 nm. It is only 1 nm for α particles of ^{241}Am (LET = 43 keV/µm). Figure I-5 shows that the α-particles have a continuous, highly ionizing track. On the contrary, high-energy photons are sparsely ionizing (scattered energy deposits). The track can be mainly described with small energy deposits (spurs) because γ-rays mainly produce high kinetic energy electrons.

[5] *It must be noted that the interaction sites are not infinitely small points but have a certain extension, defined by the penetration length of emitted electrons in matter (~1 nm in condensed matter).*

Electrons have a LET inversely proportional to the square of their speed[6]. As electrons lose energy by interactions with the atoms of the medium, their LET increases (see Figure I-6)[21]. Ionization clusters are therefore observed at the end of the electrons tracks[22], [23]. The appearance of such high LET can be compared to the Bragg peak of ions[7]. In the case of the electrons produced by soft X rays (blue area in Figure I-6), their calculated LET is in the range of tens of keV/µm, with a maximum at approximately 100 eV, corresponding to very compact tracks[24].

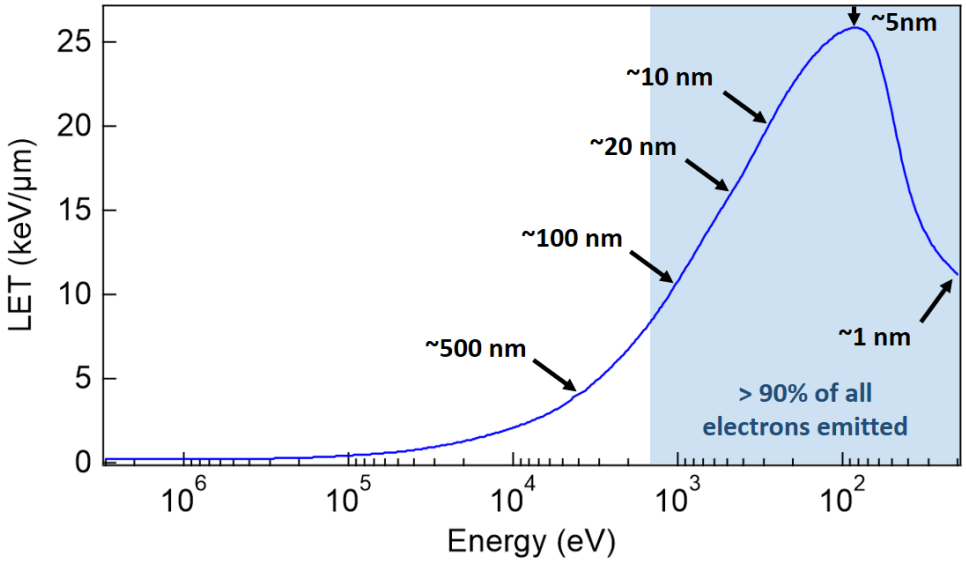

Figure I-6: LET of electrons as function of their energy. Distance traversed by the electrons along the track are shown by arrow. (figure from [21]*)*

The main point is to investigate the link between the track structure and the critical events generated in the irradiated medium. In particular, the notion of spurs was historically defined following the distribution of the radical species formed by the ionization of water molecules[25]–[27].

I.1.4. Water radiolysis

Studying aqueous samples requires investigating the different pathways of water molecules' decomposition under irradiation during the physico-chemical and chemical

[6] The Bethe formula for the stopping power of non-relativistic electrons establishes an inverse proportion with the square of their velocity at large velocities. This formula is based on the assumption that the velocity of the incident electron is large compared to the velocities of the atomic electrons[181].

[7] For ions, a high energy transfer occurs at the end of the track because the effective interaction cross-section increases as the energy of the charged particle decreases. It is called the Bragg Peak in honor of its first observer Henry Bragg.

stages (see Figure I-1). Indeed, as mentioned above, water molecules can not be neglected as they absorb most of the energy. Excitation and ionization of water molecules lead to the production of molecular and radical species :

$$H_2O \rightarrow HO^{\cdot}, H^{\cdot}, e_{aq}^{-}, H_3O^{+}, O_2^{\cdot -}, H_2O_2, H_2 \qquad \text{(I-3)}$$

This radiation chemistry, or radiolysis, first described by Giesel[28] at the beginning of the twentieth century, is still widely studied to date as it underlies a large variety of fields from medicine to the nuclear industry. The general scheme of water radiolysis is presented in Figure I-7[26].

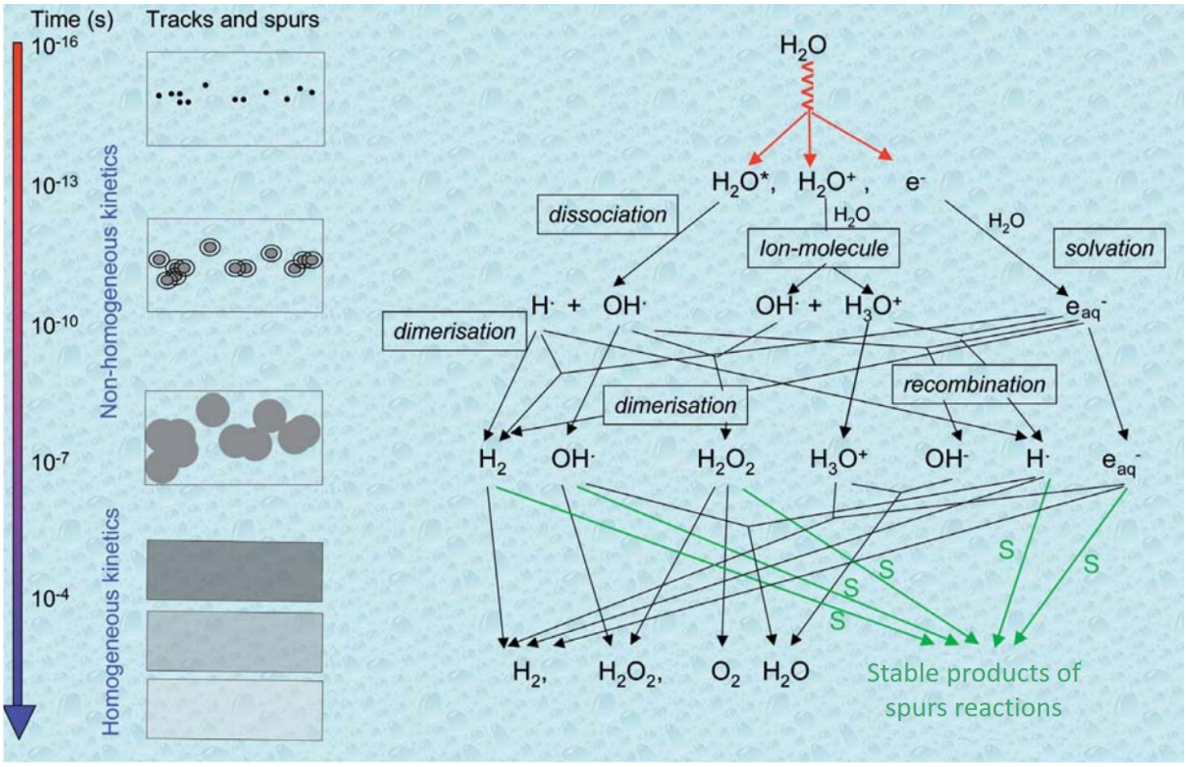

Figure I-7: Summary of transient species reactions occurring in water radiolysis over the various temporal stages. On the left, schematic evolution of spatial distribution of ionizations along the track. (image adopted from [26])

The radiolytic chemical yield defines the radiolytic species production, noted G(x)[29]. It corresponds to the ratio between the number of chemical species (x) consumed or produced by radiolysis and the amount of energy absorbed. It is commonly expressed in mol/J or molecules per 100 eV. Radiolytic radicals generally react very quickly and do not accumulate. Therefore, G-values for these species are good indicators of the track's time- and spatial- structure [30]. The evolution of the repartition of the species in the track as a function of time is presented schematically in Figure I-7. The determination of G-values constituted a first way to describe the evolution of species following heterogeneous energy

deposits[29]. Primary yields are defined as the yield of radicals and molecules formed after approximately 1 µs. Table I-1 shows, as an example, the values obtained for the irradiation of aerated aqueous media by γ-rays or α-particles.

Table I-1: Reactive oxygen species production from water obtained after 100 ns to 1µs [31], [32]

G values (µmol/J)	**Radicals**				**Molecular products**		
	e_{aq}^-	$HO^\cdot$	$H^\cdot$	$O_2^{\cdot-}/HO_2^\cdot$	H_3O^+	H_2O_2	H_2
γ-rays (0.1-10 MeV) LET of 0.2–0.3 keV/µm	0.28	0.28	0.062	0.003	0.28	0.074	0.047
5.3 MeV α-particles LET of 108 keV/µm	0.044	0.052	0.028	0.056	0.044	0.15	0.163

In the case of water radiolysis, we observe an increase in the primary yield of molecular products, which is correlated to a decrease of radicals primary yields, as the LET increases[33]. Such observation highlights that sub-microsecond intra-track reactions can occur for high ionization density events (which are more abundant in high LET tracks) [19]. Indeed, when spurs overlap, it promotes reactions between radicals generated inside the track (e_{aq}^-, $HO^\cdot$, $H^\cdot$). As radicals recombine, their G-value decreases promoting the one of molecular products[34]. These variations in primary yields are well described by the diffusion models developed by Magee *et al.,* which take into account (1) the variation of the LET along the track, (2) intra-track reactions, and (3) competition between radicals scavenging reaction and recombination[18], [35][36]. This model has been adopted and further developed by many authors in order to describe by computational methods the experimental observations[25], [36]–[38]. Similarly, other studies have successfully used Monte-Carlo calculations[39], [40]. In particular, simulations evidenced a minimum G($HO^\cdot$) for low energy electrons (<1 keV) as illustrated in Figure I-8. Such simulations support the fact that low-energy electrons behave like high LET particles, as they deposit their energy in nanometric volume. However, given the low penetration of soft X-rays (only a few µm in liquid water[41]), experimental studies remain very scarce[42], [43]. We must also notice that cross-sections used in the simulations is quite uncertain, and the exact density of sub-keV electrons tracks remains unknown.

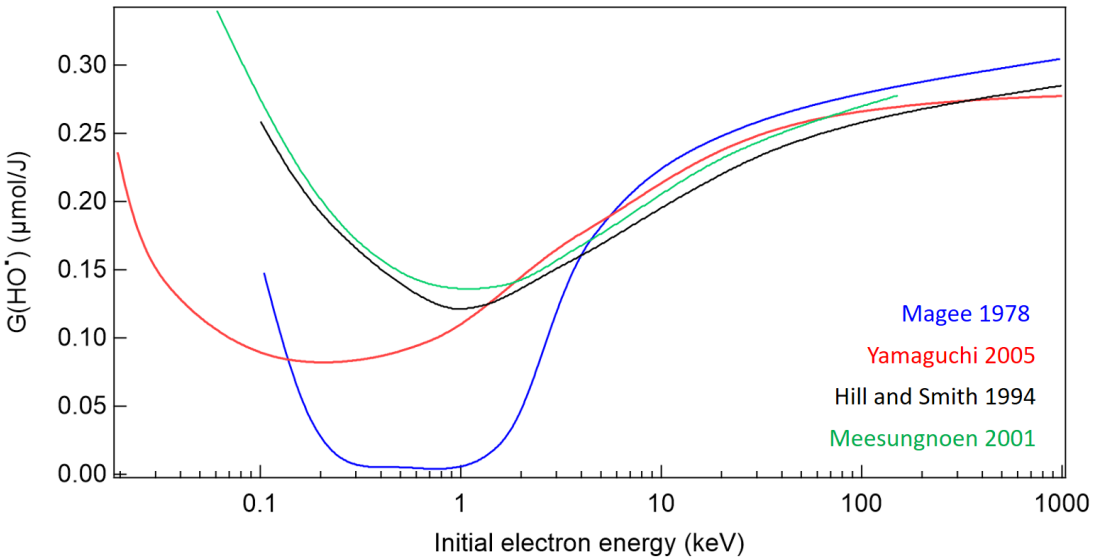

Figure I-8: Simulations found on the literature [23], [38]–[40], *reporting the variation of the primary yields of* $HO^{\cdot}$ *radicals produced upon radiolysis of pure liquid water at 25 °C as a function of incident electron energy.*

Another observation from Table I-1 is the yield of hydroperoxyl/superoxide couple ($O_2^{\cdot-}/HO_2^{\cdot}$). Contrary to other radicals, its primary G-value increases with the LET. Studies in the literature report in particular significant amounts of $HO_2^{\cdot}$ produced in heavy ion tracks (high LET)[44]–[47]. Experiments conducted in anoxic conditions (deaerated medium) also showed that the production yield of ($O_2^{\cdot-}/HO_2^{\cdot}$). increases over time for high LET particles. However, it is not the case for low LET radiations (γ-rays or X-rays) where measured yields are extremely low in similar conditions[48]. If, to some extent, the evolution of G($O_2^{\cdot-}/HO_2^{\cdot}$) is still well described by the theoretical methods mentioned above for low LET radiations, these models fail to explain the G value for high LET (>100-150 keV/µm)[30], [44]. It was thus suggested that the formation of superoxide anions could originate from water multi-ionization deexcitation pathways[49], [50]. This hypothesis was then validated by theoretical approaches[51]. Indeed, it was shown that when the multiple ionization of water molecules was taken into account in the Monte Carlo simulations, the increase in the production of $O_2^{\cdot-}/HO_2^{\cdot}$ radicals for high LET particle was well described[52]. Mechanisms involved were further studied using *ab initio* molecular dynamic theoretical approaches[53], [54]. Unfortunately, to date, experimental studies on multiple photoionization processes are mostly limited to gas phase studies due to the critical technical constraints present in the liquid phase[55]–[57].

I.2. Investigation of biological consequences

The main difficulty in understanding the radiation damage to biomolecules lies in the fact that they are initiated at very different timescales. On the one hand, direct effects, induced by the direct photoionization of the target, occur at the femtosecond timescale. On the other hand, indirect effects, coming from the reaction with radicals, start at the microsecond time scale. These processes can lead to very different biological effects and are therefore difficult to decipher. In the context of radiotherapy, numerous studies have tried to investigate the mechanisms involved in cell inactivation. A first approach is to irradiate a complete biological system, such as a living cell, to study the general consequences and relate them to the specific damage of the biomolecules *in situ* ("Top-down" approach). A second approach is to focus the analysis on isolated molecules of biological interest to oversee the origin of the damage ("Bottom-up" approach).

I.2.1. "Top-down" approaches

Pioneering "top-down" approaches have shown that soft X-rays were much more effective at inducing cellular inactivation and chromosomal aberrations than ^{60}Co γ-rays[58]–[60] in plant or animal cells. In such cases, radio-induced damage can no longer be predicted with macroscopic concepts such as the dose deposited in matter or the LET of the incident radiation. Following the analysis of the track structure, it became evident that against all expectations, the critical events were not initiated by energy deposition at the micron scale (chromosome-scale) but at the nanometer scale. From then on, it was crucial to investigate the deterioration of DNA constituting the chromosomes.

DNA is formed by a two-stranded helix. The strands are formed by a sequence of nucleotides linked together by phosphodiester bonds. Each nucleotide comprises a nucleobase, a pentose (deoxyribose for DNA), and a phosphate group. Therefore, the radio-induced lesions on such complex macromolecules can be very diverse (altered or lost DNA bases, strand breaks, DNA intra- and inter-strand crosslinks, DNA-protein crosslinks). The cell tries to repair DNA damages through enzymatic processes. A lack of repair or an error in the repair constitutes the triggering event of the death or transformation of cells (mutation or chromosomic aberration)[61], [62].

Biological effects were initially evaluated mainly through single- or double-strand breaks (SSB or DSB)[63]. SSB is caused by the rupture of the phosphate-sugar bonds that link together sequences of nucleotides, which form the DNA strands. It is commonly admitted that SSB have only a minor impact on cell inactivation as they are quickly repaired[64]. DSB occur when the two chains are broken at sites distant by less than 10 base pairs [17]. It constitutes a more critical damage because it is more complex and therefore more challenging to repair by the cell[65]. For most cells exposed to X and γ-rays, SSB was found to be more frequent than DSB damage (ratio of 25:1)[8][26]. For high-LET particles, not only the proportion of DSB increased, but the cell inactivation was correlated to the un-repaired damages [66], [67]. From then, the notion of "clustered damage", first suggested by Goodhead and co-workers using soft X-rays[68], was adopted. These "locally multiply damaged sites" are not only resulting from DSB but also from a combination of many lesions, such as nucleobases oxidation or bonds alteration. In light of these studies, it was admitted that the lethality of radiations was correlated to the increase of the complexity of clustered damages[69].

Studies were conducted on DNA aqueous solutions to investigate indirect effects. Irradiations, carried out in the presence of ROS scavengers, demonstrated the high involvement of hydroxyl radicals ($HO^{\cdot}$) in strand breaks formation[70], [71]. Especially, it is interesting to note that Fulford and co-workers used plasmids DNA as a scavenging method for indirect measurement of $HO^{\cdot}$ radicals produced under soft X-rays irradiation [42]. For radiations of high LET, quantifications of base lesions allowed to decipher the contribution of direct or indirect effect[72], [73]. Comparison of irradiation performed in cells and aqueous solutions evidenced the same contribution of indirect effect [74]. It validates the fact that aqueous systems provide suitable conditions to study indirect effects. However, working on liquid samples can be challenging for low penetration radiation (low-energy electrons, soft X-rays). It explains the scarcity of experimental studies conducted at ambient pressure using soft X-rays[75], [76]. These few studies have highlighted the complexity of the damage mechanisms caused by secondary electrons generated in the matter, notably following K-ionization events[77], [78]. Finally, even if

[8] *Modified bases were produced in the same amount as SSB damage.*

the irradiation of biomolecules in a liquid aqueous medium allows to quantify indirect effects, they do not allow to establish a hierarchy between direct and indirect effects. In this optic, researchers have developed studies in parallel on isolated biomolecules either in a gas phase or dry films.

I.2.2. «Bottom-up» approaches

"Bottom-up" approaches aim to access the physical mechanisms of radiation damage at the molecular level. It is achieved by studying simple systems, such as isolated biomolecules in vacuum, to remove the solvent's contribution. A primary advantage of this approach is that experimental results are more quickly compared to theoretical and computational studies, as the system is simplified. Such experiments emerged decades ago to study photo-excitation/photoionization and fragmentation processes induced by various radiations. VUV and soft X-ray photo-absorption experiments were widely developed for larger and larger systems. It all began with small molecules[79]–[82]. However, it quickly got applied to complex macromolecules such as proteins, thanks to the development of soft ionization methods, as electrospray ionization (ESI), which allow putting into the gas-phase these fragile molecular edifices[83], [84]. It was, for instance, applied to soft X-rays irradiations to focus on K-ionization effects[85]–[87].

Similarly, pioneer experiments, conducted with low-energy electrons (3-20 eV) by Boudaïffa *et al.*[88], brought new information on the mechanisms involved in direct damages[89]. Studies have been carried out in gas-phase or dry DNA films to investigate the mechanisms involved in the damage[90], [91]. It demonstrated the considerable ability of low-energy electrons to generate DNA damage (SSB and DSB), even for electron energy in the range below the ionization threshold (<10 eV)[13], [92], [93]. It also explains the particular interest in the non-local deexcitation phenomena after an X-ray ionization (ICD, ETMD), which also lead to the emission of low kinetic energy electrons. In a biological environment, DNA molecules are generally surrounded by water molecules. Therefore, some experiments tried to take into account the hydration processes on DNA films[94]–[97]. These studies highlighted the crucial role of the DNA strand solvation sphere. Finally, the main question is to know if data are transposable to biological effects in the cell.

From top-down and bottom-up observations, it became evident that the success of repair attempts is highly dependent on the nature of the initial physical and chemical injuries. However, experimental and theoretical results evidenced that the dissociation dynamics strongly depend on molecules' intrinsic properties (bonding nature, electronic and three-dimensional structure, interactions with their molecular environment). Hence, the importance of developing both liquid phase irradiation techniques and spectroscopic analysis methods in order to access the different steps of radiation mechanisms.

I.3. Soft X-ray spectroscopic studies on biomolecules

I.3.1. State of the art

The last century was marked by the success of various soft X-rays-based techniques, either in absorption (XAS) or in emission (Auger and X-ray photoelectron spectroscopy, respectively AES and XPS). They are now well-established techniques to explore the electronic and structural properties of biological systems. New techniques were developed from the growing interest in electron microscopy, such as transmission X-ray microscopy (TXM or Scanning TXM) for biomolecules[98]. Indeed, soft X-rays bring (1) spectral resolution, (2) depth sensitivity, and (3) chemical sensitivity. These three properties are linked to the energy range of soft X-rays (100 eV- 2 keV). By definition, the spectral resolution is directly related to the wavelength of the incident beam (IUPAC[9] definition of the resolving power [99]). The other two are due to the low penetration of soft X-rays and their ability to interact mainly with the core electrons of the atoms constituting the biological matter through the photoelectric effect.

For photons, the absorption of the beam in a homogeneous sample of a thickness (x) can be expressed by:

$$T = {}^{I}/_{I_0} = e^{-\mu(E)x} \qquad \text{(I-4)}$$

Where I is the transmitted intensity, I_0 is the incident intensity and μ is the linear attenuation coefficient that depends on the photon energy (E). The mass attenuation coefficient is expressed by:

$$\left(\frac{\mu}{\rho}\right) = \frac{N_A}{M}\sigma = \sum_i \left(\frac{\mu}{\rho}\right)_i \cdot w_i \qquad \text{(I-5)}$$

Where N_A is the Avogadro number, M is the molecular weight, and σ is the photoabsorption cross-section. If the sample is composed of different atom types (i), the mass attenuation coefficient of the compound $\left(\frac{\mu}{\rho}\right)$ can be calculated using the mass attenuation coefficient $\left(\frac{\mu}{\rho}\right)_i$ and the fraction by weight (w_i) of the atomic constituent i.

Using the previous Equations (I-4) and (I-5), it is possible to calculate the penetration distance, or attenuation length (1/μ), in the case of soft X-rays. For electrons, the effective

[9] *International Union of Pure and Applied Chemistry*

attenuation length commonly refers to the average distance that an electron, with a given energy, can travel in the material without undergoing inelastic loss. This distance is commonly defined as the inelastic mean free path (IMFP, noted λ) [100].

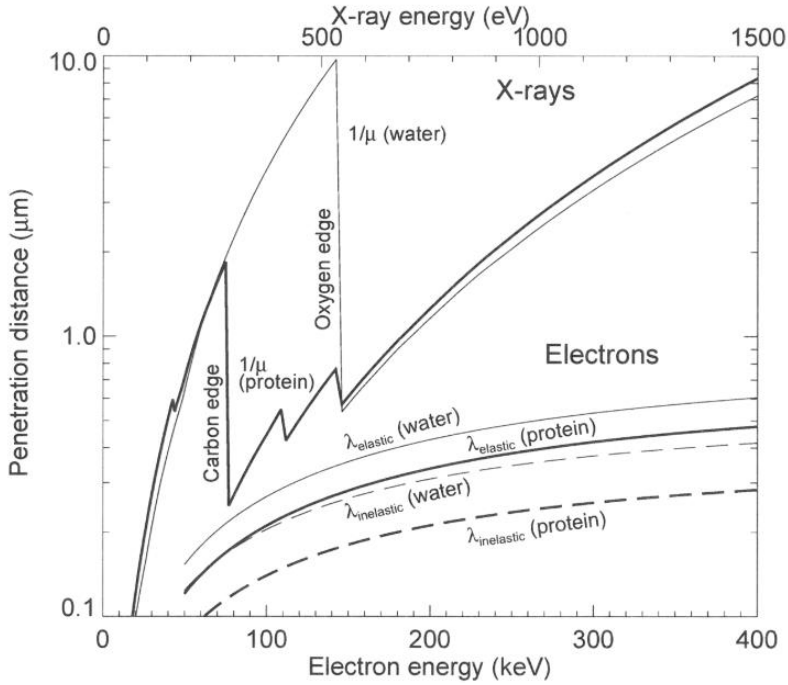

Figure I-9: Penetration distances in water and protein for high energy electrons and X-rays (image from [101]*).*

Figure I-9, from [101], presents the penetration distances in the case of soft X-rays and high-energy electrons as a function of the energy of the particles. Data are presented for liquid water and a biological sample (protein).

The first observation from penetration curves is that, even if soft X-rays are more penetrating than electrons (penetration <1 µm for an electron of hundred keV energy), their penetration length is only of few microns (~2-10 µm) in water. However, in the "water window", which is the spectral region delimited by the carbon K-edge (at 284 eV) and the oxygen K-edge (at 540 eV), soft X-rays may be more absorbed in organic matter than in water (depending on the solute composition and concentration). Such absorption differences (nearly one order of magnitude) provide great contrast when studying biological samples as the water appears "transparent" compared to the strong absorption of carbon-based molecules[102], [103]. Figure I-9 also highlights that the interaction of soft X-rays with matter results in absorption edges. K-edge structures and near-edge resonances are indeed observed when the X-ray energy becomes larger than the threshold energy needed

to remove a K-shell electron or to excite it in the neutral molecular system, respectively. To further investigate the electronic structure, X-ray absorption spectroscopy was developed (XAS)[104], [105]. An absorption spectrum is generally divided into two parts: the region called NEXAFS (Near Edge X-Ray Absorption Fine Structure) and the region called EXAFS (Extended X-Ray Absorption Fine Structure)[106]. Such spectroscopic methods are perfectly adapted to study the radiation-induced processes on biological samples during microscopy analysis[107], [108].

Historically, XAS was limited to studying condensed-phase samples in an ultra-high vacuum given the low penetration of soft X-rays. Experiments conducted on hydrated films, for instance, allowed to investigate the role of water in radio-induced damages[109]–[112]. Following this interest in solvent effects, several technological setups were developed to study liquids. The first strategy was to form a liquid cell suitable for a vacuum environment[113], [114]. It was achieved using two highly transparent Si_3N_4 windows. With the advent of microfluidics, new systems were developed to renew the fluid. Such systems not only prevent beam damage but also allow testing new experimental conditions (gas pressure, liquid mixture, temperature)[115]–[117]. In parallel, Faubel and co-workers were developing under-vacuum liquid microjets[118], which paved the way for liquid XAS[119], [120]. Finally, XAS studies are also performed in the gas phase. Following a "bottom-up" approach, the new set-up was coupled to spectroscopy techniques, such as mass spectrometrum, in order to understand better biomolecules fragmentation and the effect of Auger decay at the atomic scale[121], [122]. To date, mass spectrometry spectra can even be used to reconstruct the near-edge structure with the advent of Near-edge X-ray absorption mass spectrometry (NEXAMS)[85].

XPS or AES spectroscopy can also bring essential information on electronic states[123]. In the low energy range (50 eV – 2 keV), photons can probe the electronic structure of matter, such as the properties of the highest occupied molecular orbital (HOMO) and the lowest unoccupied molecular orbital (LUMO)[124]. Such information is crucial to obtain a complete description of the processes involved in photoionization and retrieved information on the chemical structure and chemical bonds. Contrary to the NEXAFS spectroscopy, which requires changing the photon energy to probe the absorption

thresholds, XPS can be performed with monoenergetic photons, making it very popular in surface laboratories.

I.3.2. X-ray photoelectron spectroscopy (XPS)

I.3.2.i. Principle of XPS

Soft X-rays are widely used for XPS. As stated in the name, it analyzes the kinetic energy of the PE emitted by a sample irradiated under an X-ray beam *via* the photoelectric effect (previously described in section I.1). XPS was initiated by Siegbahn and his co-workers in 1957 with the development of the Electron Spectroscopy for Chemical Analysis (ESCA, Nobel prize of physics in 1981). They highlighted that the binding energy of core levels in molecules is specific to one type of atom (C, O, N, ...) and provides direct information on the chemical environment[125]. Therefore, this technique is a method of choice for the identification, characterization, and atomic quantification in samples [126]. Since the first set-up, XPS has known several improvements in terms of sample environment and can now be performed on samples in the gas, solid, and liquid states. However, the principle of analysis remains almost unchanged.

XPS can be roughly described by a three-step-process in the case of condensed matter[127]:

1) Absorption and ionization of the sample under X-ray irradiation (initial state),

2) Response of atom and creation of PE (final state),

3) The electron's transport to the surface and its escape.

In photoemission, the system containing N electrons (initial state) evolves in a configuration with N-1 electron and one hole (final state). The energy released through the photoelectric effect (i.e., the kinetic energy of the PE E_k) can be calculated using Equation (I-6):

$$E_k = h\nu - E_B - \varphi_{sample} \quad \text{(I-6)}$$

where E_B is the binding energy of the considered core level and φ_{sample} is the work function of the sample, which corresponds to the energy difference between the reference vacuum level at the surface and the Fermi level[128]. The kinetic energy distribution of the emitted PE can be measured using an electrostatic analyzer (see description of the instrumentation in Chapter II). The XPS spectrum thus recorded will present the atomic contributions of

the species present in the chemical compound. It is thus possible to identify core levels' peaks with respect to the binding energy scale. By convention, XPS spectra are presented by decreasing binding energy. Figure I-10 illustrates the principle of XPS measurements[129].

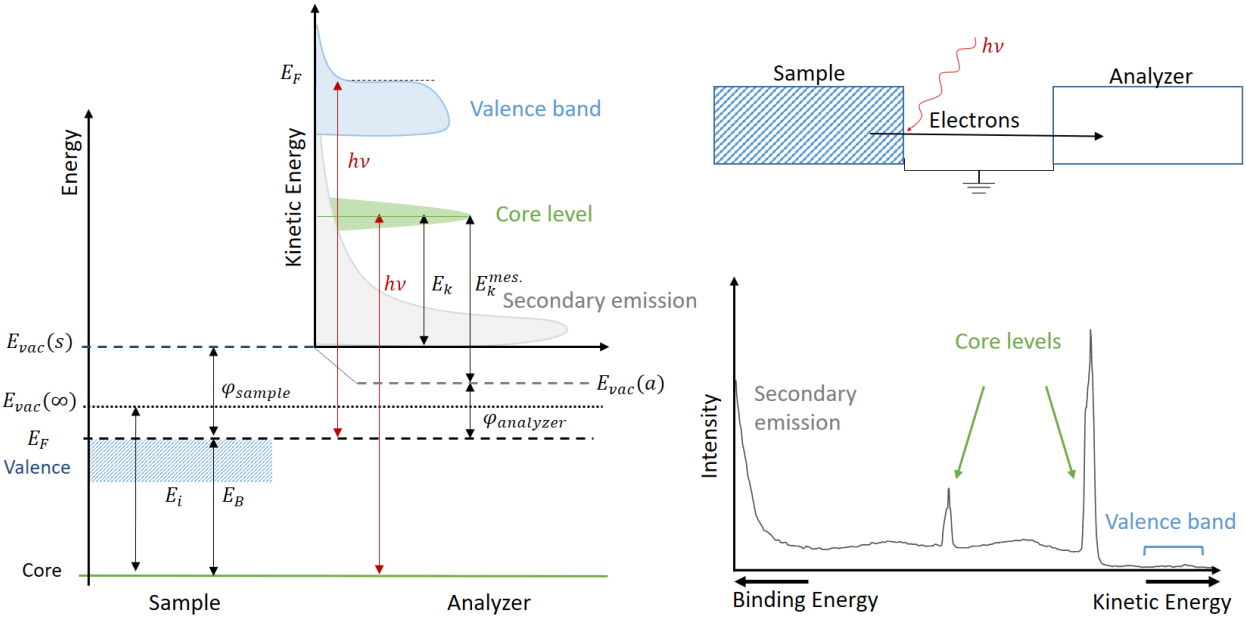

Figure I-10: Scheme of XPS measurement principle: Energy diagram of photoexcitation of electrons in a solid and photoelectron spectrum. Image adapted from [129].

In order to retrieve information of the occupied electronic states of the system, it is necessary to calibrate the spectra, i.e., to define the vacuum level of reference properly. Usually, for solid-state physics, the reference vacuum level is not taken for an electron at rest at an infinite distance $E_{vac}(\infty)$ but in a free space at the surface of the sample ($E_{vac}(s)$) [130], [131]. The electron can therefore still feel the electric field of the surface, creating an energy shift with respect to $E_{vac}(\infty)$[132], [133]. Figure I-10 describes the case of a good electrical contact between the sample and the analyzer (thermodynamic equilibrium). Their Fermi levels are therefore aligned. At the spectrometer level, the kinetic energy measured ($E_k^{mes.}$), which is referenced to the vacuum level of the analyzer $E_{vac}(a)$, can thus be expressed with respect to the Fermi level:

$$E_k^{mes.} = h\nu - E_B - \varphi_{analyzer} \qquad (I\text{-}7)$$

with $\varphi_{analyzer}$ the work function of the spectrometer. In most cases, the work function of the spectrometer and the incident photon energy are known parameters of the

experimental setup. By measuring the PE kinetic energy $E_{k,mes}$, it is then possible to access the binding energy E_B of the electronic level from which the PE originates.

I.3.2.ii. XPS spectrum features

As illustrated in Figure I-10, an XPS spectrum is composed of several peaks corresponding to PE emission. By identifying the energies associated with each peak, it is not only possible to determine the nature of the atoms present in this material but also their chemical environment. Each peak generally presents a Voigt profile where the position, intensity, and width (or Full-Width Half-Maximum (FWHM)) are characteristic of the electronic levels of the elements present in the material.

- Position

The first information obtained by peak fitting analysis is the position of the peak with respect to the binding energy scale. Nevertheless, one must note that the binding energy is not associated with a single electron level but is the difference between the energy of the N electrons of the non-ionized atom in the ground state (initial state) and the energy of the N-1 electrons of the ionized atom (final state). Therefore, the final state of the atom also affects the value of the binding energy [134]. All factors that could influence the initial or final states will modify the electrostatic potential felt by the core-electron and will thus modify its binding energy. The binding energy difference between two different chemical forms of the same atom is called a "chemical shift" (noted ΔE)[135], [136]. It is a short-range effect and is due to the localization of atoms of the core levels.

The initial state energy variation comes mainly from the Coulombic interaction between core and valence electrons. This electrostatic interaction is determined by the charge distribution on the emitting atom and therefore depends on its vicinity. In the case of a bond between two atoms of different electron densities, the valence electron density is displaced towards the withdrawing atom (most electronegative atom). The electropositive atom, therefore, reaches a higher oxidation state. As the extraction of an electron from an electron-depleted environment will require more energy, this results in an increase of the binding energy. On the contrary, the binding energy of the withdrawing atom will decrease.

Chemical shifts are usually discussed qualitatively even if some computational approaches have now been developed (based on density functional theory (DFT) methods)[137], [138]. In condensed matter, the vicinity of the atom (local chemical and physical environment) could also affect its charge distribution[134]. Similarly, for ionic species, the charge network around the emitter atom could have a significant influence (Madelung contribution)[139].

Concerning the final state, its energy is directly related to the relaxation process. Intra-atomic relaxations are generally considered to have a negligible contribution. On the other hand, extra-atomic relaxations can have significant influences depending on the nature of the bonds formed between the emitter atom and its neighbors[140], [141].

- Intensity

The study of XPS peak intensities allows quantitative analyses. However, this operation requires to take into account many factors as illustrated by the expression of the measured XPS peak intensity (I_i^{peak})[142], [143]:

$$I_i^{peak} = \sigma_i \lambda_i N_i C \qquad \text{(I-8)}$$

where σ_i is the photoionization cross-section for a core-level K of an element i, λ_i the inelastic mean free path (IMFP) of the electrons emitted from the K shell of the i element, N_i the average atomic concentration of element "i" in the surface under analysis, and C refers to all other factors related to quantitative signal detection (assumed to remain constant during the time of the experiment).

The photoelectric cross-section varies with photon energy approximately as $(h\nu)^{-3}$[144]. Therefore, it is maximum when the energy of the incident radiation is close to the binding energy of the target atom (as soon as it is higher). In the condensed phase, an electron undergoes several collisions with neighboring atoms. It is well illustrated by the low value of their inelastic mean free path in liquid water presented in Figure I-11[145], [146]. In fact, the XPS depth sensitivity directly depends on the attenuation length of the PE ejected from matter[147] and, in turn, on their LET. The attenuation length or mean escape depth (MED) is commonly defined by the thickness of the sample layer from which the electrons can escape. If the effects of elastic-electron scattering in the material are ignored, the MED of the detected electrons is given by[148]:

$$MED_{electrons} = \lambda \cos\theta \qquad \text{(I-9)}$$

where θ is the electron emission angle with respect to the surface normal.

The MED is, therefore, maximal when the emission is normal to the surface (θ =0).

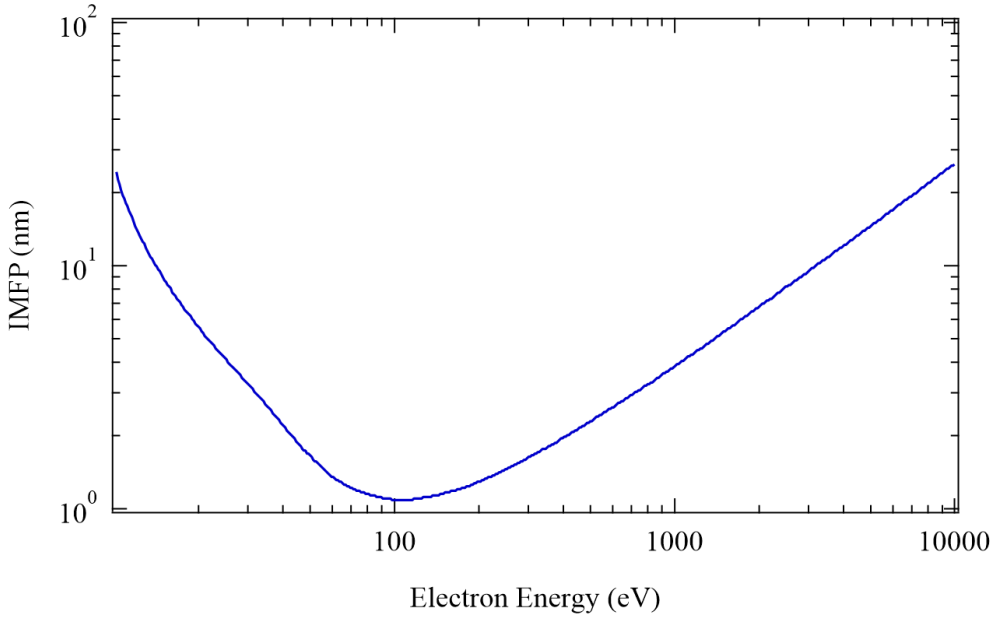

Figure I-11: Electrons inelastic mean free path (IMFP) in liquid water. Data are presented as a function of electron energy. (Theoretical values calculated by [145]*)*

From Equation (I-9), the intensity of electrons emitted (I) from a depth x, for a given material is given by the Beer-Lambert relationship[149] [10]:

$$I = I_0 e^{-x/\lambda \cos\theta} \qquad \text{(I-10)}$$

According to Equation (I-10), we observe that the IMFP strongly influences the XPS sensitivity. As λ increases when the PE energy increases (for PE energies >100 eV), it is possible to probe deeper into a sample by increasing the incident photon energy as it will increase PE kinetic energies. Usually, it is evaluated that more than 95% of the electrons contributing to the XPS spectrum come from a depth of $\sim 3 \cdot \lambda cos\theta$ (corresponding to 2-10 nm in liquid water). This result highlights the fact that XPS remains a surface characterization technique.

- Peak broadening

The full resolution (i.e., the FWHM) of a peak is a convolution of the X-ray energy resolution, the analyzer properties (broadening), and the studied element's intrinsic line-

[10] *Equation (I-10) is true if elastic scattering is neglected.*

width. The broadening relative to the instrumentation (extrinsic) is usually assumed to be Gaussian[135]. It depends either on the energy resolution of the source or the analyzer. In the first case, it directly depends on the energy distribution of the incident photons. The resolving power of the monochromator will, therefore, directly impact the width of the peak. The extrinsic resolution will be further described in Chapter II (section II.2.1). The broadening effect resulting from the photo-emission process is related to the lifetime of the ionized core-hole state (namely τ)[150]. It is usually assumed to be Lorentzian in nature and follows the relation[151]

$$FWHM_{Lorentzian} = \hbar/\tau \qquad \text{(I-11)}$$

The less stable the vacancy, the shorter τ will be. Therefore, photoionization of the deeper electronic layers of an atom (higher binding energy) leads to ionized states whose lifetime becomes shorter and shorter. It thus results in a gradual broadening of the lines: $s_{FWHM} > p_{FWHM} > d_{FWHM} > f_{FWHM}$.

- Secondary structure

In an XPS spectrum, performed on condensed matter, the prominent peaks (PE or AE) are often accompanied by several secondary structures[152], [153].

Satellite peaks can appear due to multi-electronic effects occurring during the photoionization. The outgoing PE can indeed have a strong interaction with one of the valence electrons. If it leads to the ejection of the electron, from the outer shell in the continuum (double ionization of the atom), the satellite peak is called “shake off”. On the other hand, if it brings the valence electron to a higher-energy level, the PE undergoes intrinsic energy losses. It can lead to a “shake-up” satellite peak located a few electron volts above its core level central peak position[149]. Satellite peaks can be significant in the studies of transition materials (elements with non-filled valence layers). They can also appear in aromatic organic compounds due to the π orbital (transition $\pi \rightarrow \pi^*$)[154].

As illustrated by the ”grey structure” in Figure I-10, PE and AE signals come out of an inelastic background due to secondary emission. Before leaving the surface, PE can indeed interact with other electrons and lose energy as they try to escape the sample (extrinsic losses). It leads to the production of other electrons of lower kinetic energy. The

signal of these electrons is thus superimposed with the electrons of low kinetic energy emitted through the photoionization process.

I.3.3. Recent developments for XPS studies

XPS has proven to be an excellent tool for studying biological samples in the solid phase as it directly brings information about the sample's chemical composition and environment[155], [156]. Nevertheless, numerous biological systems are surrounded by water molecules. It is therefore mandatory to be able to apply all the spectroscopy techniques to the liquid phase. Conventional XPS systems work under high vacuum conditions. It is because the IMFP of electrons directly depends on inelastic scattering by surrounding molecules. From this constraint, liquid samples are usually not considered "vacuum friendly" according to their proportion to volatilize. Therefore first liquid experiments, performed by Siegbahn's team, were limited to liquid with low vapor pressures[157], [158]. Thanks to the development of an under vacuum liquid micro-jet, volatile liquid samples, such as water, have become studyable[157], [159]. The successful implementation of this system for XPS measurements relies on three conditions. At first, the molecular flow of the gas phase must not be limiting for the detection of electrons. This is ensured by the Knudsen condition, which relates the diameter of the liquid jet (D_{jet}) and the inelastic mean free path of electrons through the vapor pressure surrounding the jet (λ_{H_2O})[160]:

$$D_{jet}/\lambda_{H_2O} < 0.5 \qquad \text{(I-12)}$$

Secondly, the vapor flow must be limited to avoid saturation of the pumping system. This condition is usually ensured by performing differential pumping or using skimmers at the entrance to the spectrometer lens system. Finally, the velocity of the liquid must be high enough to prevent the jet from freezing. Following these conditions, studies of highly volatile solvents, such as water (vapor pressure equal to 6 mbar at 0°C [161]), were accessible using liquid jets of micrometer diameter. To date, liquid micro-jets have become a relatively common experimental set-up on synchrotron facilities[153], [162]. Growing interest arises from the fact that such an environment allows studying ultrafast dynamical processes that could occur in aqueous samples following K-ionization (protonation, Auger decay, ICD, ETMD)[163].

Another strategy is to develop an XPS spectrometer dedicated to near ambient pressure analysis (NAP-XPS)[164], [165]. Such conditions are particularly adapted to the study of samples in "real environment" conditions and focus on understanding interfacial reactions between a solid or a liquid and its surrounding gas phase. NAP-XPS analyzers typically operate at pressures ranging from almost 1 mbar to 100 mbar[166]. It is achieved by reducing the distance between the analyzer and the ionization zone to match the low IMFP of the PE in such an environment. Finally, as for XAS experimental set-ups, fluidic cells also emerge to study liquid in ultra-high vacuum conditions[167]–[169]. It is also important to note that XPS is mandatory to fully interpret XAS measurements and thus to understand the chemical bonding properties of samples [170].

As explained before, in the case of a K-shell ionization, multiple electrons (PE and AE) can be ejected from the molecular system. They share part of the energy deposited by the photon into the molecule. Thus, having a technique to measure in coincidence (for one photon energy) the PE energy and its correlated AE can help to simplify the comprehension of complex Auger spectra and give valuable input for the models concerning doubly charged species. Dedicated spectrometers were developed to study multiple ionization processes, such as a ”magnetic bottle” time of flight electron spectrometer, which will be further described in the following chapters. Usually used for gas-phase studies[171], [172],[173], this electron-electron coincidence spectroscopy technique (APECS) has been recently adapted to liquids [174]. As a ”magnetic bootle” can detect efficiently low kinetic energy electrons (<20 eV), it also is a good tool to study ICD or ETMD phenomena, and thus the energy transfer between the solute and the solvent after a K-shell ionization. Other types of coincidence techniques were developed as electron-ion coincidence (PEPICO)[81], ion-ion coincidence (PIPICO)[56]. However, they are used only for small biomolecules isolated in the gas phase.

I.4. Objectives of the PhD

Understanding the processes of light-matter interaction is the basis of many scientific interrogations. In photochemistry, simple excitation events in the UV, corresponding to an energy deposition of a few eV per molecule, are relatively well described. To a certain extent, the effects of valence ionization by high energy particles are also known (deposition of a few tens of eV leading, in particular, to the breaking of OH and CH bonds) by radiolysis studies. In contrast, the effects of inner shell ionizations, bringing energy deposition of several hundreds of eV at the scale of an atom, are still poorly understood in the condensed phase. While they remain rare events, when an environment is exposed to high energy particles, their damaging effects on biomolecules, proteins, and DNA could be very significant[175] and be the limiting factor for structural studies, in particular, with X-ray microscopes or high energy free electron (XFEL) lasers[108], [176]. It is now clear that soft X-rays (100 eV-2 keV) are the ideal candidate to study such phenomenon since they interact with the core-electrons of biological matter and produce very dense ionization tracks[177].

A central difficulty in studying irradiation mechanisms in liquid samples lies in the fact that the events take place at different time scales, beginning with the energy deposition ($<10^{-15}$ s), passing through the physico-chemical and inhomogeneous chemistry stages (10^{-15} s $< t < 10^{-6}$ s) and leading to biological damage at longer time scales. In order to have a complete description of the processes following an inner-shell ionization, it is, therefore, necessary to adopt different strategies. Therefore, this project will be split into two different axes. One will be interested in the energy deposition processes and involved mechanisms of the photoionization in the liquid phase (~fs timescale). The other one will focus on the understanding of the subsequent radiochemistry initiated in liquid aqueous samples.

Soft X-rays remain very difficult to handle at atmospheric pressure because of their low penetration in liquid water (~10 µm). Therefore, the primary objective of this thesis is to develop the use of new experimental set-ups dedicated to liquid experiments on soft X-ray synchrotron beamlines. **We will first present the implementation of a dedicated microfluidic cell for liquid irradiation under a low penetration beam.**

Using very sensitive methods, we will try to bring more information on the **radiolysis of water in these dense ionization environments**. Once solvated, molecules see their structural and dynamic molecular properties modified. The strong interaction with surrounding water molecules can lead to ultrafast energy transfer[178]. Even if chemical probes can help study different ranges of time and energy, they do not allow studying early processes under the femtosecond timescale. To that aim, it is crucial to perform spectroscopic measurements in the liquid phase. Thanks to the recent development of an under vacuum liquid microjet[163], it would be possible to evaluate the solvent effect on the solvated molecules' electronic structure. **We also aim to perform these measurements using conventional and coincidence electron spectroscopy** to decipher the photoionization mechanisms. Finally, we will try to **investigate the inevitable radiation damage** occurring during the spectroscopic measurement[179], [180]. Even if these processes are known, they are still poorly described for liquid samples and require further study for the liquid microjet.

Bibliography Chapter I

[1] A. Thompson *et al.*, "X-ray Data Booklet," Lawrence Berkeley National Laboratory, 2009.

[2] N. Bohr, "The penetration of atomic particles through matter," *Niels Bohr Collect. Work.*, vol. 8, no. C, pp. 423–568, Jan. 1987.

[3] J. H. Hubbell, *Bibliography and current status of K, L, and higher shell fluorescence yields for computations of photon energy-absorption coefficients*. Gaithersburg, 1989.

[4] H. Nikjoo, D. Emfietzoglou, and D. E. Charlton, "The Auger effect in physical and biological research," *Int. J. Radiat. Biol.*, vol. 84, no. 12, pp. 1011–1026, 2008.

[5] M. Drescher *et al.*, "Time-resolved atomic inner-shell spectroscopy," *Nature*, vol. 419, no. 6909, pp. 803–807, Oct. 2002.

[6] A. I. Kuleff and L. S. Cederbaum, "Tracing ultrafast interatomic electronic decay processes in real time and space," *Phys. Rev. Lett.*, vol. 98, no. 8, pp. 1–4, Dec. 2007.

[7] T. Jahnke, "Interatomic and intermolecular Coulombic decay: The coming of age story," *J. Phys. B At. Mol. Opt. Phys.*, vol. 48, no. 8, 2015.

[8] I. Unger *et al.*, "First Observation of Electron Transfer Mediated Decay in Aqueous Solutions: A Novel Probe of Ion Pairing," *arXiv.org*, Apr. 2016.

[9] V. Stumpf, K. Gokhberg, and L. S. Cederbaum, "The role of metal ions in X-ray induced photochemistry," *Nat. Chem.*, vol. 8, no. 3, pp. 237–241, May 2015.

[10] L. S. Cederbaum, J. Zobeley, and F. Tarantelli, "Giant intermolecular decay and fragmentation of clusters," *Phys. Rev. Lett.*, vol. 79, no. 24, pp. 4778–4781, 1997.

[11] R. Santra, J. Zobeley, and L. S. Cederbaum, "Electronic decay of valence holes in clusters and condensed matter," *Phys. Rev. B - Condens. Matter Mater. Phys.*, vol. 64, no. 24, pp. 1–10, 2001.

[12] J. Zobeley, R. Santra, and L. S. Cederbaum, "Electronic decay in weakly bound heteroclusters: Energy transfer versus electron transfer," *J. Chem. Phys.*, vol. 115, no. 11, pp. 5076–5088, Sep. 2001.

[13] Y. Dong, Y. Gao, W. Liu, T. Gao, Y. Zheng, and L. Sanche, "Clustered DNA Damage Induced by 2-20 eV Electrons and Transient Anions: General Mechanism and Correlation to Cell Death," *J. Phys. Chem. Lett.*, vol. 10, no. 11, pp. 2985–2990, 2019.

[14] M. Tubiana, J. Dutreix, A. Dutreix, and P. Jockey, *Bases physiques de la radiothérapie et de la radiobiologie*. Masson & cie, 1963.

[15] G. V. Buxton, *Radiation Chemistry - Present Status and Future Trends*, vol. 4, no. 3. 2001.

[16] D. T. Goodhead, "Energy deposition stochastics and track structure: What about the target?," *Radiat. Prot. Dosimetry*, vol. 122, no. 1–4, pp. 3–15, 2006.

[17] G. Kraft, M. Krämer, and M. Scholz, "LET, track structure and models," *Radiat. Environ. Biophys.*, vol. 31, no. 3, pp. 161–180, Sep. 1992.

[18] A. H. Samuel and J. L. Magee, "Theory of radiation chemistry. II. Track effects in radiolysis of water," *J. Chem. Phys.*, vol. 21, no. 6, pp. 1080–1087, 1953.

[19] A. Mozumder and J. L. Magee, "Model of tracks of ionizing radiations for radical reaction mechanisms.," *Radiat. Res.*, vol. 28, no. 2, pp. 203–214, 1966.

[20] D. T. Goodhead, "Track Structure Considerations in Low Dose and Low Dose Rate Effects of Ionizing Radiation," in *Effects of Low Dose and Low Dose Rate Radiation*, vol. 16, Academic Press, Inc., 1992, pp. 7–44.

[21] A. I. Kassis, "Molecular and cellular radiobiological effects of Auger emitting radionuclides," *Radiat. Prot. Dosimetry*, vol. 143, no. 2–4, pp. 241–247, Feb. 2011.

[22] H. Nikjoo and D. T. Goodhead, "Track structure analysis illustrating the prominent role of low-energy electrons in radiobiological effects of low-LET radiations," *Phys. Med. Biol.*, vol. 36, no. 2, pp. 229–238, 1991.

[23] J. L. Magee and A. Chatterjee, "Theory of the chemical effects of high-energy electrons," *J. Phys. Chem.*, vol. 82, no. 20, pp. 2219–2226, Oct. 1978.

[24] A. Cole, "Absorption of 20-eV to 50,000-eV Electron Beams in Air and Plastic," *Radiat. Res.*, vol. 38, no. 1, p. 7, Apr. 1969.

[25] H. Yamaguchi, "A spur diffusion model applied to estimate yields of species in water irradiated by monoenergetic photons of 50 eV-2 MeV," *Int. J. Radiat. Appl. Instrumentation. Part*, vol. 34, no. 5, pp. 801–807, 1989.

[26] J. B. Melanie Spothem, Mehran Mostafavi, Thierry Douki, *Radiation chemistry: from basics to applications in materials and life sciences*. 2008.

[27] S. M. Pimblott and A. Mozumder, "Structure of electron tracks in water. 2. Distribution of primary ionizations and excitations in water radiolysis," *J. Phys. Chem.*, vol. 95, no. 19, pp. 7291–7300, 1991.

[28] F. Giesel, "Ueber Radium und radioactive Stoffe," *Berichte der Dtsch. Chem. Gesellschaft*, vol. 35, no. 3, pp. 3608–3611, 1902.

[29] C. Ferradini and J.-P. Jay-Gerin, "La radiolyse de l'eau et des solutions aqueuses : historique et actualité," *Can. J. Chem.*, vol. 77, no. 9, pp. 1542–1575, 1999.

[30] W. G. Burns and H. E. Sims, "Effect of radiation type in water radiolysis," *J. Chem. Soc. Faraday Trans. 1 Phys. Chem. Condens. Phases*, vol. 77, no. 11, pp. 2803–2813, 1981.

[31] S. Le Caër, "Water radiolysis: Influence of oxide surfaces on H2 production under ionizing radiation," *Water (Switzerland)*, vol. 3, no. 1, pp. 235–253, 2011.

[32] G. Baldacchino *et al.*, "Importance of radiolytic reactions during high-LET irradiation modalities: LET effect, role of O2 and radiosensitization by nanoparticles," *Cancer Nanotechnol.*, vol. 10, no. 1, 2019.

[33] A. O. Allen, "Radiation Chemistry of Aqueous Solutions," *J. Phys. Colloid Chem.*, vol. 52, no. 3, pp. 479–490, Mar. 1948.

[34] J. A. LaVerne and R. H. Schuler, "Decomposition of water by very high linear energy transfer radiations," *J. Phys. Chem.*, vol. 87, no. 23, pp. 4564–4565, 1983.

[35] A. K. Ganguly and J. L. Magee, "Theory of Radiation Chemistry. III. Radical Reaction Mechanism in the Tracks of Ionizing Radiations," *J. Chem. Phys.*, vol. 25, no. 1, pp. 129–134, Jul. 1956.

[36] S. M. Pimblott and J. A. LaVerne, "Diffusion-kinetic theories for LET effects on the radiolysis of water," *J. Phys. Chem.*, vol. 98, no. 24, pp. 6136–6143, 1994.

[37] H. A. Schwarz, "Applications of the spur diffusion model to the radiation chemistry of aqueous solutions," *J. Phys. Chem.*, vol. 73, no. 6, pp. 1928–1937, 1969.

[38] H. Yamaguchi, Y. Uchihori, N. Yasuda, M. Takada, and H. Kitamura, "Estimation of Yields of OH Radicals in Water Irradiated by Ionizing Radiation," *J. Radiat. Res.*, vol. 46, no. 3, pp. 333–341, 2005.

[39] M. A. Hill and F. A. Smith, "Calculation of initial and primary yields in the radiolysis of water," *Radiat. Phys. Chem.*, vol. 43, no. 3, pp. 265–280, 1994.

[40] J. Meesungnoen, A. Filali-Mouhim, S. Mankhetkorn, and J.-P. Jay-Gerin, "Comment on 'Experimental Determination of the Dependence of OH Radical Yield on Photon Energy: A Comparison with Theoretical Simulations' by Fulford et al. (J. Phys. Chem. A 1999, 103 , 11345−11349)," *J. Phys. Chem. A*, vol. 105, no. 10, pp. 2125–2126, Mar. 2001.

[41] B. L. Henke, E. M. Gullikson, and J. C. Davis, "X-Ray Interactions: Photoabsorption, Scattering, Transmission, and Reflection at E = 50-30,000 eV, Z = 1-92," *At. Data Nucl. Data Tables*, vol. 54, no. 2, pp. 181–342, Jul. 1993.

[42] J. Fulford, P. Bonner, D. T. Goodhead, M. A. Hill, and P. O'Neill, "Experimental determination of the dependence of OH radical yield on photon energy: A comparison with theoretical simulations," *J. Phys. Chem. A*, vol. 103, no. 51, pp. 11345–11349, 1999.

[43] L. Vyšín *et al.*, "Chemical Dosimetry in the 'Water Window': Ferric Ions and Hydroxyl Radicals Produced by Intense Soft X Rays.," *Radiat. Res.*, vol. 000, 2020.

[44] G. Baldacchino *et al.*, "Effets de TEL dans la radiolyse de l'eau. Expériences de radiolyse pulsée avec les ions lourds," *J. Chim. Phys. Physico-Chimie Biol.*, vol. 96, no. 1, pp. 50–60, 1999.

[45] J. A. LaVerne and R. H. Schuler, "Track effects in water radiolysis with high-energy heavy ions," *J. Phys. Chem.*, vol. 90, no. 22, pp. 5995–5996, Oct. 1986.

[46] J. A. LaVerne, R. H. Schuler, and W. G. Burns, "Track effects in radiation chemistry: Production of HO2• within the track core in the heavy-particle radiolysis of water," *J. Phys. Chem.*, vol. 90, no. 14, pp. 3238–3242, 1986.

[47] W. G. Burns, R. May, and K. F. Baverstock, "Oxygen as a Product of Water Radiolysis in High-LET Tracks. I. The Origin of the Hydroperoxyl Radical in Water Radiolysis," *Radiat. Res.*, vol. 86, no. 1, p. 1, Apr. 1981.

[48] A. Appleby and H. A. Schwarz, "Radical and molecular yields in water irradiated by .gamma.-rays and heavy ions," *J. Phys. Chem.*, vol. 73, no. 6, pp. 1937–1941, Jun. 1969.

[49] C. Ferradini and J. P. Jay-Gerin, "Does multiple ionization intervene for the production of HO2/. Radicals in high-let liquid water radiolysis?," *Radiat. Phys. Chem.*, vol. 51, no. 3, pp. 263–267, 1998.

[50] G. H. Olivera *et al.*, "Multiple ionization in the earlier stages of water radiolysis," *Phys. Med. Biol.*, vol. 43, no. 8, pp. 2347–2360, Aug. 1998.

[51] B. Gervais, M. Beuve, G. H. Olivera, M. E. Galassi, and R. D. Rivarola, "Production of HO2 and O2 by multiple ionization in water radiolysis by swift carbon ions," *Chem. Phys. Lett.*, vol. 410, no. 4–6, pp. 330–334, 2005.

[52] B. Gervais, M. Beuve, G. H. Olivera, and M. E. Galassi, "Numerical simulation of multiple ionization and high LET effects in liquid water radiolysis," *Radiat. Phys. Chem.*, vol. 75, no. 4, pp. 493–513, Apr. 2006.

[53] I. Tavernelli, M. P. Gaigeot, R. Vuilleumier, C. Stia, M. A. H. Du Penhoat, and M. F. Politis, "Time-dependent density functional theory molecular dynamics simulations of liquid water radiolysis," *ChemPhysChem*, vol. 9, no. 14, pp. 2099–2103, 2008.

[54] M. P. Gaigeot *et al.*, "A multi-scale ab initio theoretical study of the production of free radicals in swift ion tracks in liquid water," *J. Phys. B At. Mol. Opt. Phys.*, vol. 40, no. 1, pp. 1–12, Jan. 2007.

[55] J. H. D. Eland, "Double photoionisation spectra of methane, ammonia and water," *Chem. Phys.*, vol. 323, no. 2–3, pp. 391–396, Apr. 2006.

[56] P. J. Richardson, J. H. D. Eland, P. G. Fournier, and D. L. Cooper, "Spectrum and decay of the doubly charged water ion," *J. Chem. Phys.*, vol. 84, no. 6, pp. 3189–3194, 1986.

[57] Y. Hikosaka *et al.*, "Communication: Formation of slow electrons in the Auger decay of core-ionized water molecules," *J. Chem. Phys.*, vol. 137, no. 19, 2012.

[58] D. T. Goodhead, J. Thacker, R. Cox, and R. E. Wilkinson, "Effectiveness of $0 \cdot 3$ keV Carbon Ultrasoft X-rays for the Inactivation and Mutation of Cultured Mammalian Cells,"

Int. J. Radiat. Biol. Relat. Stud. Physics, Chem. Med., vol. 36, no. 2, pp. 101–115, Jan. 1979.

[59] J. Thacker, R. E. Wilkinson, and D. T. Goodhead, "The induction of chromosome exchange aberrations by carbon ultrasoft x-rays in v79 hamster cells," *Int. J. Radiat. Biol.*, vol. 49, no. 4, pp. 645–656, 1985.

[60] G. J. Neary, R. J. Preston, and J. R. K. Savage, "Chromosome Aberrations and the Theory of RBE," *Int. J. Radiat. Biol. Relat. Stud. Physics, Chem. Med.*, vol. 12, no. 4, pp. 317–345, Jan. 1967.

[61] M. Tubiana, J. Dutreix, and A. Wambersie, *An Introduction to Radiobiology*. Taylor & Francis, 1990.

[62] R. K. Sachs, A. M. Chen, and D. J. Brenner, "Review: Proximity effects in the production of chromosome aberrations by ionizing radiation," *Int. J. Radiat. Biol.*, vol. 71, no. 1, pp. 1–19, 1997.

[63] K. M. Prise, C. H. L. Pullar, and B. D. Michael, "A study of endonuclease III-sensitive sites in irradiated DNA: detection of α-particle-induced oxidative damage," *Carcinogenesis*, vol. 20, no. 5, pp. 905–909, May 1999.

[64] H. Nikjoo, D. Emfietzoglou, T. Liamsuwan, R. Taleei, D. Liljequist, and S. Uehara, "Radiation track, DNA damage and response - A review," *Reports Prog. Phys.*, vol. 79, no. 11, 2016.

[65] C. Richardson and M. Jasin, "Frequent chromosomal translocations induced by DNA double-strand breaks," *Nature*, vol. 405, no. 6787, pp. 697–700, Jun. 2000.

[66] R. Roots, W. Holley, A. Chatterjee, E. Rachal, and G. Kraft, "The influence of radiation quality on the formation of DNA breaks," *Adv. Sp. Res.*, vol. 9, no. 10, pp. 45–55, 1989.

[67] R. Roots, W. Holley, A. Chatterjee, M. Irizarry, and G. Kraft, "The formation of Strand breaks in DNA after high-LET irradiation: A comparison of data from in vitro and cellular systems," *Int. J. Radiat. Biol.*, vol. 58, no. 1, pp. 55–69, 1990.

[68] J. S. Bedford and D. T. Goodhead, "Breakage of Human Interphase Chromosomes by Alpha Particles and X-rays," *Int. J. Radiat. Biol.*, vol. 55, no. 2, pp. 211–216, Jan. 1989.

[69] J. F. Ward, "DNA Damage Produced by Ionizing Radiation in Mammalian Cells: Identities, Mechanisms of Formation, and Reparability," in *Progress in Nucleic Acid Research and Molecular Biology*, vol. 35, no. C, 1988, pp. 95–125.

[70] J. R. Milligan, J. A. Aguilera, and J. F. Ward, "Variation of single-strand break yield with scavenger concentration for plasmid DNA irradiated in aqueous solution," *Radiat. Res.*, vol. 133, no. 2, pp. 151–157, 1993.

[71] J. Stanton, G. Taucher-Scholz, M. Schneider, J. Heilmann, and G. Kraft, "Protection of DNA from high LET radiation by two OH radical scavengers, tris (hydroxymethyl) aminomethane and 2-mercaptoethanol," *Radiat. Environ. Biophys.*, vol. 32, no. 1, pp. 21–32, 1993.

[72] J. Cadet *et al.*, "Hydroxyl radicals and DNA base damage," *Mutat. Res. - Fundam. Mol. Mech. Mutagen.*, vol. 424, no. 1–2, pp. 9–21, 1999.

[73] J. P. Pouget, S. Frelon, J. L. Ravanat, I. Testard, F. Odin, and J. Cadet, "Formation of modified DNA bases in cells exposed either to gamma radiation or to high-LET particles," *Radiat. Res.*, vol. 157, no. 5, pp. 589–595, 2002.

[74] T. Douki, J. L. Ravanat, J. P. Pouget, I. Testard, and J. Cadet, "Minor contribution of direct ionization to DNA base damage induced by heavy ions," *Int. J. Radiat. Biol.*, vol. 82, no. 2, pp. 119–127, 2006.

[75] B. Fayard *et al.*, "Cell Inactivation and Double-Strand Breaks: The Role of Core Ionizations, as Probed by Ultrasoft X Rays," *Radiat. Res.*, vol. 157, no. 2, pp. 128–140, 2002.

[76] D. T. Goodhead, J. Thacker, and R. Cox, "Is selective absorption of ultrasoft X-rays biologically important in mammalian cells?," *Phys. Med. Biol.*, vol. 26, no. 6, pp. 1115–1127, 1981.

[77] M. A. Hervé Du Penhoat *et al.*, "Double-strand break induction and repair in V79-4 hamster cells: The role of core ionisations, as probed by ultrasoft X-rays," *Int. J. Radiat. Biol.*, vol. 86, no. 3, pp. 205–219, 2010.

[78] C. M. De Lara, M. A. Hill, T. J. Jenner, D. Papworth, and P. O'Neill, "Dependence of the yield of DNA double-strand breaks in Chinese hamster V79-4 cells on the photon energy of ultrasoft X rays," *Radiat. Res.*, vol. 155, no. 3, pp. 440–448, 2001.

[79] W. Eberhardt *et al.*, "Site-Specific Fragmentation of Small Molecules Following Soft-X-Ray Excitation," *Phys. Rev. Lett.*, vol. 50, no. 14, pp. 1038–1041, Apr. 1983.

[80] R. Weinkauf, P. Schanen, A. Metsala, E. W. Schlag, M. Bürgle, and H. Kessler, "Highly efficient charge transfer in peptide cations in the gas phase: Threshold effects and mechanism," *J. Phys. Chem.*, vol. 100, no. 47, pp. 18567–18585, 1996.

[81] P. Bolognesi *et al.*, "Photofragmentation of organic molecules of biological interest: The pyrimidine and 2Br-pyrimidine cases," *Nucl. Instruments Methods Phys. Res. Sect. B Beam Interact. with Mater. Atoms*, vol. 279, pp. 118–123, 2012.

[82] D. T. Ha, M. A. Huels, M. Huttula, S. Urpelainen, and E. Kukk, "Experimental and ab initio study of the photofragmentation of DNA and RNA sugars," *Phys. Rev. A - At. Mol. Opt. Phys.*, vol. 84, no. 3, pp. 1–11, 2011.

[83] S. Bari *et al.*, "Photodissociation of protonated leucine-enkephalin in the VUV range of 8-40 eV," *J. Chem. Phys.*, vol. 134, no. 2, 2011.

[84] T. Schlathölter *et al.*, "Multiple Ionization of Free Ubiquitin Molecular Ions in Extreme Ultraviolet Free-Electron Laser Pulses," *Angew. Chemie Int. Ed.*, vol. 55, no. 36, pp. 10741–10745, Aug. 2016.

[85] S. Dörner *et al.*, "Probing Structural Information of Gas-Phase Peptides by Near-Edge X-ray Absorption Mass Spectrometry," *J. Am. Soc. Mass Spectrom.*, vol. 32, no. 3, pp. 670–684, 2021.

[86] L. Schwob *et al.*, "Site-Selective Dissociation upon Sulfur L-Edge X-ray Absorption in a Gas-Phase Protonated Peptide," *J. Phys. Chem. Lett.*, vol. 11, no. 4, pp. 1215–1221, 2020.

[87] K. Schubert *et al.*, "The electronic structure and deexcitation pathways of an isolated metalloporphyrin ion resolved by metal L-edge spectroscopy," *Chem. Sci.*, vol. 12, no. 11, pp. 3966–3976, 2021.

[88] B. Boudaiffa, P. Cloutier, D. Hunting, M. A. Huels, and L. Sanche, "Resonant Formation of DNA Strand Breaks by Low-Energy (3 to 20 eV) Electrons," *Science (80-.).*, vol. 287, no. 5458, pp. 1658–1660, Mar. 2000.

[89] Y. Dong, H. Liao, Y. Gao, P. Cloutier, Y. Zheng, and L. Sanche, "Early Events in Radiobiology: Isolated and Cluster DNA Damage Induced by Initial Cations and Nonionizing Secondary Electrons," *J. Phys. Chem. Lett.*, vol. 12, no. 1, pp. 717–723, 2021.

[90] L. Sanche, "Low energy electron-driven damage in biomolecules," *Eur. Phys. J. D*, vol. 35, no. 2, pp. 367–390, 2005.

[91] H. Abdoul-Carime, S. Gohlke, and E. Illenberger, "Conversion of amino-acids by electrons at subexcitation energies," *Phys. Chem. Chem. Phys.*, vol. 6, no. 1, pp. 161–164, 2004.

[92] F. Martin, P. D. Burrow, Z. Cai, P. Cloutier, D. Hunting, and L. Sanche, "DNA strand breaks induced by 0-4 eV electrons: The role of shape resonances," *Phys. Rev. Lett.*, vol. 93, no. 6, pp. 6–9, 2004.

[93] Y. Gao, Y. Zheng, and L. Sanche, "Low-energy electron damage to condensed-phase DNA and its constituents," *Int. J. Mol. Sci.*, vol. 22, no. 15, 2021.

[94] E. Alizadeh and L. Sanche, "Role of humidity and oxygen level on damage to DNA induced by soft X-rays and low-energy electrons," *J. Phys. Chem. C*, vol. 117, no. 43, pp. 22445–22453, 2013.

[95] K. Fujii *et al.*, "Roles of Hydration for Inducing Decomposition of 2-Deoxy-d-ribose by Ionization of Oxygen K-Shell Electrons," *Radiat. Res.*, vol. 189, no. 3, pp. 264–272, Mar. 2018.

[96] A. Yokoya, S. M. T. Cunniffe, and P. O. Neill, "Effect of Hydration on the Induction of Strand Breaks and Base Lesions in Plasmid DNA Films by γ -Radiation," no. 1, pp. 43–49, 2002.

[97] A. Eschenbrenner *et al.*, "Strand breaks induced in plasmid DNA by ultrasoft X-rays: Influence of hydration and packing," *Int. J. Radiat. Biol.*, vol. 83, no. 10, pp. 687–697, 2007.

[98] G. Beamson, H. Q. Porter, and D. W. Turner, "Photoelectron spectromicroscopy," *Nature*, vol. 290, no. 5807, pp. 556–561, Apr. 1981.

[99] L. R. P. Butler and K. Laqua, "Nomenclature, symbols, units and their usage in spectrochemical analysis—IX. Instrumentation for the spectral dispersion and isolation of optical radiation," *Spectrochim. Acta Part B At. Spectrosc.*, vol. 51, no. 7, pp. 645–664, Jun. 1996.

[100] M.P.Seah and W.A.Dench, "Quantitative Electron Spectroscopy of Surface," *Surf. Interface Anal.*, vol. 1, no. 1, p. 2, 1979.

[101] J. Kirz, C. Jacobsen, and M. Howells, "Soft X-ray microscopes and their biological applications," *Q. Rev. Biophys.*, vol. 28, no. 1, pp. 33–130, Feb. 1995.

[102] A. P. Hitchcock, C. Morin, Y. M. Heng, R. M. Cornelius, and J. L. Brash, "Towards practical soft X-ray spectromicroscopy of biomaterials," *J. Biomater. Sci. Polym. Ed.*, vol. 13, no. 8, pp. 919–937, 2002.

[103] J. Stewart-Ornstein *et al.*, "Using intrinsic X-ray absorption spectral differences to identify and map peptides and proteins," *J. Phys. Chem. B*, vol. 111, no. 26, pp. 7691–7699, 2007.

[104] P. Guttmann and C. Bittencourt, "Overview of nanoscale NEXAFS performed with soft X-ray microscopes," *Beilstein J. Nanotechnol.*, vol. 6, no. 1, pp. 595–604, Feb. 2015.

[105] J. D. West, Y. Zhu, S. Saem, J. Moran-Mirabal, and A. P. Hitchcock, "X-ray Absorption Spectroscopy and Spectromicroscopy of Supported Lipid Bilayers," *J. Phys. Chem. B*, vol. 121, no. 17, pp. 4492–4501, May 2017.

[106] J. Stöhr, "Principles, Techniques, and Instrumentation of NEXAFS," in *Journal of Chemical Information and Modeling*, vol. 53, no. 9, 1992, pp. 114–161.

[107] R. M. Glaeser, "Limitations to significant information in biological electron microscopy as a result of radiation damage," *J. Ultrasructure Res.*, vol. 36, no. 3–4, pp. 466–482, 1971.

[108] A. Gianoncelli, L. Vaccari, G. Kourousias, D. Cassese, D. E. Bedolla, and S. Kenig, "Soft X-Ray Microscopy Radiation Damage On Fixed Cells Investigated With Synchrotron Radiation FTIR Microscopy," *Nat. Publ. Gr.*, no. January, pp. 1–11, 2015.

[109] S. Lacombe, F. Bournel, C. Laffon, and P. Parent, "Radical photochemistry in oxygen-loaded ices," *Angew. Chemie - Int. Ed.*, vol. 45, no. 25, pp. 4159–4163, 2006.

[110] P. Parent, C. Laffon, F. Bournel, J. Lasne, and S. Lacombe, "NEXAFS : a unique tool to

follow the photochemistry of small organic molecules in condensed water," *J. Phys. Conf. Ser.*, vol. 261, p. 012008, Jan. 2011.

[111] K. Fujii and A. Yokoya, "XANES spectral changes of hydrated deoxyribose induced by K -shell ionization of oxygen XANES Spectral Changes of Hydrated Deoxyribose Induced by K -Shell Ionization of Oxygen," vol. 040005, no. January, 2019.

[112] K. Akamatsu and A. Yokoya, "X-Ray Absorption near Edge Structures of DNA or its Components around the Oxygen K-shell Edge," *Radiat. Res.*, vol. 155, no. 3, pp. 449–452, 2006.

[113] B. X. Yang and J. Kirz, "Extended x-ray-absorption fine structure of liquid water," *Phys. Rev. B*, vol. 36, no. 2, pp. 1361–1364, Jul. 1987.

[114] S. Schreck, G. Gavrila, C. Weniger, and P. Wernet, "A sample holder for soft x-ray absorption spectroscopy of liquids in transmission mode," *Rev. Sci. Instrum.*, vol. 82, no. 10, 2011.

[115] C. Gosse, S. Stanescu, J. Frederick, and S. Lefrançois, "A flow cell for soft X-ray spectromicroscopy in liquid media Charlie," *J. Mater. Chem. B*, vol. 6, no. 35, pp. 7634–7639, 2020.

[116] R. Qiao *et al.*, "Soft x-ray spectroscopy of high pressure liquid," *Rev. Sci. Instrum.*, vol. 89, no. 1, 2018.

[117] D. Grötzsch *et al.*, "A sealable ultrathin window sample cell for the study of liquids by means of soft X-ray spectroscopy," *Rev. Sci. Instrum.*, vol. 88, no. 12, 2017.

[118] M. Faubel and B. Steiner, "Strong Bipolar Electrokinetic Charging of Thin Liquid Jets Emerging from 10 µm PtIr Nozzles," *Berichte der Bunsengesellschaft für Phys. Chemie*, vol. 96, no. 9, pp. 1167–1172, 1992.

[119] K. R. Wilson *et al.*, "X-ray spectroscopy of liquid water microjets," *J. Phys. Chem. B*, vol. 105, no. 17, pp. 3346–3349, 2001.

[120] E. F. Aziz, "X-ray spectroscopies revealing the structure and dynamics of metalloprotein active centers," *J. Phys. Chem. Lett.*, vol. 2, no. 4, pp. 320–326, 2011.

[121] A. R. Milosavljević, C. Nicolas, M. L. Ranković, F. Canon, C. Miron, and A. Giuliani, "K-Shell Excitation and Ionization of a Gas-Phase Protein: Interplay between Electronic Structure and Protein Folding," *J. Phys. Chem. Lett.*, vol. 6, no. 16, pp. 3132–3138, 2015.

[122] A. R. Milosavljević *et al.*, "Oxygen K-shell spectroscopy of isolated progressively solvated peptide," *Phys. Chem. Chem. Phys.*, vol. 22, no. 23, pp. 12909–12917, 2020.

[123] S. Carniato, V. Ilakovac, J.-J. Gallet, E. Kukk, and Y. Luo, "Multidimensional transition-state theory calculations for nuclear dynamics of core-excited molecules," *Phys. Rev. A*, vol. 70, no. 3, p. 032510, Sep. 2004.

[124] J. W. Smith and R. J. Saykally, "Soft X-ray Absorption Spectroscopy of Liquids and Solutions," *Chem. Rev.*, vol. 117, no. 23, pp. 13909–13934, Dec. 2017.

[125] S. Hagström, C. Nordling, and K. Siegbahn, "Electron spectroscopy for chemical analyses," *Phys. Lett.*, vol. 9, no. 3, pp. 235–236, Apr. 1964.

[126] D. R. Penn, "Quantitative chemical analysis by ESCA," *J. Electron Spectros. Relat. Phenomena*, vol. 9, no. 1, pp. 29–40, 1976.

[127] C. N. Berglund and W. E. Spicer, "Photoemission studies of copper and silver: Theory," *Phys. Rev.*, vol. 136, no. 4A, 1964.

[128] A. Kahn, "Fermi level, work function and vacuum level," *Mater. Horizons*, vol. 3, no. 1, pp. 7–10, 2016.

[129] P. Padova and P. Perfetti, "Core Photoemission," in *Encyclopedia of Condensed Matter*

Physics, Elsevier, 2005, pp. 240–251.

[130] R. V. Culver and F. C. Tompkins, "Surface Potentials and Adsorption Process on Metals," *Adv. Catal.*, vol. 11, no. C, pp. 67–131, 1959.

[131] J. Holzl and F. K. Schulte, *Solid Surface Physics - Work Functions of Metals*. 1979.

[132] W. F. Egelhoff, "Core-level binding-energy shifts at surfaces and in solids," *Surf. Sci. Rep.*, vol. 6, no. 6–8, pp. 253–415, 1987.

[133] D. Cahen and A. Kahn, "Electron energetics at surfaces and interfaces: Concepts and experiments," *Adv. Mater.*, vol. 15, no. 4, pp. 271–277, 2003.

[134] P. S. Bagus, E. S. Ilton, and C. J. Nelin, "The interpretation of XPS spectra: Insights into materials properties," *Surf. Sci. Rep.*, vol. 68, no. 2, pp. 273–304, 2013.

[135] S. Hofmann, *Auger- and X-Ray Photoelectron Spectroscopy in Materials Science: A User-Oriented Guide*. 2013.

[136] C. J. Allan, U. Gelius, D. A. Allison, G. Johansson, H. Siegbahn, and K. Siegbahn, "ESCA studies of CO2, CS2 and COS," *J. Electron Spectros. Relat. Phenomena*, vol. 1, no. 2, pp. 131–151, 1972.

[137] M. Giesbers, A. T. M. Marcelis, and H. Zuilhof, "Simulation of XPS C1s spectra of organic monolayers by quantum chemical methods," *Langmuir*, vol. 29, no. 15, pp. 4782–4788, 2013.

[138] T. Duguet, A. Gavrielides, J. Esvan, T. Mineva, and C. Lacaze-Dufaure, "DFT Simulation of XPS Reveals Cu/Epoxy Polymer Interfacial Bonding," *J. Phys. Chem. C*, vol. 123, no. 51, pp. 30917–30925, 2019.

[139] C. K. Jørgensen, "Photoelectron Spectra Showing Relaxation Effects in the Continuum and Electrostatic and Chemical Influences of the Surrounding Atoms," *Adv. Quantum Chem.*, vol. 8, no. C, pp. 137–182, 1974.

[140] C. D. Wagner, "Auger parameter in electron spectroscopy for the identification of chemical species," *Anal. Chem.*, vol. 47, no. 7, pp. 1201–1203, Jun. 1975.

[141] B. W. Veal and A. P. Paulikas, "X-ray-photoelectron final-state screening in transition-metal compounds," *Phys. Rev. Lett.*, vol. 51, no. 21, pp. 1995–1998, 1983.

[142] Omicron NanoTechnology, *EA 125 Energy Analyser User's Guide*, Ed. 2.1., vol. 49, no. 2.1. Limburger Strasse 75, 65232 Taunusstein, Germany, 2002.

[143] C. D. Wagner, L. E. Davis, M. V. Zeller, J. A. Taylor, R. H. Raymond, and L. H. Gale, "Empirical atomic sensitivity factors for quantitative analysis by electron spectroscopy for chemical analysis," *Surf. Interface Anal.*, vol. 3, no. 5, pp. 211–225, 1981.

[144] J. E. Penner-Hahn, "X-Ray Absorption," in *Reference Module in Chemistry, Molecular Sciences and Chemical Engineering*, no. July, Elsevier, 2018, pp. 404–419.

[145] D. Emfietzoglou, I. Kyriakou, R. Garcia-Molina, and I. Abril, "Inelastic mean free path of low-energy electrons in condensed media: beyond the standard models," *Surf. Interface Anal.*, vol. 49, no. 1, pp. 4–10, Jan. 2015.

[146] N. Ottosson, M. Faubel, S. E. Bradforth, P. Jungwirth, and B. Winter, "Photoelectron spectroscopy of liquid water and aqueous solution: Electron effective attenuation lengths and emission-angle anisotropy," *J. Electron Spectros. Relat. Phenomena*, vol. 177, no. 2–3, pp. 60–70, Mar. 2010.

[147] C. J. Powell and A. Jablonski, "Surface Sensitivity of Auger-Electron Spectroscopy and X-ray Photoelectron Spectroscopy," *J. Surf. Anal.*, vol. 17, no. 3, pp. 170–176, 2011.

[148] A. Jablonski, I. Tilinin, and C. Powell, "Mean escape depth of signal photoelectrons from amorphous and polycrystalline solids," *Phys. Rev. B - Condens. Matter Mater. Phys.*, vol. 54, no. 15, pp. 10927–10937, 1996.

[149] J. F. Watts and J. Wolstenholme, *An Introduction to Surface Analysis by XPS and AES*. Chichester, UK: John Wiley & Sons, Ltd, 2003.

[150] J. C. Fuggle and S. F. Alvarado, "Core-level lifetimes as determined by x-ray photoelectron spectroscopy measurements," *Phys. Rev. A*, vol. 22, no. 4, pp. 1615–1624, 1980.

[151] C. Nicolas and C. Miron, "Lifetime broadening of core-excited and -ionized states," *J. Electron Spectros. Relat. Phenomena*, vol. 185, no. 8–9, pp. 267–272, 2012.

[152] C. R. Brundle and B. V. Crist, "X-ray photoelectron spectroscopy: A perspective on quantitation accuracy for composition analysis of homogeneous materials," *J. Vac. Sci. Technol. A*, vol. 38, no. 4, p. 041001, 2020.

[153] B. Winter and M. Faubel, "Photoemission from liquid aqueous solutions," *Chem. Rev.*, vol. 106, no. 4, pp. 1176–1211, 2006.

[154] J. A. Gardella, S. A. Ferguson, and R. L. Chin, "π* ← π Shakeup Satellites for the Analysis of Structure and Bonding in Aromatic Polymers by X-Ray Photoelectron Spectroscopy," *Appl. Spectrosc.*, vol. 40, no. 2, pp. 224–232, Feb. 1986.

[155] P. B. Dengis, P. A. Gerin, and P. G. Rouxhet, "SURFACES related model compounds," *Colloids and Surfaces*, 1995.

[156] P. G. Rouxhet, N. Mozes, P. B. Dengis, Y. F. Dufrêne, P. A. Gerin, and M. J. Genet, "Application of X-ray photoelectron spectroscopy to microorganisms," *Colloids Surfaces B Biointerfaces*, vol. 2, no. 1–3, pp. 347–369, 1994.

[157] H. Siegbahn and K. Siegbahn, "ESCA applied to liquids," *J. Electron Spectros. Relat. Phenomena*, vol. 2, no. 3, pp. 319–325, 1973.

[158] K. Siegbahn, "Electron spectroscopy - an outlook," *J. Electron Spectros. Relat. Phenomena*, vol. 5, no. 1, pp. 3–97, Jan. 1974.

[159] M. Faubel, S. Schlemmer, J. P. Tocnnies, and I. Introduction, "A molecular beam study of the evaporation of water from a liquid jet," vol. 277, 1988.

[160] B. Friedrich, *Molecular Beams in Physics and Chemistry*. 2021.

[161] L. A. Guildner, D. P. Johnson, and F. E. Jones, "Vapor pressure of water at its triple point: Highly accurate value," *Science (80-.).*, vol. 191, no. 4233, p. 1261, 1976.

[162] F. Buchner, A. Lübcke, N. Heine, and T. Schultz, "Time-resolved photoelectron spectroscopy of liquids," *Rev. Sci. Instrum.*, vol. 81, no. 11, p. 113107, Nov. 2010.

[163] B. Winter, "Liquid microjet for photoelectron spectroscopy," *Nucl. Instruments Methods Phys. Res. Sect. A Accel. Spectrometers, Detect. Assoc. Equip.*, vol. 601, no. 1–2, pp. 139–150, 2009.

[164] D. F. Ogletree, H. Bluhm, G. Lebedev, C. S. Fadley, Z. Hussain, and M. Salmeron, "A differentially pumped electrostatic lens system for photoemission studies in the millibar range," *Rev. Sci. Instrum.*, vol. 73, no. 11, p. 3872, 2002.

[165] A. Jürgensen, N. Esser, and R. Hergenröder, "Near ambient pressure XPS with a conventional X-ray source," *Surf. Interface Anal.*, vol. 44, no. 8, pp. 1100–1103, 2012.

[166] S. K. Eriksson *et al.*, "A versatile photoelectron spectrometer for pressures up to 30 mbar," *Rev. Sci. Instrum.*, vol. 85, no. 7, p. 075119, 2014.

[167] J. Kraus *et al.*, "Photoelectron spectroscopy of wet and gaseous samples through graphene membranes," *Nanoscale*, vol. 6, no. 23, pp. 14394–14403, 2014.

[168] R. Endo, D. Watanabe, M. Shimomura, and T. Masuda, "In situ X-ray photoelectron spectroscopy using a conventional Al-Kα source and an environmental cell for liquid samples and solid-liquid interfaces," *Appl. Phys. Lett.*, vol. 114, no. 17, p. 173702, Apr. 2019.

[169] T. Tokushima *et al.*, "High resolution X-ray emission spectroscopy of water and its

assignment based on two structural motifs," *J. Electron Spectros. Relat. Phenomena*, vol. 177, no. 2–3, pp. 192–205, 2010.

[170] N. Mårtensson *et al.*, "On the relation between X-ray Photoelectron Spectroscopy and XAFS," *J. Phys. Conf. Ser.*, vol. 430, no. 1, p. 012131, Apr. 2013.

[171] F. Penent *et al.*, "Coincidence Auger spectroscopy," *J. Electron Spectros. Relat. Phenomena*, vol. 144–147, pp. 7–11, 2005.

[172] R. A. Bartynski, E. Jensen, S. L. Hulbert, and C.-C. Kao, "Auger photoelectron coincidence spectroscopy using synchrontron radiation," *Prog. Surf. Sci.*, vol. 53, no. 2–4, pp. 155–162, Oct. 1996.

[173] J. H. D. Eland, O. Vieuxmaire, T. Kinugawa, P. Lablanquie, R. I. Hall, and F. Penent, "Complete Two-Electron Spectra in Double Photoionization: The Rare Gases Ar, Kr, and Xe," *Phys. Rev. Lett.*, vol. 90, no. 5, p. 4, 2003.

[174] M. N. Pohl *et al.*, "Sensitivity of electron transfer mediated decay to ion pairing," *J. Phys. Chem. B*, vol. 121, no. 32, pp. 7709–7714, 2017.

[175] A. Boissière *et al.*, "DNA Core Ionization and Cell Inactivation," *Radiat. Res.*, vol. 167, no. 4, pp. 493–500, Apr. 2007.

[176] R. Neutze, R. Wouts, D. van der Spoel, E. Weckert, and J. Hajdu, "Potential for biomolecular imaging with femtosecond X-ray pulses," *Nature*, vol. 406, no. 6797, pp. 752–757, Aug. 2000.

[177] D. T. Goodhead and H. Nikjoo, "Track structure analysis of ultrasoft x-rays compared to high- and low-LET radiations," *Int. J. Radiat. Biol.*, vol. 55, no. 4, pp. 513–529, 1989.

[178] T. Jahnke *et al.*, "Ultrafast energy transfer between water molecules," *Nat. Phys.*, vol. 6, no. 2, pp. 139–142, 2010.

[179] F. Kaneko *et al.*, "Chemical evolution of amino acid induced by soft X-ray with synchrotron radiation," *J. Electron Spectros. Relat. Phenomena*, vol. 144–147, pp. 291–294, 2005.

[180] S. Ptasińska, A. Stypczyńska, T. Nixon, N. J. Mason, D. V. Klyachko, and L. Sanche, "X-ray induced damage in DNA monitored by X-ray photoelectron spectroscopy," *J. Chem. Phys.*, vol. 129, no. 6, 2008.

[181] A. Jablonski, S. Tanuma, and C. J. Powell, "Modified predictive formula for the electron stopping power," *J. Appl. Phys.*, vol. 103, no. 6, p. 063708, Mar. 2008.

Chapter II. Material ans Methods

Contents Chapter II

Chapter II. Material and methods

Working with low-penetration radiations, such as soft X-rays, requires particular technological developments, especially for the study of liquid samples. As presented in Chapter I, XPS techniques were successfully developed for the study of liquid water. Among these, an under-vacuum liquid micro-jet has been set up on the PLEIADES beamline of the SOLEIL synchrotron. In addition to the obvious information that this jet can bring thanks to XPS measurements, it was envisaged to study the damage induced to the samples. Indeed, the PLEIADES setup allows recovering the irradiated sample. Unfortunately, it was soon established that this setup was unsuitable for irradiation studies, as the damage caused by irradiation was undetectable[11]. However, this under-vacuum liquid jet provides a perfect sample environment to get more information about the electronic structure of solvated molecules and, more specifically, about core-ionization effect. Indeed, it is necessary to have more information about the ionization threshold of solvated biomolecules in order to investigate solvent-molecules interactions. From a radiobiological point of view, it is also necessary to characterize the energy of emitted electrons during the photoionization process (PE and AE). If the liquid micro-jet is classically coupled with a conventional hemispheric analyzer, it can also be coupled with a magnetic bottle type time-of-flight analyzer. This setup allows performing photoelectron/Auger electron coincidence measurements.

In the following chapter, we will describe the different technological parts involved in this thesis. The first part will describe the operation of the SOLEIL synchrotron and the characteristics of the main beamlines used during this thesis. The second part will present the different spectroscopic setups developed on the PLEIADES beamline for liquid analysis. Finally, we will present the different techniques to characterize the physico-chemical changes induced in the irradiated samples.

[11] *The irradiation inside the liquid jet may be envisioned for beamlines with higher brilliance after synchrotron upgrades for instance.*

II.1. SOLEIL Synchrotron

II.1.1. Synchrotron sources

Synchrotron facilities are specific circular particle storage rings that generate very intense radiation. The principle of synchrotron radiation (SR) emission is based on the fact that any charged particle subjected to acceleration will emit electromagnetic radiation. This manuscript focused on electron synchrotron. As the electron mass-energy can be very low in front of its kinetic energy, the frequency of the radiation can be shifted towards very short wavelengths. It confers to synchrotrons exceptional spectral continuity from the far-infrared to X-ray that cannot be achieved by any other source [1]. Historically, SR was considered stray radiation generated during high-energy physics experiments on particle accelerators [2]. Considering the exponential growth in the use of SR, dedicated facilities were designed. Second-generation synchrotrons, built in the seventies, were composed of bending magnets [3]. The north and south poles create a homogeneous magnetic field that deflects electrons to maintain them on a closed trajectory.

In third-generation synchrotrons, such as SOLEIL synchrotron (illustrated in Figure II-1), assemblies of magnets with alternating polarities (wigglers or undulators) are inserted to improve the beam characteristics (brilliance and polarization control). The brilliance, or spectral brightness[4], allows to qualify both the photon flux (number of photons per second per unit optical bandwidth[12], $n_{photons/}\Delta t \cdot 0.1\%\, BW$) and the spatial repartition of the beam (size and angular distribution.):

$$brilliance = \frac{n_{photons}}{\Delta t \cdot \varepsilon_x \cdot \varepsilon_z \cdot 0.1\%\, BW} \qquad \text{(II-1)}$$

Where ε_x and ε_z are the emittance in the horizontal and vertical direction, respectively, and can be defined as the product of the electron beam transverse size and angular divergence. Following Equation (II-1), the brilliance is defined per unit optical bandwidth (0.1% BW), i.e., the width of the optical spectrum of the output (in frequency or wavelength). It is therefore expressed in ph/(s·mrad²·mm²·0.1%BW)[5].

Synchrotron insertion devices impart a sinusoidal motion to the particle and thus reduce electron beam emittance. It, therefore, significantly increases the brilliance (10^4

[12] *As a simplification, we will refer to the flux as the number of photons per second.*

higher than with a bending magnet)[6], [7]. The higher the brilliance, the higher the spectral resolution can be reached. It explains why the brilliance is one of the essential parameters in developing fourth-generation sources.

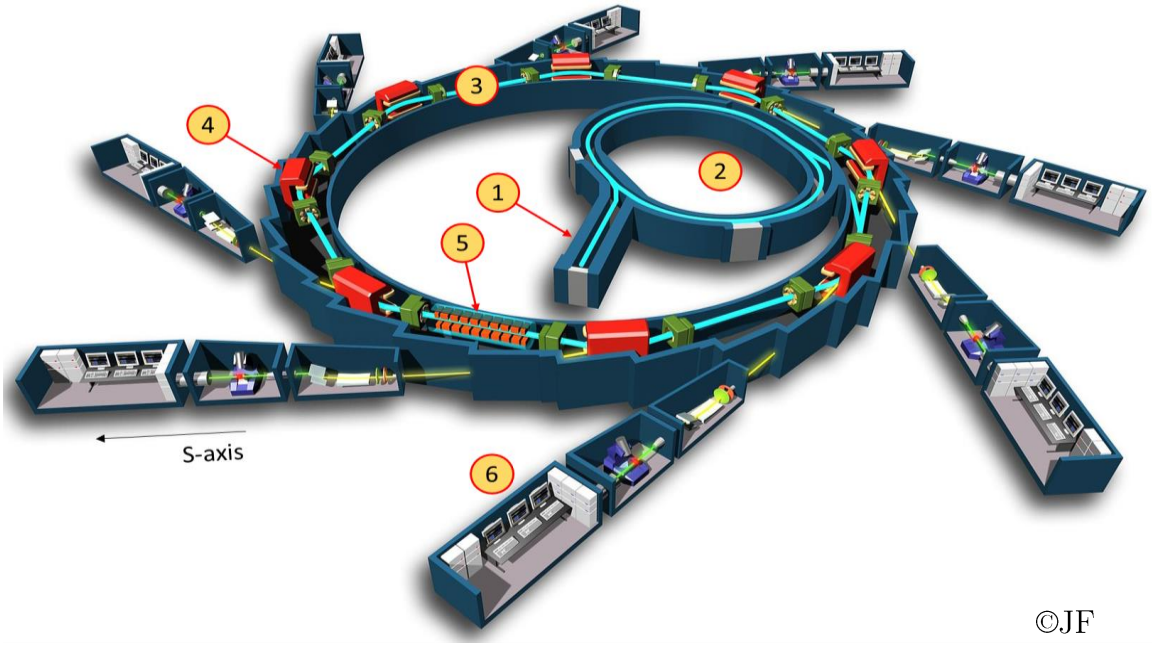

©JF

Figure II-1: Scheme of SOLEIL synchrotron: ① LINAC, ② booster, ③ storage ring, ④ bending and focusing magnets, ⑤ undulators and wigglers, ⑥ beamlines. On synchrotron referential, the s-axis is commonly defined following the beam-emission towards beamlines.

As illustrated in Figure II-1, particles are produced by an electron gun and first accelerated in a linear accelerator (LINAC) (1). It brings the electrons to high speed and an initial energy of 100 MeV and groups them in bunches. After this initial acceleration, the electron beam is directed towards a second circular accelerator called the Booster (2), whose purpose is to bring the particles to standard operating energy (2.75 GeV) before being injected into the storage ring. The energy lost by the electrons during the emission of SR is compensated by radiofrequency cavities, which allows extending the lifetime of electrons inside the storage ring[13]. In order to ensure the perfect stability of the delivered photon flux, synchronized injections of new electrons into the packets are performed (Top-up mode).

Electrons circulate several hours in the storage ring thanks to magnetic devices that control the trajectory of the electron beam. Each time their trajectory is modified, the

[13] *At SOLEIL synchrotron, each radiofrequency cavity is tuned to oscillate at 352 MHz.*

electrons lose energy and emit light: the SR. More precisely, when the beam has reached the required energy, an ideally timed particle with precisely the right energy will not be accelerated. On the contrary, particles with slightly different energies arriving earlier or later will be decelerated or accelerated to stay close to the desired energy. It guarantees the compactness of the package, called "bunch", and maintains the pulsed temporal structure of the SR. The frequency of the light pulses depends on the number of packets present in the storage ring and its circumference. At SOLEIL, different filling modes are available. The number of electron bunches in the storage ring (maximum 416) and how they are distributed will define the time structure of the light. For example, single and eight-bunches modes correspond to a delay time between two pulses of 1.2 µs and 148 ns, respectively.

Experimental laboratories, called beamlines, are installed tangentially to the storage ring to collect and shape the SR emitted using bending magnet and insertion devices (wrigglers or undulators). There are 29 beamlines at SOLEIL; each is specifically designed for dedicated applications (X-ray absorption spectroscopy and X-ray emission spectroscopy, for instance).

II.1.2. PLEIADES beamline

PLEIADES is an ultra-high resolution soft X-rays beamline initially dedicated to atomic and molecular spectroscopic studies of diluted samples (gases, clusters, and nanoparticles) and, more recently, of liquids. The beamline, illustrated in Figure II-2, comprises two undulators (HU80 and HU256) that provide a wide range of energies (from 10 to 1000 eV). A grating monochromator achieves wavelength selection. The use of four different gratings ensures a high resolution: 400 lines/mm, 600 lines/mm, 1600 lines/mm, and 2400 lines/mm. The beamline is shaped by a succession of mirrors and divided into three different branches:

- the A branch, dedicated to the study of the photoionization of ions (MAIA end station) [not used in this project],

- the B branch (central branch), where the users' experiment could be located,

- the C branch hosts two permanent end-stations dedicated to electron spectroscopies and one free port available for users' experiments.

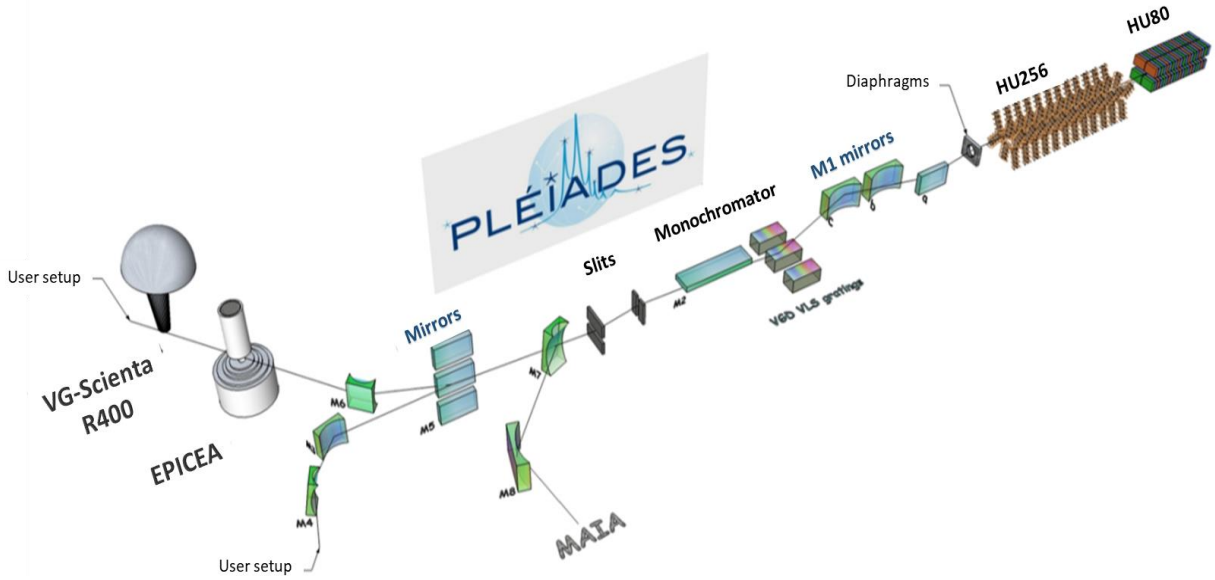

Figure II-2: Scheme of the PLEIADES beamline at SOLEIL synchrotron.

The beam fluence (energy/surface unit) is not the same for all three branches. The B Branch (central branch) provides an intense beam spot of dimensions 50×30 µm². However, the beam on the C branch can be focused on three focal points depending on the experimental station used (EPICEA, SCIENTA, or user chamber). The beam is more diffuse and is ~200 µm large along the horizontal direction at the focal point of the SCIENTA. Exit slits, placed after the monochromator, help to adapt the size of the beam spot along the vertical direction and define the photons' energy resolution. It also changes the photon flux, but not the beam fluence. In order to change the beam fluence, it is necessary to change the beam's brilliance by modifying the undulators operating parameters, for example.

Undulators are insertion devices specifically developed to enhance the brilliance of SR. It consists in a periodic arrangement of short magnets of alternating polarity that force the electrons onto a tight slalom course (see Figure II-4). Summing up many oscillations enables to enhance the radiation brightness by several orders of magnitude. The radiation produced in an undulator is very intense and concentrated in narrow energy bands in the spectrum[14]. The emitted photons' energy (or wavelength) can be finely tuned by varying the undulator's magnetic field (gap magnet or current in coils).

[14]*This amplification process is the one used for XFEL which used much larger undulators so electrons interact with emitted X-ray radiation*

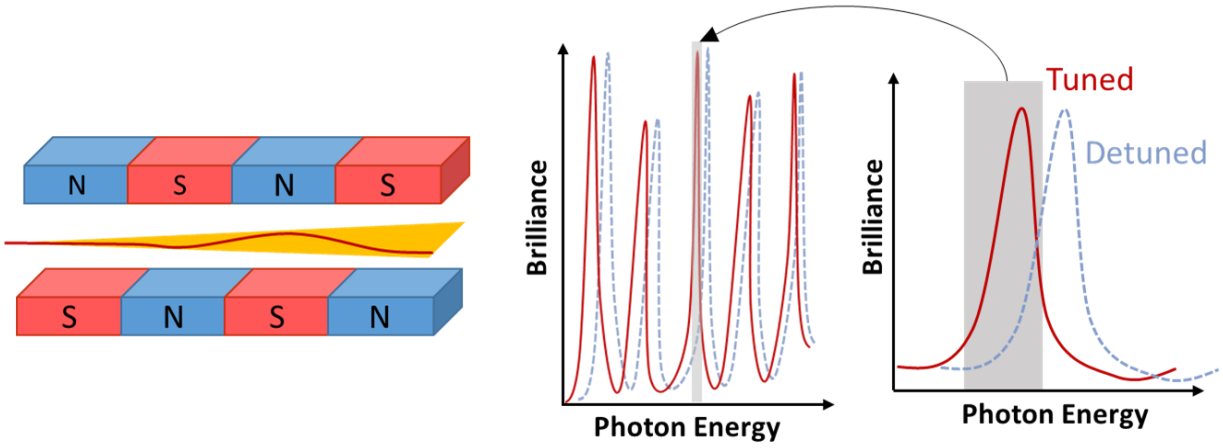

Figure II-4: Scheme of the radiation emission of an undulator and photon energies selection varying the coupling between the monochromator and the undulator. The gray rectangle respresents the bandwidth of the monochromator. In red, undulator is tuned to maximize the photon flux. In blue, the undulator is decoupled to decrease the beam fluence (detuned).

The undulator magnetic field is tuned for conventional use to get the maximum of its emission peaks to be close to the photon energy selected by the monochromator (illustrated by the grey area in Figure II-4). However, it is possible to de-couple the two devices to decrease the number of photons per area unit transmitted by the beamline. Indeed, the undulator emission is much broader in energy (several eV) than the energy selection range of the monochromator. Detuning the undulator constitutes a simple way to reduce the photon fluence. Experimentally, we observe that the photon fluence can be divided by a factor of two by detuning the undulator on PLEIADES. More generally, the photon flux on PLEIADES varies with the photon energy. At 400 eV, for instance, it is ~10^{13} ph/s for a resolution of 40.4 meV when tuned.

II.1.3. METROLOGIE beamline

The METROLOGIE beamline was initially designed to allow the characterization of optical components at their wavelength of use. It was therefore built to provide a wide spectral range from 30 eV to 40 keV. The beam originates from a bending magnet and is separated on two independent optical branches dedicated to hard X-rays and X-UV. All experiments were conducted on the X-UV branch (0.03-1.9 keV), illustrated in Figure II-5. According to the general high absorption of soft X-rays in matter, minimizing the number of reflecting surfaces is necessary. The selection of energy is performed by a

monochromator using varied line space (VLS) gratings (75, 300, and 1200 lines/mm) to cover the energy range between 30 and 1800 eV[8].

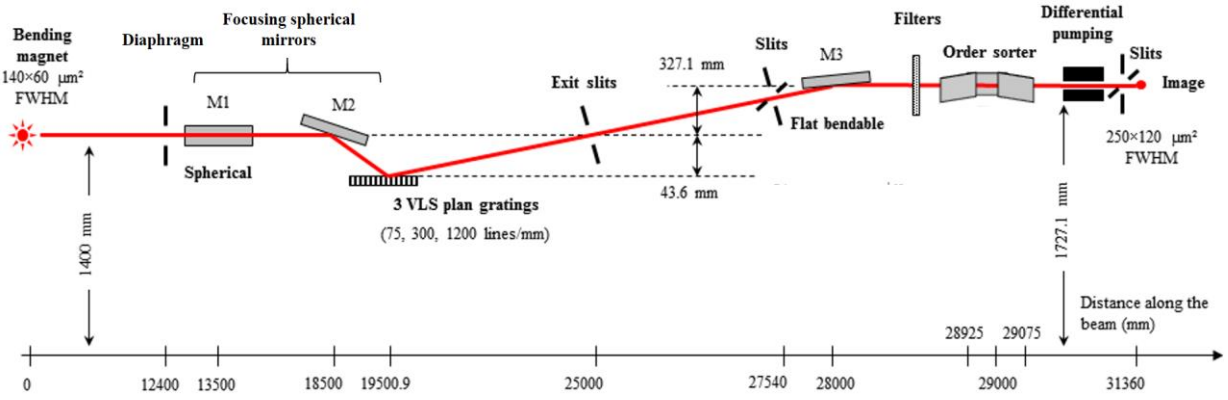

Figure II-5: Scheme of the X-UV branch of the Metrologie beamline. (Image from [56]).

Spectral purity is ensured by the use of a Low-Pass-Filter composed of a filter (different filters available) and three flat mirrors with different coatings (referred to as "order sorter" in Figure II-5.). The appropriate adjustment of this {filter/order sorter} system allows efficient rejection of the monochromator higher-orders, leading to a typical spectral purity better than 99%. The following table summarizes the different filter parameters applied according to the spectral range (see Table II-1).

Table II-1: Gratings and filters parameters on the METROLOGIE X-UV branch according to the spectral range.

Range (eV)	30-50	50-90	100-160	165-265	267-299	300-440	450-760	760-900	910-1900
Grating	R75					R300			R1200
Filter	Al 0.5 μm	Si 0.5 μm	B 0.4 µm	C 0.7 µm	Ti 0.5 μm	Ti 0.5 μm	Co 0.5 μm	Cu 0.9 μm	B 0.4µm

The photon flux inside the beamline varies from 10^9 - 10^{12} ph/s depending on the photon energy (~10^{12} ph/s at 1 keV). The resulting beam spot is approximately 250 µm wide at the focus point (see Figure II-5). Its height varies according to the monochromator exit slits.

II.1.4. Choice of the beamline

In addition to the accessible energy range, each beamline has its own specificity in terms of beam geometry, photon flux, or even space limitations in terms of experimental setup. XPS experiments were conducted on the PLEIADES beamline, which is mainly dedicated to such measurement. In particular, one permanent endstation of the C-branch is a high-resolution electron spectrometer (SCIENTA) that can be coupled with an under-vacuum liquid-jet setup.

For liquid irradiation, the first experiments were performed at air using a dedicated setup (the IRAD setup, which will be presented in Chapter III section III.1) on the METROLOGIE beamline. In addition, we assembled a vacuum chamber hosting a microfluidic irradiation cell. The entire experiment can therefore be moved between different beamlines. The second setup is more dedicated to irradiation around the carbon K-edge, where the air absorption of soft x-rays may represent a limitation, depending on the sample investigated. It is, therefore, appropriate to review the characteristics of the two environments provided by the two beamlines.

Table II-2: Summary table of the parameters of two beamlines used for liquid irradiation.

	METROLOGIE		**PLEIADES**
Set-up	**IRAD set-up (Air)**	**Vacuum Chamber**	**Vacuum Chamber**
Source	Bending Magnet		Undulator
Energy range Photon flux reaching the sample	200 – 1600 eV[15] ~10^9-10^{10} ph/s at 1-1.4 keV ~10^8 at 200 eV	30 – 1600 eV ~10^9-10^{12} ph/s	10-1000 eV 10^{13} ph/s
Polarization	Linear horizontal		Variable (elliptical, linear, circular)
Others	Set of attenuators to reduce the photon flux and high-orders rejection optical system		/

[15] *The lower energies are not accessible because the absorption in the air and the installation of the extraction will become too important. The distance between IRAD's exit window and the entrance surface of the Si3N4 membrane enclosing the liquid sample is here 2.2 mm (see Chapter III for more details).*

II.2. XPS instrumentation

XPS is ideally suited to study the early processes initiated by the ionization of matter (photoionization, excitation, and following non-radiative deexcitation pathway involved – see Chapter I for more details). In order to study these events in liquid samples, we used a liquid micro-jet installed on the PLEIADES beamline. Auger electron spectroscopy (AES) is also of particular interest to study the production of secondary electrons. Two different analyzers were therefore used. In the first part, samples were analyzed with a commercial hemispherical deflection analyzer. In the other part, the liquid jet was coupled with a magnetic bottle, developed by the LCPMR (Sorbonne University), to measure Auger electrons in coincidence with photoelectrons. Liquid samples analyses were compared to solid-state laboratory XPS analysis.

The principle of XPS spectroscopy was presented in Chapter I (section I.3.2). It has been shown that the analysis of XPS spectra provides unique information on the chemical environment at the atomic scale, such as oxidation states or electron transfers. The intensity or area of the peak also gives access to quantitative information, such as elemental composition. In addition to the position, the shape of the peaks is also essential as it contains information about the lifetime of the ionized core-hole state. As mentioned in Chapter I, the shape of the peaks is well described by a Voigt function, contribution of a Lorentzian and a Gaussian, corresponding respectively to the intrinsic and extrinsic broadening effect[16]. Depending on the sample studied (intrinsic) or the instrumentation used (extrinsic), the width of the peaks, or FWHM, could suffer from several broadening factors. The resolution (ΔE) can be calculated using the formula:

$$\Delta E^2 = \Delta E_{peak}^2 + \Delta E_{instrum.}^2 = \Delta E_{peak}^2 + \Delta E_{source}^2 + \Delta E_{analyzer}^2 \qquad (\text{II-2})$$

Where ΔE_{peak}, the natural linewidth of the XPS peak is generally described by a Lorentzian, and $\Delta E_{instrum.}$ is the instrumental resolution, described by a Gaussian. The latter is affected by the finite energy resolution of the analyzer ($\Delta E_{analyzer}$) and the line width of the incident X-rays (ΔE_{source}). The instrumentation is therefore crucial for the resolution of the measurement.

[16] *It must be stressed out that in the liquid phase, the Laurentzian contribution can not be directly related to the core-hole lifetime because of the complexity of the environment*

II.2.1. High-resolution analysis

II.2.1.i. Hemispherical Deflection Analyzer (HDA)

Modern spectrometers are electrostatic analyzers. The kinetic energy of the emitted electrons is analyzed according to the experimental parameters (polarization or energy of the photons, angle of emission). In order to guarantee a sufficiently high mean free path for the photoelectrons without dissipative collisions with gas-phase molecules, spectrometers conventionally operate under an ultra-high vacuum (at least 10^{-5} mbar[17]). The most commonly used spectrometers are equipped with a Hemispherical Deflection Analyzer (HDA), also known as concentric hemispherical analyzer (see illustration in Figure II-6.(a)).

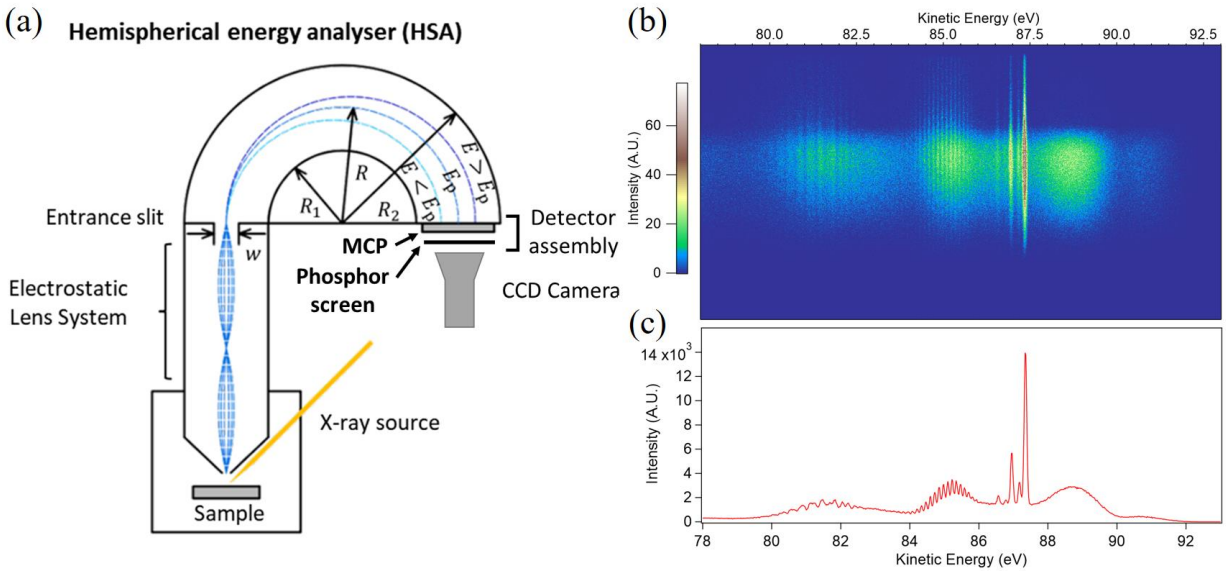

Figure II-6: Description of the hemispherical deflection analyzer principle: (a) Operating diagram of a hemispheric analyzer, (b) Reccorded image on the CCD camera, (c) Total projected XPS spectrum.

The analyzer is constituted by an electrostatic lens system that collects the electrons emitted by the irradiated sample and then focuses them on the entrance slit of the analyzer. The lens can also retard or accelerate incoming electrons to make their kinetic energies fall in the analysis window of the analyzer. The so-called pass energy defines this window (E_p). This user-selected parameter will define the trajectory of the electrons inside

[17] *For surface analysis, vacuum conditions are more restrictive because carbon contamination can be disruptive during measurements.*

the spectrometer. Indeed, once they reach the entrance slit of the analyzer, electrons are deflected by a potential difference (ΔV) that forces them to follow a curved trajectory between the two hemispheres. The relation between the pass energy and the applied potential on the hemispherical lenses is given by the following Equation:

$$e\Delta V = E_p \cdot \left(\frac{R_2}{R_1} - \frac{R_1}{R_2}\right) \qquad \text{(II-3)}$$

Where R_1 and R_2 are the radii of the two analyzer's hemispheres to which a voltage (V_1 and V_2) is applied, with $\Delta V = V_1 - V_2$. This potential will disperse the electrons according to their kinetic energy along the axis perpendicular to the entrance slit opening. Electrons are then detected and counted by a detector.

During this thesis, we mainly used a VG-Scienta R4000 wide-angle lens, which used a position-sensitive detector. This detector comprises a micro-channel plate (MCP) and a phosphor screen equipped with a CCD camera. The MCP is an electronic device that multiplies each incoming electron around a million times. This electron pulse is accelerated to the phosphor screen producing a visible light flash detectable by the CCD camera. Data were recorded using Igor software from Wavemetrics ©. A typical image registered by the detector area is presented in Figure II-6.(b). The second axis of the CCD sensor array of the camera is perpendicular to the energy axis. Therefore one side of the image is the energy dispersion (kinetic energy), and the other is the spatial distribution[18]. The recorded image allows us to identify the signal originating from the gas surrounding the micro-jet, which appears as long narrow line segments along the non-dispersive axis (vertical lines on Figure II-6.(b)). Indeed, gas-phase molecules are flowing everywhere around the jet. Respectively emitted electrons would therefore fill the whole solid angle collection of the analyzer entrance. However, they are also discriminated by the maximum collection angle imposed by the liquid jet setup's electron skimmer before the spectrometer lens entrance (experimental details are given in section II.2.1.iii). The image reflects such effect by the lack of signal at both ends of the non-dispersive axis[19]. The liquid jet has a limited ionization volume that is inferior to what the electron skimmer can collect, and thus it is

[18] *The detector image can also be presented in angular distribution in case of angular mode detection.*
[19] *The spatial distribution is limited by the skimmer, so the vertical lines do not cross the whole image.*

fully observed on the image. The XPS spectrum is directly obtained by the image's projection on the energy axis (see Figure II-6.(c)).

While recording a spectrum, Ep is fixed in order to maintain a constant energy resolution. The energy filter resolution (ΔE) is a crucial factor in XPS analysis. Indeed, suppose the difference in energy between two XPS peaks, each corresponding to a different chemical environment, is less than ΔE. In that case, the peaks become un-differentiable, and the information about the atom's environment is lost. $\Delta E_{analyzer}$ directly refers to the FWHM of the transmitted line of the analyzer. It is determined by choice of pass energy and the width of the analyzer entrance slit (w) as pointed out in the following Equation[9]:

$$\frac{\Delta E_{analyzer}}{E_p} = \frac{w}{2R} - \frac{\alpha^2}{4} \qquad \text{(II-4)}$$

Where R is the mean radius of electrons trajectory and α is the acceptance angle. The lens system defines the acceptance angle. It is limited by physical apertures in the lens and therefore remains nearly constant throughout the entire energy range.

Following Equation (II-4), decreasing the pass energy will increase the resolution. However, the range of kinetic energies detected around E_p will also decrease (see Figure II-6.(a)). Typically the kinetic energy window detected is around 10% of E_p. One must keep in mind that decreasing the pass energy also affects the number of electrons transmitted by the hemispheric analyzer and thus the signal-to-noise ratio. Thus according to the wanted resolution and the time allocated for the measurement, it is essential to determine the best values for the pass energy and the entrance slit width.

II.2.1.ii. Solid XPS analysis

- Experimental laboratory setup

The solid samples were studied using an industrial XPS analyzer Kratos Axis Ultra (measurements performed by Jocelyn Leroy on the characterization platform of the LICSEN laboratory (CEA)). Industrial XPS allow the measurement of photoelectrons emitted normally to the sample. The X-ray beam is generated by an Al K_α anode (1.486 keV) and results in a fixed X-ray spot size. All spectra were recorded using an entrance aperture of 300×700 µm². The detection is ensured by an HDA equipped with a position-sensitive detector. Samples are deposited on gold-coated glass plates (solution dried at the

surface) or on copper tapes (crystals directly deposited). They are then installed on a 300 mm sample holder, inserted in the sample treatment chamber (pressure $<10^{-7}$ mbar). Charge effects are compensated using a charge neutralization system: an electron gun (also called Flood Gun) that produces low-energy electrons during analysis. This low-energy electrons source (typically 1.85 eV) provides consistent charge compensation and allows the analysis of semiconductor or non-conductor materials. All the neutralizer parameters remained constant during analysis. This spectrometer was used to study organic molecules (sugar, proteins, and small molecules) in the solid phase. Data are extracted in VAMAS format and analyzed with CasaXPS software.

- Calibration and data treatment

At the beginning of the analysis, a large energy window is probed with high pass energy (E_P=160 eV). This survey scan (Figure II-7.(a)) gives an overview of the elements present in the sample. Then, high-resolution spectra allow identifying the atomic contributions more precisely (Figure II-7.(b)).

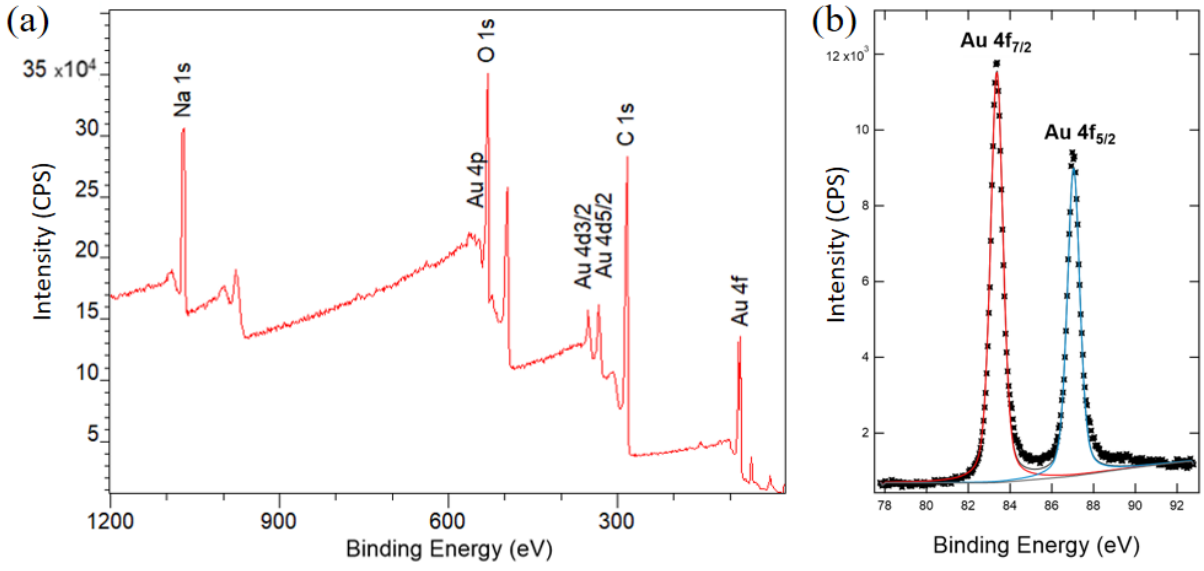

Figure II-7: (a) Survey spectra of an organic sample deposited on gold coated glass plates (E_P=160 eV), (b) High resolution region of the Au4f (E_P=40 eV pass energy). Results of the fitting procedure are represented by the red and blue curves.

For the analysis, the spectrometer is previously calibrated using a reference gold sample ($Au4f_{7/2}$ BE at 83.9 eV, with respect to the Fermi level). The signal from hydrocarbon contamination (C1s photoemission) detected on the gold reference sample was found at

284.8 eV binding energy. This value, similar to the one measured in the literature for the C-C/C-H signal[10], was chosen to calibrate spectra recorded on copper tapes. The FWHM of the gold peak defines the resolution under the recording conditions. It has been measured to be equal to 0.86 eV, 0.5 eV and 0.35 eV for pass energies of 160 eV, 40 eV and 20 eV, respectively.

In order to optimize $\Delta E_{analyzer}$, high-resolution regions were acquired at constant pass energy of 40 eV or 20 eV. Short acquisition time spectra were recorded before and after each measurement to check that the samples did not suffer from any degradation. The decomposition of photoemission peaks is carried out after subtracting the continuous background related to secondary electrons, simulated with a non-linear baseline from a Tougaard model[11]. An example of gold Au4f peaks is presented in Figure II-7.(b)). The XPS signals were fitted by Voigt functions represented by a sum of Gaussian and Lorentzian distributions available in the CasaXPS® software (SGL(m) sum formula)[12]. The mixing value (m) was defined to have 70% of Gaussian distribution and 30% of Lorentzian distribution (SGL(30)). Fitting parameters were properly constrained to have 3:4 peak area ratios (corresponding to the statistical population of the spin-orbit coupling) and equal FWHM[13].

II.2.1.iii. Liquid sample XPS analysis

- Liquid micro-jet setup

The technique of liquid jet under vacuum, developed by Faubel and coworkers[14], [15], was successfully implemented on the PLEIADES beamline in the last few years. This device allows performing electron spectroscopy measurements on various liquid systems, including highly volatile liquids. Under vacuum, a liquid jet requires specific technical strategies, not only in terms of vacuum but also regarding the scattering of electrons by the vapor phase[16]. The entire setup installation is presented in Figure II-8. The liquid sample is pumped using an HPLC pumping system (WATREX P102) and pushed through a narrow fused-silica nozzle (Microliquids® design) at high backing pressure. It results in a jet of 40 or 60 microns diameter under vacuum, depending on the diameter of the nozzle used. A degassing system is integrated inside this liquid injection system to remove bubbles and dissolved gasses which could disrupt the jet. In addition, an in-line 2-µm filter can be

installed to prevent disruptive micrometric particles. The liquid jet is installed in an aluminum holder. This latter is drilled with two holes (1-mm diameter and 5 mm long) in order to allow the irradiation by the synchrotron light and its exit towards a photodiode (see the liquid jet assembly ① in Figure II-8). Above the jet, a conical titanium piece provides a 300 µm hole that acts as a skimmer for out-going electrons. The liquid jet assembly can be translated in the direction parallel to the SR beam (s) and in the vertical direction (z), using piezo electric translation stages. Generally, the jet is placed at the working distance from the electron analyzer (4 cm diameter entrance aperture). It corresponds to a distance of 2.5 mm between the entrance of the skimmer and the jet.

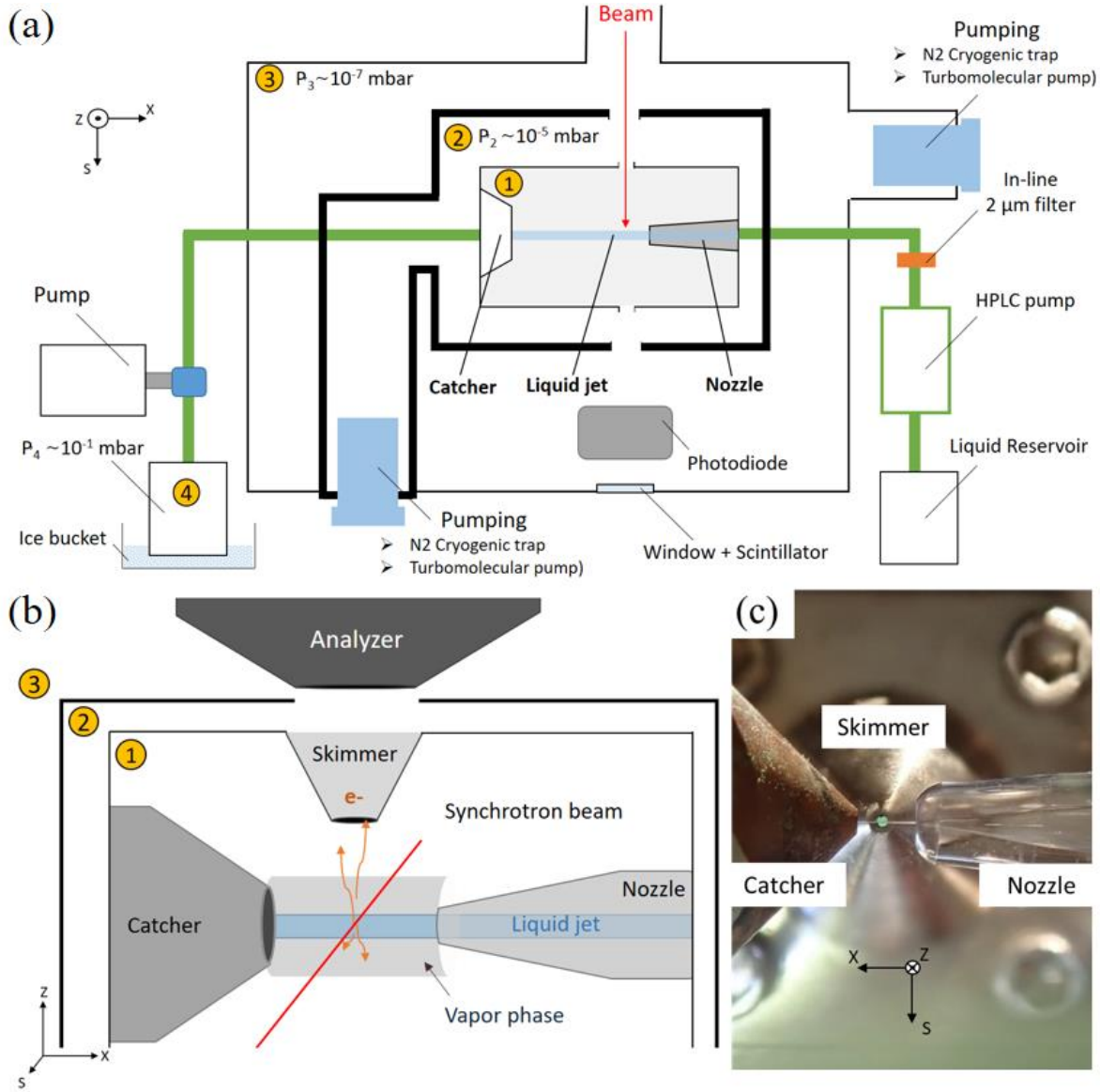

Figure II-8: Vacuum liquid jet installation on the PLEIADES beamline. (a)-(b) Illustrative sketches of the experiment, respectively top-view and profile-view: ① Liquid-jet assembly, ② Liquid box ③ Analyzer chamber, ④ Collection Bottle; (c) Pictures of the top-view. The s-axis refered to the SR beam-axis.

The liquid jet assembly is then inserted in an aluminum box, namely "liquid box" ② in Figure II-8, of dimensions 7x8x15 cm^3. This box carries two 3-mm diameter holes for the synchrotron light entrance and exit and one 5 mm diameter hole in a titanium piece, through which the emitted electrons pass on their way to the analyzer. Once the liquid assembly is inserted in the liquid box, both sets of holes are aligned by construction. Three-axis motorization helps to align the liquid box to the analyzer entrance and the SR beam. The liquid box and the analyzer chamber (③ in Figure II-8) are pumped with primary and turbomolecular pumps. Liquid nitrogen cold traps help the pumping by adsorbing residual gas molecules, mainly water. The holes' small vacuum conductance helps maintain a pressure of ~8.10^{-6} mbar inside the analyzer chamber while the pressure is stabilized at ~10^{-4} mbar in the liquid box. The jet flow is 1.5 $mL.min^{-1}$ preventing the liquid from freezing despite its low surface temperature (estimated to be less than -60°C)[14]. It also provides a constant renewal of the irradiated surface area, making it free from contamination or beam damage. The specificity of the PLEIADES setup is the implementation of a heated and pumped catcher in which the jet enters. The liquid is then collected in a collection bottle maintained at 7 mbar thanks to a backing pump (see ④ Figure II-8). Therefore, it is possible to perform additional analytical analyses on the collected liquids contrary to systems using cold traps to freeze the liquid outlet[17].

As schematized in Figure II-8.(b), the irradiated area includes the water vapor phase. Indeed, the beam's diameter is a hundred microns, so X-rays also interact with the vapor phase surrounding the 40 µm-diameter liquid micro-jet. Therefore, it is necessary to perform an accurate alignment to maximize the signal originating from the liquid jet.

Moreover, the gas-phase spectral contribution can also be discriminated by applying a bias voltage to the sample (see Figure II-9.(a)). In Figure II-9, the value of the voltage applied on the liquid jet is subtracted from each spectrum's electrons' kinetic energy. At around 50 volts, the O1s contribution of the liquid is well separated from the gas phase contribution, as the electrons from the gas do not feel the same field. We can see that the gas phase peak also broadens as the perturbing electric field intensity increases. Therefore, a small gold-coated metallic connector is implemented in the fluidic system (located 20 cm

upstream of the nozzle). This latter allows to electrically ground the jet flowing inside or apply a bias voltage to sufficiently conductive liquid samples[20].

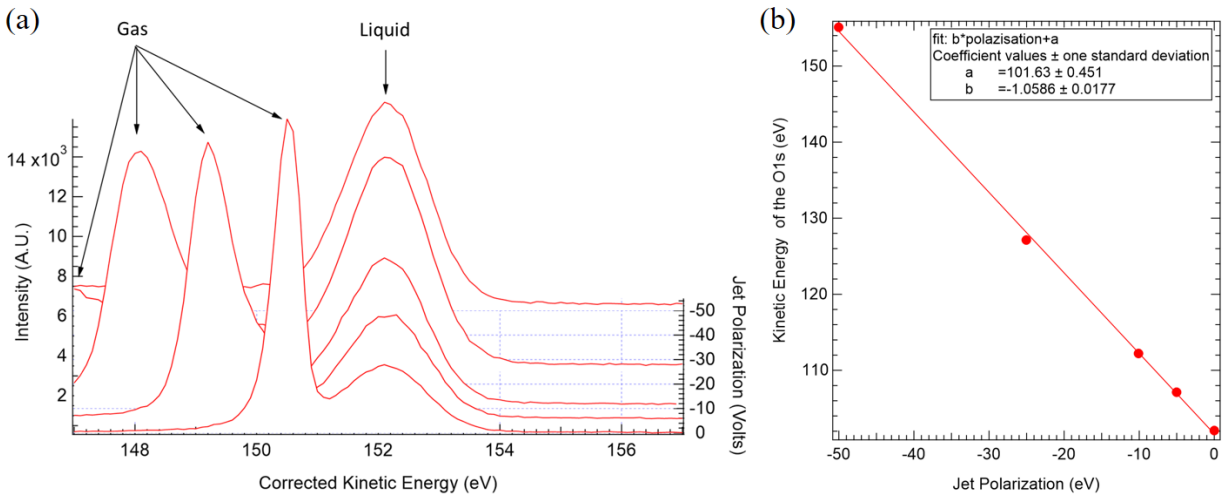

Figure II-9: (a) Different O1s XPS spectra of 50mM NaCl solution at different voltage polarizations of the liquid jet. Each spectrum has its kinetic energy substrated by the voltage applied. (b) Relation found by fitting between the voltage applied and the maximum of the O1s XPS peak of the liquid contribution.

The bias is applied using a highly stable voltage supply (Delta Elektronika, SM 70 – AR 24). One must also know that liquid spectroscopy of pure water induces experimental artifacts. More specifically, in contact with the glass nozzle, the liquid will be re-organized to form a counter ion layer and equilibrate the negative surface of the silica (acidic hydroxyl function)[18]. This potential shift interferes with the emitted electrons leading to their acceleration or retardation[19]. XPS liquid experiments are therefore always performed in samples containing a minimum of salts (millimolar range) to homogenize the distribution of charges in the liquid[18].

- Calibration and data treatment of liquid XPS spectra

Even if XPS has been performed on liquids for a few decades, it is only recently that the question has been raised of how accurate the calibration of the liquid water UPS-XPS is [20]–[22]. The present work's binding energy of electrons coming from the liquid phase was calibrated using the gas-phase water molecules signal at each photon energy. Indeed,

[20] *An electrical connection ensures that the jet and the catcher are always at the same potential.*

experimental electrons binding energies for gaseous water are well known in the literature. In particular, the O1s signal maximum is located at 539.89 eV[23]–[25], and the adiabatic ionization energy of the X $1B_1$ state of H_2O^+ is 12.621 eV[26]. Depending on the photon energy range investigated, one of these two signals was recorded to calibrate the spectra of the samples. Reference spectra were recorded on low concentration salt solutions (classically NaCl 0.05 M). The electrical contact of the jet with the analyzer is therefore ensured, which allows the alignment of the Fermi levels (Figure I-10, in Chapter I). Energies are therefore given with respect to the reference vacuum level of the analyzer. Knowing the work function of the spectrometer could thus allow to calibrate the measurements with respect to the Fermi level. This value was recently calculated using a gold wire and evaluated for a pass energy of 20 eV to be $\varphi_{analyzer}$ =3.93 eV (see supporting information of [21][21]). The analyzer work function is pass energy dependent. Moreover, this work function can also evolve with time due to changes in contact potentials in the lens system, especially when the spectrometer, as the SCIENTA, is used to study different kind of samples such as nanoparticles. A maximum change of 0.1 eV (for a 50 eV pass energy) was measured a year apart.

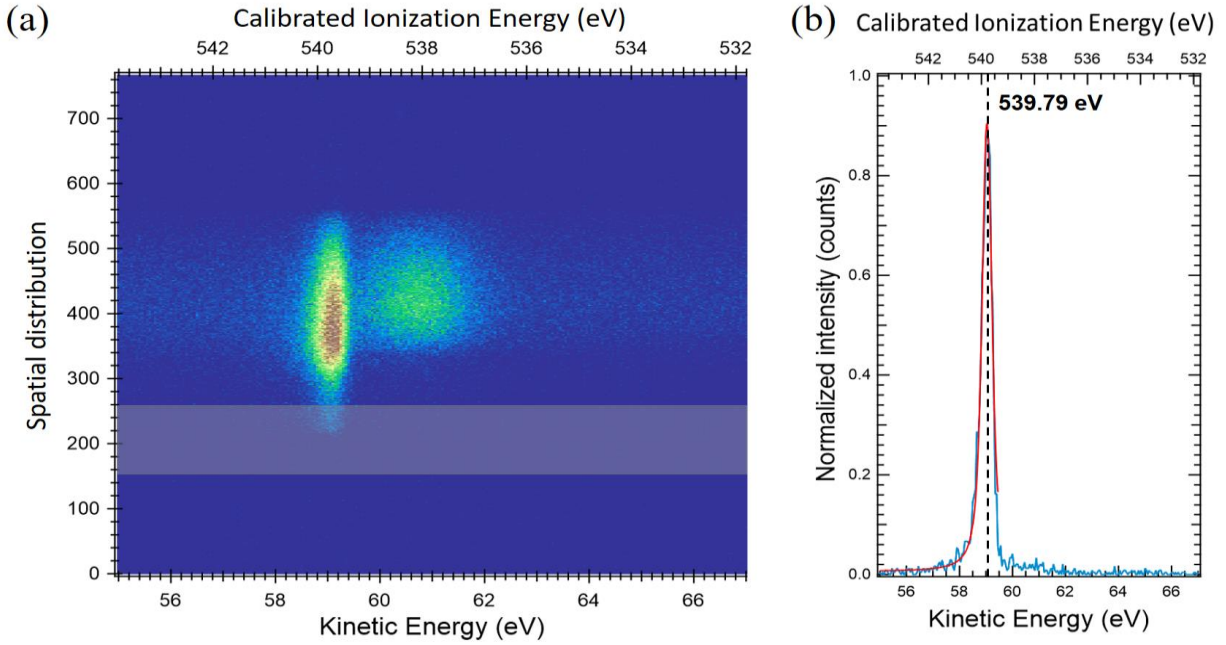

Figure II-10: Calibration procedure on liquid jet data obtained on NaCl 0.05M at 600 eV: (a) Image on the detector, (b) Extracted profile of the gas phase.

[21] *Otherwise* $\varphi_{analyzer}$ *is usually given by the manufacturer.*

Figure II-10 illustrates the calibration procedure for an O1s spectrum (0.05 M NaBz solution) recorded with a photon energy of 600 eV. First, the image of the spectrometer detector allows differentiating the liquid phase and the gas phase of the aqueous sample (see the broad signal along with the spatial distribution in Figure II-10). The profile of the gas phase peak is then extracted, taking care not to integrate the liquid phase signal[22]. This latter can be fitted by a Gaussian function and calibrate the photon energy (here at 539.79 eV [27]). Spectrum recorded using the liquid jet setup are therefore referenced with respect to the infinite vacuum level. PE intensity signals are therefore plotted as a function of ionization energy.

Once calibrated, all liquid spectra were fitted by Gaussian/Lorentzian Sum Form (Voigt function) similarly to previous solid analysis fitting. The background was subtracted by a Tougaard function. The instrumental energy resolution is calculated using the beamline broadening (ΔE^2_{source}) and the one of the analyzer ($\Delta E^2_{analyzer}$). The first one depends on the monochromator exit slits and the photon energy. The second one is determined by the analyzer entrance slits and the pass energy. Typically, a resolution of 0.03 eV can be achieved at 100 eV photon energy and 10 eV pass energy for valence spectra and 0.2 eV for O1s spectra recorded at 600 eV with 50 eV pass energy. Calibration for a valence spectrum is shown in Chapter V, Figure V-7.

II.2.2. Coincidence measurement

II.2.2.i. Principle

During core-ionization processes, several electrons are emitted following the absorption of one photon according to this simplified scheme: $M + h\nu \rightarrow M^{+*} + e^-_{PE} \rightarrow M^{2+} + e^-_{AE}$ with e^-_{PE} the photoelectron and e^-_{AE} the Auger electron. The Auger decay intervenes in the few femtoseconds' range, while typical laboratory timing resolution for electronic events is on the order of the hundreds of picoseconds. Thus a photoelectron and its corresponding Auger electron appear to be emitted simultaneously. In the case of classical spectroscopy (non-coincidental), commonly performed with an HDA to reach high kinetic energy

[22] *The further it is selected from the micro-jet, the less it is influenced by the liquid and thus will be referred with respect to the infinite vacuum level* $E_{vac}(\infty)$ [54]

resolution, it is possible to record XPS spectra and AES spectra. Unfortunately, the interpretation of Auger spectra is usually complex. Indeed, it presents many complicated features, such as contributions from different inner-shell vacancies or satellites for instance[28]. In order to retrieve all information from the Auger process, it is necessary to realize Auger PhotoElectron Coincidence Spectroscopy measurements (APECS).

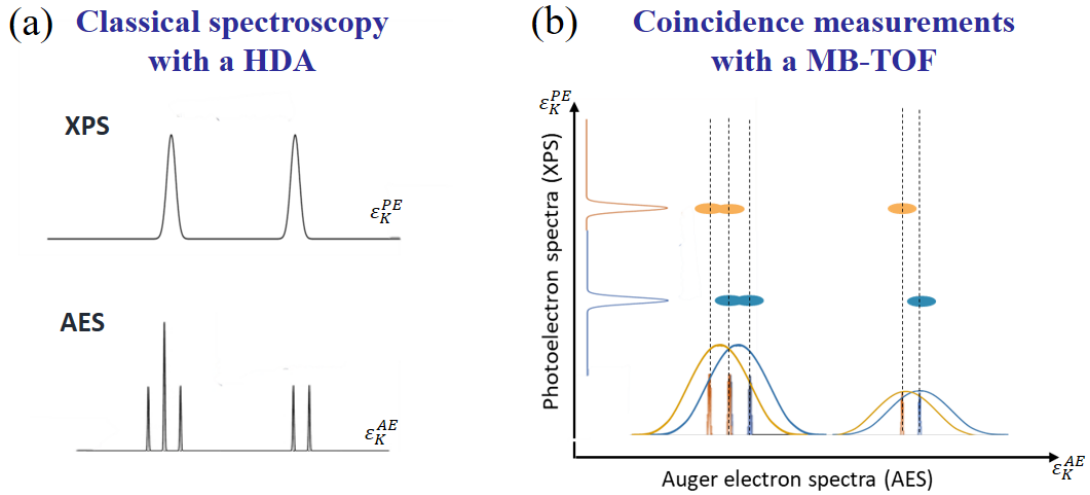

Figure II-11: Schematic diagram of the photoelectron-Auger process demonstrating the correlation between the Auger and photoelectron kinetic energies: Informations retrieved (a) with an hemispheric analyser (b) using a magnetic bottle. Scheme of 2D-map highlighting the coincidence "islands" which originates from Auger decay processes.

APECS consists in measuring emitted AE in coincidence with the corresponding PE. Such experiments, therefore, allow us to get free from the disruptive contributions (different inner-shell vacancies, satellites) and display the correlation between AE and PE. Indeed, the correlated events can be directly identified by plotting the XPS spectra versus the AES spectra to highlight coincidence "islands" to correlate the events as illustrated in Figure II-11.(b).

II.2.2.ii. Magnetic bottle time of flight spectrometer

Various coincidence techniques have been used to investigate Auger decay. The electron-electron coincidences setups were commonly based on the use of two different electrostatic analyzers [29], [30], or two time-of-flight spectrometers[31]. The development in 2003 of a magnetic bottle spectrometer by J. Eland[32] initiated significant progress in

gas phase electron-electron coincidence measurements as this setup allows to collect almost all the electrons emitted by the irradiated sample[28].

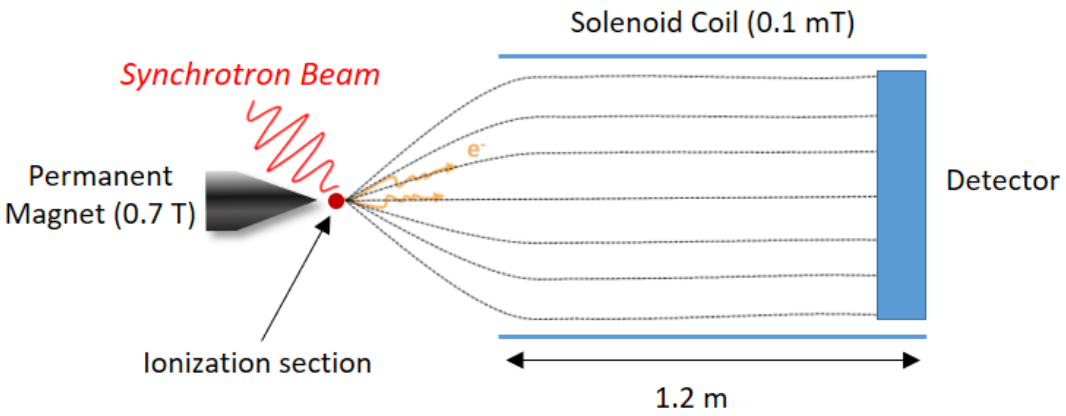

Figure II-12: Scheme of the magnetic bottle principle.
Dotted lines represent magnetic field lines.

The Magnetic Bottle Time-Of-Flight (MB-TOF) measures electrons' time of flight from the light-matter interaction area to the detector. The measure of the electron TOF value (T) allows distinguishing fast and slow electrons. Indeed, T is directly related to the velocity of the electrons (v) and the length of the magnetic bottle (L) ($T = L/v$). Consequently, it gives direct access to the kinetic energy of electrons ($E=1/2mv^2$). We can then relate the experimental TOF value to the electrons' kinetic energies deduced from the literature by knowing the photon energy. MB-TOF principle was first described by Beamson *et al.*[33] and then by Kruit *et al.*[34]. It acts as a magnetic mirror that pushes the electrons and parallelizes their trajectories. This analyzer is specially designed to study multi-electronic processes thanks to its very high efficiency in collecting electrons. Indeed, as illustrated in Figure II-12, the MB-TOF analyzer consists of a strong and inhomogeneous magnetic field with a bottle shape, which leads electrons towards the detector. Magnetic field lines (dotted lines in Figure II-12) are created by a conical permanent magnet (with a strong magnetic field, 0.7 T) and a solenoid coil (weak magnetic field zone, ~10^{-4} T). The field lines thus created allow to collect the electrons ejected by the sample, defined here as the ionization zone, in almost the whole 4π solid angle[32]. Therefore, it is well adapted to study inner shell photoionization by detecting

photoelectrons in coincidence with the resulting Auger electrons, thanks to the temporal structure of the SR light.

In order to measure electron TOF, it is necessary to tag the detection of the first electron with the SR photon pulse to record all the events generated by only one light pulse. This type of TOF experiment is therefore performed using the single-bunch mode of the synchrotron. Indeed, the slowest electrons must have the time to reach the detector before the electrons produced by the next bunch are detected. At SOLEIL synchrotron, the time framework in single-bunch mode is 1.2 µs. The system's measurement range is, however, not limited to 1.2 µs[23]. Therefore, once a first electron is detected (the fastest one), it records the time-of-flight of the successive electrons (1 or 2 in the case of multiple ionizations) with respect to the first one. It then reconstructs the full energy distribution for all electrons emitted in coincidence. However, the TOF spectra for a single electron (single ionization) will only be defined modulo [1.2 µs]. The high electrons collection of the MB allows the detection of 2, 3, or 4 electrons in coincidence.

Nevertheless, fortuitous coincidences may occur when too many events are detected. Therefore, the counting rate must be limited to a few thousand counts per second. It is adjusted by modifying the beamline parameters to reduce photons flux.

II.2.2.iii. Experimental setup

Coincidence measurements were performed by coupling the MB-TOF spectrometer with the liquid micro-jet. In this project, we used the experimental setup developed by the LCPMR in the context of the ANR project. This setup is an evolution of the previous MB-TOF setup (HERMES: High Energy Resolution Multi Electron Spectrometer) developed to study multiple photoionization processes in the gas phase [28], [32], [35], [36]. The spectrometer chamber is formed by a tube, called a drift tube, to create the homogeneous magnetic field required (~0.1 mT in this case). Briefly, a titanium tube (90 mm diameter, 1.2 m-length) hosts a solenoid (kapton® isolated copper wire). The titanium tube is electrically insulated and can be polarized to accelerate/decelerate the electrons by

[23] *If the synchrotron time framework is shorter than the TOF in the magnetic bottle, it is possible to use a chopper. It will interact regularly with photon bunches and therefore increase the time between two successive bunches*[55].

applying an appropriate electric potential. This parameter can be necessary to optimize the resolution, as the ΔE/E ratio defines the resolution. A double layer nickel-iron alloy (mu-metal) shielding is added around the drift tube and the interaction chamber. It avoids Earth's and external magnetic perturbations. Finally, two turbomolecular pumps (600 L/min) are added. One is installed at the spectrometer entrance, and the other one at the end, near the electrons detector. This detector is based on micro-channel plates (MCP) coupled with delay lines systems (Roentdek®). The overall detection efficiency for one electron is evaluated to be ~70%[24][28]. This efficiency is directly related to the efficiency of the MCP (active surface).

Coupling the MB-TOF with the liquid jet requires many adjustments because of the evaporation of the sample. Indeed, the detector system should be kept under high vacuum ($<10^{-5}$ mbar), whereas the pressure in the micro-jet chamber can reach 10^{-3}-10^{-4} mbar (see section II.2.1.iii). This vapor phase can be disruptive for coincidence measurements as it significantly increases the density of events generated in the ionization zone. Moreover, given the low penetration of soft X-rays, only the illuminated part of the liquid micro-jet is probed. In order to anticipate these problems specific to the condensed phase, the first tests were carried out with a metallic wire to mimic the liquid jet. It revealed the importance of the permanent magnet's position with respect to the ionization zone. The magnet's design was adapted to come as close as possible to the micro-jet without losing magnetic strength in the current setup. For this purpose, a soft iron cone (5 mm base-diameter and 20 mm long) is fixed at the top of the permanent magnet (SmCo conic cylinder of 24 mm base-diameter) to concentrate the magnetic field lines. It results in a field of ~0.8 T at the tip of the soft iron cone. This magnet assembly is installed on an XYZ motion controlled by three Nano-motors allowing accurate alignment under vacuum. The magnet assembly can be completely extracted from the liquid jet holder for maintenance outside the vacuum. Figure II-13 presents the setup used in our experiments. The experimental liquid setup remains identical to the one previously described (Figure II-8), except that the MB-TOF spectrometer replaces the HDA spectrometer.

[24] *An efficiency of 70% on the PE, leading to an efficiency of ~50% for the two electrons events.*

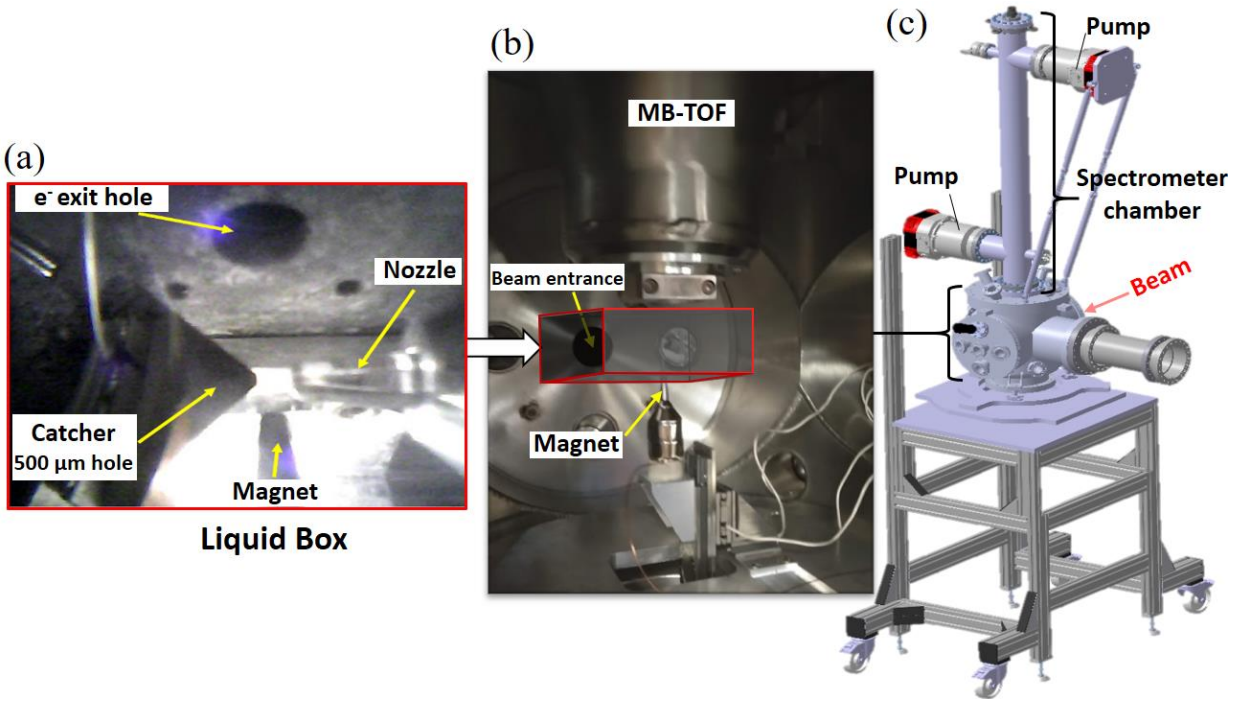

Figure II-13: Illustration of the set-up coupling the liquid jet and the MB-TOF spectrometer: (a) Photograph inside the liquid box presenting the liquid assembly, (b) Photograph inside the experimental chamber, (c) Diagram of the entire set-up.

In the first photograph (Figure II-13.(a)), taken from the inside of the liquid box, one can recognize the liquid jet assembly (nozzle and catcher). The electron skimmer, initially present on the top of the jet, has been removed, leaving a 5 mm electron exit hole. The conical magnet is placed at a distance of approximately 1 mm from the liquid jet. This box is then inserted into the experimental chamber as illustrated in Figure II-13.(b) and (c). The spectrometer entrance is located 4 cm above the micro-jet axis. Pre-alignment of the electron-hole of the liquid box and the spectrometer chamber is carried outside vacuum using a laser. The head of the magnetic bottle was specially designed with a small 5 mm diameter entrance allowing differential pumping. A manual valve was added to isolate the spectrometer from the experimental chamber simplifying the venting when needed.

II.2.2.iv. Coincidence data analysis

Data acquisition is achieved with the program "Labview"(recording of the time of flight (TOF) of the electrons). The software Igor Pro, from Wavemetrics, allows the treatment of these data using procedures written by P. Lablanquie [36]. These procedures allow us to revisit the detected events' histograms by filtering or keeping only the events in which a chosen number of electrons were detected in coincidence. The first step is to determine

precisely the photon beam energy. To that aim, a leak of Argon gas is generated in the analyzer chamber. Comparing the experimental Ar $2p_{3/2}$ threshold (248.6 eV[37]) allows recalibrating the monochromator (via an electron yield measurement). Then a set of spectra is recorded, increasing the photon energy and thus increasing the kinetic energy of Ar $2p_{3/2}$ and Ar $2p_{1/2}$ PE. Characteristic spectra are presented in Figure II-14.

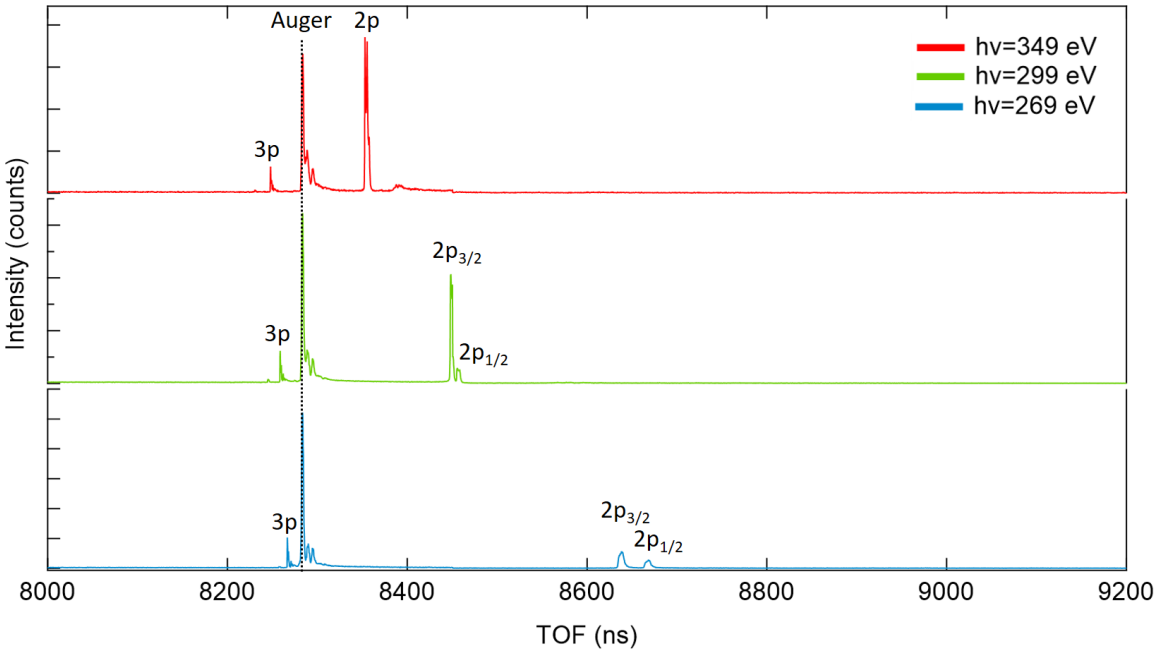

Figure II-14: Set of argon spectra from simple ionization of argon. Results are presented in time of flight (ns) of the emitted electrons for different photon energy. Data are synchronised with the synchrotron ring-clock (event generated by only one bunch of photons) with a scaling of 1 ns.

It illustrates the resolution performance of the spectrometer. Indeed, at high photon energy (far from the ionization threshold), the Ar2p photoelectrons have high kinetic energy. From the spectrum recorded at 349 eV (red spectrum), one can observe that the 2p peaks are almost not resolved. Indeed at this kinetic energy, the resolution is $\Delta E/E \sim 2\%$ of the emitted electron energy. The spin-orbit coupling imposes a shift of 2.12 eV between the two Ar2p peaks[38]. The resolution of ~2 eV does not allow a complete separation of the two peaks. On the contrary, at low kinetic energy, the resolution increases.

In order to improve the energy resolution, a potential can be applied to the solenoid to decelerate the electrons. Another strategy would have been to increase the length of the bottle, but this is fixed by spatial constraints (mobility of the experimental setup). Each photoelectron signal is fitted with a Gaussian function to retrieve the TOF value (T).

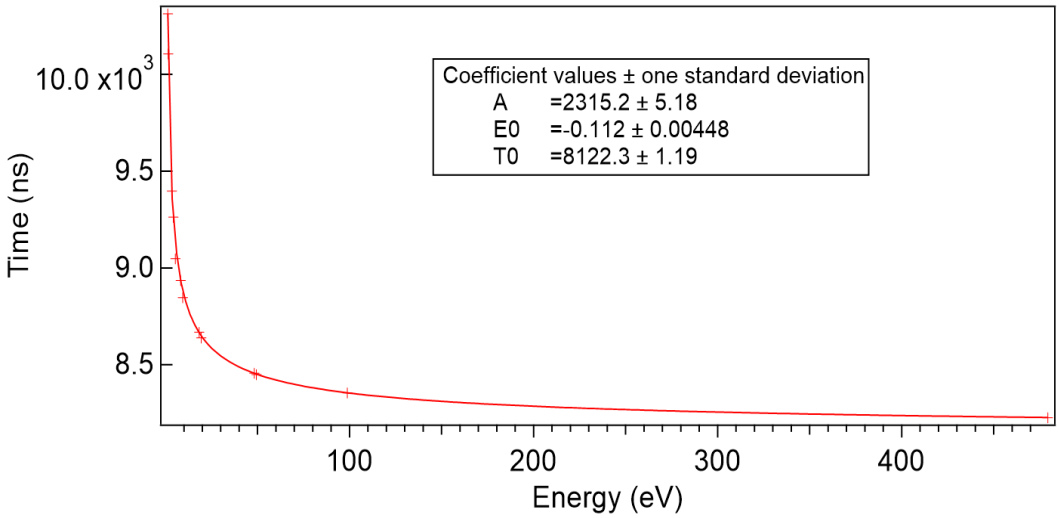

Figure II-15: Calibration curve obtained by plotting experimental photoelectrons TOF as a function of their kinetic energy determined from referenced binding energy values from the literature. Data are fitted to equation (II-5) in order to retrieve the parameters (A, E_0 and T_0), necessary for converting TOF into kinetic energy (see text for more details).

A correspondence table is established between the measured time of flights and the corresponding theoretical kinetic energies of the Ar 2p and O1s XPS signal measured at various photon energies. The corresponding calibration curve is presented in Figure II-15. In order to have a higher energy point, we also used the signal of the O1s gas-phase water molecules recorded by flowing an aqueous solution in the liquid jet. The calibration curve can be fitted using the relation:

$$T = \frac{A}{\sqrt{E_k + E_0}} + T_0 \qquad \text{(II-5)}$$

Where T is the time of flight of the electrons, E_k their kinetic energy, T_0 the TOF of the first electron recorded (origin), A is a constant and E_0 is a correction factor for the energy[25]. These fitting parameters are then used to convert TOF values in kinetic energy and in binding energy (knowing the photon energy).

In order to disentangle correlation events, the photoelectron spectrum is plotted as a function of the Auger electron spectrum. More concretely, the energy of the first detected electron is plotted versus the energy of the second detected electron as presented through the 2D –map illustration (see Figure II-11).

[25] E_0 *is necessary when the electrons trajectory can be disturbed (by the polarization field at the analyzer entrance for instance).*

II.3. Physico-Chemical and Bio-Chemical analysis

Different chemicals were irradiated with soft X-rays. Depending on the nature of the sample, different characterization techniques can be applied. After specifying the origin of chemicals used, the conditions for referenced irradiation conducted with Gamma-rays are presented. It is followed by a description of the different physico-chemical and biochemical analyses carried out to evaluate the changes induced by irradiation.

II.3.1. Chemicals products

Benzoate salts. Chemicals of sodium benzoate (NaBz) and hydroxybenzoates (sodium 2-hydroxy-benzoate (Na 2-HOBz), 3-hydroxy-benzoate (Na 3-HOBz) and 4-hydroxy-benzoate (Na 4-HOBz)) were purchased from Sigma Aldrich (purity ≥ 99.6%) and used as received. Solutions of concentrations in the 0.01 to 1 M range were prepared by dissolving the NaBz salt in water. Solutions were freshly prepared using MilliQ water (of resistivity 18.2 MΩ.cm and with less than 10 ppb of organic carbon content), resulting in a pH of 8.1. Non-irradiated NaBz solutions very often present a residual fluorescence emission due to partial hydroxylation with time. Specific benzoate lots were chosen with regard to their low fluorescence emission to minimize the fluorescence background.

Bovine Serum Albumin (BSA). Lyophilized BSA (Sigma, ref A0281) was dissolved at 40 g/L and dialyzed against pure water (100 volumes, Dialysis membrane retention threshold of 3.5 kDa Spectra/Por®3, Spectrum Labs). The solution was centrifuged at 14 000 g for 5 minutes at 4 °C and filtrated (0.22 µm) before use. The pH of 7.2 was measured at 20 °C with a Mettler Toledo S220 pHmeter and an InLab Nano electrode. The final protein concentration was determined by UV-vis spectrophotometry (Shimadzu UV-2450 spectrophotometer) using a molar extinction coefficient of 43,824 $M^{-1}.cm^{-1}$ at 280 nm[39].

Ferri-Cytochrome-c. Cytochrome c from equine heart (Sigma, 9007-43-6 purity >95%) was dissolved in pure water; Concentration was determined by UV-vis spectrophotometry using a molar extinction coefficient of ε_{410nm}=103,770 $M^{-1} \cdot cm^{-1}$ [40].

WST8. WST-8 is a water-soluble tetrazolium salt dye molecule was obtained from Cliniscience (Nanterre, France). Solution of concentration 50 to 300 µM were prepared in MilliQ water and quantified by UV-visible absorption spectrophotometry at 450 nm.

Superoxide Dismutase. Superoxide dismutase bovine (recombinant, expressed in E. Coli., purity >95%) was purchased from Sigma Aldrich Sigma (product SRP6107).

Phosphate Buffer. Commercial solution (1 M) from Sigma Aldrich (ref P3619-1GA).

Acetonitrile (ACN). Sigma Aldrich (ref 34851), suitable for HPLC, gradient grade, purity ≥99.9%.

II.3.2. γ-rays Irradiation

All standards were irradiated with a ^{137}Cs based on GammaCell® irradiator (3000 Elan, Nordion). The photon energy associated is 660 keV. Experiments were conducted in aerated conditions in glass vials. Thanks to holders, samples are positioned at the middle of the GammaCell®, and vials are kept open during the irradiation. The dose deposited in each sample is determined using a Fricke solution irradiated in the exact same conditions as the sample (position, aeration, mass irradiated).

Fricke dosimetry is a chemical dosimetry method based on the oxidation of iron (II) to iron (III)[41]. The solution is composed of Mohr's salt (6.10^{-3} mol.L^{-1}), which is the source of iron (II), sulfuric acid (0.4 mol.L^{-1}), and potassium chloride (10^{-3} mol.L^{-1}). The solution is then oxygenated by stirring overnight before use. The solution is kept in the dark to avoid oxidation by ambient light. The species produced by the radiolysis of water interact with iron. The radiolytic yield of iron (III) can be deduced by the absorption at 304 nm by spectroscopy[26]. The dose is determined by the following relationship:

$$D = \frac{\Delta A}{\varepsilon_{Fe^{3+}}^{304} \cdot G(Fe^{3+}) \cdot \rho \cdot l} \qquad \text{(II-6)}$$

With ∆A the absorption difference at 304 nm between the irradiated and non-irradiated sample, $\varepsilon_{Fe^{3+}}^{304}$ the molar extinction coefficient of iron (III) at 304 nm (2196 L.mol^{-1}.cm^{-1} at 298K), ρ the density of the solution (1.024 kg.m^{-3}) and l the path length of the cell. To perform the dosimetry, a series of irradiation is conducted varying the time of exposure.

[26] *The molar extinction coefficient of iron (II) representing 0.05% of that of iron (III), its contribution is negligible at this wavelength.*

Exposure times usually do not exceed 15 minutes to avoid over-irradiating the dosimeter (over-consumption). Fricke samples are then analyzed by UV-analysis. The dose rate is determined by plotting the dose values against the exposure time. The average dose rate at the center of the GammaCell® was 4.6 Gy/min.

II.3.3. Fluorescence analysis

Fluorescence measurements were performed using a FluoroMax-4 spectrometer from Horiba (Kisshoin, Japan) with a dual monochromator allowing user-defined variable wavelength settings. The lamp is a 150 W-xenon arc lamp. The excitation monochromator has an optical range of 220 – 600 nm blazed at 330 nm. The emission monochromator has an optical range of 290 – 850 nm blazed at 500 nm. The fluorescence signal is then detected by the photomultiplier tube (PMT) R928P (290-850 nm). The linear range for photon counting is 0-2 million cps. Above this range, the detector loses its linear response. A second reference detector monitors the xenon lamp to correct intensity and temporal fluctuations in the source during excitation scans. All data are acquired with FluorEssence™ software. Benzoate solution fluorescence analyses were recorded at room temperature with an excitation wavelength of 300 nm. The same model of fluorimeter was used at SOLEIL Synchrotron.

Nevertheless, due to the low signal quality of this spectrometer (electronic noise spikes), the measurements were recorded in kinetic mode. Each sample fluorescence signal was measured just after collection and re-evaluated at the end of the beamtime together with the calibration standards (described below). Emission spectra were recorded on random samples to control the spectrum pattern.

- Fluorescence calibration of the benzoate dosimeter

Benzoate solutions were studied at $\lambda_{excitation}$ = 300 nm and $\lambda_{emission}$ = 406 nm according to the spectral response of the 2-hydroxybenzoate emission. Standard samples for calibration were prepared, adding known amounts of Na 2-HOBz to NaBz solutions. The concentration of Na 2-HOBz ranged from 10^{-7} to 10^{-4} M. Calibration curves for the emitted fluorescent signal (F) can be fitted by using a linear regression:

$$F = F_0 + F_1[Na\ 2\text{-}HOBz] \quad \text{(II-7)}$$

Where F_1 is the slope and F_0 is the residual fluorescence. F_0 may vary due to the aging of the solution and should be measured regularly to characterize the evolution of the irradiated sample. Typical calibration curves of Na 2-HOBz are presented in Figure II-16, and fitting parameters are presented in the following Table II-3[42]. Uncertainties are statistical errors obtained on the fitting parameters.

Table II-3: Fitting parameters from calibration curves

[NaBz] (M)	***F_1 (counts / M)***	***F_0 (counts)***	***R^2***
0.01 M	*2.05E+11 ±1.28E+10*	*2.24E+03 ±1.66E+03*	*0.999495*
0.1 M	*1.90E+11 ±1.60E+10*	*1.22E+04 ±3.55E+03*	*0.999099*
1 M	*7.06E+10 ±6.07E+09*	*4.83E+04 ±1.32E+03*	*0.996583*

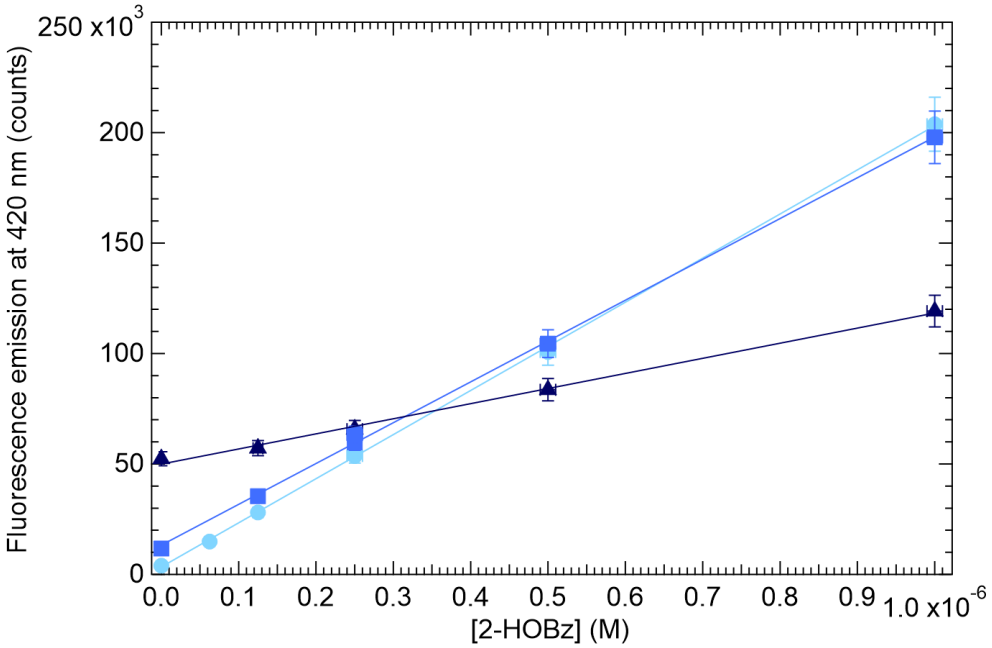

*Figure II-16: Calibration curves for the fluorescent signal emitted by Na 2-HOBz diluted in NaBz solutions at different concentrations: light to dark blue correspond to 0.01 M, 0.1 M and 1 M. Experimental data were fitted to a straight line of equation F = F1 * [Na 2-HOBz] + F0*

An inner-filter effect, *i.e.*, partial absorption of both the excitation and emission signals by the solution[43]–[45], affects the 2-HOBz fluorescence signal for the 1 M NaBz solution, which leads to a slower, but still linear, increase of the fluorescence signal with the 2-HOBz concentration.

- Reference dosimetry Irradiation

In order to check the behavior of the benzoate dosimeter, reference γ-rays irradiations were performed. Samples were irradiated using the protocol previously described with the GammaCell®. For each benzoate concentration studied, a series of irradiation was conducted varying the dose (i.e., the exposure time inside the GammaCell®). Benzoate solutions were then analyzed by fluorescence measurement. Typical results obtained for 10 mM benzoate solutions are presented in Figure II-17.(a). The maximum intensity (406 nm) is converted to 2-HOBz concentration ([2-HOBz]) using the calibration curves (Figure II-17 and Table II-3)[27]. By studying the evolution of [2-HOBz] as a function of the dose, a linear relationship is observed in Figure II-17.(b).

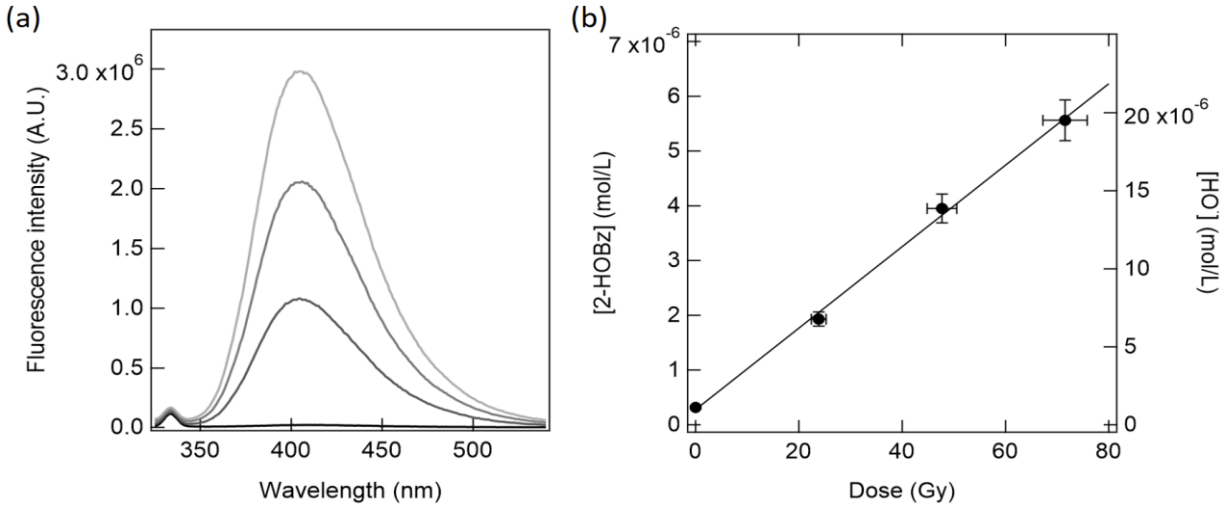

Figure II-17: Determination of the hydroxyl radical yield for gamma irradiation. Presented data were obtained on NaBz 10 mM aerated solutions: (a) Fluorescence signal curves obtained for increasing time of exposure, (b) Deduced hydroxyl radical concentration as a fonction of the dose. The hydroxyl concentration was deduced from calibration curves obtained with the same fluorimeter with the same solution varying the concentration of Na 2-HOBz.

The production yield G($HO^{\cdot}$) is deduced from the slope of this linear curve. The concentration of hydroxyl radicals ($[HO^{\cdot}]$) is estimated by taking into account the hydroxylation yield (~30%)[46]–[48]. The value obtained for 10 mM benzoate solutions was $G(HO^{\cdot})^{\gamma}_{0.01M}$= 0.261±0.015 µmol/J. This value, obtained in aerated conditions at ambient temperature is consistant with the literature value ($G(HO^{\cdot}) = 0.28$ µmol/J) [49].

[27] *Each time, calibration solutions were freshly prepared and analyzed under the same conditions.*

II.3.4. Off-line UV analysis

Off-line UV-analysis refers to the analysis of collected irradiated samples. Measurements were performed on a Jasco spectrometer using a suprasil Quartz HELLMA cell (ref 105.250-QS: 100 µL, path length 1 cm). For quick analysis, measurements were performed on a nanodrop spectrophotometer (Nanodrop 2000, Thermo Scientific)[50]. Such devices present a surface analysis pre-treated to minimize the contact with the liquid to be analyzed. It results in a retained stable droplet. A mechanical arm system crushes the drop, leaving a 1 mm path length to perform the measurement.

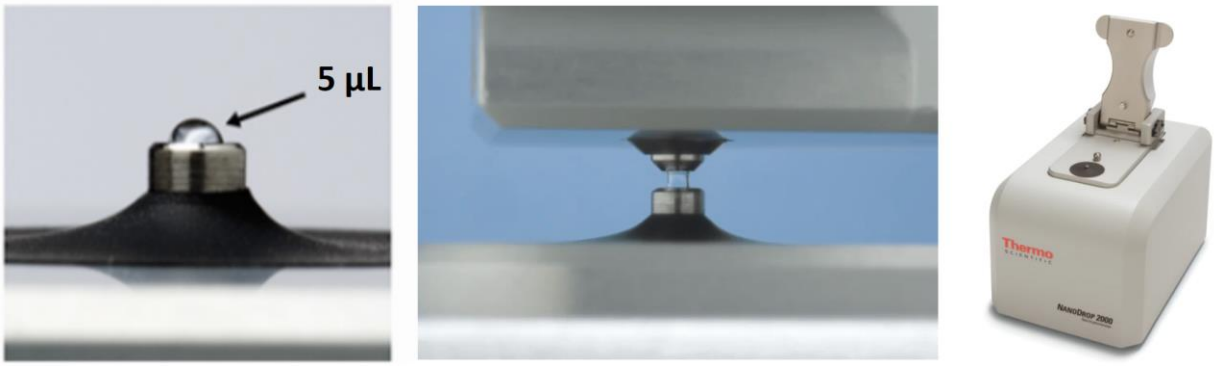

Figure II-18: Nanodrop principle (images from ThermoFischer website)

The absorbance accuracy of the Nanodrop is 3% for a signal of 0.74 optical density at 350 nm. This device is less precise than the JASCO spectrophotometer (0,03% absorbance accuracy) but reduces sample volume analysis from 5 to 1 µL (as illustrated in Figure II-18).

II.3.5. Liquid Chromatography coupled to mass spectrometry

II.3.5.i. Principle

Liquid-chromatography coupled to mass spectrometry (LC-MS) analysis allows the separation of the isomers to quantify their production. Liquid chromatography-mass spectrometry (LC-MS) is the method of choice for sample analysis. LC-MS consists in separating chemical compounds before their injection in a mass spectrometer. The chromatography is based on the affinity of the chemical compound with a static phase (column) and a mobile phase (eluent). In addition, the column will "retain" the compounds,

while the eluent will push them out, allowing their separation. The goal is to adapt the static and mobile phases according to the sample's chemical properties to be studied to obtain the best separation (optimized conditions are given below in section II.3.5.iii). In our case, the LC-MS was performed on solutions of benzoate and hydroxy-benzoate in order to decipher the products formed during the irradiation. Indeed, the irradiation of benzoate solutions can lead to several mono-hydroxylated products with a similar m/z value (hydroxylation either in ortho-, meta- or para- position). Experiments were performed on an Agilent 1200 (Agilent Technologies) on the DISCO Beamline with the help of Alexandre Giuliani. This apparatus is directly coupled to a linear quadrupole ion trap mass spectrometer (LTQ).

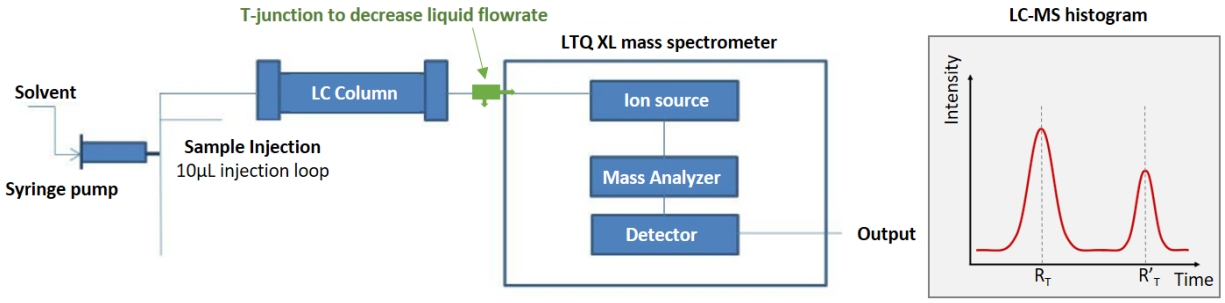

Figure II-19: Principle of the LC-MS analysis. Obtaining a histogram which allows to identify the chemical solutes according to their respective retention time (R_T).

II.3.5.ii. LTQ spectrometer

Mass spectrometry (MS) is a well-known powerful tool for the analysis of charged molecules. Ions formed in the gas phase by the electrospray ionization (ESI) technique are separated by mass analyzers specifically designed to select the ions based on their mass-to-charge (m/z) ratios[51]. In our case, we used a commercial linear quadrupole ion trap mass spectrometer (LTQ XL from Thermo Scientific).

Sample molecules are ionized and desolvated into the gas phase by the electrospray ionization source (ESI). The ESI technique consists in applying a high voltage (positive or negative) to a liquid to create an electrically charged aerosol. In the positive mode, this source generates precursor ions $[M+nH]^{n+}$, where M indicates the molar weight of the target molecule, n is the ion charge state, and H is the number of protons formed. The

number of precursor ions produced depends on the solution (buffer, structure) and the ESI parameters (voltage). The following equation (II-8) gives the mass-to-charge ratio:

$$\frac{m}{z} = \frac{M+n}{n} \qquad \text{(II-8)}$$

The charged particles are collected by an ion sweep cone and transferred through a heated capillary and a lens system. The analyzer system comprises the ion optics (quadrupole and octupole ion filters), the mass analyzer (a linear quadrupole ion trap), the ion detection, and an electronic control system.

The injection of the sample can be done using a syringe pump or through capillaries at a user-defined flow rate. These capillaries can couple the mass spectrometer to a liquid chromatography pump for LC/MS analysis as detailed in the following section.

II.3.5.iii. Benzoate LC-MS separation

Successive commercial solutions of benzoate (Bz) and hydroxy-benzoates (2-HOBz, 3-HOBz, and 4-HOBz) were injected to optimize the LC-MS separation of the irradiated solution. More specifically, each sample was injected into the LC at a flow rate of ~5µL/min, and the elution is followed by the mass data recorded as a function of time (histogram or chromatogram). As soon as one of the solutes reaches the ESI source, a peak of intensity proportional to the amount of this solute is detected. The eluted compound is identified on histograms by its retention time (RT), the difference between its injection time in the column, and its entry time in the detector. It is possible to "filter" the total ions current (TIC) signal by selecting a particular m/z value. This filtering is particularly interesting when the composition of the injected sample is known. Of course, the method should be optimized to have sufficiently different retention times for each solution component to be studied. However, it is necessary to find a compromise not to have a total time of analysis too long. The eluent is generally generated by mixing two buffer solutions (A and B) which are generally an aqueous phase (water-based) and an organic one (here based on acetonitrile). Working with two separated buffers facilitates the optimization of the method as several conditions can be tested without preparing new solutions. It is possible to work in isocratic conditions (ratio A:B constant during the whole

elution) or by applying a gradient (varying the ratio A:B during the elution). The optimized conditions for benzoate are presented in the following Table II-4.

Table II-4: LC-MS analytical parameters for the separation of sodium benzoate and its mono-hydroxylated products.

Buffer solutions	**A:** Acetonitrile + 0.01 M phosphate buffer **B:** Water + 0.01 M phosphate buffer			
LC column	Column µRPC C2/C18 ST 4.6/100 mm, 100 Å (Pharmacia Biotech, cod. N° 17-5057-01)[52]			
Eluent	Ratio A:B = 90:10 – isocratic conditions, flow rate 0.25 mL/min			
Solutes tested	NaBz (m/z 121)	Na 2-HOBz (m/z 137)	Na 3-HOBz (m/z 137)	Na 4-HOBz (m/z 137)
Elution time (R_T)	3 min	6.1 min	1.95 min	1.8 min

Figure II-20 presents a typical histogram obtained after injecting a mixture of the four chemicals: NaBz, 2-, 3-, 4- mono-hydroxylated benzoate (black curve). Typical elution times previously determined (Table II-4) allow identifying the different peaks present in the chromatogram even if they present the same m/z ratio. The peak at R_T= 1 min corresponds to the dead volume of the column (totally non-retained salts)

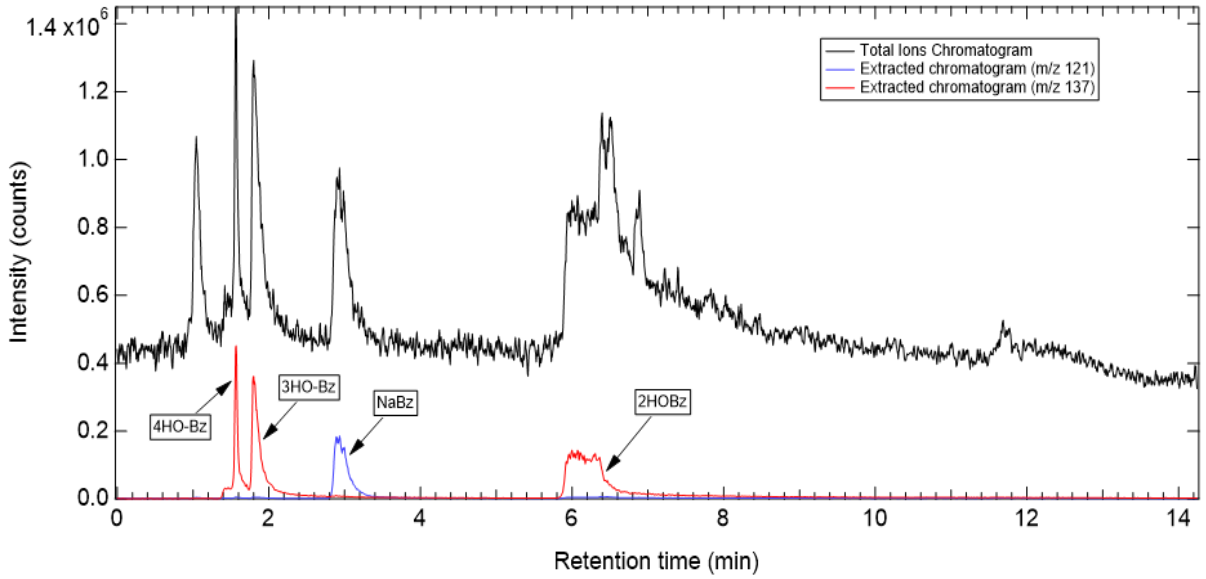

Figure II-20: LC-MS histogram obtained for injection of commercial solutions. Identification of the respective elution time by analysis of the extracted chromatograms at m/z=121 (blue) for Bz and m/z=137 (red) for HOBz isomers.

II.3.6. Gel electrophoresis

For the protein samples (cytochrome C and BSA), the irradiated samples were deposited on Tris-HCl SDS-page gels (pH 6.8) to perform electrophoresis. The principle of electrophoresis is based on the migration of a charged molecule in a gel of polymers (polyacrylamide) under the influence of an electric field. The use of sodium dodecyl sulfate (SDS) inside the polyacrylamide gel allows denaturing the proteins. This denaturation essentially eliminates the influence of the structure and charge, so the proteins are separated solely based on their polypeptide chain length. It is also possible to add a reducing agent (such as beta-mercaptoethanol) to cleave disulfide bonds critical for properly folding the proteins. In such conditions, proteins unfold into linear chains with a negative charge proportional to the polypeptide chain length. The comparison between non-reduced and reduced conditions can allow the detection of eventual multimeric forms of the protein. The system used to perform electrophoresis was the Mini-PROTEAN® TGX™[53]. We decided to use hand-cast gels in order to optimize the separation parameters easily. The percentage of acrylamide inside the SDS-page gels was adjusted following the recipe presented in Table II-5. All reactants presented in the table and the protein loader solution (Laemmli solution #1610737) and running buffer SDS-Page (#1610732) were purchased from Bio-Rad.

Table II-5: Recipes for handcast gel. The percentage of acrylamide inside the resolving gel was adapted following these indications.(Data from BioRad guide [57])

	Stacking Gel	Resolving Gel		
	4%	7.5%	12%	X%
30% Acrylamide/bis	1.98 ml	3.75 ml	6.0 ml	0.5 × X ml
0.5M Tris-HCl, pH 6.8	3.78 ml	—	—	—
1.5M Tris-HCl, pH 8.8	—	3.75 ml	3.75 ml	3.75 ml
10% SDS	150 µl	150 µl	150 µl	150 µl
diH_2O	9 ml	7.28 ml	5.03 ml	11.03–(0.5 × X) ml
TEMED	15 µl	7.5 µl	7.5 µl	7.5 µl
10% APS	75 µl	75 µl	75 µl	75 µl
Total Volume	15 ml	15 ml	15 ml	15 ml

The thickness of the gel is determined by the spacer plates, which were 1 mm thick. The size of the wells accessible with the comb varied from 10 µL to 20 µL. However, to ease the sample deposition, we always deposited two-thirds of the maximal volume to prevent mixing the solutions. The voltage applied during the electrophoresis remained equal to 200 V during the whole migration (run time 35-40 min). At the end of the migration, gels were stained by an Instant blue solution (based on Coumassie blue stain), which usually detects 10-50 ng protein per band. Once stained, the gels were rinsed with water and photographed with a FUJIFILM LAS-3000. Images were analyzed with GelAnalyzer® software.

II.3.7. Qualitative carbon contamination analysis

Scanning Electron Microscopy (SEM) is a powerful microscopy technique for solid samples' analytical or chemical characterization. In the context of this project, it has been shown as a great tool to characterize the fooling of the microfluidic cell after irradiation (see results presented in Chapter III).

SEM works on the principle of scattering electrons on the surface of the sample. It consists of an electron beam generated by applying a high voltage on a tungsten filament. The electron beam is focused on the sample by an electromagnetic lens. The energy transferred to the sample knocks out electrons from the sample, called secondary electrons. A scanning electron detector is equipped with a positive bias grid to attract these electrons. A SEM image is therefore composed of each signal point transmitted by the raster scan generator.

Working with electrons imposed working in a high vacuum environment (10^{-6} mbar inside the chamber) to avoid scattering the primary electron beam. We suspected that irradiation of the microfluidic cell under vacuum could induce carbon deposition at the surface of the silicon chips enclosing the cell (the microfluidic cell design is described in Chapter III section III.1). Therefore, to check our hypothesis, SEM measurements were performed on the microfluidic silicon chip alone, with the help of Stéphane LORCY on IPANEMA (Synchrotron SOLEIL). The microscope MEB-FEG ZEISS Supra55VP is equipped with an Energy Dispersive X-ray Analysis (EDX) that provides elemental identifications. X-rays are emitted if the secondary electrons leave inner shell vacancies behind (fluorescence, see Chapter I for more details). EDX analysis gives a spectrum that

displays peaks correlated to the elemental composition of the investigated sample. Energies of the peaks present are automatically identified thanks to an X-ray emission file of known energies. The elements' detection threshold is 500 ppm, which was ideally suited for a qualitative analysis of carbon contamination on the surface of silicon nitride windows after irradiation. Silicon chips were directly deposited on an aluminum holder and maintained with a copper clip. No further optimization of the samples conduction was performed, and some charge-effect was therefore observed.

Bibliography Chapter II

[1] I. Nenner, J. Doucet, and H. Dexpert, "Rayonnement synchrotron et applications," *Techniques de l'ingénieur*, Ref: P2700 V2, 10. July 1996.

[2] A. Bharti and N. Goyal, "Fundamental of Synchrotron Radiations," *Synchrotron Radiat. - Useful Interes. Appl.*, pp. 1–10, 2019.

[3] E. M. Rowe and F. E. Mills, "Tantalus I: a Dedicated Storage Ring Synchrotron Radiation Source.," *Part Accel*, vol. 4, no. 4, pp. 211–227, 1973.

[4] D. M. Mills, J. R. Helliwell, Å. Kvick, T. Ohta, I. A. Robinson, and A. Authier, "Report of the Working Group on Synchrotron Radiation Nomenclature – brightness, spectral brightness or brilliance?," *J. Synchrotron Radiat.*, vol. 12, no. 3, pp. 385–385, May 2005.

[5] S. Mobilio, F. Boscherini, and C. Meneghini, *Synchrotron Radiation*, vol. 54, no. 5. Springer, 2015.

[6] H. Winick, "Fourth generation light sources," in *Proceedings of the 1997 Particle Accelerator Conference (Cat. No.97CH36167)*, IEEE, pp. 37–41, 1997.

[7] M. Couprie and J. Denard, "Une Source De Lumière Dédiée À La Recherche," no. 1, pp. 18–23.

[8] T. Harada, "Design and application of a varied-space plane grating monochromator for synchrotron radiation," *Nucl. Instruments Methods Phys. Res. Sect. A Accel. Spectrometers, Detect. Assoc. Equip.*, vol. 291, no. 1–2, pp. 179–184, May 1990.

[9] Omicron NanoTechnology, *EA 125 Energy Analyser User's Guide*, Ed. 2.1., vol. 49, no. 2.1. Limburger Strasse 75, 65232 Taunusstein, Germany, 2002.

[10] P. Swift, "Adventitious carbon?the panacea for energy referencing?," *Surf. Interface Anal.*, vol. 4, no. 2, pp. 47–51, Apr. 1982.

[11] M. P. Seah, "Background subtraction," *Surf. Sci.*, vol. 420, no. 2–3, pp. 285–294, Jan. 1999.

[12] V. Jain, M. C. Biesinger, and M. R. Linford, "The Gaussian-Lorentzian Sum, Product, and Convolution (Voigt) functions in the context of peak fitting X-ray photoelectron spectroscopy (XPS) narrow scans," *Appl. Surf. Sci.*, vol. 447, pp. 548–553, Jul. 2018.

[13] S. Hofmann, *Auger- and X-Ray Photoelectron Spectroscopy in Materials Science*. Springer, 2013.

[14] M. Faubel, S. Schlemmer, and J. P. Tocnnies, "A molecular beam study of the evaporation of water from a liquid jet," Z. Phys. D-*Atoms, Molecules and Clusters,* vol. 10, pp. 269-277, 1988.

[15] M. Faubel, "Photoionization and Photodetachment: Part I," *World Sci.*, vol. 10A, pp. 634–690, 2000.

[16] R. Dupuy, C. Richter, B. Winter, G. Meijer, R. Schlögl, and H. Bluhm, "Core level photoelectron spectroscopy of heterogeneous reactions at liquid–vapor interfaces: Current status, challenges, and prospects," *J. Chem. Phys.*, vol. 154, no. 6, p. 060901, 2021.

[17] F. Buchner, N. Heine, I. V Hertel, and T. Schultz, "Time-resolved photoelectron spectroscopy of solvated electrons in aqueous NaI solution," *Phys. Chem.Chemical Physics*, vol. 12, pp. 14629–14634, 2010.

[18] N. Preissler, F. Buchner, T. Schultz, and A. Lübcke, "Electrokinetic charging and evidence for charge evaporation in liquid microjets of aqueous salt solution," *J. Phys. Chem. B*, vol. 117, no. 8, pp. 2422–2428, 2013.

[19] M. Faubel and B. Steiner, "Strong Bipolar Electrokinetic Charging of Thin Liquid Jets Emerging from 10 µm PtIr Nozzles," *Berichte der Bunsengesellschaft für Phys. Chemie*,

vol. 96, no. 9, pp. 1167–1172, 1992.

[20] G. Olivieri, A. Goel, A. Kleibert, D. Cvetko, and M. A. Brown, "Quantitative ionization energies and work functions of aqueous solutions," *Phys. Chem. Chem. Phys.*, vol. 18, no. 42, pp. 29506–29515, 2016.

[21] L. Pérez Ramírez *et al.*, "The Fermi level as an energy reference in liquid jet X-ray photoelectron spectroscopy studies of aqueous solutions," *Phys. Chem. Chem. Phys.*, vol. 23, no. 30, pp. 16224–16233, 2021.

[22] B. Credidio *et al.*, "Quantitative electronic structure and work-function changes of liquid water induced by solute," *Phys. Chem. Chemical Physics*, vol. 24, pp. 1310-1325, 2021.

[23] M. Faubel, B. Steiner, and J. P. Toennies, "Photoelectron spectroscopy of liquid water, some alcohols, and pure nonane in free micro jets," *J. Chem. Phys.*, vol. 106, no. 22, pp. 9013–9031, 1997.

[24] B. Winter, E. F. Aziz, U. Hergenhahn, M. Faubel, and I. V. Hertel, "Hydrogen bonds in liquid water studied by photoelectron spectroscopy," *J. Chem. Phys.*, vol. 126, no. 12, pp. 0–6, 2007.

[25] K. Nishizawa *et al.*, "High-resolution soft X-ray photoelectron spectroscopy of liquid water," *Phys. Chem. Chem. Phys.*, vol. 13, no. 2, pp. 413–417, 2011.

[26] S. Y. Truong, A. J. Yencha, A. M. Juarez, S. J. Cavanagh, P. Bolognesi, and G. C. King, "Threshold photoelectron spectroscopy of H2O and D2O over the photon energy range 12-40 eV," *Chem. Phys.*, vol. 355, no. 2–3, pp. 183–193, 2009.

[27] R. Sankari *et al.*, "Vibrationally resolved O1s photoelectron spectrum of water," *Chem. Phys. Lett.*, vol. 380, no. 5–6, pp. 647–653, 2003.

[28] F. Penent *et al.*, "Coincidence Auger spectroscopy," *J. Electron Spectros. Relat. Phenomena*, vol. 144–147, pp. 7–11, 2005.

[29] R. A. Bartynski, E. Jensen, S. L. Hulbert, and C.-C. Kao, "Auger photoelectron coincidence spectroscopy using synchrontron radiation," *Prog. Surf. Sci.*, vol. 53, no. 2–4, pp. 155–162, Oct. 1996.

[30] I. N. Kukhto and V. A. Tolkachev, "ror n on)," vol. 64, no. 3, pp. 312–317, 1997.

[31] J. Viefhaus *et al.*, "Interference Effects between Auger and Photoelectron Studied by Subnatural Linewidth Auger-Photoelectron Coincidence Spectroscopy," *Phys. Rev. Lett.*, vol. 80, no. 8, pp. 1618–1621, Feb. 1998.

[32] J. H. D. Eland, O. Vieuxmaire, T. Kinugawa, P. Lablanquie, R. I. Hall, and F. Penent, "Complete Two-Electron Spectra in Double Photoionization: The Rare Gases Ar, Kr, and Xe," *Phys. Rev. Lett.*, vol. 90, no. 5, p. 4, 2003.

[33] G. Beamson, H. Q. Porter, and D. W. Turner, "The collimating and magnifying properties of a superconducting field photoelectron spectrometer," *J. Phys. E.*, vol. 13, no. 1, pp. 64–66, 1980.

[34] P. Kruit and F. H. Read, "Magnetic field paralleliser for 2π electron-spectrometer and electron-image magnifier," *J. Phys. E.*, vol. 16, no. 4, pp. 313–324, 1983.

[35] P. Lablanquie, F. Penent, and Y. Hikosaka, "Multi-electron coincidence spectroscopy: Double photoionization from molecular inner-shell orbitals," *J. Phys. B At. Mol. Opt. Phys.*, vol. 49, no. 18, 2016.

[36] P. Lablanquie *et al.*, "Multi-electron coincidence spectroscopy: Triple Auger decay of Ar 2p and 2s holes," *J. Electron Spectros. Relat. Phenomena*, vol. 220, pp. 125–132, 2017.

[37] T. X. Carroll, J. D. Bozek, E. Kukk, V. Myrseth, L. J. Sæthre, and T. D. Thomas, "Line shape and lifetime in argon 2p electron spectroscopy," *J. Electron Spectros. Relat. Phenomena*, vol. 120, no. 1–3, pp. 67–76, 2001.

[38] C. D. Wanger, W. M. Riggs, L. E. Davis, J. F. Moulder, and G. E.Muilenberg, "Handbook of X-ray Photoelectron Spectroscopy," in *Surface and Interface Analysis*, U. Eden Prairie, Minnesota, Ed. 1981.

[39] P. Qu, H. Lu, S. Yan, and Z. Lu, "Influences of cationic, anionic, and nonionic surfactants on alkaline-induced intermediate of bovine serum albumin," *Int. J. Biol. Macromol.*, vol. 46, no. 1, pp. 91–99, Jan. 2010.

[40] W. D. Butt and D. Keilin, "Absorption spectra and some other properties of cytochrome c and of its compounds with ligands," *Proc. R. Soc. London. Ser. B. Biol. Sci.*, vol. 156, no. 965, pp. 429–458, Nov. 1962.

[41] H. Fricke and E. J. Hart, "The Oxidation of Fe ++ to Fe +++ by the Irradiation with X-Rays of Solutions of Ferrous Sulfate in Sulfuric Acid," *J. Chem. Phys.*, vol. 3, no. 1, pp. 60–61, Jan. 1935.

[42] L. Huart *et al.*, "A microfluidic dosimetry cell to irradiate solutions with poorly penetrating radiations: a step towards online dosimetry for synchrotron beamlines," *J. Synchrotron Radiat.*, vol. 28, no. 3, pp. 778–789, 2021.

[43] A. V. Fonin, A. I. Sulatskaya, I. M. Kuznetsova, and K. K. Turoverov, "Fluorescence of dyes in solutions with high absorbance. Inner filter effect correction," *PLoS One*, vol. 9, no. 7, 2014.

[44] Q. Gu and J. E. Kenny, "Improvement of inner filter effect correction based on determination of effective geometric parameters using a conventional fluorimeter," *Anal. Chem.*, vol. 81, no. 1, pp. 420–426, 2009.

[45] N. N. Zhadin, "Correction of the Internal Absorption Effect in Fluorescence Emission and Excitation Spectra from Absorbing and Highly Scattering Media: Theory and Experiment," *J. Biomed. Opt.*, vol. 3, no. 2, p. 171, Apr. 1998.

[46] I. Loeff and A. J. Swallow, "On the Radiation Chemistry of Concentrated Aqueous Solutions of Sodium Benzoate," *J. Phys. Chem.*, vol. 68, no. 9, pp. 2470–2475, Sep. 1964.

[47] W. A. Armstrong and D. W. Grant, "The Aqueous Benzoate System as a Sensitive Dosimeter for Ionizing Radiations," *Can. J. Chem.*, vol. 38, no. 6, pp. 845–850, 1960.

[48] L. Huart *et al.*, "Soft X-ray Radiation and Monte Carlo Simulations: Good Tools to Describe the Radiation Chemistry of Sub-keV Electrons," *J. Phys. Chem. A*, vol. 124, no. 10, pp. 1896–1902, 2020.

[49] G. Baldacchino, A. E. Commission, and Y. Katsumura, *Recent Trends in Radiation Chemistry*, no. April 2014. World Scientific Publishing Co. Pte. Ltd., 2010.

[50] P. Desjardins and D. Conklin, "NanoDrop microvolume quantitation of nucleic acids," *J. Vis. Exp.*, no. 45, pp. 1–5, 2010.

[51] E. Hoffmann and V. Stroobant, *Mass spectrometry Mass spectrometry*, vol. 1040, no. 2. 2016.

[52] Healthcare, "µRPC C2/C18 Data Sheet."

[53] Laboratories Bio-Rad, "A Guide to Polyacrylamide Gel Electrophoresis and Detection," *Bio-Rad*, p. 47, 2012.

[54] D. Cahen and A. Kahn, "Electron energetics at surfaces and interfaces: Concepts and experiments," *Adv. Mater.*, vol. 15, no. 4, pp. 271–277, 2003.

[55] K. Ito *et al.*, "Application of a simple asynchronous mechanical light chopper to multielectron coincidence spectroscopy," *Rev. Sci. Instrum.*, vol. 80, no. 12, p. 123101, Dec. 2009.

[56] M. Idir *et al.*, "Le pôle de métrologie de SOLEIL," *J. Phys. IV*, vol. 138, no. 1, pp. 265–274, Dec. 2006.

Chapter III. Implementation of a microfluidic cell

Contents Chapter III

Chapter III. Implementation of a microfluidic cell

The first soft X-rays irradiations of liquids, performed by the team, were carried out at air. It was achieved using a specific beam extraction setup (IRAD). This setup was historically developed by Annie Chetioui and co-workers (Sorbonne University) to irradiate biological samples at the LURE (Laboratoire d'Utilisation du Rayonnement Électromagnétique)[1], [2]. Figure III-1 illustrates its installation on the METROLOGIE beamline. Briefly, it consists of a three-stage differential pumping system enclosed by a square 150 nm-thick silicon nitride (Si_3N_4) window. Silicon nitride windows are highly transparent to soft X-rays. Transmission values vary between 91.2 and 96.4% over the energy range from 1.0 to 1.4 keV[3][28]. This setup allows maintaining the 10^{-7} mbar pressure behind the exit window against the beamline's 10^{-8} mbar pressure. A manual shutter allows control of the beam exposition and, therefore, the time of exposure of the irradiated sample.

The IRAD setup offers the possibility to change the sample environment quickly. Indeed, irradiation at atmospheric pressure does not impose specific constraints other than those of the synchrotron environment (restricted space, micro-beam). Nevertheless, the thickness of all materials crossed by the synchrotron beam must be accurately characterized and optimized to calculate the effective absorption of soft X-rays in matter. Especially, the distance between the exit window of the beamline and the sample position (along the s-axis, see Figure III-2), referred to as an "air gap," must be carefully measured given the significant absorption of soft X-rays in the air (~20% / mm at 1.28 keV[3]).

The initial liquid environment was provided using a Plexiglas semi-micro cuvette (PMMA, 1 mL) illustrated in Figure III-2. A 7 mm hole was drilled to fix a silicon nitride membrane, identical to the one glued at the exit of the IRAD setup. The alignment of the window, with respect to the beam, was performed by placing a small photodiode inside the empty cell.

[28] *Calculated for Si_3N_4, with a 2.68 g/cm³ density [Huszank et al., 2016)].*

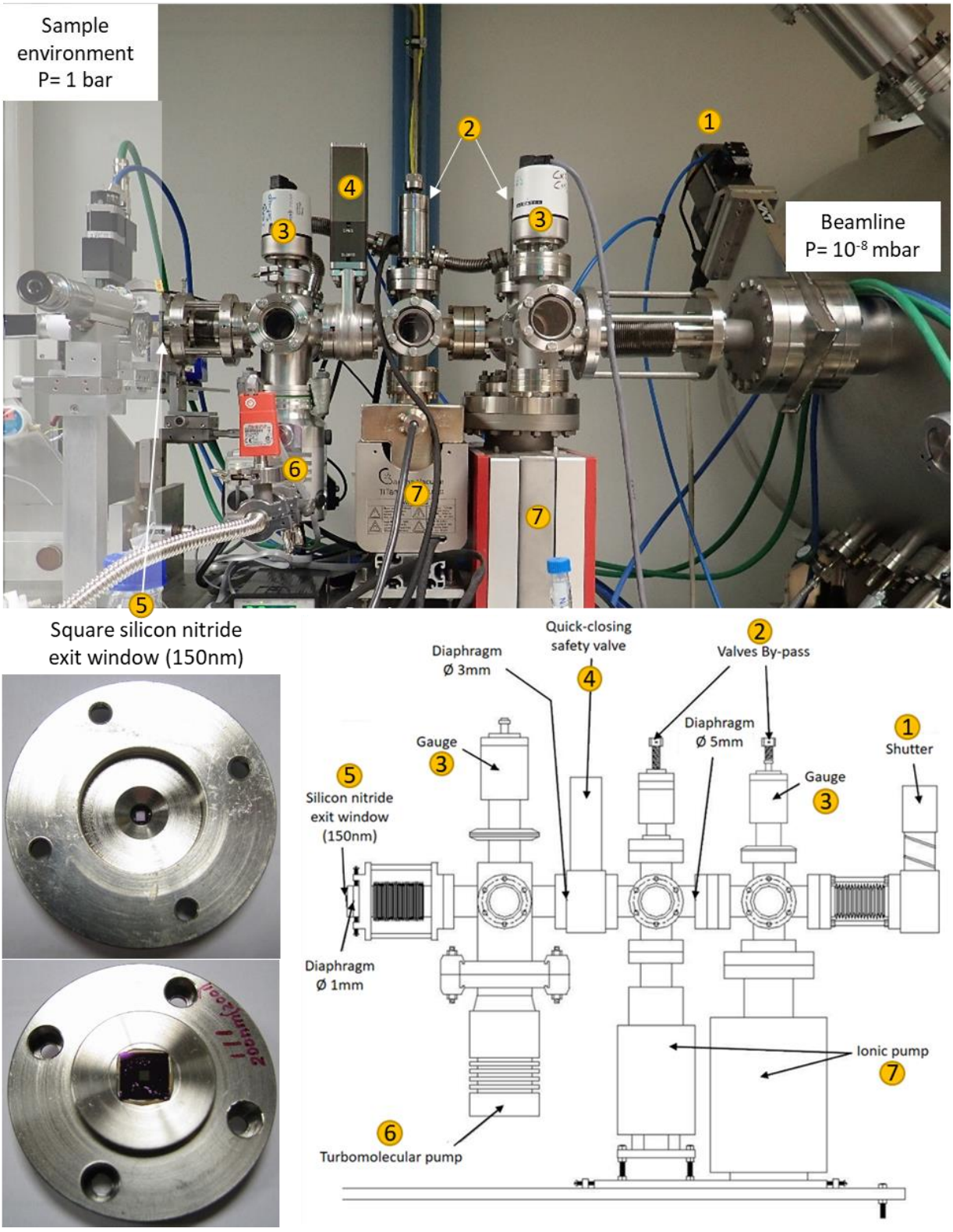

Figure III-1: Description of the installation of IRAD set-up for the extraction of METROLOGIE soft X-ray beam: photograph and scheme.

Thanks to a fixed sample holder, and the use of the same cell, experiments were easily reproducible. All irradiations were performed in aerated conditions as the top surface of the cell was in contact with air during irradiation. The dose delivered to the sample was

calculated using a photodiode (AXUV-100G Ti/C from International Radiation Detector, Torrance, California, USA) [2], [4], [5][29]; see section III.2 for more details about the sample and detector positioning. It is easily controlled by varying the time of exposure. However, the attenuation length of soft X-rays in liquid water varies from 1 to 7 µm in the 0.2 to 1.5 keV energy range, leading to very high dose rates at the surface of the 1 cm-thick sample. In order to achieve more homogeneous irradiations, we decided to reduce the liquid thickness (referred to as $h_{solution}$) by implementing a microfluidic device (illustrated in Figure III-2).

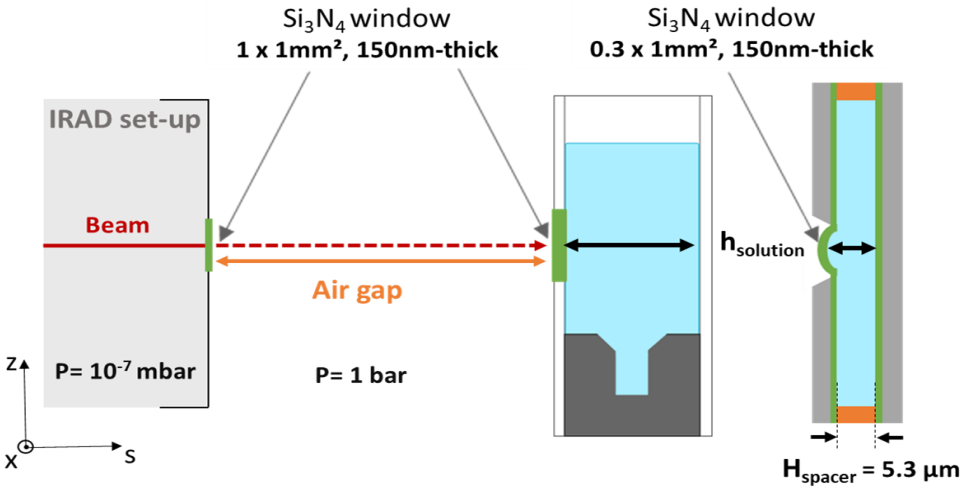

Figure III-2: Sketch of the previous and current set-up for liquid irradiation at air.

Microfluidic cells provide a reduced and well-defined sample environment leading to several advantages: sample and time saving, sequential injection of samples, control of dissolved gasses, for instance. However, the installation in front of a synchrotron beam requires new developments to ensure a perfect alignment of the micro-size window with respect to the micro-size beam. After a short presentation of the device, this chapter will introduce the different developments carried out to successfully implement the microfluidic cell on synchrotron beamlines. In particular, it will present the difficulties in terms of alignment, characterization, and evaluation of uncertainties when irradiating a liquid under static or dynamic conditions (fluid in circulation).

[29] *It must be noted that the measured signal on the photodiode with respect to the distance to the exit window allows to evaluate the contribution of high-order harmonics [36].*

III.1. Presentation of the microfluidic cell

The microfluidic device was created by Corinne Chevallard from the LIONS (CEA, Saclay), in collaboration with Charlie Gosse (ENS, Paris), Stéphane Le François and Stefan Stanescu (Synchrotron SOLEIL, Saint-Aubin)[6], [7]. The microfluidic cell was dedicated to STXM measurements and was therefore specifically designed for an installation inside the under vacuum microscope chamber of the HERMES beamline[7].

The cell consists of two silicon chips assembled in a homemade fluidic carrier that allows the liquid to flow between them. The two silicon chips are embedded between two (polymer polydimethylsiloxane) elastomers forming a sandwich (PDMS gaskets in Figure III-3). This assembly is itself embedded in a polytetrafluoroethylene (PTFE)/metal holder (Gavard, Arrou, France). A clamping system that consists of a stainless steel (SST) hollow bolt and a brass nut compresses PDMS gaskets. It ensures the complete tightness of the flow cell under hydrodynamic pressures.

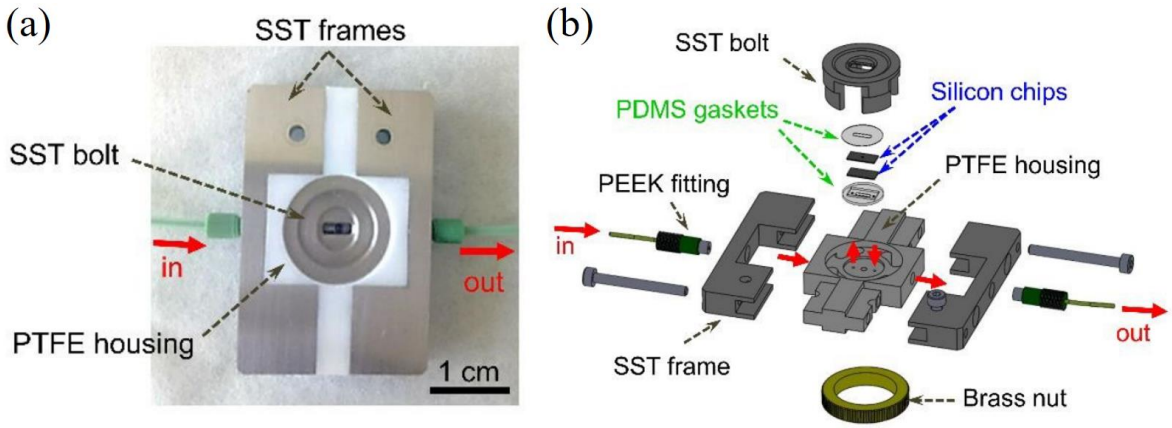

Figure III-3: Microlfuidic cell home-made holders developped by Gosse et al. (a) Microfluidic device photograph (b) Exploded view drawing. (Image from [7])

On the HERMES beamline, the beam is of nanometric size (~25 nm of diameter). Therefore the silicon nitride windows dimensions do not need to be significant. In order to work in transmission, both membranes carried windows, and the thickness of the microfluidic channel was approximately 3 µm or less. Standard windows dimensions are 0.1×0.3 mm^2 large and 50 nm thick, perpendicular one to another once the cell is mounted. This choice is motivated by the fact that the resulting square shape of the window sandwich obtained is more reproducible than the one formed by two parallel windows.

Indeed, the membranes assembly in the PDMS gaskets can induce a slight alignment difference (~2 µm) that is no more crucial when forming this square shape[7]. In order to study damage induced by soft X-ray exposure, the detection of a chemical signal requires increasing the volume of irradiated fluid. The thickness of the channel should be increased to absorb most of the beam in the sample, taking into account the attenuation length of soft X-rays in water (4.7 µm at 1.28 keV). Also, the irradiated area should be extended to the dimension of the beam. Therefore, membrane dimensions and alignment processes have been re-designed to comply with these new constraints (increasing window dimensions and the microfluidic channel thickness).

III.1.1. Silicon membranes design

III.1.1.i. Initial design

In order to increase the dimension of the irradiated area without compromising the robustness of the cell, we decided to design a cell with a single-window on the membrane facing the beam (see Figure III-4).

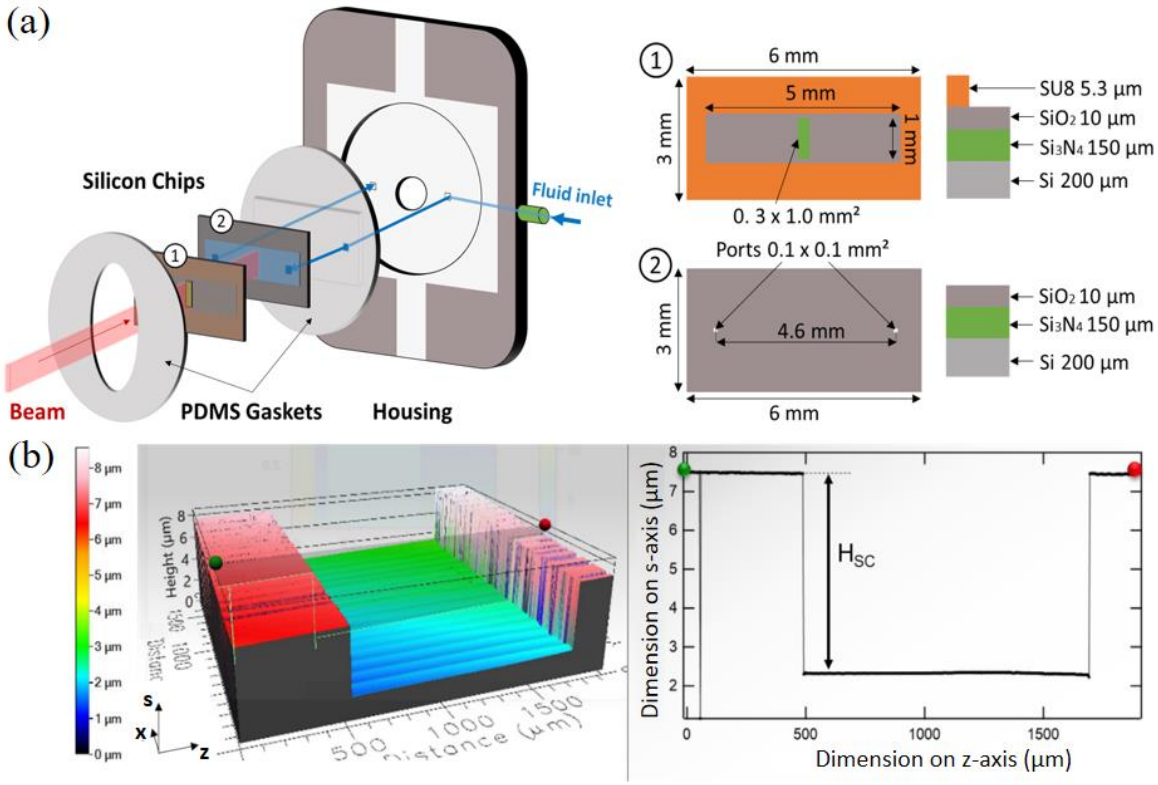

Figure III-4: Initial design of the microfluidic cell with a single window: (a) Exploded view of the microfluidic device and membranes specifications. (b) Measurement of the height of the SU-8 spacer by interferometry. Average profile was plotted in the s-z plane.

Both silicon chips (Silson, Southam, UK) are 200 µm thick and 3 × 6 mm² in size. The Si chip ① facing the X-ray beam supports a low stress (≤ 250 MPa) silicon membrane at the center, which is 150 nm thick and 0.3×1 mm² large. The silicon chip at the backside, namely chip ②, has two side holes (0.1×0.1 mm²), which allow the fluid to flow through the microchannel of the cell. The microfluidic channel is formed by a rectangular hollow spacer, made of SU-8-photoresist, carried by chip ①.

The spacer nominal thickness was 5 µm instead of 3 µm in order to increase the achievable flow rates[30] (see section III.4.2.i for more details). After reception of the order, the thickness was characterized using an optical interferometer (smartWLI Prime, Schaefer Technologie GmbH, Langen, Germany) equipped with a 20X Mirau objective (see Figure III-21 for the measurements principle). Indeed, this spacer delimits the volume of liquid enclosed between the chips during the experiment and therefore needs to be precisely characterized (see thickness measurement in Figure III-4.(b)). The microfluidic channel dimensions were found to be 1.2 mm wide, 5 mm long, and 5.3 µm thick, leading to an enclosed volume of ~32 nL. In this configuration, referred to as the "initial design", alignment cannot be performed using the transmitted light. We, therefore, needed to develop a robust protocol in order to carry out precise dosimetry.

III.1.1.ii. Transmission design

In order to implement the microfluidic cell in a vacuum chamber, it became necessary to re-design the silicon chips to carry out transmission measurements. Indeed, space constraints became limiting under vacuum, and the transmitted beam's use could considerably simplify the alignment. After validating the robustness of the initial design under vacuum, we installed a second window at the back of the cell. The first tests were conducted using a tiny window like the one already used for STXM measurements (rectangular window 0.1×0.3 mm² large and 50 nm thick). This setup allowed us to test the strength of the sandwich under vacuum (the front window dimensions remained 0.3×1 mm²). The success of these tests led us to re-design the back window to fit with the

[30] *Achievable flowrates were <10 µL/min at 1.8 bar for the STXM design using a 3 µm-thick spacer.*

dimensions of the front one. Photography and 3D-drawing of the complete sandwich of the" transmission design" are presented in Figure III-5).

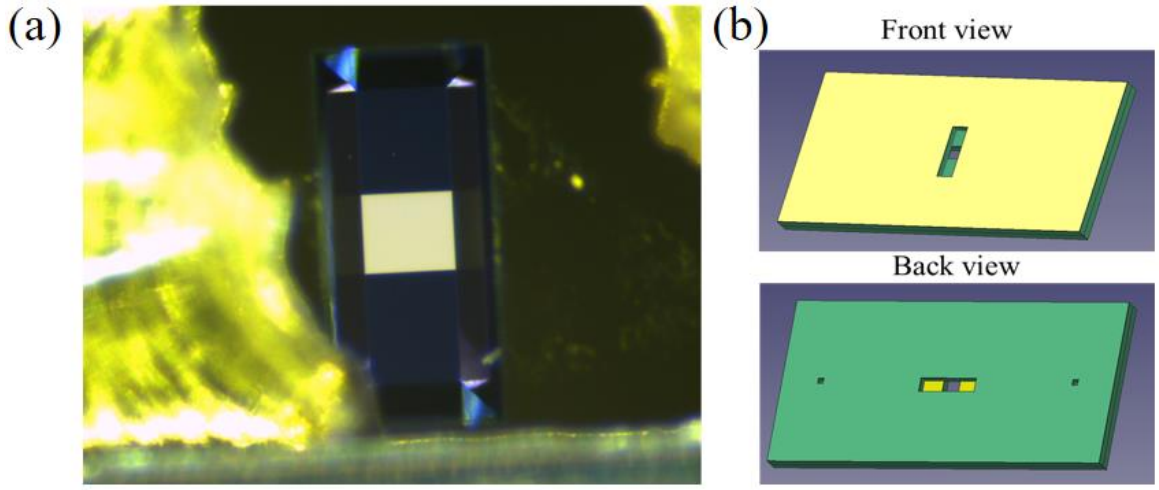

Figure III-5: New design of silicon membranes for transmission measurement: (a) Microscope picture of the resulting square, (b) 3D view of the membranes sandwich.

In this new design, the back chip carries a silicon nitride window of almost the same size as the front-one[31] but rotated by 90°. The reproducibility of the mounting was characterized using a microscope. This design is named "transmission design".

III.1.1.iii. Mounting the cell

Elastomer gaskets are made from a mixture of polydimethylsiloxane (PDMS) resin and PDMS cross-linking agent in a 9:1 ratio from the Sylgard silicone elastomer kit (Sylgard 184). The mixture is placed under vacuum (45 min), ensuring the absence of bubbles. The mixture is then poured into gasket molds and placed in an oven at 60°C for 2 to 3 days. Once de-molded, the gaskets are pierced with biopsy punches of different diameters: fluid inlets are provided by 1 mm diameter holes (2 holes) and light-transmission by a central 2 mm hole.

The cells are mounted in a dust-free environment (ISO 5 ADS Laminaire cabinet, Aulnay-sous-Bois, France) using a pair of tweezers. Contrary to common practice, the assembly is mounted in a dry state, meaning that no water droplet is initially sandwiched between the two chips. Moreover, no O_2-plasma pre-treatment is needed. Indeed, ethanol

[31] *We tested two designs: One with a back window of dimension 0.3×1 mm², the other one 0.25×1 mm².*

injection after cell mounting is very effective and much more practical than plasma exposure to prevent the formation of air pockets[8]. This solvent, having a better wettability and thus lower contact angle, helps to remove "disruptive" bubbles. Those bubbles indeed induce large flow rate fluctuations that can prevent measurements. The fluidic system facilitates this pre-filling of the cell and the subsequent replacement with the working solvent.

III.1.1.iv. Fluidic actuation

The fluidic actuation is based on a pressure regulator (MFCS-EZ, Fluigent, Le Kremlin-Bicêtre, France) that adjusts the reservoir's gas pressure. It results in an actuating pressure difference, ΔP, between the inlet and outlet of the fluid system. This device, unlike a flow controller, protects the membranes against overpressure. In this system, we are working in the range of 0 to 2 bar. It can be supplied with compressed air or any other gas bottle. Flow rate is monitored with flowmeters located downstream and upstream of the device, as presented in Figure III-6. The measurement of the flow rate is based on temperature detection. More precisely, a microheater increases locally the temperature of the fluid (around 1°C). This variation is detected on both sides of the heater. The flow rate is calculated based on the spread of the heat. Two different sizes of flow units (S or M, Fluigent) were used to allow flow measurements in the range 0.42 - 80 µL/min with an accuracy of 5%.

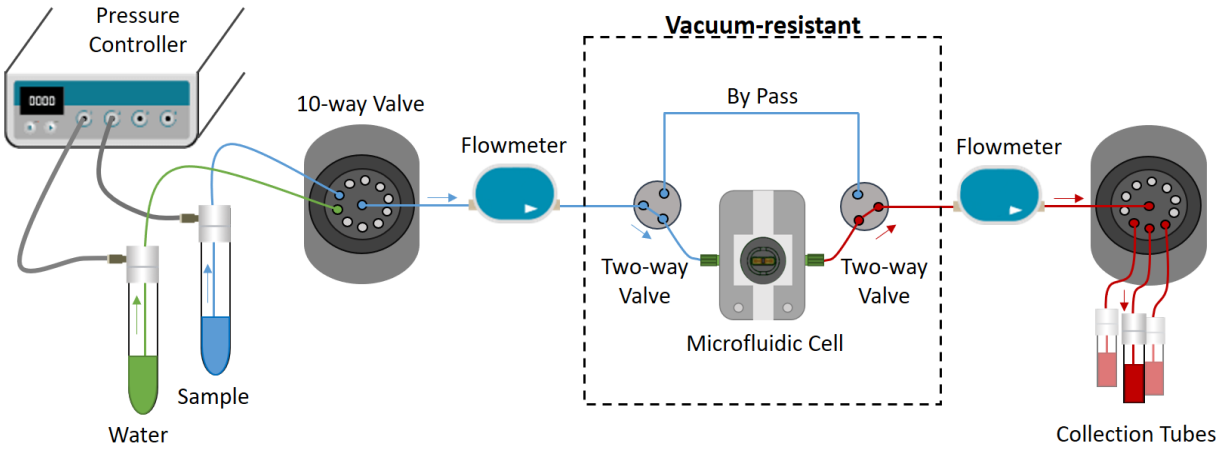

Figure III-6: Fluidic actuation of the microfluidic device.

The solution to be injected is selected using a 10-way bi-directional valve (M-switch, Fluigent), which allows the sequential injection of up to 10 different solutions. It is particularly useful for conditioning the microfluidic cell, which requires first injecting ethanol for pre-wetting the system, then water, and finally the solution to be irradiated. A second one could also be installed before the collection tubes to automate the collection of one to ten tubes. For fluid circulation, we used fluorinated ethylene-propylene (FEP) and polyetheretherketone (PEEK) tubings with an inside diameter of 0.01". Two bi-directional 2-way valves (2-switch, Fluigent) allow the fluid to by-pass the cell and, therefore, promptly renew most of the solution in the fluidic system. Indeed, according to the small cross-section of the microfluidic cell, its hydrodynamic resistance is one order of magnitude greater than the one of the by-pass capillary. The selection of the cell path, in a second step, completes the fluid renewal in the microfluidic system. All materials used have been chosen to ensure the total chemical inertness of the microfluidic system.

III.2. Setup for irradiation at atmospheric pressure

The first irradiations were conducted on the Metrologie beamline using the previously described IRAD setup (see Figure III-1). The "initial design" of the cell was used at this time carried (only one window at the front). Therefore, two detecting devices, namely a YAG:Ce crystal[32] and a photodiode, were used to perform the alignment and the beam characterization[33]. The two detectors were placed on either side of the dosimetry cell, on a standard x–z translation table (AXMO, MNT9 model, 0.2 mm precision, Brétigny/Orge, France) (see Figure III-7). Prior to mounting the entire setup on the beamline, the relative positions of the two detectors, with respect to the center of the microfluidic cell, were measured using an optical level (Wild HeerBrugg, Heerbrugg, Switzerland). Each device was additionally mounted on a one-direction manual translation stage (s-axis). Once the entire setup is installed on the beamline, these stages allow one to adjust the air gaps independently, i.e., the distance between the detecting device and the IRAD exit window. Due to the device housings, the exact air gaps were 2.2 mm for the microfluidic dosimetry cell, 3.06 mm for the photodiode, and 1 mm for the YAG:Ce crystal. Characterization of air gaps is of particular importance to determine the deposited dose[34].

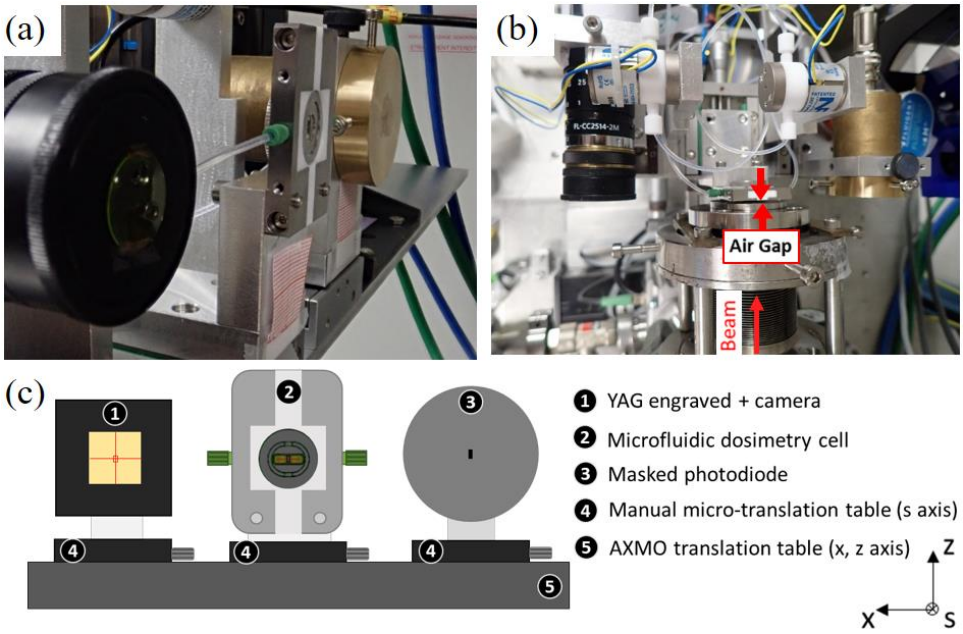

Figure III-7: Alignment devices for irradiation at air: (a) Profile view, (b) Top view, (c) Sketch.

[32] *The choice of this scintillator is detailed bellow in section III.3.4.*

[33] *Of course, they can still be used with the cell in the "transmission desgin", when experiments are performed using the IRAD set-up (for pre-alignment and dosimetry).*

[34] *Determination of the dose deposited in the sample (dosimetry calculation) will be further described in section III.4*

- Beam geometry

The first detector consists of a 50 µm-thick scintillator crystal (YAG:Ce crystal from Crytur, Turnov, Czech Republic) installed in front of a CCD camera (acA2500-20gm, Basler, Ahrensburg, Germany) (see ① in Figure III-7.(c)). It allows visualizing the shape of the extracted beam by converting X-rays to visible light. The horizontal (x) and vertical (z) axis, as well as a rectangle with the dimension of the Si_3N_4 microfluidic cell window (0.3×1 mm^2), were etched on the scintillator crystal surface to provide a spatial reference. Figure III-8 presents the different images recorded by the camera varying the exit slits of the beamline monochromator. These slits were adjusted to match the cell's dimensions along the z-axis (height of 1 mm). The use of the YAG:Ce crystal showed that, when opening the slits more than 500 µm, the shape of the beam appears distorted. Indeed, a rounded shape at the bottom right of the beam is visible. This latter was attributed to the beam interception by the diaphragms of the differential pumping stage (see Figure III-1).

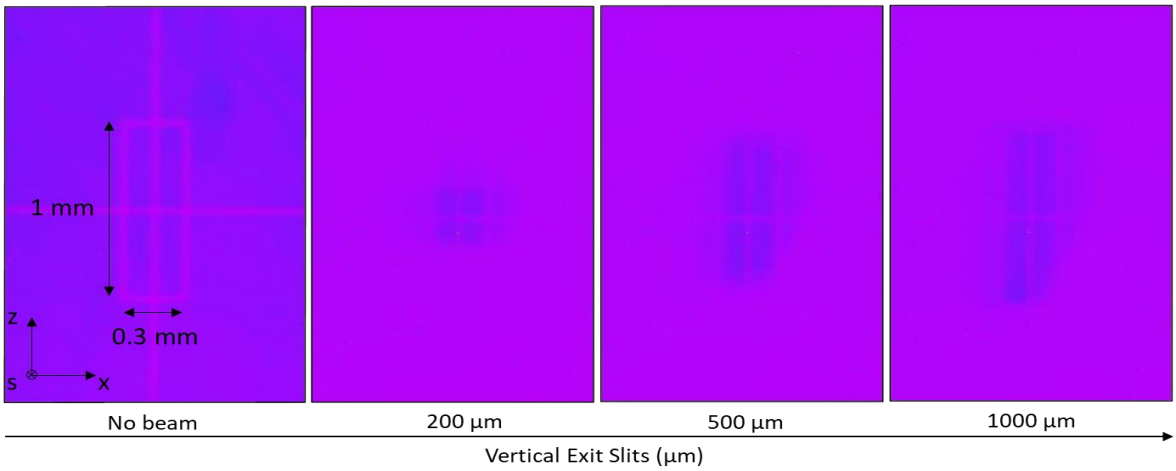

Figure III-8: Visualization of the beam geometry using the etched scintillator coupled to a camera. Photographs obtained varying the exit slits opening.

We carried out various optimizations, notably by adjusting the IRAD device's position with respect to the beam, without significantly improving this characteristic. Concerning the horizontal broadening, it remains unchanged as the optical characteristics of the beamline determine it. The use of the YAG:Ce crystal showed that opening slits more than 500 µm should not benefit the irradiation. Indeed, it seems that for 1 mm exit slits,

the vertical dimension of the beam is larger than the window's dimension and will therefore not increase the sample illumination.

- Beam alignment

On the other side of the cell, a calibrated photodiode, previously used with the static cell, was positioned to measure the beam's intensity. As the photodiode delivers a current proportional to the photon flux density values (photons/cm^2/s) integrated over the whole photosensitive area (1 cm^2), it is necessary to reduce this area according to the microfluidic cell window dimensions in order to actually quantify the photon flux (photons/s) received by the sample. The first experiments were conducted using a brass mask featuring a central rectangular hole with dimensions almost similar to the ones of the dosimetry cell window (see Figure III-9.(a)). This system also constituted a simple way to center the devices in front of the beam [9]. Nevertheless, we decided to improve this setup by directly fixing real membranes on an brass mask, as illustrated in Figure III-9.(b).

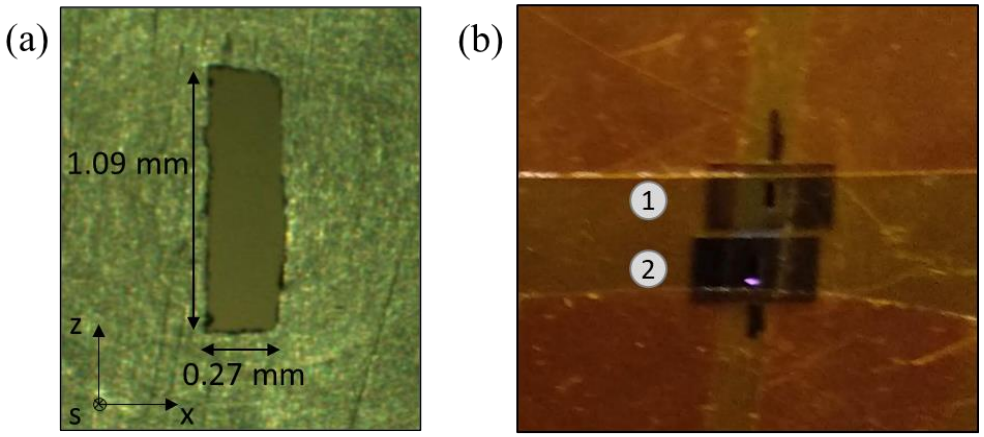

Figure III-9: Photograph of the masks mounted on the photodiode in order to mimic the cell irradiation window: (a) Drilled brass mask, (b) Silicon membranes taped to a brass mass: ① broken and ② intact membranes.

More precisely, we drilled a 2.5 mm diameter hole and fixed two membranes. The window of the upper membrane was removed using a thin needle, and fragments were removed entirely using compressed air before scotching the frame on the mask. The second window remained intact. The interest of this configuration is to estimate more precisely the photon flux at the window/solution interface, particularly by directly measuring the transmission of the silicon nitride windows.

- Beam intensity

In order to measure the dose deposited in the sample, it is necessary to measure the flux of the photon beam. This measurement is carried out using the photodiode device. At first, measurements were conducted using the drilled brass mask[9].

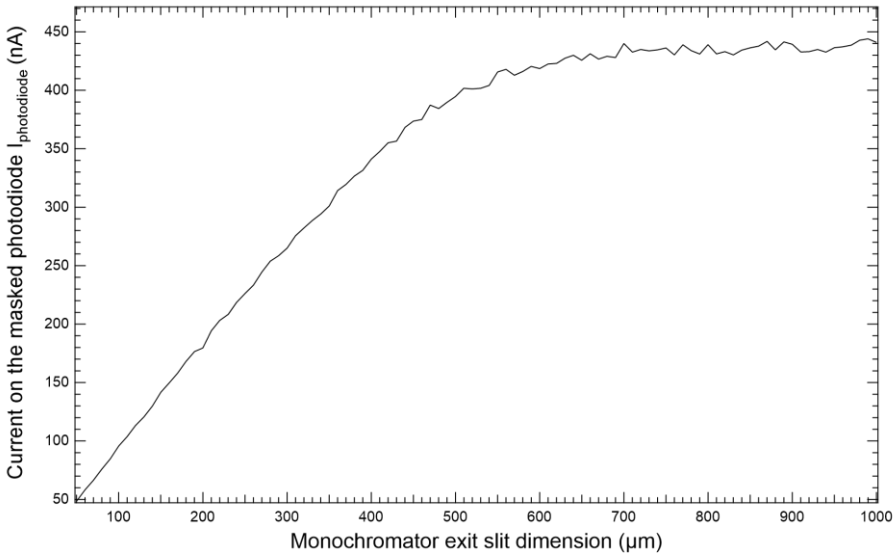

Figure III-10: Current measured at the masked photodiode as a function of the dimension of the beamline monochromator exit slit.

The current was measured by varying the opening of the monochromator slits. As observed in Figure III-10, the current increases linearly with the slits opening and reach a plateau around 500 µm. This result is consistent with the YAG:Ce observations, where the engraved area was almost totally irradiated with 500 µm exit slits (see Figure III-8). The linearity observed for 100-500 µm exit slits demonstrates the good alignment of the IRAD setup and the brass mask.

Secondly, we characterized the beam using the silicon membranes taped on the brass mask. We centered the photodiode in front of the beam and recorded the current varying the photon energy. Figure III-11.(a) presents the results obtained with the removed and intact membranes. As expected, the beam is attenuated by the silicon nitride window. The current ratio for the intact membrane versus the removed one enables us to estimate the experimental value of the transmission coefficient of the membrane. The transmission

values obtained at different photon energies were compared to the theoretical one calculated with CXRO (see Figure III-11.(b)).

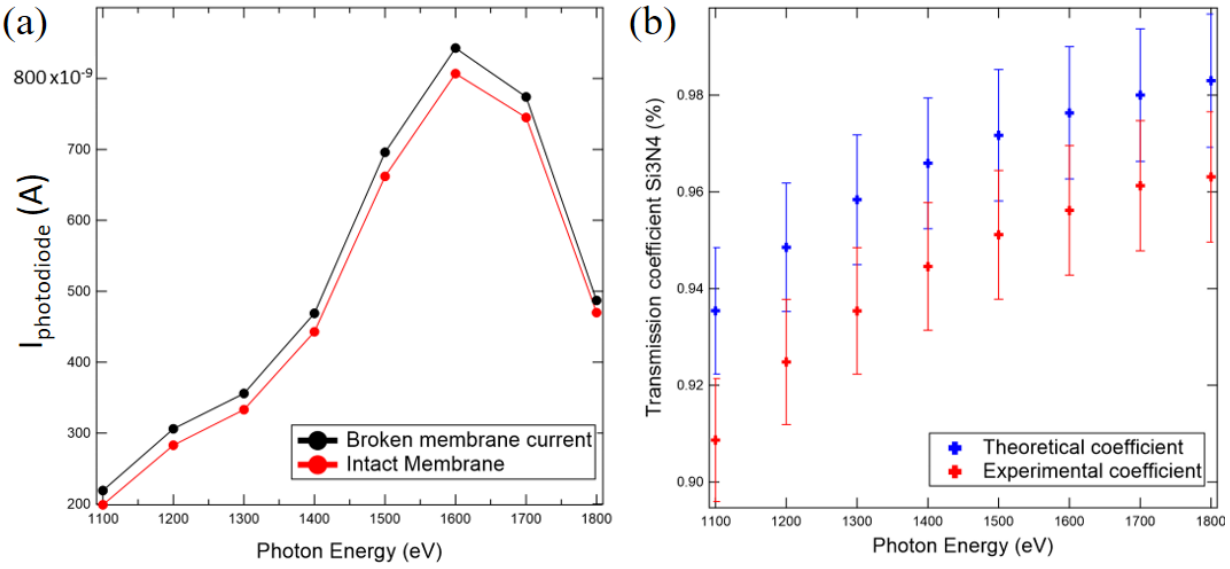

Figure III-11: Si_3N_4 membranes transmission measured on the Metrologie beamline as a function of photon energy: (a) Current measured with the photodiode carrying the two membranes (broken and unbroken), (b) Comparison of theoretical and experimental silicon nitride transmission coefficients calculated for a 150 nm-thick Si_3N_4.

The error on calculated values originates from the composition, density, and thickness of the Si_3N_4 window. It is estimated to be 1.4% at 1280 eV[9]. It has the same global effect on all calculated transmissions, except that it depends slightly on the photon energy. The uncertainty related to the alignment of each window in front of the beam is considered systematic (5,6%[9]) and is therefore not included in the error bars shown in Figure III-11. Finally, the error on the current measurement is estimated to be 3.3% [9]. Coefficients are found to be similar, taking into account all these sources of uncertainties (total error calculated using a quadratic sum) (see Figure III-11.(b)).

III.3. Setup for irradiation under vacuum

III.3.1. Implementation in a vacuum chamber

Following the validation of the microfluidic cell using the "initial design" on the METROLOGIE beamline, we decided to implement a vacuum chamber to facilitate the setup installation on different synchrotron beamlines. Indeed, the setup size is primarily reduced (<1 m large), and the coupling at the end of a beamline is direct. In addition, this setup will reduce the attenuation of the synchrotron beam, which is required to irradiate solutions at low photon energies (around the carbon, oxygen, and nitrogen K-shells). The vacuum chamber was first installed on the PLEIADES beamline, as presented in Figure III-12.

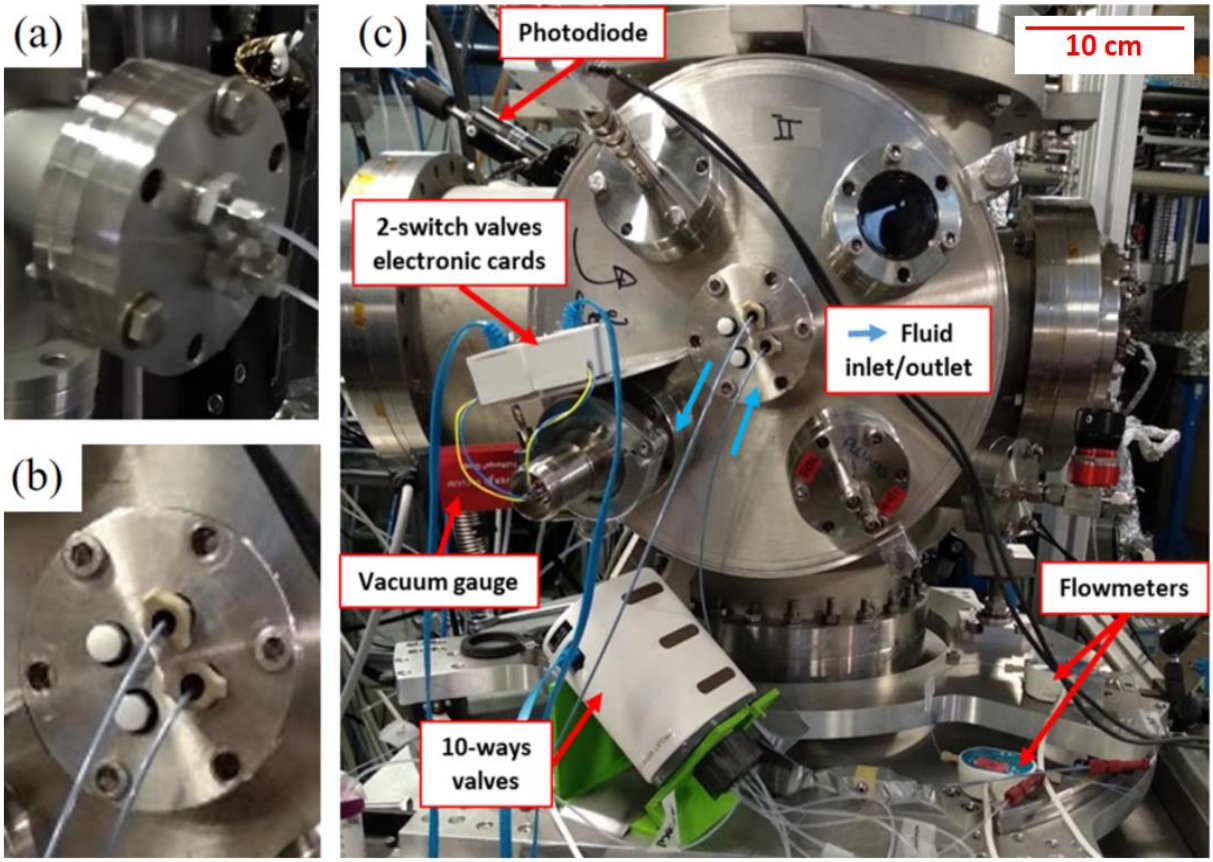

Figure III-12: Installation of the vacuum chamber on PLEIADES beamline. (a)-(b) Outlet flanges for fluidic actuation, (c) Photograph of the vacuum chamber.

Outlet flanges were specially designed for the installation of the microfluidic cell. Except for the cell and 2-switch valves for the by-pass (see section III.1.1.iv), all electronic devices for fluidic actuation are left outside the chamber. At first, we adapted Swagelok-

type screws with steel collars and Teflon, which were directly sealed on the flange (Figure III-12.(a)). However, this system was changed because it was not suitable for the recurrent dismantling of the setup. Indeed, we noticed a deformation of the Teflon capillaries due to the repeated tightening, which resulted in vacuum leaks. In order to allow an easier dismantling of the system, we installed new steel adapters, initially designed for gas inlets (CLUZEAU, Ref: Adapt 10-32 Fem ¼ - 28 Mâle). These adapters were adapted to the microfluidic capillaries' diameter by drilling the hole. This connector allows PEEK adapters to be directly screwed, making them easy to dismantle (Figure III-12.(b)). Cluzeau connectors are screwed with Viton seal guaranteeing a vacuum of about 10^{-6} mbar. The vacuum was ensured using primary and turbomolecular pumps. We performed several tests under different vacuum conditions (from 10^{-3} to 10^{-6} mbar) to control the strength of the membranes under vacuum, and we checked the tightness of the system by controlling the fluid flows.

III.3.2. Beam characterization

- Beam intensity

For installation under vacuum, the photon flux can be directly measured with the beamline characterization devices[35]. However, it is essential to refer the signal to a calibrated photodiode due to carbon deposition or aging. Therefore, a dedicated photodiode was implemented in the vacuum chamber to measure the photon flux.

- Beam geometry

The geometry of the beam was optimized using an engraved YAG:Ce crystal similar to the one presented earlier. The YAG:Ce crystal was fixed on under vacuum translation tables (Attocube nano-motors, x-, s- and z-axis). The YAG:Ce position was aligned with the beam. Then, we followed the beam geometry at the sample plane while moving the exit slits of the monochromator (see Figure III-13). One must know that in order to be able to move freely, the weight fixed on these tables must not exceed 120 g. This criterion

[35] *The beam dimensions were always kept smaller than those of the microfluidic cell window for experiments performed on the PLEIADES beamline.*

prevents the installation of sizeable electronic detection devices such as photodiodes or Faraday cages directly on the translation tables. Therefore, the beam optimization on the YAG:Ce was made possible by installing an external camera on a window of the vacuum chamber[36]. As observed in the photographs, the geometry of the beam is easily adaptable by varying the monochromator exit slits. The YAG:Ce etchings allow adjustment of the beam shape to the dimensions of the microfluidic cell window.

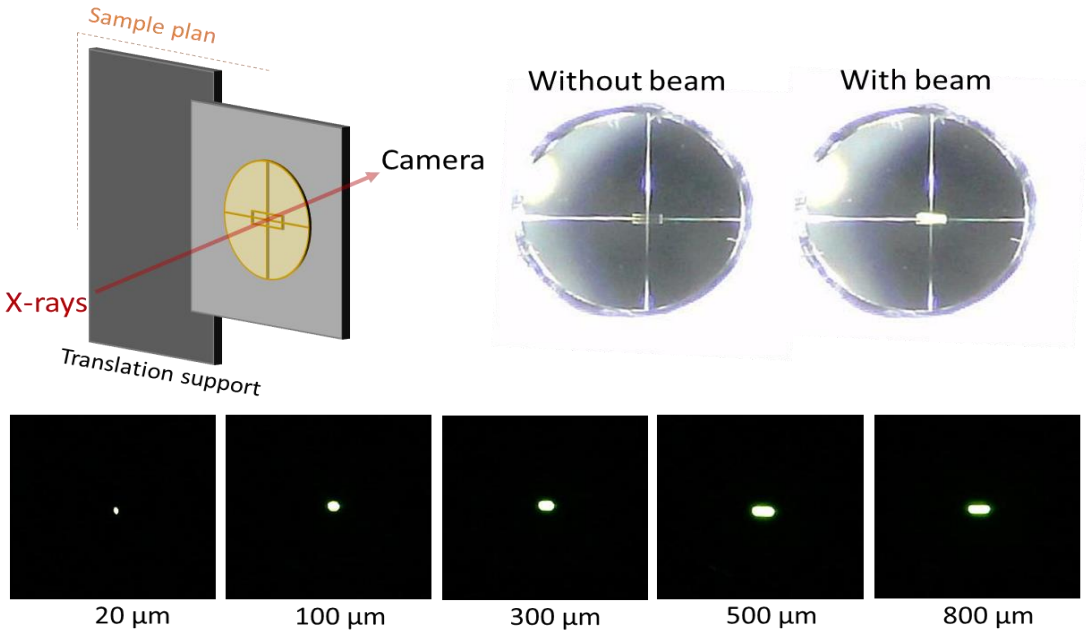

Figure III-13: Optimization of the beam geometry under vacuum: Installation of a YAG crystals etchings with the same dimension as those of the microfluidic cell window (0.3×1 mm²), on the translation table and visualization on a camera. Photographs of the beam image on the YAG:Ce crystal are presented varying the monochromator exit slits.

III.3.3. First under-vacuum alignment

The first tests for under vacuum irradiations were conducted using the "initial design" of the cell, which carried only one window at the front (section III.1.1.i). It was, therefore, necessary to develop systems to align the cell with the synchrotron beam. In order to translate the cell under vacuum, the cell was mounted on the same under vacuum translation tables as the YAG:Ce crystal (see section Beam characterizationIII.3.2). These tables allow a stroke of 6 cm along the vertical axis and 3 cm along the horizontal axis, with a precision of 10 nm. These tables, electronically controlled, ensure the stability of

[36]*Another reason is that the camera was not suitable for vacuum conditions.*

the position by active control of the motors. In addition, an internal reference system allows accurate position retrieval.

Our first setup is presented in Figure III-14. A circular carbon tape was placed on the Stainless steel bolt surrounding the opening of the microfluidic device. Salicylate salts were deposited on it to visualize the beam (when illuminated, salicylate salts emit a visible violet light[10]). In addition, a silicon nitride membrane, whose window was previously removed, was taped to the Teflon support of the microfluidic device. The hole was then filled with salicylate salts. We carefully referenced the two windows' positions to allow relative alignment once the device was installed in the chamber.

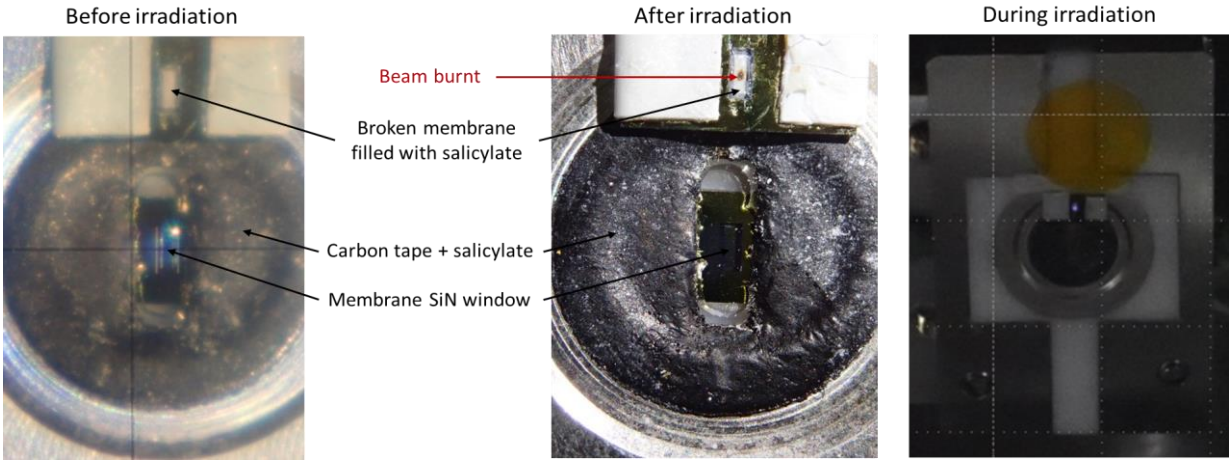

Figure III-14: Photograph of the first setup developed to perform under vacuum alignment of the microfluidic cell with respect to the synchrotron beam: Carbon scotch tape and salicylate salts are used to visualize the beam (purple light visible during irradiation). A broken membrane, filled with salicylate salts, alows to center the device.

This device allows a first rough alignment on the carbon tape and then a more precise alignment on the window thanks to the removed membrane, which allows visualizing the window's size. Although successful, this setup does not allow the alignment process to be repeated, as shown by the surface condition of the salicylate burnt by the beam exposure. However, it has proven the high resistance of the silicon nitride window under the synchrotron beam (PLEIADES beam flux ~10^{12}-10^{13} ph/s). Therefore, we decided to install a second window of silicon nitride at the back of the first one to be able to work in transmission (see "transmission design" section III.1.1.ii).

III.3.4. SiPM-based transmission detection device

III.3.4.i. Principle

Thanks to the new design of the microfluidic cell, it was possible to work in transmission. Therefore, we developed a specific setup using a silicon photomultiplier (SiPM) to work in transmission. This setup will be referred to as the SiPM-based transmission detection device.

SiPM are known for their high sensitivity (possibility of single-photon detection), small size, light weight (less than 30 g with the electronic card), and their accessible prices, which makes them a tool of choice for this type of technical development. Two sizes of SiPM cells were chosen PM11xx-WB (1 mm² surface area composed with 25 µm pixels) and PM3315-WB (3 mm² surface area with 15 µm pixels) for a broad reading range (all technical details can be found on KETEK product Data Sheets[11]). SiPM are only sensitive to UV-Vis light and must be coupled with a scintillator to convert the X-ray beam into visible light. The scintillator was chosen according to its absorption in the soft X-ray range (200 eV - 2 keV) and according to the sensitivity of the SiPM evaluated by its photo-detection efficiency[37] as presented in Figure III-15 (data from [12][13]). Crystals of YAG:Ce crystal exhibit excellent characteristics for soft X-rays detection. A crystal was therefore implemented in front of the SiPM.

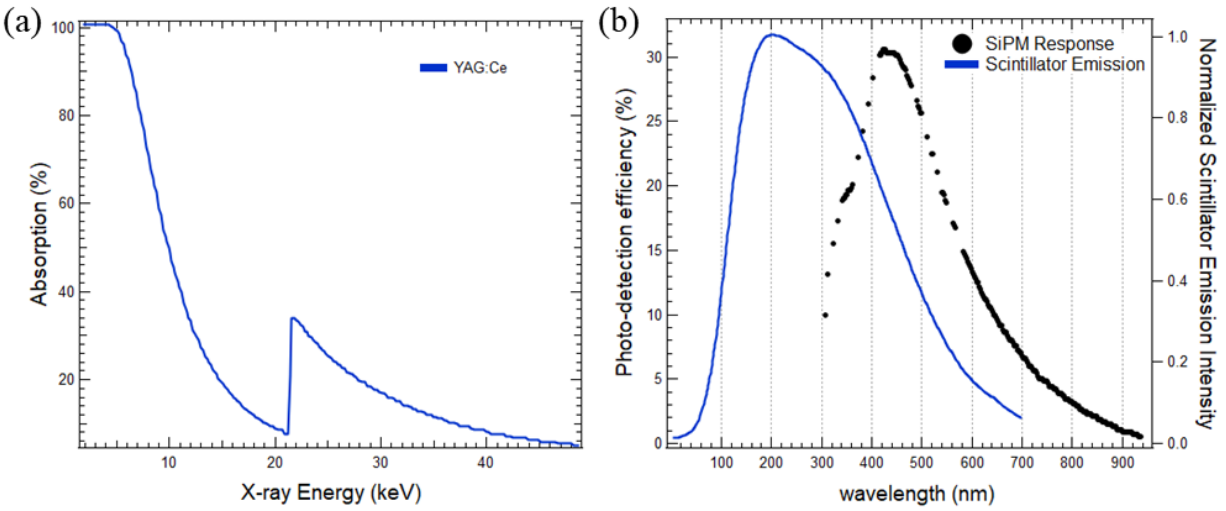

Figure III-15: Spectral properties of the scintillator and the SiPM: (a) absorption spectra of the scintillator varying the photon energy, (b) emission spectra of the scintillator (blue curve) and SiPM response (black curve) as a function of the wavelength. (data from [12][13])

[37] *See Appendix I for more details about SiPM.*

SiPM are connected to Printed Circuit Board (PCB), known as PEPCB-EVAL, of two different models. The first model (RES-P) presents two sockets: one for the bias voltage and one for the signal (given in direct current). The second one (MCX-P) presents three sockets: the bias voltage, the signal output, and the monitor. The readout is alternative current and is therefore adapted for count rates. The monitor path corresponds to 10% of the initial SiPM signal and is therefore helpful in the case of high photon flux. An amplifier can also be used in the opposite case. Except for the electronic cards connected to the SiPM, all electronic components are left outside the vacuum chamber to avoid overheating. In order to implement the couple SiPM/scintillator crystal at the back of the cell, homemade holders were specifically designed (see Figure III-16).

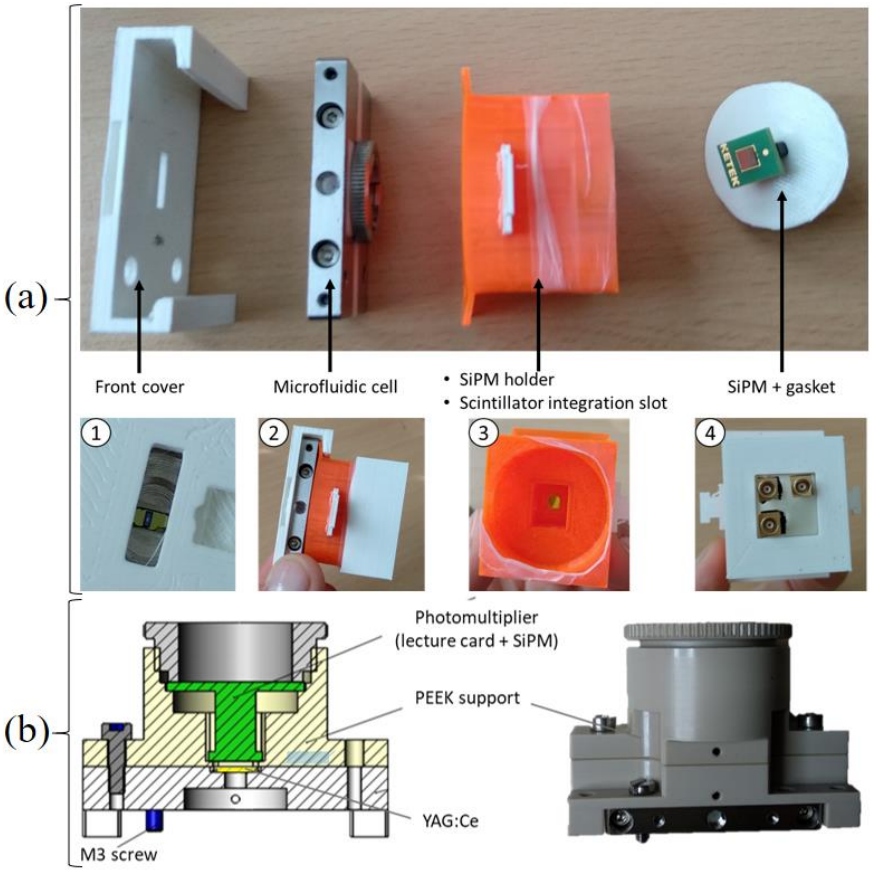

Figure III-16: Implementation of the SiPM-based transmission detection device: (a) First 3D-printed polymer holder: ① Front view, ② Profile view, ③ Inside view, ④ Back view. (b) Final design of the holder: sectional view and photograph of the PEEK support.

The first version was homemade and printed in polylactide by 3D printing. A set of interlocking parts constitutes it. The SiPM is then directly inserted at the back of the holder and maintained with a homemade seal and a cover. The YAG:Ce crystal is

integrated at the front of the SiPM, thanks to a slot in the body of the holder, designed for this purpose. The holder then fits onto the microfluidic cell. The whole assembly is maintained by a cover that slides into the front of the cell. The latter has holes to access the cell's mounting holes and allow fixation to the translation tables' holder. An integrated slot in the cover allows the insertion of a scintillator visible from the front side (see Figure III-16.(a)). Thanks to it, the beam can be easily detected by eye. By observing from outside the vacuum chamber, it is therefore easy to perform a rough alignment. After a few tests under vacuum, the final design was developed in collaboration with Stéphane Lefrançois (Synchrotron SOLEIL, SMIS beamline). The final piece was machined in PEEK by the GAVARD society. This material is indeed highly compatible with vacuum conditions and offers excellent robustness. This design has added holes to ensure the outgassing of potentially trapped air pockets during the pumping stage. The main difference between the two designs is the overlapping of the parts that are now screwed together. It allows specific parts to be detached independently. In particular, it is possible to change the SiPM chips or electronic cards without dismantling the whole setup from the translation tables when the cell is mounted. Once installed under vacuum, the whole setup (translation table, microfluidic cell, and transmission detection device) is spatially optimized, as illustrated in Figure III-17.

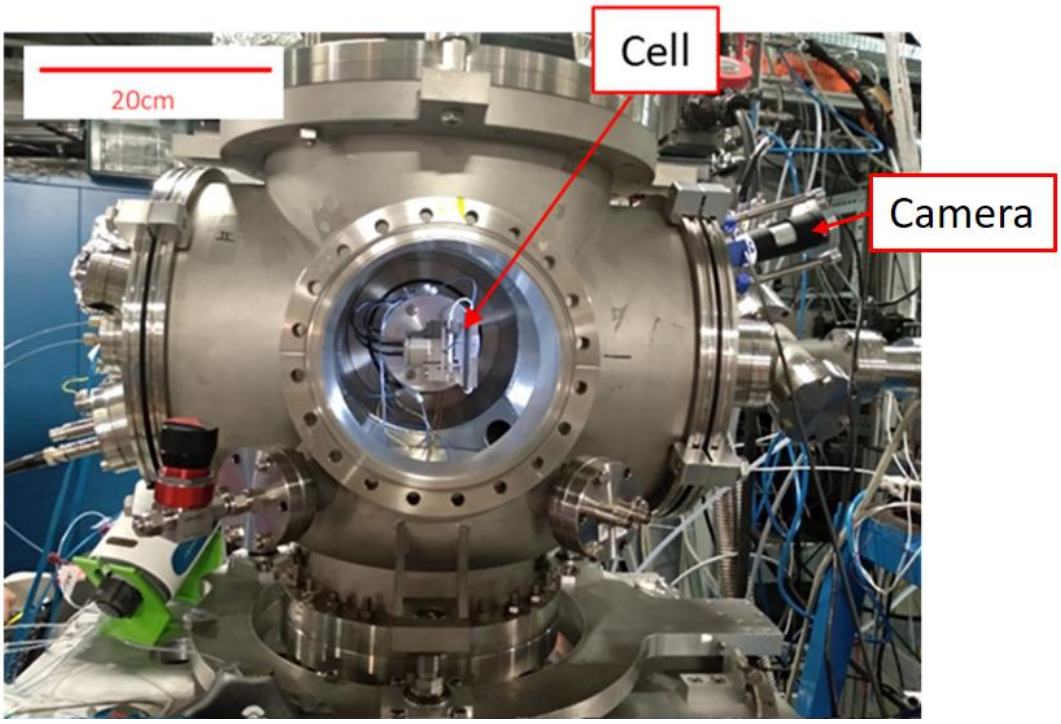

Figure III-17: Installation of the set-up under vacuum.

III.3.4.ii. Proof of concept at Air

The SiPM-based transmission detection device was first validated at the air. Such experiments were performed on the Metrologie beamline using the IRAD setup and the brass mask with the two membranes described in the section III.2. The photon flux was measured on the masked photodiode at 1.28 keV photon energy with 500 µm exit slits.

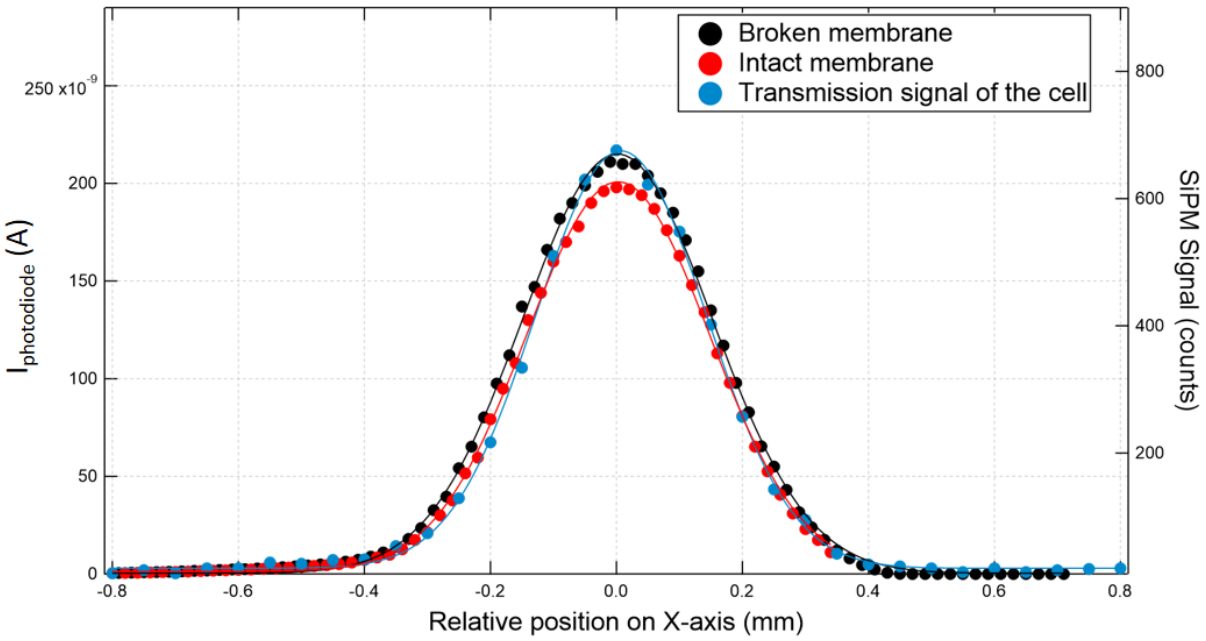

Figure III-18: Validation of the SiPM-based transmission detection device: Current measurement through broken and intact membranes using the brass mask on the photodiode and comparison with the signal measured by the SiPM placed at the back of the empty microfluidic cell.

Figure III-18 compares the signal measured along the X-axis through the removed and the intact membranes on the photodiode and the one obtained by the SiPM setup[38]. A Gaussian function well fits these data. This Gaussian shape likely results from the convolution of a Gaussian (corresponding to the beam profile 230 µm) with a 0.3 mm rectangle function (corresponding to the microfluidic window). It suggests that the FWHM of the beam profile is higher than 300 µm (silicon nitride window width)[14]. The FWHM of the transmitted beam is perfectly similar to the one measured on the photodiode. It, therefore, demonstrates that the response of the SiPM+Scintillator in this range of photon flux (~10^9-10^{10} ph/s) is linear.

[38] *Measured through the empty microfluidic cell.*

III.3.4.iii. Under-vacuum alignment procedure

Once the SiPM-based detection device developed, alignment was performed directly using the transmitted beam. The cell was emptied of all liquid (filled with air) to maximize the signal (to limit the attenuation in the cell's channel). Scanning horizontally (X-axis) and vertically (Z-axis), it is possible to reconstruct a 2D map of the transmitted beam. Horizontal and vertical profiles can be extracted from this image to determine the beam's centered position in the cell (Figure III-19).

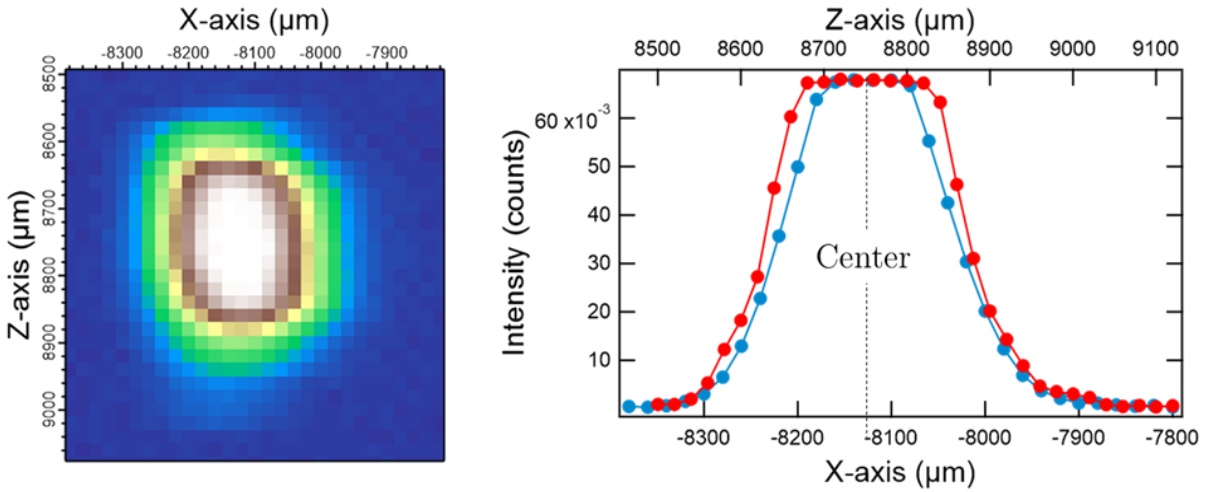

Figure III-19: Alignment of the cell using transmission beam signal on SiPM: 2D map and extracted profiles on X-axis (blue curve) and Z-axis (red curve). Data were acquired at 800 eV with 500 µm exit slits, 100x300 µm² back window, empty cell.

Simple 1D scans can be performed along both directions to control the stability of the beam once the cell is centered. Such quick scans (~2 min to 5 min, depending on the resolution chosen) are particularly interesting as the beam's position can vary with the photon energy. This procedure can thus be performed several times during the experiment.

III.4. Dosimetry and factors of influence

III.4.1. Definition

As mentioned in the introduction, the absorbed dose, D, is defined as the energy deposited in the system per unit of mass. The dosimetry process consists in determining the dose. It can be based on physical measurements (for instance, using a photodiode) or chemical measurements (using a calibrated chemical dosimeter). This section details the calculations performed using a photodiode to determine the dose deposited in this project's irradiation setups.

- Using the static cell

When irradiating a solution in the static cell, the dose is inhomogeneously deposited in the liquid, owing to the exponential decrease of the beam intensity through the centimeter-thick sample. One can then consider an average dose, which corresponds to the total number of photons absorbed in the solution divided by the mass of the irradiated solution. This average dose can be calculated using the following equation:

$$D = \frac{E \cdot \Delta\varphi_{solution} \cdot \Delta t}{m} = \frac{E \cdot \Delta\varphi_{solution} \cdot \Delta t}{\rho_{solution} \cdot V_{solution}} \qquad \text{(III-1)}$$

Where E is the photon energy of the beamline, $\Delta\varphi_{solution}$ is the number of photons absorbed per unit of time in the solution, Δt is the exposure time, and the mass of sample irradiated (m) can be expressed as the product of the volumetric mass density ($\rho_{solution}$) by the volume ($V_{solution}$) of the solution. Among the different parameters of Equation (III-1), $\Delta\varphi_{solution}$ is the only one that cannot be straightforwardly measured. However, it can be deduced from the flux measured at the photodiode surface ($\varphi_{photodiode}$), taking into account the absorption properties of the different materials the beam goes through[15]. It results in the following equation:

$$\Delta\varphi_{solution} = \varphi_{photodiode} \cdot T_{Si3N4} \cdot T_{air} \cdot (1 - T_{solution}) \qquad \text{(III-2)}$$

where T_{Si3N4} is the transmission factor through the static cell's Si_3N_4 window, $T_{solution}$ is the transmission of the solution (equal to zero in a centimeter-thick sample, in the case of soft X-rays), and T_{air} is the transmission factor resulting from the air gap between the photodiode and the irradiation cell (see Figure III-2). Transmission coefficients can be directly calculated using the NIST website (values from [3]), but this requires perfect setup knowledge. The dose rate, which is the dose absorbed per unit of time, was calculated for

different conditions of irradiations using the static cell (containing 1 mL of the sample) and the IRAD setup on the METROLOGIE beamline (irradiation at air)[39]. Typical obtained values are presented in Table III-1.

Table III-1: Typical values of dose rates for given photon energies using the static cell.

E (eV)	Average dose rate (Gy/min)	Attenuation length in water (µm)	Surface dose rate (kGy/min)
215	$8.33 \cdot 10^{-4}$	0.95	2.9
350	$2.49 \cdot 10^{-3}$	3.3	2.5
400	$2.10 \cdot 10^{-3}$	4.7	1.5
1280	0.138	4.7	200

Surface doses can be estimated by taking into account the linear attenuation coefficient of the solution ($\mu_{solution}$) and the area of the photon beam (S) at the sample position:

$$D_S = D \cdot \frac{\mu_{solution} \cdot V_{solution}}{S} \quad \text{(III-3)}$$

S is estimated to be 0.3 mm² below 400 eV and 0.15 mm² at 1280 eV[5]. As illustrated in Table III-1, the low penetration of soft X-rays (1-5 µm) leads to very high dose rates at the sample's surface. In order to perform more homogeneous irradiation, the volume of the solution was reduced to reach a thickness in the micrometer range, thanks to the development of the microfluidic cell.

- Using the microfluidic cell (Dynamic conditions)

The flow is a pressure-driven Poiseuille flow with a parabolic profile in the microfluidic channel in both the s and z directions[16]. The mean exposure time, Δt, can be expressed in terms of the mean velocity of the fluid passing in front of the beam, which in turn is related to the volumetric flow rate, Q. The previous Equation (IV-4) becomes:

$$D = \frac{E \cdot \Delta\varphi_{solution}}{\rho_{solution} \cdot Q} \quad \text{(III-4)}$$

The flowmeter can directly measure the flow rate. Therefore, similarly to the previous case, $\Delta\varphi_{solution}$ can be calculated using Equation (III-2). Typical doses achieved with this

[39] *The static cell's window was positioned 3.525 mm (resp. 1.525 mm) from the IRAD setup's exit window at 1280 eV (resp. below 400 eV).*

setup at air (METROLOGIE beamline) or under vacuum (PLEIADES beamline) are presented in Table III-2.

Table III-2: Typical values of dose rates for given photon energies using the microfluidic cell

E (eV)	Photons flux at the photodiode's surface (ph/s)	Flow rate (µL/min)	Average Dose (kGy)
400	~$1 \cdot 10^{13}$ (PLEIADES)	5	~4
800	~$7 \cdot 10^{12}$ (PLEIADES)	5	~3
1280	~$7 \cdot 10^{9}$ (METROLOGIE)	5	~0.03

According to the much higher photon flux on the PLEIADES beamline, average doses are in the kGy range. However, the monochromaticity of the photon energy is not guaranteed as no higher-order filtering is available, contrary to the METROLOGIE beamline. It must be noted that the passage under vacuum removes the absorption factor (T_{air} in Equation (III-2)) and can lead to an increase of ~30% of the dose at 400 eV (considering an air gap of 1 mm).

III.4.2. Characterization of the microfluidic cell parameters

III.4.2.i. Hydrodynamic parameters

As stated above, the flow rate controls the exposure time during dynamic irradiations, i.e., when the fluid is in circulation. This parameter must therefore be precisely characterized. The flow rate was measured as a function of the actuation pressure for various concentrations of benzoate solutions. Results are presented in Figure III-20.

A typical flow rate in the microchannel of the cell is 13 µL/min when injecting a solution with a low benzoate concentration (10 mM) or pure water, with an actuation pressure of 1 bar. To obtain the same flow rate for higher benzoate concentrations, we need to apply a larger actuation pressure difference ΔP, meaning that the hydrodynamic resistance increases. Experimental data can be fitted with a linear equation:

$$\Delta P = R_{tot} * Q \quad \text{(III-5)}$$

Where R_{tot} is the total hydrodynamic resistance of the fluidic system.

The viscosity of each solution was determined using an Ostwald viscometer. This U-shaped glass capillary viscosimeter is used to measure the time taken for a volume of liquid

to flow down through a capillary. The measured time is directly proportional to the kinematic viscosity (η) using a conversion factor that depends on the viscosimeter. We used a viscosimeter with a nominal constant of 0.00948 (mm^2/s)/s (adapted for kinematic viscosity ($\nu = \eta/\rho$) ranging from 0.3 to 1 mm^2/s). Measurements were performed on solutions at room temperature (21.3°C). Determined values of η were 0.995, 1.004 and 1.106±0.002 mPa.s, for the three solutions tested (0.01 M, 0.1 M and 1 M, respectively).

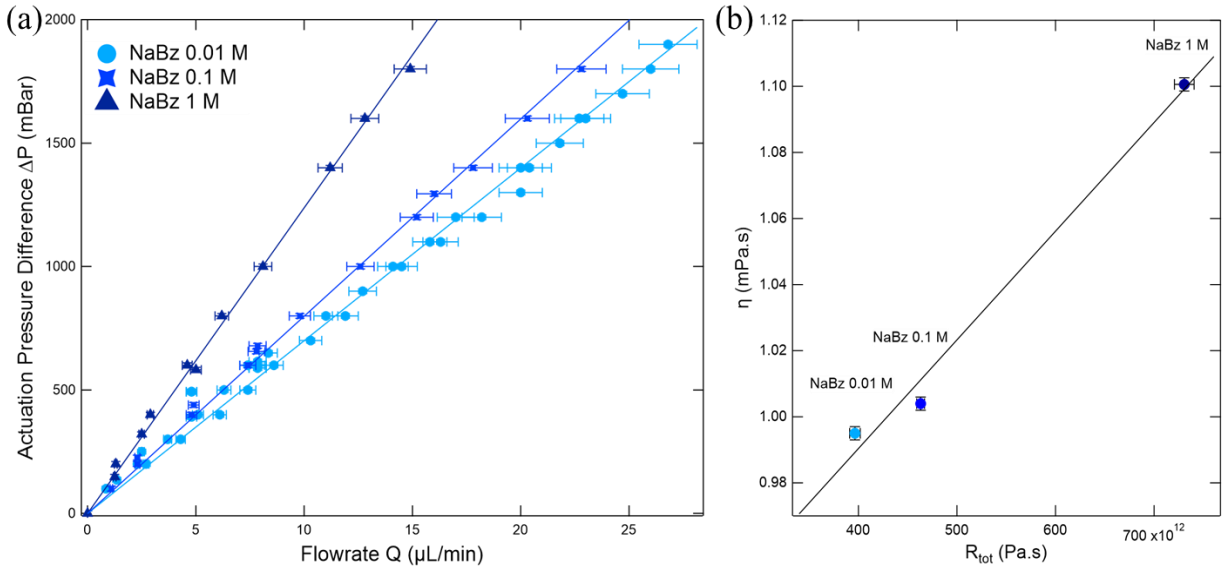

Figure III-20: Hydrodynamic parameters of the microfluidic cell measured for different sodium benzoate concentrations: light to dark blue correspond to 0.01 M, 0.1 M and 1 M: (a) The actuation pressure difference (ΔP) as a function of average flowrate value (Q) reported by upstream/downstream flowmeters, (b) Experimental viscosity measured by an Oswald viscosimeter (error of 0.006 mPa.s) plotted as function of the deduced hydrodynamic resistance R_{tot}. Data are fitted with a linear regression.

For a given microfluidic actuation setup, all internal diameters of microfluidic devices (capillaries, flowmeters, valves) are perfectly known. Therefore, for each element, the theoretical hydrodynamic resistance can be calculated [16]. Inside tubings and devices (valves, flowmeters), presenting a circular cross-section of diameter D and length L[40], the hydrodynamic resistance is expressed as:

$$R_{th} = \frac{128\eta L}{\pi D^4} \qquad \text{(III-6)}$$

[40]*Even if some portions of the fluidic circuit are not circular (in commercial devices in particular) the dimensions remain very large compared to those imposed by tubings and the microfluidic cell and thus induce a very small error on the calculation of the resistance.*

Inside the microfluidic cell, where the cross-section is a rectangle of width W and height H, it is expressed as:

$$R_{th} = \left[\frac{12\eta L}{WH^3}\right] \cdot \left[\frac{1 - 192H}{\pi^5 W}\right]^{-1} \quad \text{(III-7)}$$

The values obtained in our assembly are presented in the following table (all parameters are detailed in Appendix II.1). These values can be compared with the experimental hydrodynamic resistance ($R_{tot}(experimental)$) deduced from the slope of experimental curves (see Figure III-20).

Table III-3: Experimental and theoretical values of hydrodynamic resistance and the relative difference between both.

	R_{tot}(theoretical) $(Pa.s)$	R_{tot}(experimental) $(Pa.s)$	**Relative difference**
NaBz 10 mM	4.17 E+14	3.97 E+14	2.5%
NaBz 100 mM	4.44 E+14	4.63 E+14	2.1%
NaBz 1 M	4.86 E+14	7.31 E+14	20.1%
Water (via By-Pass)	4.71E+13	4.02 E+13	7.9%

We observe that the relative difference between those values is less than 10%, except for the highest concentration (NaBz 1 M). Therefore, the theoretical model constitutes an excellent approximation to estimate the expected experimental values and check that the circuit is working correctly. The difference for the highly concentrated solution is not fully explained. Indeed, the flow-sensors error is estimated to be less than 5% by the constructor. We checked the consistency of this value (5% on flow rates) by weighing samples of different concentrations collected at different flow rates and comparing them to the volume indicated by the flowmeter (data not shown). In this project, we will only consider this uncertainty in the error bars for all solutions injected.

III.4.2.ii. Membrane bulging

The microfluidic device was designed with a thickness H_{spacer} of 5.3 µm (see Figure III-2 and Figure III-4) to perform homogeneous irradiation. Nevertheless, thin Si_3N_4 windows experience some bulging under the applied hydrodynamic pressure. Therefore, the fluid thickness ($h_{solution}$) becomes greater than H_{spacer} almost everywhere. This bulging influences the number of photons absorbed in the solution (see Equation (III-2))

and thus the dose (see Equation (III-4)). The deformation of the membrane was therefore characterized using an optical interferometer (smartWLI Prime, Schaefer Technologie GmbH, Langen, Germany) equipped with a 20X Mirau objective.

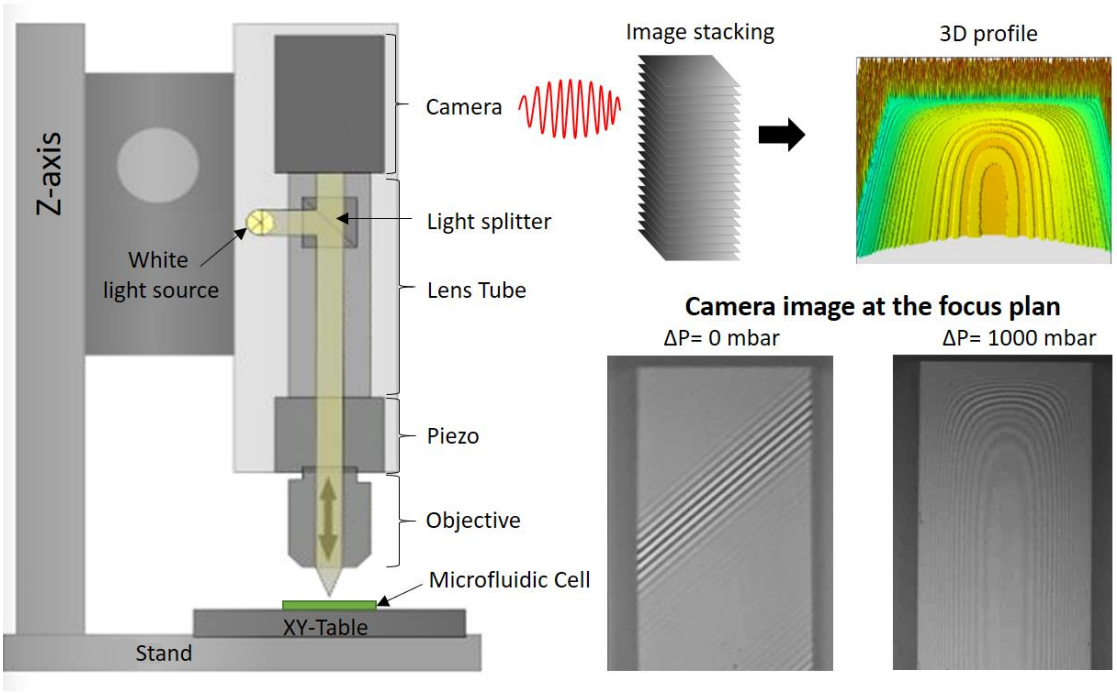

Figure III-21: Vertical interferometry measurement principle: a white light source, split in two parts by a partially reflecting mirror, illuminates the reflective sample. A fringe analysis at different vertical positions allows to detect any variation on the sample surface.

As illustrated in Figure III-21, parallel fringes are observed in the case of a perfectly horizontal surface (image at actuation pressure ΔP=0 mbar). However, the fringes vary according to the bulge of the membranes (image at ΔP=1000 mbar). The camera moves in equidistant steps along the Z-axis (vertical axis) using a piezo motor. The stacking of the images allows the reconstruction of the 3D profile of the surface.

By scanning the Si_3N_4 window at a given flow rate Q, i.e., a given actuation pressure difference ΔP, the profilometer provides a 2D map of the bulging Figure III-22.(a). The profile along the z-axis testifies to the homogeneous deformation of the membrane (for -300 < z < 300 µm). Transverse deformation profile at the center (z = 0) of the membrane ($h_{solution} = H_{spacer} + h_{\Delta P}$) can, in particular, be extracted from this map. The profile along the x-axis (Figure III-22.(c)) can be fitted with a parabolic function in a first approximation[17], [18]. It allows determining the maximum deformation value $h_{\Delta P max} = h_{\Delta P(x=0,\ z=0)}$.

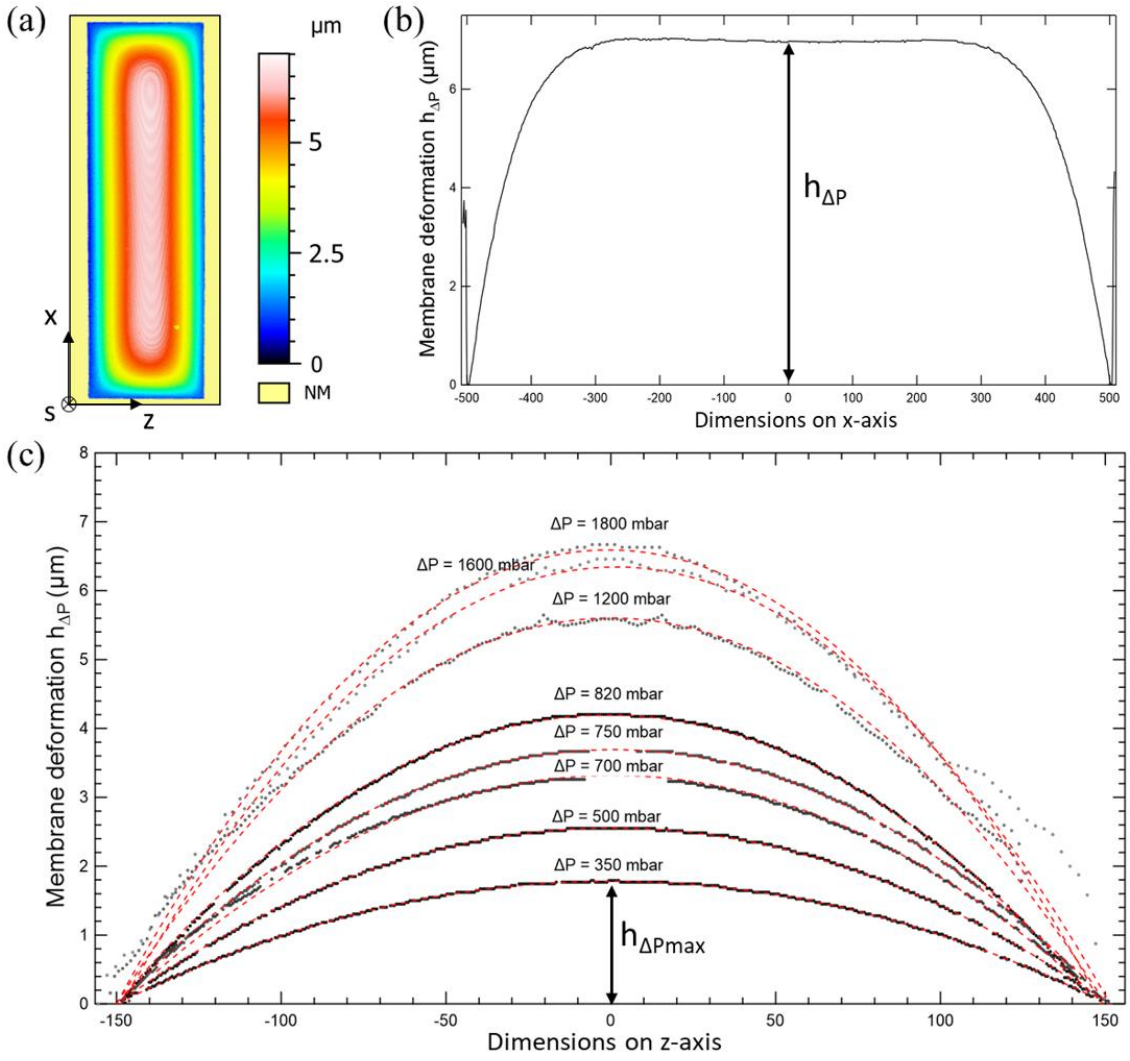

Figure III-22: Characterization of the Si_3N_4 membrane deformation during the injection of a 0.01 M NaBz solution under an actuation pressure difference ΔP= 800 mbar. (a)Profilometry scan providing a 2D map of the bulging, (b)Deformation profile along the z-axis. (c)Deformation profile along the x-axis: raw data (black symbols) and parabolic fit (red line) obtained at different actuation pressure. Maximum deformation ($h\Delta P_{max}$) is defined as the top value of the parabola.

Results presented in Figure III-22 demonstrate that such thin membranes (150 nm Si_3N_4) can undergo strong elastic deformations under the hydrodynamic pressure associated with liquid flow. We observe, for example, that the thickness at the center of the cell ($h_{solution}$) doubles above 1 bar, reaching more than 10 µm.

The bulging of Si_3N_4 membranes under differential pressure depends directly on the membrane's mechanical properties, but the fluid's viscosity is also important. As presented in section III.4.2.i, the hydrodynamic resistance varies with the fluid's viscosity, and the actuation pressure needed for a given flow rate will depend on the fluid's viscosity. Dose deposition measurements are calculated from the flow rate and the beam's absorption in

the solution, which depends on the channel's thickness and thus the deformation. It is, therefore, necessary to evaluate the deformation variation according to the flow rate.

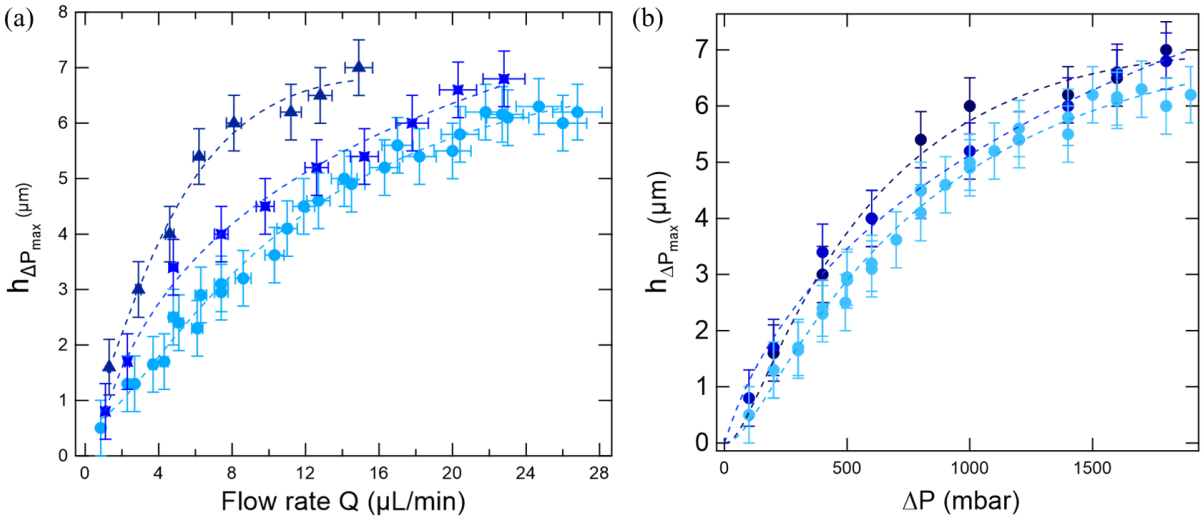

Figure III-23: Maximum deformation for three different concentrations of the flowing benzoate solution: light to dark blue correspond to 0.01 M, 0.1 M and 1 M: (a) as a function of the flowrate (Q), (b) as a function of the actuation pressure ΔP. Dotted lines are only a guide to the eye.

Three concentrations of benzoate solutions were studied. For all solutions, the deformation of the Si_3N_4 membrane increases almost linearly for flow rates up to 8 µL/min and then reaches a plateau at about 7 µm (Figure III-23.(a)). As observed in Figure III-23.(b), it seems that there is no effect from the solution itself (such as surface tension). Similar results were observed in both membranes design (the "initial design" and the "transmission design"). The addition of a window at the back has no significant influence on the deformation except that it is twice that with one window ($h_{solution}=H_{spacer}+2h_{\Delta P}$).

III.4.3. Evaluation of the errors on the dose calculation

III.4.3.i. Uncertainties on the dose using the IRAD setup

Following the characterization of the setup, the error of each parameter in Equation (III-4) are perfectly known. All uncertainties are summarized in Table III-4 for experiments conducted on the METROLOGIE beamline.

Table III-4: Uncertainties of the production yield of both 2HB and HO. Values are given for a 0.01 M benzoate solution irradiated with a 1.28 keV energy beam but can vary with photon energy or benzoate concentration.

Source	Uncertainty (%)
Photon flux measurement ($\varphi_{photodiode}$)	3.3
Transmission of the photodiode-to-membrane air gap (T_{air})	2.2
Centering of the beam on the photodiode and the membrane	5.6
Transmission of the silicon nitride membrane ($T_{Si_3N_4}$)	1.4
Flow rate measurement	5
Transmission of the solution irradiated at 8 µL/min^{-1} ($T_{solution}$)	10†
Chemical dosimeter calibration	6.25†
Total error	**⩽15**

†Increases with the concentration

The photon intensity (3.3%) uncertainty was estimated by considering previous measurements using the photodiode on the METROLOGIE beamline[5]. The one on the air gap transmission (2.2%) was determined by measuring the devices positioning in front of the IRAD setup by an optical level. The error on the relative positioning of the synchrotron beam and sample environment (5.6%) has been assessed by calculating the effect of a 50 µm misalignment. The error on the photon transmission through the Si_3N_4 window of the dosimetry cell (1.4%) was estimated according to uncertainties on the stoichiometric composition of the Si_xN_y material (from Si_3N_4 to SiN), its thickness (10%), and on the material density. Reported values for the latter parameter actually vary between 2.68 g.cm^{-3}[19] and 3.1 g.cm^{-3} (manufacturer specifications). Still, the largest uncertainty is related to evaluating the X-ray transmission coefficient of the solution as this factor is strongly dependent on the hydrodynamic pressure. At high flow rates (>10 µL/min), this uncertainty can reach 16%, owing to the large deformation of the membrane. Besides, high flow rates will decrease the deposited dose and therefore reduce the accuracy of fluorescence measurements. Therefore, the benzoate solution (irradiated in the microfluidic cell) is more accurate at low flow rates (less than 10 µL/min) where errors due to membrane deformation remain limited. Finally, the error on the fluorescence measurements is deduced from the variations of the calibration curves (see Chapter II section II.3.3). It is estimated to be 6.5% at low benzoate concentration (0.01 M) but can reach 8.0% at high concentrations due to fluorescence re-absorption. However, the main

factor that impedes the accurate determination of the fluorescence signal is not the systematic error on fluorescence measurements but the residual fluorescence of the non-irradiated solution, which becomes the main source of error of the fluorescence signal when considering concentrated solutions. Since the errors were considered independent of each other, the total relative error on the hydroxyl production yield was calculated using the quadrature method[20].

III.4.3.ii. Uncertainties on the dose using the vacuum chamber

Under vacuum, errors specific to the IRAD setup need no longer be considered (those related to the air gap). Moreover, the error on the deformation is reduced as the membranes are already bulged due to the vacuum environment[41]. However, the main disruptive element performing soft X-rays under-vacuum irradiation remains the carbon contamination[21]. Indeed, at air, oxygen prevents the formation of a carbon layer at the surface of the silicon nitride window formed by carbon cracking[22]–[24]. From the literature, the carbon deposition layer can easily reach 50 nm for high fluences (~ 500 mJ/cm²). On PLEIADES, the fluence is around 450 mJ/cm² at the C K-edge (290 eV) for the optimized beam geometry ($0.3 \cdot 1$ mm²). The beam's transmission through a carbon layer of 50 nm can be as low as 58% at 290 eV (just above the C-K edge). This value was calculated using a graphite density of 2.2 g/cm³[3]. A 50 nm carbon layer would therefore lead to an error of the dose of 58%! Even if primarily overestimated in our case, the error from carbon contamination remains significant and can be disruptive for under vacuum use of the microfluidic cell.

[41] *The relative difference between the maximum deformation and real size of the microfluidic channel is reduced and can be considered systematic.*

III.5. Irradiation and collection protocols

III.5.1. Static irradiation in the microfluidic cell

After setting up the device, the samples to be irradiated are injected into the microfluidic cell. Rinsing with pure water between solutions avoids mixing the solutions in the circuit and ensures the smooth running of the experiment. Irradiations were at first conducted inside the microfluidic cell under non-flowing conditions (Q=0). More precisely, a volume of benzoate solution was confined in the microfluidic cell and in the capillaries between the cell and the 2-switch valves located upstream and downstream of the cell by closing these valves. In such conditions, a volume of 26 µL of benzoate solution is confined.

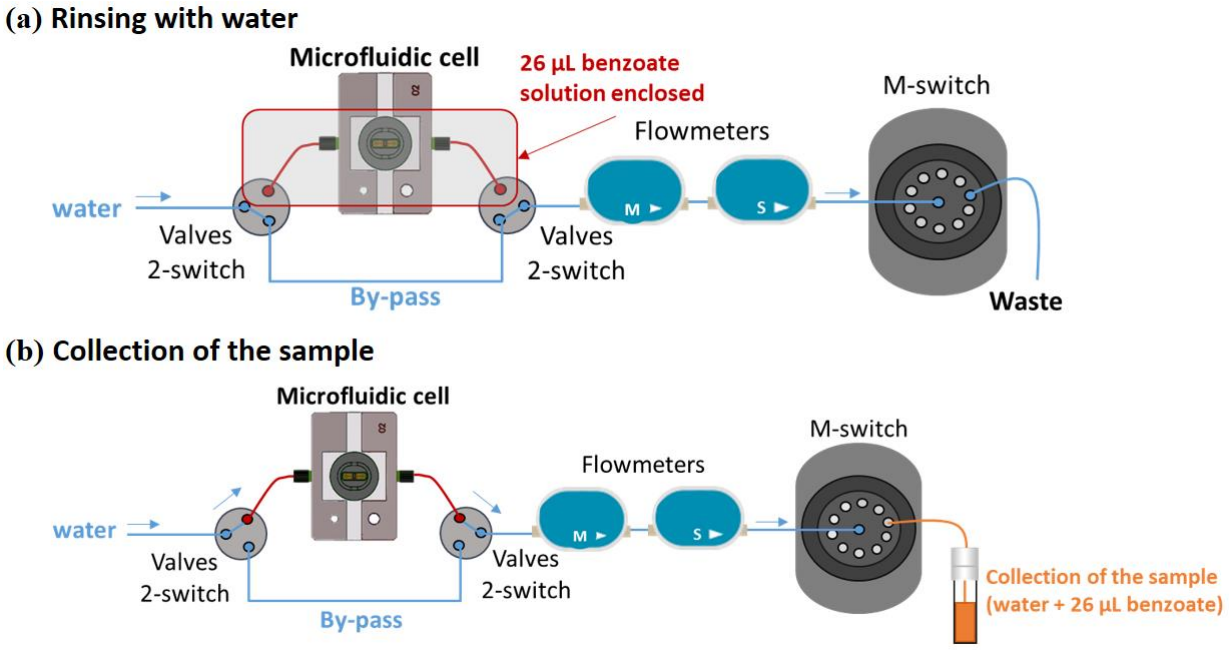

Figure III-24: Scheme of static irradiations steps: (a) Enclosing benzoate solution inside the microfluidic cell and rinsing the rest of the circuit with water while irradiating the cell. (b) Collection of the sample by flowing water through the microfluidic cell.

This volume was first evaluated by injecting a solution of 2-HOBz inside the circuit, closing the valves to isolate the microfluidic cell, and rinsing the rest of the circuit with pure water flowing through the by-pass. After flowing 2 mL of water through the circuit *via* the by-pass, the liquid enclosed inside the cell was released at 20 µL/min. A volume of 135 µL of the solution was collected[42].

[42] *The volume of 135 µL corresponds to ~3 times the volume downstream of the cell. It was estimated from hydrodynamic calculations and ensures that all the solution of interest is collected.*

A series of samples were collected in this manner with a solution containing 2-HOBz in known concentration. Fluorimetry analysis was conducted on the collected sample. Two methods determined the concentration of [2-HOBz]. The first one was by using a calibration curve performed with non-diluted solutions and then applying a factor of 4.5 (= 26/135). The other was by using a calibration curve performed with solutions diluted in pure water (26 µL adding 109 µL of pure water). Comparison with calibration curves allowed us to determine the dilution factor of the 2-HOBz released and determine the volume of 26±2 µL. This value was in good agreement with theoretical hydrodynamic calculations as presented in III.4.2.i. The irradiation protocol is very similar. Once confined, the solution is irradiated for a given amount of time (Δt). During irradiation, the rest of the microfluidic circuit (capillaries, flowmeters) was washed by flowing water through the by-pass at a high flow rate (> 60 µL/min). After irradiation, 135 µL of liquid was collected at 20 µL/min. As the valves were closed during irradiation, the amount of irradiated liquid was always the same, and errors were limited to the sample weighting after collection. Irradiated samples were then analyzed by fluorimetry. In this case, the dose deposited in the sample is determined using Equation (III-1) and a volume of solution ($V_{solution}$) equal to 135 µL (see section III.4.1).

III.5.2. Dynamic irradiation

III.5.2.i. Automatization of the sample collection

The main interest in implementing a microfluidic device is that the sample can be renewed during irradiation by working in flowing conditions. For these dynamic irradiations, samples were at first collected manually by timing the collection. Afterward, a collection/rinsing system was programmed using the Microfluidic Automation Tool from Fluigent. This software was specially developed for running time-based experiments. An easy "drag and drop" graphic interface helps create protocols for completely automated experiments (see Appendix II.2). More precisely, the program allows setting a constant flow rate and measures the volume of irradiated fluid thanks to flowmeters monitoring. As mentioned in section III.1.1.iv, it is possible to irradiate volumes of fluids at different flow rates and collect the samples in different tubes using a 10-ways valve at the end of the fluidic circuit. Once the correct volume of fluid is irradiated, the system switches back

to the waste tank to start a rinsing protocol before the following irradiation. Just like manual irradiations, it lets a volume of irradiated fluid go to the waste tank to ensure the collection of a stable and homogeneous sample (see details in Appendix II.2.). This system allows collecting up to 9 samples before changing the capillaries connecting the valve and the samples (which remain filled with liquid). This system allows a noticeable saving of time, improves reproducibility, and suppresses eventual errors of manipulation. It is also possible to program the beamline to synchronize the monochromator energy selection to change the photon energy between two samples. In dynamic conditions, the dose is calculated using Equation (III-4) (see section III.4.1).

III.5.2.ii. Towards online UV-analysis

In order to improve the level of sensitivity of the analysis, we decided to place a UV-vis detection cell downstream of the microfluidic cell. We used a flow cell allowing absorbance measurements on 2 µL samples, as illustrated in Figure III-25.(a) (Peek SMA-Z-2.5 detection flow cell from IDIL Fibres Optiques). This Z geometry of the detection cell allows illuminating the sample with a path length of 2.5 mm[43]. The light is then collected via an optical fiber (600 µm Premium Fiber, polarization-resistant, 3 m) to a portable spectrophotometer (QE Pro) also from IDIL Fibres Optiques (Lannion, France). The QEPro is a high-performance spectrometer with a high sensitivity thanks to a large dynamic range (typically 85,000 counts per channel). Its variable integration time is easily adjustable (from 8 ms to 3.6 s), and the buffering (up to 15 000 spectra) ensures data integrity at high collection rates. Moreover, it contains a thermoelectric cooler to provide high stability over long-term measurements. Since the sample is analyzed directly after its irradiation, it is possible to define the non-irradiated sample as the reference sample and directly analyze the relative signal and make extensive averaging.

This setup also allows controlling that the microfluidic circuit is correctly rinsed. Indeed, it allows us to directly analyze the liquid irradiated after coming out of the microfluidic cell and reaching the detection cell (see Figure III-25). Knowing the capillaries dimensions and the average velocity of the fluid (flow rate, pressure), it is possible to

[43] *Value from the constructor*

evaluate the time for the fluid to reach the detection cell (either from the irradiated area or from the entrance of the circuit). More precisely, as already detailed in section III.4.2), all hydrodynamic parameters can be evaluated. Hydrodynamic parameters are presented in Appendix II.1.

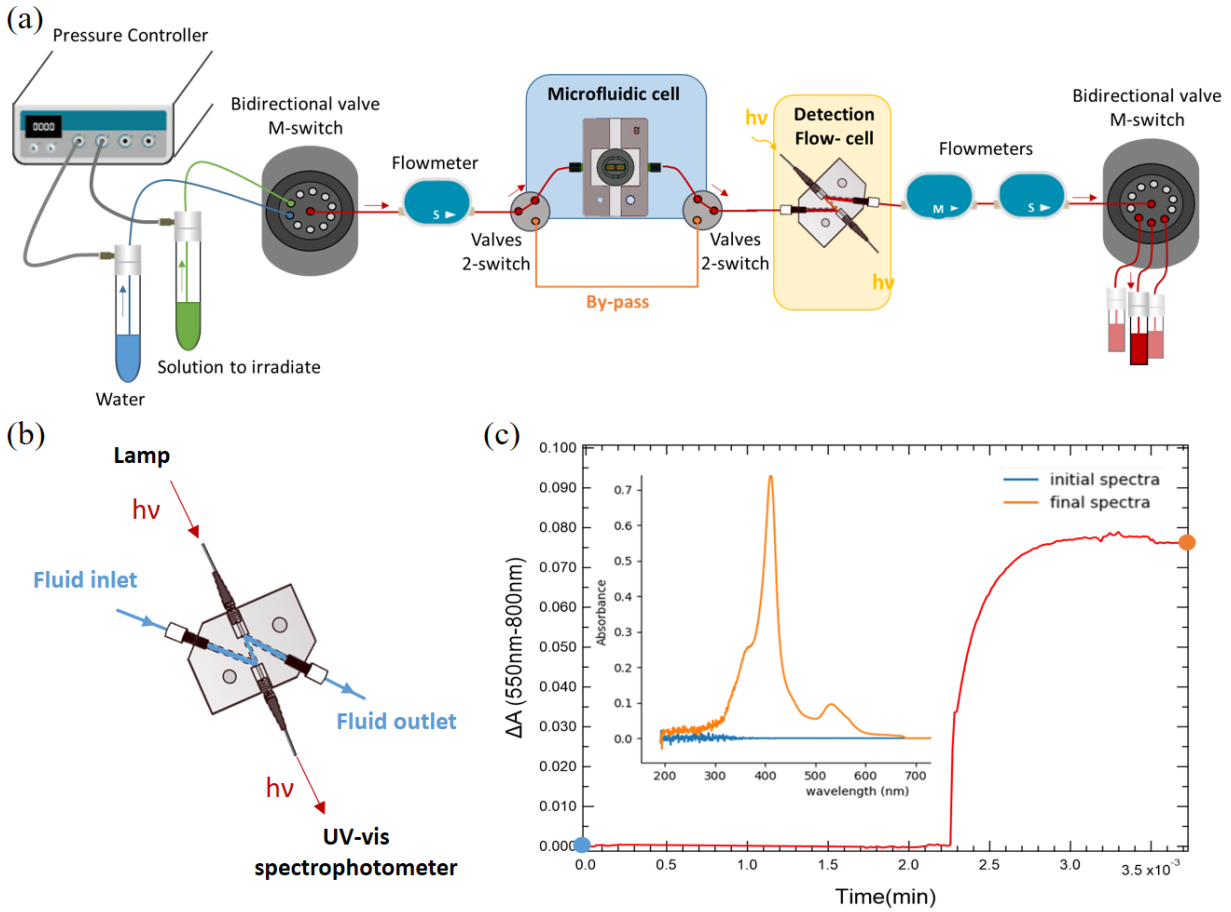

Figure III-25: Implementation of a UV-Vis detection flow-cell inside the microfluidic circuit in order to conduct on-line analysis (a) Schematic view of the microfluidic circuit, (b) scheme of the flow detection cell, (c) Absorbance spectra: kinetic evolution (red line), initial spectra of water (corresponding to the blue dot), final spectra of the CytC injected sample (orange dot).

Theoretically, a volume of 120 µL is enclosed in the capillaries between the injection (first M-switch, see Figure III-25) and the detection flow cell when passing through the by-pass. Experimentally, we effectively observed the signal increasing after ~2 min when injecting the liquid at a flow rate of 60 µL/min through the by-pass. A dilution front is observed and will be further discussed in Chapter IV. Data were recorded using the Oceanview software® and treated by a homemade Python program (see Appendix II.3 for more details).

III.5.3. Limitation

As previously mentioned in evaluating dosimetry errors (see section III.4.3), carbon contamination can be disruptive for quantitative analysis. Indeed, the error on the dose will be directly linked to the thickness of the carbon layer (transmission coefficient of the layer). Thus, it became imperative to find a way to characterize this carbon layer. More precisely, at the end of the beamtime conducted on the PLEIADES beamline, we noticed that the surface of the silicon nitride window was entirely "burnt" (see Figure III-26).

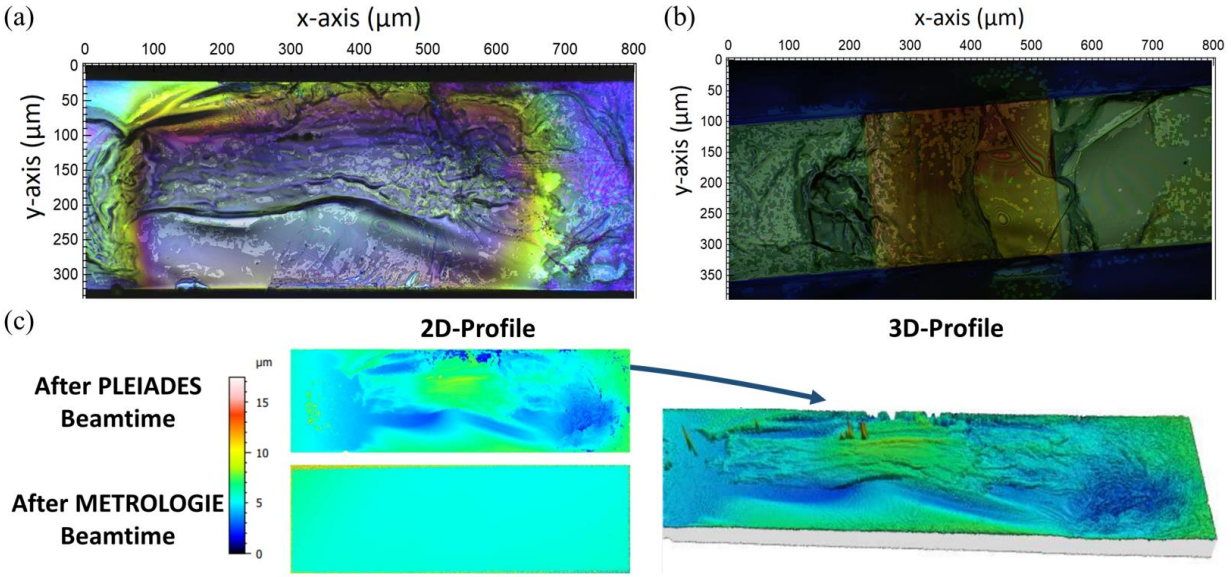

Figure III-26: Characterization of the silicone membrane windows after irradiation at the C K-edge on the PLEIADES beamline (after three days of experiments) (a)-(b) Microscope images of the front window (a) and back window (b); (c) Interferometry 2D and 3D profiles of the front window. Blue areas reveal ~2 µm relief that are corresponding to non-reflective areas.

The main hypothesis is a carbon contamination of the cell entrance window. Indeed, by irradiating above the carbon C_{1s} ionization threshold, carbon-chain molecules (coming from the setup (Kapton, microfluidic device) can be cracked by the beam and deposited as a thin film of carbon. This phenomenon is well known for soft X-rays beamline and can be very disruptive for experiments at the C K-edge[25]. In a vacuum of 10^{-6} mbar, experiments from the literature evaluated a carbon layer of 6-20 nm for a beam of 350 mJ/cm²[21]. In our case, the photon energy fluence reaches 150-500 mJ/cm². A carbon layer of tens of nanometers could explain that the surface of the Si_3N_4 window is no longer reflective (see Figure III-26.(c)). However, we also observed a substantial flow rate decrease

during the irradiation on the PLEIADES beamtime that an external carbon layer could not explain. Using a Scanning Electron Microscope (SEM), we performed Energy-dispersive X-ray spectroscopy (EDX) analysis on membranes irradiated during PLEIADES and METROLOGIE beamtimes. Such measurements allow identifying the composition of a sample qualitatively. Moreover, varying the acceleration voltage applied on the electron gun, it is possible to probe the different layers of the target, as illustrated in Figure III-27. Experiments were conducted using the MEB of the IPANEMA beamline at the SOLEIL synchrotron, thanks to Stephane Lorcy.

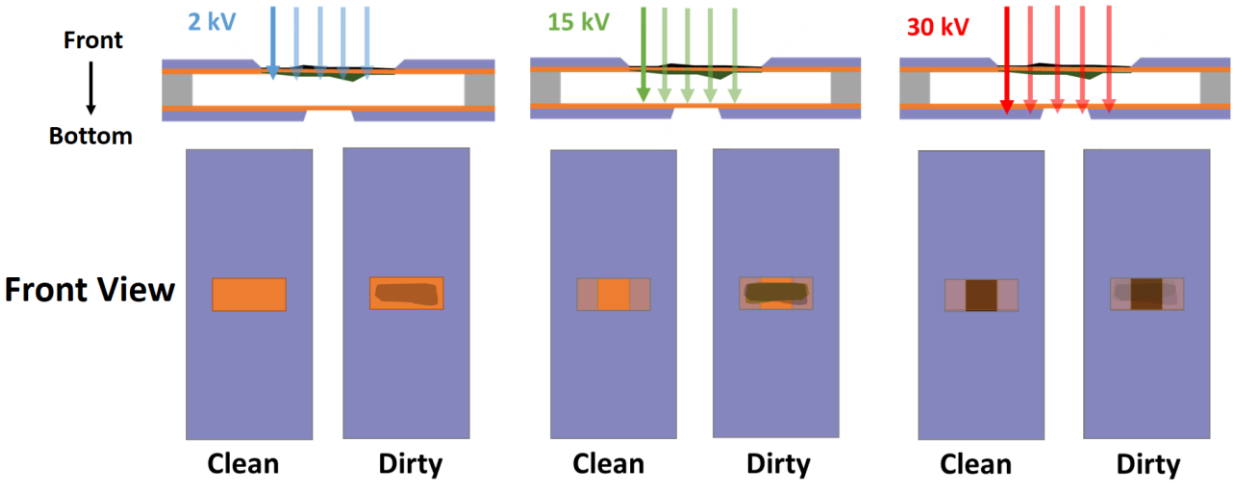

Figure III-27: Schemes (not to scale) illustrating the probed layers of the membrane sandwich according to the incident electron energy. The expected 2D maps from the front view are also shown in the case of clean or dirty membranes. The expected contaminant can be either on the surface of the irradiated membrane or inside (positioned almost randomly in the diagram).

Spectra obtained from EDX analysis of the front membrane (irradiated one) are compared in Figure III-28 for membranes used respectively during the PLEIADES and the METROLOGIE beamtime. The energy of incident electrons was 50 kV to probe the entire sandwich (see Figure III-27).

From this analysis, the presence of adventitious carbon and oxygen is evident on the membrane irradiated during the PLEIADES beamtime. Indeed, not only does the signal of impurities increases (C, N, O, Na), but we also notice a decrease of the silicon signal compared to the membrane irradiated during the METROLOGIE beamtime.

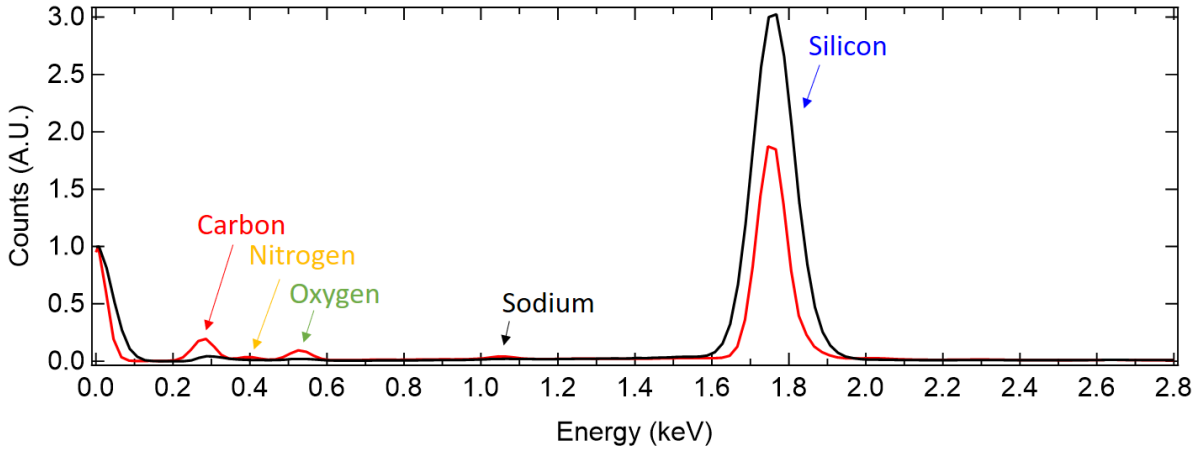

Figure III-28: EDX spectra measured on the front side of the silicon membranes carrying the irradiated silicon nitride window. Data recorded at 50 kV for membranes irradiated on PLEIADES (Red) and METROLOGIE (black) are compared.

In order to retrieve more information, 2D map analyses were carried out at different energies. At first, we analyzed the front window. As schematized in Figure III-27, 2D map analysis gives direct information about the presence of impurities and their location and composition. However, one can note that the expected 2D-map for 2 kV and 15 kV are very similar[44]. Indeed, a 150 nm Si_3N_4 window is highly transparent to electrons[26]. Therefore, it is impossible to precisely define the position of the carbon contamination, which could be inside the sandwich (in the microfluidic channel) or outside (deposit on the external window). However, by comparing results obtained at 15 kV and 30 kV, it should be possible to prove the presence of impurities inside the sandwich. Results for PLEIADES are presented in Figure III-29.

Figure III-27 and Figure III-29 show that incident electrons have enough energy to pass entirely through the Si_3N_4 windows' sandwich for both voltages. It is noticeable by observing the black square at the intersection area of the two membranes in the SEM images. However, the ejected electrons do not have the same energy in the two cases. Therefore, in the case of impurities at the surface or inside the sandwich, emitted electrons may not have enough energy to reach the detector (because of scattering). In the silicon EDX 2D map in Figure III-29, one can observe that the silicon from the back membrane is probed at 30 kV. However, at 15 kV, a black spot masks the silicon fluorescence. By

[44] *Also observed experimentally.*

crossing information retrieved from carbon and oxygen, we can say that there is organic matter inside the microfluidic cell[45].

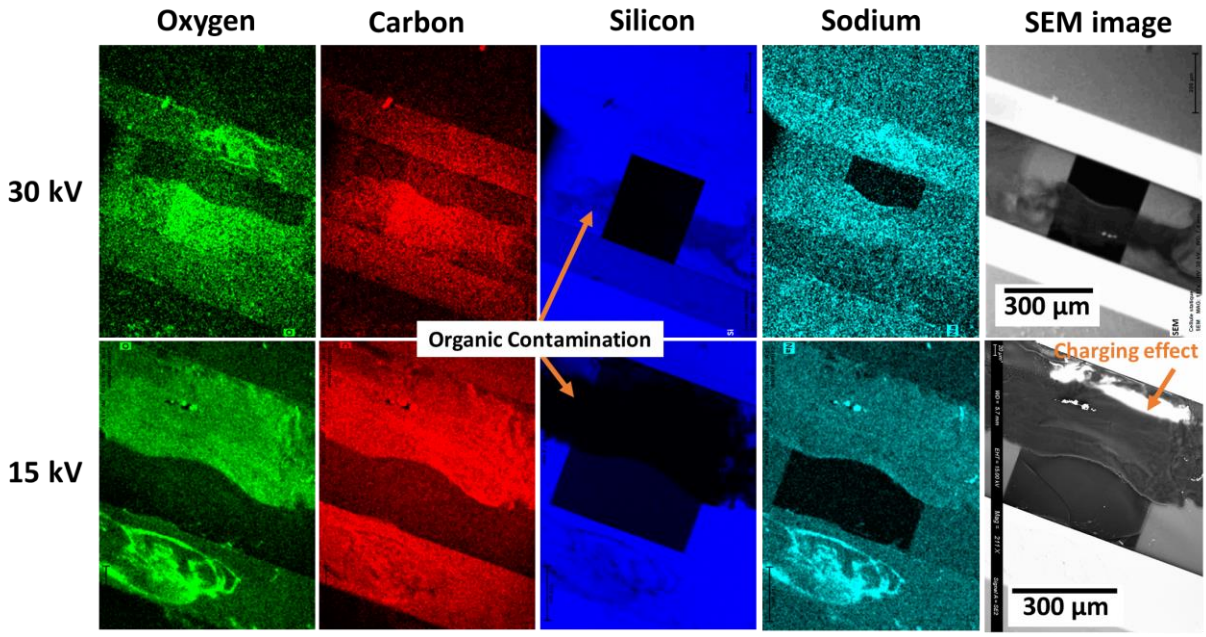

Figure III-29: EDX images obtained for the front silicon nitride membrane irradiated on PLEIADES. Comparison of results obtained with electrons produced at 15 kV and 30 kV.

According to the appearance of the irradiated front window (Figure III-26), it is therefore likely that there are not only impurities on the inside but also on the outside of the window. In order to disentangle the position of the different layers, we performed similar measurements looking from the backside of the cell. From this side, no carbon contamination is expected from the top membrane as the window is not facing the beam. Photons are indeed almost entirely absorbed by the fluid during the irradiation and do not risk damaging the cell back window. This time we are comparing 2D maps acquired at voltages of 2 kV and 30 kV.

On the 2D maps presented in Figure III-30, we noticed a significant signal from oxygen and carbon atoms. This area coincides with a decrease in the signal from silicon and nitrogen atoms. It indicates that contamination is located inside the microfluidic channel. Indeed, increasing the voltage to 30 kV, the signal from nitrogen appears again. This contamination is in good agreement with the previous analysis. However, at 30 kV,

[45] *The presence of sodium is not clear as the low signal intensity could originate from background noise.*

the signal of carbon and oxygen seems to increase. Therefore, it is likely that a deposit on the outer face of the irradiated window (containing carbon and oxygen) is also present.

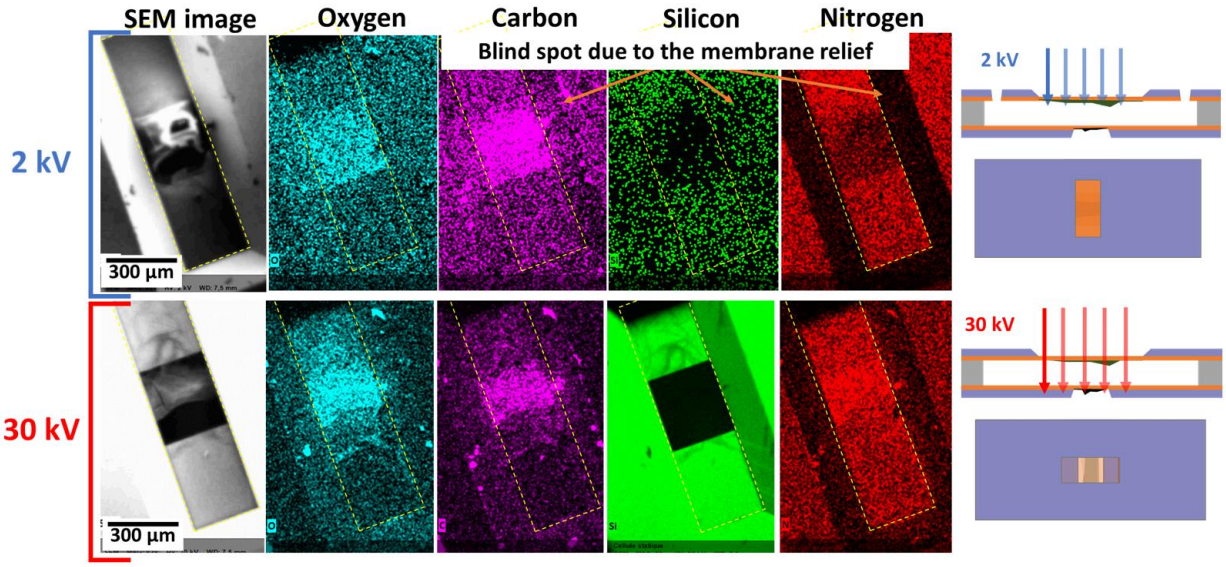

Figure III-30: EDX 2D map analysis from the back of the membranes sandwich. Data were reccorded applying a voltage of 2 or 50 kV. Sheme of the analysis are represented (not at scale).

For STXM measurements on the HERMES beamline, the strategy adopted to reduce the carbon contamination (outside the microfluidic cell) is to maintain a continuous flow of oxygen in the experiment chamber (a pressure of oxygen $\sim 4 \cdot 10^{-8}$ mbar) [22]. This strategy effectively removes carbon contamination and thus allows for carbon K-edge measurements[27]. It also explains why the "burnt" appearance of the window never occurred on METROLOGIE beamtimes where the microfluidic cell is irradiated at air. For the contamination from inside, the problem is more challenging to solve. The main hypothesis for its origin is the high flux and the absence of heat dissipation under vacuum. The same conditions are used on the STXM beamline. However, the beam spot is generally 25 nm large. Therefore, the degradation of biological samples is avoided by moving the beam (thus changing the irradiated area). In our case, the beam dimensions needs as close as large as possible in order to conduct homogeneous irradiations. A strategy could be to design a membrane carrying several windows in order to be able to change the irradiated area. Another strategy could be to enlarge the microfluidic channel to allow irradiation at higher flow rates. It might, in turn, reduce the homogeneity of the dose deposit in the cell's depth (microfluidic channel thickness ≈ attenuation length of the incident beam) so that the best compromise must be found

III.6. Conclusions on Chapter III

The microfluidic environment of the new irradiation cell brings several advantages for synchrotron irradiation. The first one is time-saving because it reduces the volume of irradiated solution (by a factor of 5). The experimental times are thus significantly reduced, even taking into account the rinsing and collection times of the irradiated samples as presented in Table III-5. A second advantage is that irradiation is performed more homogeneously because the thickness of the liquid is in the same order of magnitude as the attenuation length of the beam.

Table III-5: Comparison table of experimental times in static cell and microfluidic cell.

		Static Cell		**Microfluidic cell (dynamic conditions)**		
Energy	**Dose**	Irradiated volume	**Time required**[46]	Irradiated volume	Flow rate Q (µl/min)	**Time required**[47] - **Filling** - **Irradiation** - **Collection**
1280 eV	**110 Gy**	1 mL	**13h**	200 µL	1.25	**2h30**
	60 Gy	1 mL	**~7h**	200 µL	2.5	**1h30**
	30 Gy	1 mL	**3h30**	200 µL	5	**1h**

The development of such microfluidic devices for irradiation on synchrotron beamlines highly improved the accessibility of experiments conducted upon soft X-rays exposure. In order to perfectly characterize the setup, irradiations were at first performed at air. The main limitation was thus related to the strong attenuation of the beam, which limits the range of accessible energies. This problem was solved by implementing a vacuum chamber. However, it also imposes finding a way to reduce carbon contamination, such as oxygen flux.

Using a microfluidic cell in front of a micro-sized beam imposes to determine all the uncertainties carefully. If the alignment procedure is now fully operational, the bulging of the membranes still needs to be improved for easier use of the cell. Indeed, if at photon

[46] 3.525 mm air gap between the static cell window and IRAD's window.

[47] 2.2 mm air gap between the microfluidic cell window and IRAD's window. Liquid thickness is resp. 5, 6, and 7 µm for Q equal to resp. 1.25, 2.5, and 5 µL/min (see section III.4.2.iii for more details).

energies below 270 eV, or in the 550–880 eV interval, the X-ray beam is almost entirely absorbed by the water film[3], it is not the case when increasing the photon energy. As the attenuation length increases, determining the bulging becomes essential, as it will modify the number of photons absorbed by the solution and, therefore, the dose. To be in the bulging-independent regime, one should ensure that the 5.3 µm-thick film absorbs more than 95% of the beam. Increasing the nominal microchannel thickness is a way to reach this bulging-independent regime for other photon energy values, although at the cost of diluting the radiolytic products, and may be problematic for very low doses. For energies with considerable attenuation lengths in water (i.e., in the hard X-ray domain), one can use thicker membranes to limit the bulging and reach the electronic equilibrium in the medium, which ensures a proper measurement [28]. For example, using 3 µm-thick Si_3N_4 windows will limit the deformation to 1/20th of the one observed here[29], i.e., to less than 350 nm, while allowing to work with X-rays down to 10 keV (secondary electrons have ranges of about 1.5 µm in Si_3N_4). Under these conditions, the water film is almost transparent to X-rays (transmission > 0.997), while capturing enough dose (about 1 Gy at 10 keV and 10^{10} ph.s^{-1}) at a low flow rate (3 µL/min) to allow measurements using a fluorescent dosimeter of the benzoate/coumarin family. The system presented here should therefore apply to intermediate and hard X-ray beamlines. Finally, the bulging problem will probably have a technical solution in the near future, as membranes stabilized by a pillar array[30], exhibiting low deformation underflow, are now commercially available.

Finally, the main advantage of the microfluidic setup remains the high adaptability of such an environment both from a chemical and a physical point of view. The cell can indeed easily be used with a large variety of chemical samples. It can also easily be coupled with various spectrometers (UV, fluorimetry, Raman, mass spectrometry…). Such developments are currently ongoing for mass-spectrometry. As a perspective, it would be interesting to develop ways to perform *in situ* measurements directly in the irradiated area.

Bibliography Chapter III

[1] M. A. Herve Du Penhoat *et al.*, "Lethal effect of carbon K-shell photoionizations in Chinese hamster V79 cell nuclei: Experimental method and theoretical analysis," *Radiat. Res.*, vol. 151, no. 6, pp. 649–658, 1999.

[2] B. Fayard *et al.*, "Cell Inactivation and Double-Strand Breaks: The Role of Core Ionizations, as Probed by Ultrasoft X Rays," *Radiat. Res.*, vol. 157, no. 2, pp. 128–140, 2002.

[3] B. L. Henke, E. M. Gullikson, and J. C. Davis, "X-Ray Interactions: Photoabsorption, Scattering, Transmission, and Reflection at E = 50-30,000 eV, Z = 1-92," *At. Data Nucl. Data Tables*, vol. 54, no. 2, pp. 181–342, Jul. 1993.

[4] F. N. Gobert *et al.*, "Chromosome aberrations and cell inactivation induced in mammalian cells by ultrasoft X-rays: Correlation with the core ionizations in DNA," *Int. J. Radiat. Biol.*, vol. 80, no. 2, pp. 135–145, 2004.

[5] L. Huart *et al.*, "Soft X-ray Radiation and Monte Carlo Simulations: Good Tools to Describe the Radiation Chemistry of Sub-keV Electrons," *J. Phys. Chem. A*, vol. 124, no. 10, pp. 1896–1902, 2020.

[6] C. Gosse *et al.*, "Development of a fluidic cell to image precipitation reactions by x-ray microscopy," *TRANSDUCERS 2017 - 19th Int. Conf. Solid-State Sensors, Actuators Microsystems*, no. June, pp. 1734–1737, 2017.

[7] C. Gosse *et al.*, "A pressure-actuated flow cell for soft X-ray spectromicroscopy in liquid media," *Lab Chip*, 2020.

[8] I. Pereiro, A. Fomitcheva Khartchenko, L. Petrini, and G. V. Kaigala, "Nip the bubble in the bud: A guide to avoid gas nucleation in microfluidics," *Lab Chip*, vol. 19, no. 14, pp. 2296–2314, 2019.

[9] L. Huart *et al.*, "A microfluidic dosimetry cell to irradiate solutions with poorly penetrating radiations: a step towards online dosimetry for synchrotron beamlines," *J. Synchrotron Radiat.*, vol. 28, no. 3, pp. 778–789, 2021.

[10] D. K. Bedford and M. F. S. J. Mann, "Soft X-ray (0.1-4.5 nm) fluorescence of tetraphenyl-butadiene and sodium salicylate," *J. Phys. E.*, vol. 17, no. 10, pp. 866–867, Oct. 1984.

[11] KETEK GmbH, "PEVAL-KIT-MCX Evaluation Kit for Optical Bench Mount," *Prod. Data Sheet*, 2017.

[12] KETEK GmbH, "Product Data Sheet SiPM – Silicon Photomultiplier PM3325-EB / PM3350-EB," *Data Sheet*, pp. 5–7, 2017.

[13] "Crytur Website." [Online]. Available: https://www.crytur.cz/materials/yagce/.

[14] T. C. Pataky, J. Vanrenterghem, and M. A. Robinson, "The probability of false positives in zero-dimensional analyses of one-dimensional kinematic, force and EMG trajectories," *J. Biomech.*, vol. 49, no. 9, pp. 1468–1476, 2016.

[15] R. L. Owen, J. M. Holton, C. Schulze-Briese, and E. F. Garman, “Determination of X-ray flux using silicon pin diodes,” *J. Synchrotron Radiat.*, vol. 16, no. 2, pp. 143–151, 2009.

[16] H. Bruus, "Lecture Notes Theoretical microfluidics," *Physics (College. Park. Md).*,

vol. 18, no. 33235, p. 363, 2008.

[17] M. E. Holtz, Y. Yu, J. Gao, H. D. Abruña, and D. A. Muller, "M icroscopy M icroanalysis In Situ Electron Energy-Loss Spectroscopy in Liquids," *Microsc. Microanal.*, pp. 1027–1035, 2013.

[18] M. K. Small and W. D. Nix, "Analysis of the accuracy of the bulge test in determining the mechanical properties of thin films," *J. Mater. Res.*, vol. 7, no. 6, pp. 1553–1563, 1992.

[19] R. Huszank, L. Csedreki, Z. Kertész, and Z. Török, "Determination of the density of silicon–nitride thin films by ion-beam analytical techniques (RBS, PIXE, STIM)," *J. Radioanal. Nucl. Chem.*, vol. 307, no. 1, pp. 341–346, 2016.

[20] S. V. Gupta, *Measurement Uncertainties*, no. 82. Berlin, Heidelberg: Springer Berlin Heidelberg, 2012.

[21] A. F. G. Leontowich and A. P. Hitchcock, "Secondary electron deposition mechanism of carbon contamination," *J. Vac. Sci. Technol. B, Nanotechnol. Microelectron. Mater. Process. Meas. Phenom.*, vol. 30, no. 3, p. 030601, 2012.

[22] S. Swaraj, R. Belkhou, S. Stanescu, M. Rioult, A. Besson, and A. P. Hitchcock, "Performance of the HERMES beamline at the carbon K-edge," *J. Phys. Conf. Ser.*, vol. 849, no. 1, 2017.

[23] T. Koide, T. Shidara, M. Yanagihara, and S. Sato, "Resuscitation of carbon-contaminated mirrors and gratings by oxygen-discharge cleaning 2: Efficiency recovery in the 100–1000-eV range," *Appl. Opt.*, vol. 27, no. 20, p. 4305, 1988.

[24] T. Koide, T. Shidara, K. Tanaka, A. Yagishita, and S. Sato, "In situ dc oxygen-discharge cleaning system for optical elements," *Rev. Sci. Instrum.*, vol. 60, no. 7, pp. 2034–2037, 1989.

[25] C. Chauvet *et al.*, "Carbon contamination of soft X-ray beamlines: Dramatic anti-reflection coating effects observed in the 1 keV photon energy region," *J. Synchrotron Radiat.*, vol. 18, no. 5, pp. 761–764, 2011.

[26] E. A. Ring, D. B. Peckys, M. J. Dukes, J. P. Baudoin, and N. De Jonge, "Silicon nitride windows for electron microscopy of whole cells," *J. Microsc.*, vol. 243, no. 3, pp. 273–283, 2011.

[27] G. Held *et al.*, "Ambient-pressure endstation of the Versatile Soft X-ray (VerSoX) beamline at Diamond Light Source," *J. Synchrotron Radiat.*, vol. 27, no. May, pp. 1153–1166, 2020.

[28] A. Bridier, J. J. Broerse, J. R. Johnson, A. M. Kellerer, J. T. Lyman, and J. Zoetelief, *The Dosimetry of Ionizing Radiation*. Elsevier, 1985.

[29] P. Martins, P. Delobelle, C. Malhaire, S. Brida, and D. Barbier, "Bulge test and AFM point deflection method, two techniques for the mechanical characterisation of very low stiffness freestanding films," *EPJ Appl. Phys.*, vol. 45, no. 1, 2009.

[30] J. F. Creemer *et al.*, "An all-in-one nanoreactor for high-resolution microscopy on nanomaterials at high pressures," *Proc. IEEE Int. Conf. Micro Electro Mech. Syst.*, pp. 1103–1106, 2011.

Chapter IV. Chemistry initiated upon soft X-rays exposure

Contents Chapter IV

Chapter IV. Chemistry initiated upon SXs exposure

As presented in Chapter III, we developed a liquid irradiation setup dedicated to low penetration radiation irradiation. Working with liquids is of primary interest as, not only the ionization of the target molecule itself is involved in the degradation process, but also the solvent molecules[1]. For biomolecules, it is, for example, known that hydration is an essential factor on which radiation damage is highly dependent[2], [3]. Not only because it impacts the conformation of the biomolecules [2], [4], [5], but also because it modifies their electronic structure [6], [7]. The following chapter will present our advances in understanding the physico-chemical events generated by low-energy photon dose deposition processes in a liquid aqueous medium. At first, we will present our results on the analysis of SXs track structure. This study was conducted by following hydroxyl radical production using a scavenging chemical method. First, we will present the data obtained using a static irradiation set-up for liquid irradiation in a 1 mL cell. In the second part, a microfluidic device was developed explicitly for irradiation with low penetrating radiation. The reduction of the liquid thickness at the irradiated area allows more homogeneous irradiation than the 1 cm-thick static cell. The microfluidic cell, dedicated to dynamic irradiation conditions, provides an environment adapted to study the effect of core-ionization, as it can easily be implemented on synchrotron beamlines. We will focus on results obtained around K-shell ionization thresholds involving metallic ions (Na, Mg). Finally, we will present the limitations of this microfluidic setup and the perspectives for its application. Most of the experimental data are supported by theoretical calculations performed by collaborators of the ANR project. The simulations discussed in the context of this thesis were not performed by myself.

IV.1. ROS production and dosimetry

IV.1.1. Basic principle of the radical scavenging methods

In order to bring a better description of the radiochemistry initiated by the dose deposition processes under SX exposure, it is necessary to characterize the water radiolysis. It is indeed known that the dissociation processes of water molecules lead to the formation of various reactive radical or molecular species (ROS) (see Chapter I for more details). From a radiotherapeutic point of view, the production of ROS must be well known to define biomolecules degradation pathways, known as indirect effects[8]. ROS reactivity is in particular widely studied *in vivo* as it constitutes the heart of the well-known oxidative stress[9]. In view of giving a proper description of the energy deposition processes of radiation, ROS are also of great interest. Indeed, their production yield, characterized by the G-value, is intimately related to the spatial structure of the light/matter energy transfer[10]. Therefore, detecting ROS inside the sample constitutes a way to evaluate the dose deposited inside the sample. Unfortunately, as their name indicates, ROS are extremely reactive. Their short lifetime (<1 µs) often hinders direct detection. Taking advantage of the high reactivity of ROS, one strategy is to insert an external compound to detect them. More precisely, this substrate will react with one or several ROS species, resulting in the production of detectable and relatively stable products that can be quantified on longer time scales[11]. It is commonly referred to as a scavenging reaction. In most cases, the response of the chemical system is proportional to the dose deposited. In such conditions, the concentration (ΔC) of the species X formed during the irradiation of the scavenger can be related to the dose deposited (D) and the production yield G(X):

$$\Delta C = G(X)\rho D \qquad \text{(IV-1)}$$

With ρ the volumetric mass density of the solution. Knowing the dose deposited in the sample, it is, therefore, possible to determine the G-value by measuring the concentration of species formed. Reciprocally, any scavenger that undergoes a quantifiable chemical change under irradiation can constitute a dosimeter, as the detection of the product allows the calculation of the absorbed dose. A large variety of detection methods can be considered (electrochemistry, UV/vis spectrophotometry, luminescence, vibrational spectroscopy...), depending on the properties of the product formed. The most commonly

used aqueous dosimeter is the Fricke dosimeter[12]. Its detection is based on the oxidation of ferrous sulfate ions. The Fe^{3+} production can originate through reactions with several ROS and can be followed using UV-visible spectrophotometry. The G-value, corresponding here to $G(Fe^{3+})$, was experimentally determined for various radiation exposures ([13]–[17]). However, it can be helpful to have a dosimeter specific to a particular ROS. In such cases, the G-value measured will be directly related to the G-value of the ROS scavenged. Therefore, such dosimeters can act as a probe of the targeted species and bring direct information on its production.

IV.1.2. Hydroxyl radicals quantification and LET characterization

Among the species formed during water radiolysis (see Chapter I, Equation (I-3)), the hydroxyl radical $HO^{\bullet}$ is known as a highly oxidizing species and has long been studied in biochemistry and radiobiology. It is generally considered as the most reactive and damaging among all ROS[18]. According to hydroxyl radicals' high reactivity, scavenging methods are very efficient at quantifying their production yield [19], [20]. The efficiency of this procedure lies in the reaction affinity between the scavenger and the ROS, but more importantly, in the sensitivity of the product detection method. Standard scavenging methods are presented in Table IV-1.

Table IV-1: $G(HO^{\bullet})$ values from the literature determined for various ionizing radiations (scavenging times longer than 1 ns*)*.

Irradiation source	*LET (keV/µm)*	*G(HO•) (µmol/J)*	*Dosimeter*	*Ref*
^{60}Co γ-rays 1.33 MeV	*0.2**	*0.29*	*Benzoate*	[21]
		0.27	Coumarin	[22]
Deuteron 20.9 MeV	*4.5*	*0.196*	*Formic acid*	[23]
X-rays: Al K-shell 1.49 keV		*0.072*	*DNA plasmids*	[24]
Synchrotron 300-600 eV	*520**	0.023	Terephthalic acid	[25]
18 MeV/Nucleon carbon	*632*	*0.032*	*Formic Acid*	[26]
5 MeV He^{2+} ions	*1015*	*0.004*	*Formic Acid*	[23]

** LET of secondary electrons.*

As shown in the literature, the G($HO^{\cdot}$) value decreases as particles LET increases. The observed decrease is a direct consequence of the high ionization density for high LET particles, which leads to very fast recombination (<10^{-6} s) of the hydroxyl radicals (intra-track reactions). These events may therefore take place even before scavenging occurs. The time evolution of the species produced in a spur was simulated by kinetic diffusion models, such as those developed by Pimblott and co-workers[27]. Figure IV-1.(a) presents the evolution of the production yield of hydroxyl radical $HO^{\cdot}$ produced in fast electrons (low LET particles) tracks. Such simulations take into account the competition between the diffusion and the reactions between species during the non-homogeneous chemical step. As shown in Figure IV-1.(a), the G($HO^{\cdot}$) value decreases by approximately a factor of two between 10^{-11} and 10^{-8} s. This value then reaches a plateau at approximately 10^{-6} s, which corresponds to the primary $HO^{\cdot}$ yield.

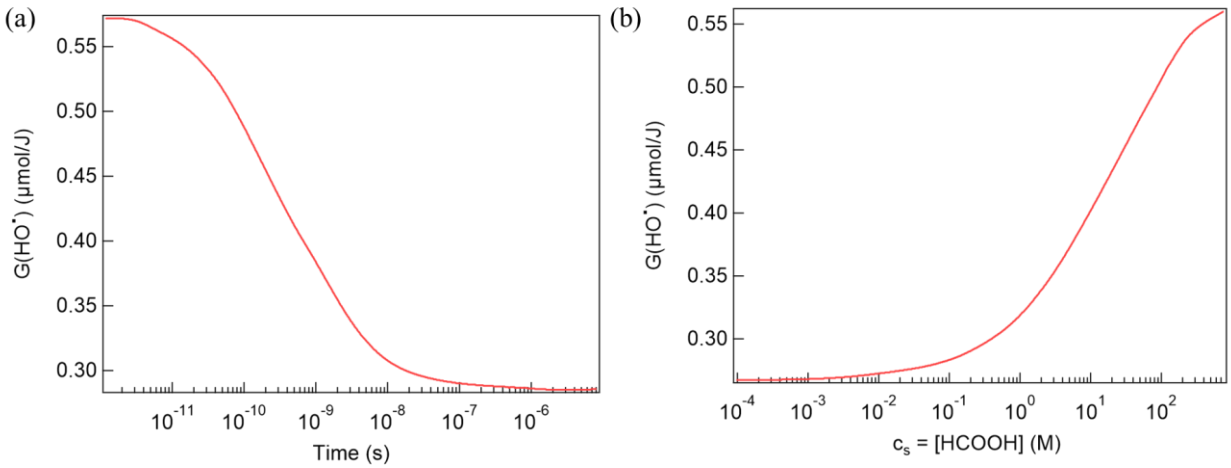

Figure IV-1: Evolution of the production yield of hydroxyl radicals (a) as a function of time in pure water and (b) as a function of the chemical scavenger's concentration (Formic acid). Data are from Pimblott et al.[27].

Figure IV-1.(b) represents the radiolysis of "pure" water reconstructed by a chemical scavenging method, using the formic acid as a scavenger of $HO^{\cdot}$. The G($HO^{\cdot}$) value is found similar to the primary $HO^{\cdot}$ yield at low scavenger concentrations (10^{-4} – 10^{-2} M) and increases by approximately a factor of two as the scavenger's concentration increases. Indeed, the scavenging time of ROS is directly related to the concentration of the scavenger. More precisely, the size of the spurs increases with time (diffusion) and increases the probability of scavenging reactions over recombination reactions. As the concentration

of scavengers increases, the probability that they react with the target at a shorter time increases. Varying the concentration of the scavenger (c_s), it is, therefore, possible to probe the target production at different timescales. This process is well illustrated by the following relation[27], [28]:

$$Scavenging\ Time = \frac{1}{k_s \cdot c_s} \qquad (IV\text{-}2)$$

Where k_s is the reaction rate between the target and the scavenger. The product $k_s \cdot c_s$ represents the scavenging capacity (expressed in s^{-1})[29]. The conventional range of concentration used for scavengers is around 10^{-5} to 10^{-3} M. This range generally allows to access to the production yield in the homogeneous chemistry timescale (>10^{-6} s)[48] (plateau value, see Figure IV-1). Of course, the accessible timescale also depends on the system's scavenging capacity (k_s*[scavenger]).* If the scavenger's concentration increases (up to ~1 M), it is possible to access a shorter time. The main limitation of working at high scavenger concentrations is that an increasing proportion of the ionization can occur directly on the scavenger itself. Similarly, indirect reactions can also be considered for high density of ionizations, such as high LET particles track. Indeed, the more radicals are produced, the more new intermediate reactions may occur and decrease the yield measured by scavenging.

As presented in Table IV-1, the G($HO^{\cdot}$) seems to decrease in the SX range. In fact, many theoretical approaches already evidenced a minimum G($HO^{\cdot}$) for low energy incident electrons(at ~1 keV) as already presented in Chapter I (see Figure I-11)[30]–[33]. This minimum was associated with the high production of radicals in spurs and so, their fast recombination. The low production yield supports the fact that low-energy electrons behave like high LET particles. Monte Carlo (MC) simulation codes are a great tool to obtain such theoretical track-structure analysis. MC calculations are indeed known to reproduce the stochastic nature of particle-matter interactions[34], [35]. However, MC codes use ionization cross-sections as input[36]. Such values, although well-established when target water molecules are in the gas phase[37], [38], remain barely described in the liquid phase [39]–[41]. More recently, the cross-section calculation model was improved to bring a more realistic description of the water in both liquid and vapor phases [42]. This

[48] *On average, reaction rate constants for chemical probes are in the order of 10^8-10^9 $M^{-1}s^{-1}$[145]*

study investigates cross sections for electron impact energy from 20 eV to keV. The authors conclude that the influence of the water phase on the ionization process is all the more important when the incident energy decreases and is particularly critical in the sub-keV range.

To date, measurements have mostly been performed for high-energy photons but remain scarce for photons of energy <1.8 keV [25], [43]. The only experimental works in the sub-keV range were published by Fulford[24] and more recently by Vysin[25]. The team of Fulford *et al.* determined the dependence of the primary yield of $HO^{\cdot}$ radicals ($G(HO^{\cdot})$) on photon energy using aqueous solutions of plasmid DNA as a probe. These authors measured the yield of single-strand breaks (SSB) induced within DNA in order to sample the number of hydroxyl radicals present at the spur expansion completion time. This corresponds to a homogenization time of $\sim 10^{-6}$ s after the initial deposition of energy. The data obtained with photons varying in energy from 0.28 keV (C_K X-rays) to 1.25 MeV (^{60}Co γ-rays) were normalized to the yield of SSB for ^{60}Co γ-rays to estimate $G(HO^{\cdot})$[49]. They observed a minimum $HO^{\cdot}$ yield at around 1.5 keV with a value of $G(HO^{\cdot})$=0.072 µmol/J. This minimum was found to be in a relatively good agreement with theoretical calculations[31], [32]. In the recent study of Vysin and co-workers, the $G(HO^{\cdot})$ value was determined in the "water window"-range (going from the carbon K-edge at 284 eV (C1s) to the oxygen K-edge at 543 eV (O1s)), measuring the fluorescence of terephthalic acid. The obtained value of $G(HO^{\cdot})$=0.023±0.003 µmol/J confirmed the high density of ionizations in SXs track.

At the end of the fifties, Armstrong developed a method using benzoate as a scavenger[44]–[46], which our team modernized. This aromatic compound presents a high reactivity with the hydroxyl radicals, leading to fluorescent hydroxylated forms: 2, 3, and 4-hydroxybenzoate. This method has proven to be very effective for the quantification of $HO^{\cdot}$ production in various contexts (confined water radiolysis[47], peroxymonosulfate (PMS)-based advanced oxidation processes[48]). Under irradiation, aromatic hydroxylation occurs predominantly at the ortho-position, leading to the production of the 2-hydroxybenzoate (2-HOBz)(see Figure IV-2[44], [49], [50]). At pH ~8.1-8.8, 2-HOBz

[49] *Referenced value taken was $G(HO^{\cdot})$=0.29µmol/J for ^{60}Co γ-rays.*

exhibits a high fluorescence yield, whereas 4-hydroxy-benzoate fluoresces at lower wavelengths and 3-hydroxy-benzoate is only fluorescent when doubly deprotonated (basic pH) [47]. Moreover, double hydroxylation products are usually in almost undetectable quantities[51]. The formation of 2-HOBz will therefore be the only one probed during our experiments.

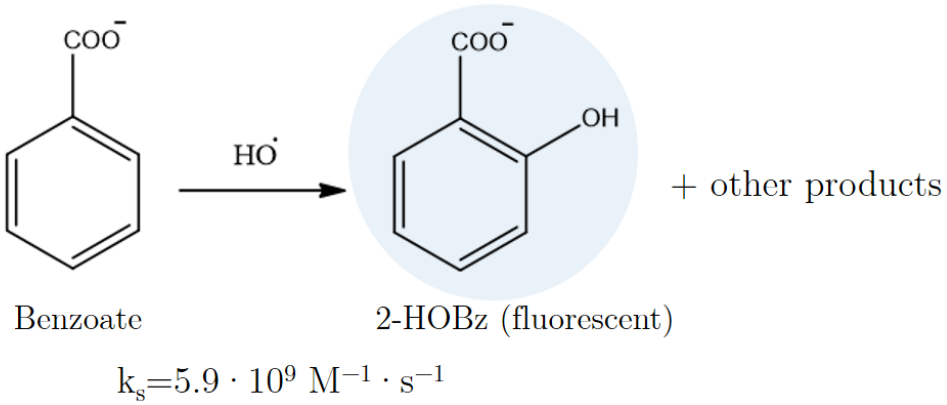

Figure IV-2: Benzoate scavenging reaction: production of 2-hydroxy-benzoate (2-HOBz)

The scavenging reaction rate is $k_s = 5.9 \cdot 10^9\ M^{-1} \cdot s^{-1}$[50]. Performing irradiation on solutions of various concentrations, from 10^{-3} to 1 M, allows us to investigate scavenging times in the $1.7 \cdot 10^{-7} - 1.7 \cdot 10^{-10}$ s range (deduced from Equation (IV-2)). Moreover, the fluorescence allows detecting very small concentrations of $HO^{\cdot}$. Such sensitivity is necessary given the low dose achieved in soft X-ray irradiation. Among the other sensitive fluorescent scavengers commonly used, such as coumarin [52] or rhodamine[53], the benzoate system remains the most suitable for our study according to its specificity and bio-compatibility. Indeed, sodium benzoate salts are particularly adapted for synchrotron irradiation as they are non-toxic and highly soluble in water (up to 2 M).

IV.2. Investigation of the track structure

In 2015, the team performed irradiations using a 1 cm-thick static cell. Experiments were conducted at air on the METROLOGIE beamline using the IRAD set-up (details on the set-up are given in Chapter III). At the beginning of my PhD, I participated in the analysis of these experiments. After having characterized the photon flux and ensured the correct alignment of the experimental set-up, it is possible to calculate the dose deposited in the exposed solution (see dosimetry details presented in section III.4). The results of a series of benzoate samples (10 mM) irradiated at 1.28 keV are shown in Figure IV-3. Irradiation times were respectively 60, 170, and 300 min. Irradiated solutions were then analyzed by fluorimetry to quantify the amount of 2-HOBz produced and determine the equivalent concentration of hydroxyl radicals (see Chapter II, section II.3.3 for more details on the fluorescence measurement).

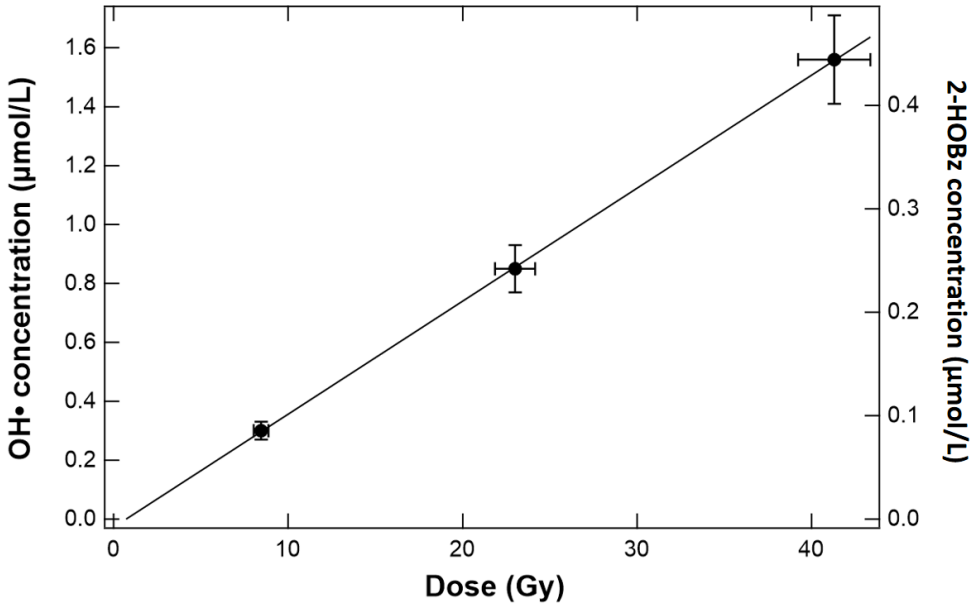

Figure IV-3: Concentration of $HO^{\cdot}$ radicals formed in aerated 0.01 mol/ L NaBz solutions irradiated with 1.28 keV X-rays as a function of dose. Data were fitted by using a linear regression.

Figure IV-3 presents the evolution of $HO^{\cdot}$ radicals concentration as a function of the dose deposited under SXs irradiation. A linear increase is observed. The slope results in a G($HO^{\cdot}$) value of 0.038±0.003 µmol/J for this 10 mM benzoate solution. In order to control the dosimeter's behavior, solutions were irradiated in glass vials with well-defined ^{67}Cs γ-rays as a reference. Our value, obtained at 1280 eV, is about two times smaller than that

measured by Fulford and co-workers at 1487 eV with Al K-α X-rays)[24]. However, as previously mentioned, the experimental values of Fulford *et al.* are not specific to $HO^{\cdot}$ radical production. They can therefore differ from the "real" G($HO^{\cdot}$) value despite the normalization with γ-rays irradiation.

The evolution of G($HO^{\cdot}$) values as a function of photon energy was also investigated (see *Figure IV-4*). The global evolution of experimental data obtained with benzoate solutions (presented in red) is in good agreement with the one of Fulford[24], even if values are somewhat lower (especially around the minimum at 1 keV).

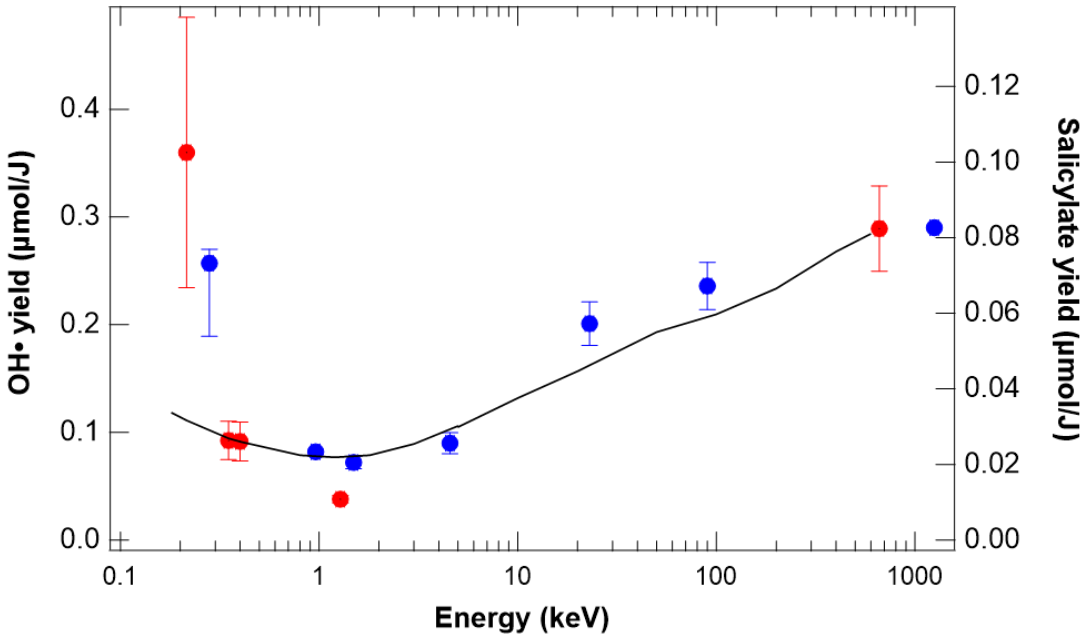

Figure IV-4: Yield of $HO^{\cdot}$ radicals as a function of photon energy (red symbols). The benzoate sodium concentration is 0.01 mol/L. Measurements by Fulford et al.[24] (blue symbols) are also presented. The experimental results are compared to MC simulations for monoenergetic electrons (solid line).

Experimental data were compared to MC calculations performed by Benoît Gervais (CIMAP UMR6252, Caen, France). The method provides the spatial distribution of $HO^{\cdot}$ initiated by electrons transport in liquid water. The three temporal stages of radiation/matter interaction[54], namely the physical stage, the physico-chemical stage, and the chemical stage, are simulated. The medium considered is made of liquid water, in which molecular oxygen and benzoate are solvated at a prescribed concentration and uniformly distributed. The considered oxygen concentration was $[O_2]$=0.26 mM, associated with an air pressure of 1 bar, while the benzoate concentration varied from 1 to 10^3 mM.

The MC simulations show that the $HO^{\cdot}$ yield determined for individual electrons is ~0.08-0.09 µmol/J in the 0.4-1.2 keV energy range. This value is very similar to the one obtained by irradiation of protons which have LET value of 20 keV/µm[55].

It must be noted that the presence of O_2 influences the measured production yield of hydroxyl radical. Indeed, O_2 has a significant scavenging effect on the solvated electron (diffusion-controlled rate $k_{s(e^-)}=1.9 \cdot 10^{10}\ M^{-1} \cdot s^{-1}$ [56]) which, in turn, protects $HO^{\cdot}$ radicals from reactions with solvated electrons. As presented in Chapter III (Table III-1) surface dose rates reach a few hundreds of kGy/min for 1.28 keV photons in the static cell. Such high surface dose rates could lead to benzoate and molecular oxygen depletion in the surface layer of the sample. Nevertheless, using very unfavorable approximations, we have shown that the benzoate concentration would be reduced by approximately 20% at the surface of the 1 mM NaBz solution, and the O_2 concentration by at most 34%[57]. These calculations were estimated without considering the O_2 supply from the top of the static cell (interface between liquid and air). As a consequence, depletion of Bz or O_2 cannot account for the low 2-HOBz yield measured.

As presented in Figure IV-4, the calculated $HO^{\cdot}$ yield (solid line) exhibits a minimum around 1.2 keV and reproduces the experimental data. Although a good agreement is observed between the experiment and simulation around 400 eV, the MC simulation using monoenergetic electrons appears to underestimate the $HO^{\cdot}$ yield at lower energies. Let us now compare the overall features of mono-energetic electrons and photons tracks. When the photon energy is below the O1s edge (B_K = 0.54 keV), photon absorption processes are related to outer shells ionization of water. Then further excitation and ionization are associated with the photoelectron emission (physical stage). Thus, the $HO^{\cdot}$ yield energy dependence should be very similar for mono-energetic electrons and photons (with the same energy E). However, when the photon energy is above the O1s, photons have sufficient energy to remove oxygen K-shell electrons, and K-shell ionization dominates (~95% of probability)[58], [59]. Therefore, a significant amount of doubly charged water molecules must be considered due to the Auger process and the emission of an AE with ~0.5 keV kinetic energy[60].

Energy deposition patterns following the absorption of a photon (1 and 10 keV, either in the outer shell or K-shell in water) are represented schematically in Figure IV-5.

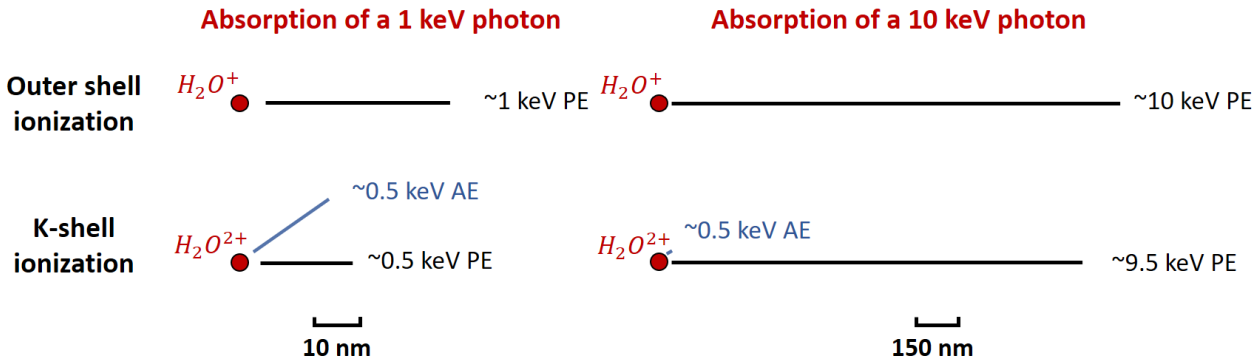

Figure IV-5: Scheme of water molecule photoionization. The black and blue lines represent, respectively, photoelectron (PE) and Auger electrons (AE) tracks. The lateral extension of the electron tracks is not represented.

In Figure IV-5, the line length represents the average maximum distance between the electron emission point and energy deposition events. They are equal to 21, 43 and 1570 nm for 0.5, 1 and 10 keV electrons respectively[61]. The distance between the beginning of the electron tracks and the photo-ionized water molecule is assumed to equal the emitted electrons' inelastic mean free path (IMFP). For electrons of energy 0.5, 1 and 10 keV, IMFP are respectively, 2.4, 4.0 and 26 nm[62]. For outer shells ionization (valence shell ionization), a single electron is emitted with energy slightly lower than the photon energy. However, after K-shell ionization, two electrons are emitted from the same point in space. PE and AE tracks may thus overlap and thus enhance early reactions of radiolytic radicals. If at 10 keV, this phenomenon is minor as only 5% of the dose goes to the AE, it can be of major importance in the sub-keV range. In particular, MC simulations estimated a decrease of 20% of the G($HO^{\cdot}$) at 1 keV between outer-shell and K-shell photo-absorption due to this track overlap effect[57]. Also, considering the limitation of MC simulations for sub-keV electrons, this effect could explain the factor two observed between calculations (mono-energetic electrons) and experimental data (mono-energetic photons). Moreover, the direct ionization of the solvated benzoate by electrons was not considered in the simulations, even if its ionization threshold (at ~6 eV) is below the electronic excitation of water. Despite the low benzoate concentration, this excitation pathway could represent an efficient deexcitation pathway for electrons that do not have enough energy to excite water. These electrons, with an energy lower than 7.3 eV, are commonly referred to as sub-excitation electrons[63]. The ionization of solvated benzoate by sub-excitation

electrons would lead to the release of an additional solvated electron and the partial destruction of the benzoate without the formation of hydroxylated products. Therefore, simulations and experimental results support the fact that SXs behave as high LET particles.

In order to determine the initial production of $HO^{\cdot}$, the benzoate concentration was varied to probe shorter scavenging times (see Equation (IV-2)). Different concentrations of NaBz solutions were prepared to study production yields in the range of 170 ns to 170 ps.

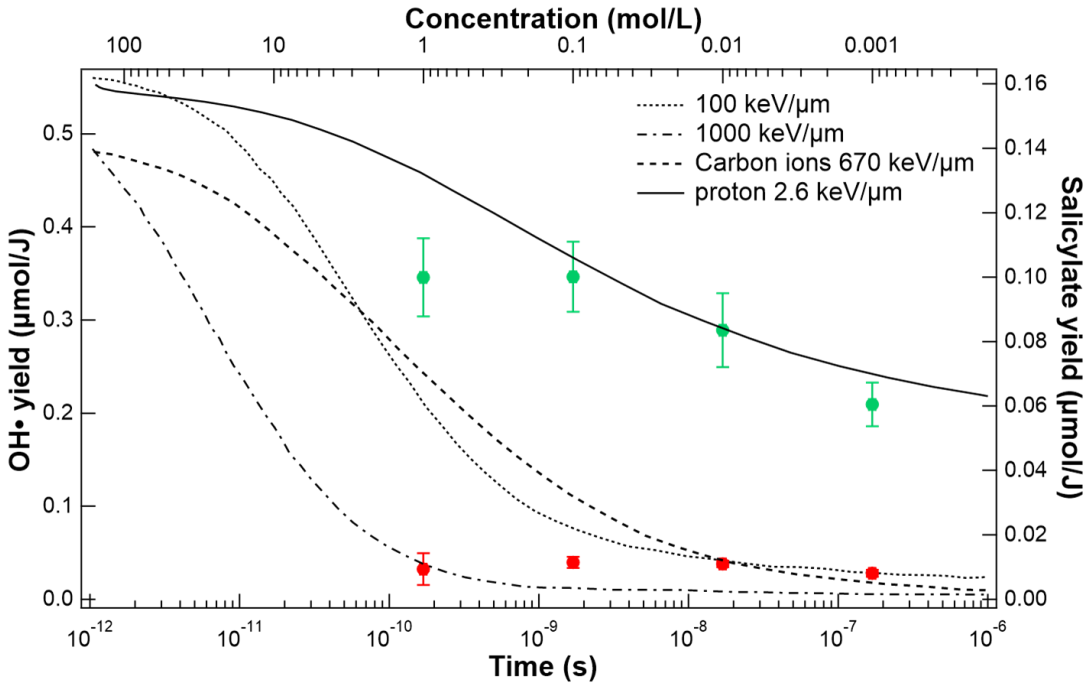

Figure IV-6: Yield of $HO^{\cdot}$ radicals in aerated sodium benzoate solutions irradiated with 1.28 keV X-rays (red) and ^{137}Cs γ-rays (green), as a function of scavenging time. Experimental results are compared to the results from MC simulations[54] for 2.6 keV/µm protons (solid line) and 670 keV/µm carbon ions (dashed line), and results from diffusion-kinetic models[29] for 100 (dotted line) and 1000 keV/µm (dashed dotted line) particles.

Experimental results, presented in *Figure IV-6*, are compared to MC simulations[54] and diffusion-kinetic models[29]. Theoretical calculations are performed for pure liquid water. However, the initial stages of water radiolysis can be affected by the presence of the scavenger for highly concentrated solutions. Indeed, as previously mentioned, at some point, the direct ionization of the solute can no longer be neglected. One could envision that not only the depletion of benzoate needs to be considered, but also the formation of

other reactive intermediates that can potentially react with $HO^{\cdot}$. Another effect to consider, is the degradation of 2-HOBz itself. Indeed, the increase in $HO^{\cdot}$ scavenging with the benzoate concentration leads also to an increase in their probability of cross reaction. In both cases, the scavenging capacity is locally diminished and the $HO^{\cdot}$ yield effectively measured will appear lower than the actual yield. The significance of this effect is unfortunately rather difficult to estimate without a dedicated simulation. Keeping this in mind, we can still compare the γ-rays and 1.28 keV behaviors. In the scavenging time range investigated, the $HO^{\cdot}$ production remains ten times lower than the production observed for γ-rays irradiation. This behavior is characteristic of very high LET radiations, such as heavy ions. Indeed, experimental hydroxyl G-values measured under high-energy heavy ion irradiation is $G_{100\ ns}(HO^{\cdot})$= 0.09 µmol/J (Ar^{18+} of 90 keV/µm)[64]. In our study, the time dependence of the salicylate yield suggests a LET close to or higher than 100 eV/nm by comparing it to the data of Pimblott and LaVerne[29]. Following theoretical studies from the literature, the maximal LET expected for electrons is 25−30 eV/nm at ~200 eV[65], [66]. In this LET range, the expected hydroxyl yield should be higher than 0.1 µmol/J for scavenging times below the microsecond range[67]. Even when taking into account the experimental uncertainties, our hydroxyl yield measurements are significantly lower. An obvious limitation of MC simulation is the uncertainty regarding the cross-sections used to model the transport of low-energy electrons, as discussed in recent papers[36], [68]. As mentioned above in this section, another possible explanation lies in the quasi-simultaneous production of two sub-keV electrons, the photo- and AE, which obviously may increase the local ionization density compared to the emission of a single electron with the same total energy. These experiments, therefore, highlight the crucial effect of core-ionization, which can lead to highly complex radio-damaging processes[69]

IV.3. Towards online dosimetry on synchrotron beamlines

SXs are known as low penetration radiation. As previously presented, it results in high dose rates at the surface of thick samples (compared to the attenuation length) in the condensed phase. To overcome the inhomogeneous dose deposition that can appear in liquid samples, we implemented a microfluidic cell[50] to perform irradiation, as detailed in Chapter III. In order to pave the way for synchrotron beamline dosimetry, benzoate solutions of different concentrations were injected into the microfluidic cell.

IV.3.1. First test in non-flowing conditions

Injecting benzoate solutions in the microfluidic cell constitutes a good way to set up a dosimetry device, as the production of 2-HOBz is known to be proportional to the dose delivered to the sample. Moreover, the irradiation window of dimensions 1×0.3 mm^2 allows to sample the deposited dose on a submillimeter scale, and therefore to map an irradiation field. In order to test the limits of the microfluidic system and attempt to access more significant dose depositions using the IRAD device (air irradiation), irradiations were performed under static conditions. Specifically, the valves upstream and downstream of the cell were closed to enclose a 26±2 µL volume of liquid (see Chapter III, section III.5.1 for more details). The exposure time of the liquid in front of the synchrotron beam was controlled to determine the dose. The total volume of liquid collected (135 µL) takes into account a dilution factor by the pure water present in the capillaries downstream the cell.

The first experiment was performed by irradiating the cell for a constant exposure time and varying the cell's position in front of the beam. The current was also measured for various positions of the photodiode along the x-axis to reconstruct the beam intensity profile along this direction. During this experiment, the photodiode was covered with the brass mask, which had a 270 µm-wide rectangular aperture (grey data). Results are compared in Figure IV-7. After passing through the dosimetry cell's 300 µm wide Si_3N_4 window, the beam intensity was calculated by convoluting the Gaussian beam profile (with

[50] *The initial device was developed for STXM measurement by Gosse et al.[146]*

a FWHM of 230 µm)[51] by the rectangular function (with a width of 300 µm). The resulting curve (red curve) exhibits a FWHM of 321 µm.

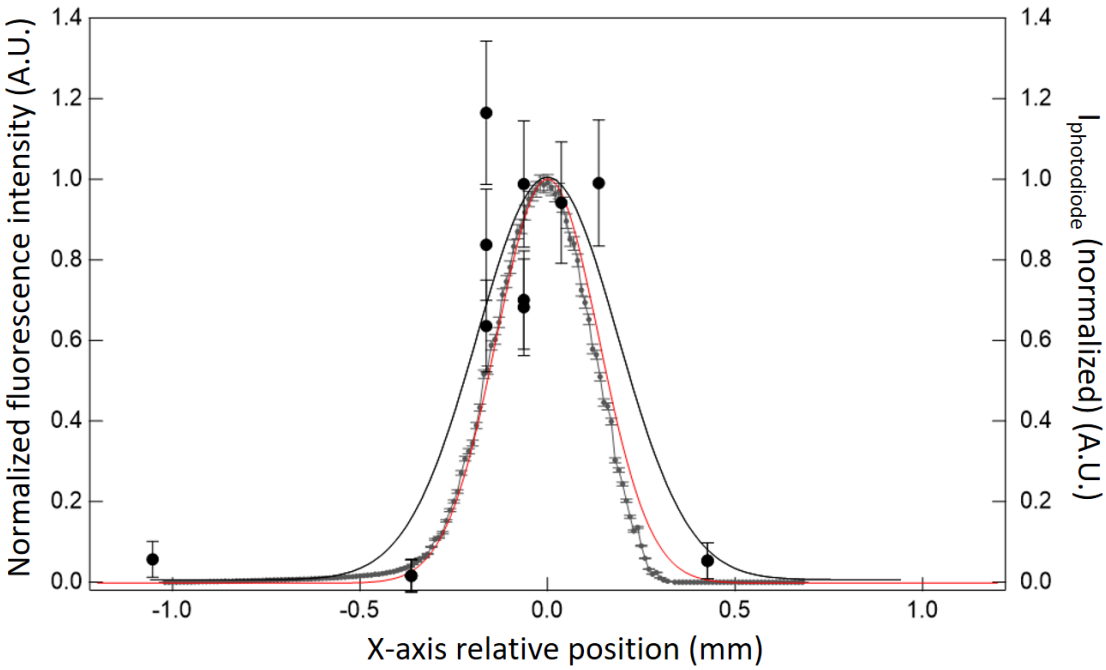

Figure IV-7: Normalized fluorescence signal to the center signal (X=0 mm) measured for a 10 mM benzoate solution irradiated during 20 minutes with 1.28 keV soft X-rays in non-flowing conditions (black symbols and curve). The current measured with the masked photodiode as a function of its position along the x-axis is displayed for comparison (grey symbols). The red plot corresponds a calculated profile (see text for more details).

As shown in Figure IV-7, experimental data present large error bars because the dilution factor leads to a low fluorescence signal. More precisely, the exposure times were ~20 minutes to obtain a signal at least 3 times higher than the background. In addition, there are experimental errors due to dilution uncertainties (possible evaporation of the liquid during collection, which affects the dilution factor, uncertainties on the weighing of the collected fraction). The data obtained were fitted with a Gaussian function. The obtained value of FWHM for experimental data is equal to 550±190 µm. This result is twice as high as the simulated value (321±5 µm). Moreover, even taking into account the uncertainties, we observed that the data were not perfectly reproducible.

[51] *This value was deduced from the masked photodiode current measurements (Figure IV-7, grey symbols).*

In order to check the linearity of the benzoate response, irradiation series were performed by varying the exposure time (20 min, 40 min, and 60 min). Two similar experiments were performed on the same batch of 10 mM benzoate solution (Figure IV-8).

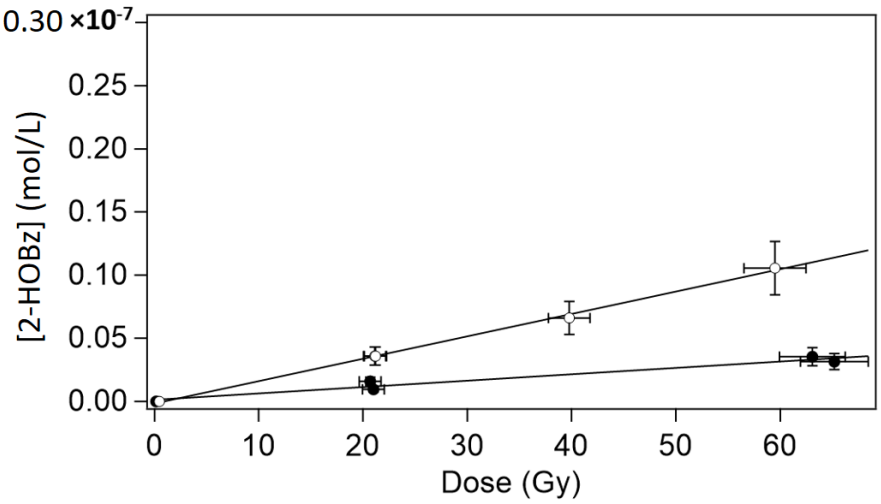

Figure IV-8: Evolution of the 2-HOBz produced in irradiated benzoate solution in non-flowing irradiations. Two series of experiments (plain and empty symbols) are presented as function of the calculated average dose.

The only difference between the two experiments is that the whole microfluidic device was rinsed with pure water between the two sets of measurements. The curves show a linear evolution of the 2-HOBz concentration with the dose. However, the slopes are different for the two series of irradiations performed in the same conditions. More precisely, in static conditions, the two obtained 2-HOBz production yields were $G(2\text{-HOBz})^{static}_{10mM}=1.8 \cdot 10^{-3}$ µmol/J and $G(2\text{-HOBz})^{static}_{10mM}= 4.7 \cdot 10^{-4}$ µmol/J. Therefore, the results are one or two orders of magnitude lower than the results obtained with the static cell, which were in the range of 10^{-2} µmol/J. These results seem to indicate an over-consumption of benzoate or dissolved O_2, in the microfluidic cell, under static conditions. It should be noted that the dose rate in the portion of the microfluidic channel exposed to SXs is in the same order of magnitude as the dose rate at the surface of the solution in the 1-cm thick static cell[52]. In the 1-cm thick cell, however, diffusion along the s-axis prevents a depletion in benzoate and oxygen[57]. The thickness of the microfluidic channel (5.3 µm) here appears insufficient to prevent over-consumption of benzoate and/or O_2,

[52]*The cells windows are positioned at exactly the same distance from the exit widow of the IRAD setup.*

under static conditions, at such high dose rates (hundreds of kGy/min at 1280 eV, see Table III-1 in Chapter III).

In order to investigate the over-consumption of the dosimeter, experiments could be performed using higher concentrations of benzoate salts. However, the fact that fluidic conditions help to solve this problem by renewing the fluid seems to indicate that the diffusion of the species is the limiting factor. In the case where oxygen is the limiting factor, one could consider experiments conducted with solutions saturated in oxygen. However, in this case, the renewal of the solution also appeared as a better strategy.

IV.3.2. Proof of concept in dynamic conditions

Following the evident limitation of the set-up when performing static irradiations, the behavior and sensitivity of the dosimeter inside the microfluidic cell were then evaluated by performing irradiation in dynamic conditions. More precisely, a solution of NaBz (10 mM) was injected at a fixed flow rate. Flowing solutions were irradiated at 1.28 keV and collected in order to measure their fluorescence. Once a sample was collected, we moved the position of the cell along the x-axis in order to profile the beam spot horizontally. This process was repeated at different times during the beamtime.

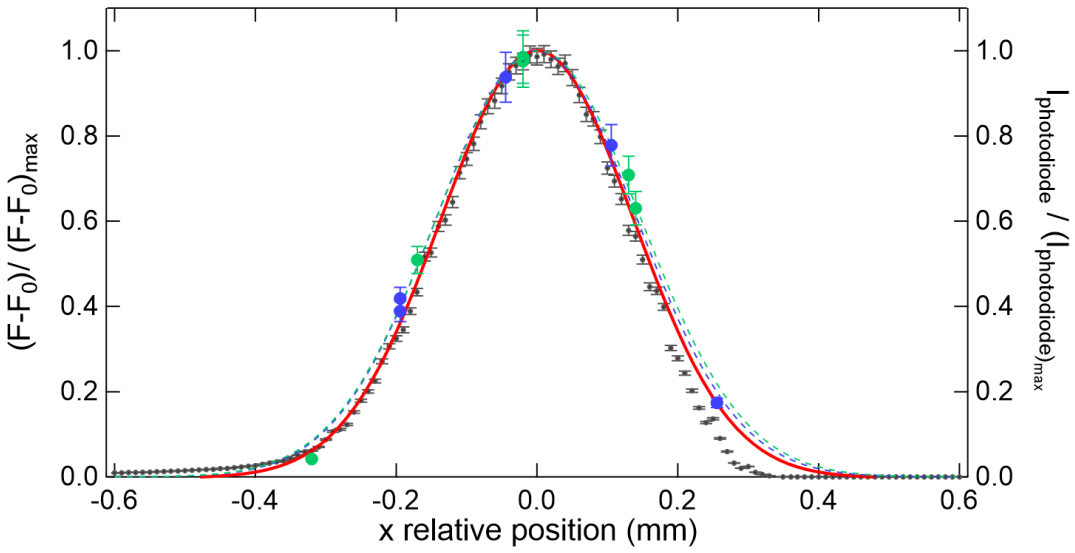

Figure IV-9: Normalized fluorescence signal (to the signal at X= 0 mm) resulting from the irradiation at 1.28 keV of two batches of 0.01 M benzoate solution, in the microfluidic dosimetry cell. Solutions were irradiated at respectively 5 µL/min (green) and 8 µL/min (blue). As for static irradiations, data were compared with the signal measured on the masked photo-diode (grey symbols) and the simulated beam profile (red).

Two different batches of 10 mM NaBz solutions were successively used to detect potential reproducibility issues and were flowing at respectively 8 µL/min (blue symbols) and 5 µL/min (green symbols). As for static irradiation performed using the microfluidic cell, results were compared to the signal of the photodiode (grey symbols) and the calculated convolution (red curve). Ex-situ fluorescence signals of irradiated samples were normalized to the maximum signal and plotted as a function of the microfluidic cell relative position along the x-axis. Error bars were calculated considering the dispersion of the fluorescence calibration curve. The curves representing the normalized fluorescence intensity for the two different flow rates entirely overlap and can be well fitted by Gaussian functions (dotted lines) with full width at half-maximum (FWHM) equal to 342±17 µm for Q = 5 µL/min and 336±15 µm for Q=8 µL/min. This value of FWHM is in complete agreement with the 321 µm expected by the simulated beam profile (convolution of the beam's signal with a rectangular function). These fluorescence measurements ensure that the fluorescence response of the irradiated dosimeter is proportional to the received beam intensity in the whole range of the experiment. It also highlights the high sensitivity of the dosimeter as the difference between the FWHMs calculated and experimentally measured is less than 10%. Finally, it must be noted that the cell's centered position, determined by fluorescence measurement or using the photodiode centered position and the distance between the two devices (measured with an optical level, see Chapter III for more details), never exceeded a 20 µm difference. It, therefore, demonstrates the correct positioning of the dosimetry cell in front of the beam.

In order to bring a step further the implementation of the microfluidic cell, in dynamic conditions, as a dosimeter, the production yield of hydroxyl radicals was evaluated by quantifying the 2-HOBz concentration in irradiated solutions of various concentrations. Results are presented as a function of the dose in Figure IV-10.(a). As expected, a linear evolution is observed. Once all uncertainties are evaluated, data can be fitted to linear functions. The G($HO^{\cdot}$) values deduced from these curves are presented in Table IV-2.

Table IV-2: G(HO$^{\cdot}$) production yield determined through the quantification of 2-HOBz produced in sodium benzoate solutions under γ-rays and SXs irradiation. The data obtained in 2015 using the static cell are highlighted in grey.

[NaBz]		0.01 M		0.1 M (2020)	1 M (2020)
G(HO$^{\cdot}$) (µmol/J)	**1.28 keV**	0.038 ±0.004		0.040 ±0.006	0.032 ±0.017
	^{137}Cs	0.261 ±0.015		0.346 ±0.038	0.346 ±0.042
	1.28 keV	0.025 ±0.004 (2019)	0.024 ±0.004 (2020)	0.026 ±0.003	0.026 ±0.003
	^{137}Cs	0.261 ±0.015		0.391 ±0.032	0.382 ±0.035

Newly determined G(HO$^{\cdot}$) values were found slightly lower (given uncertainties) than those obtained using the static cell. In order to control the behavior of the solutions," reference irradiations using ^{137}Cs γ-rays were carried out (Figure IV-10.(b)). These results were found similar to those from previous analyses conducted in 2015.

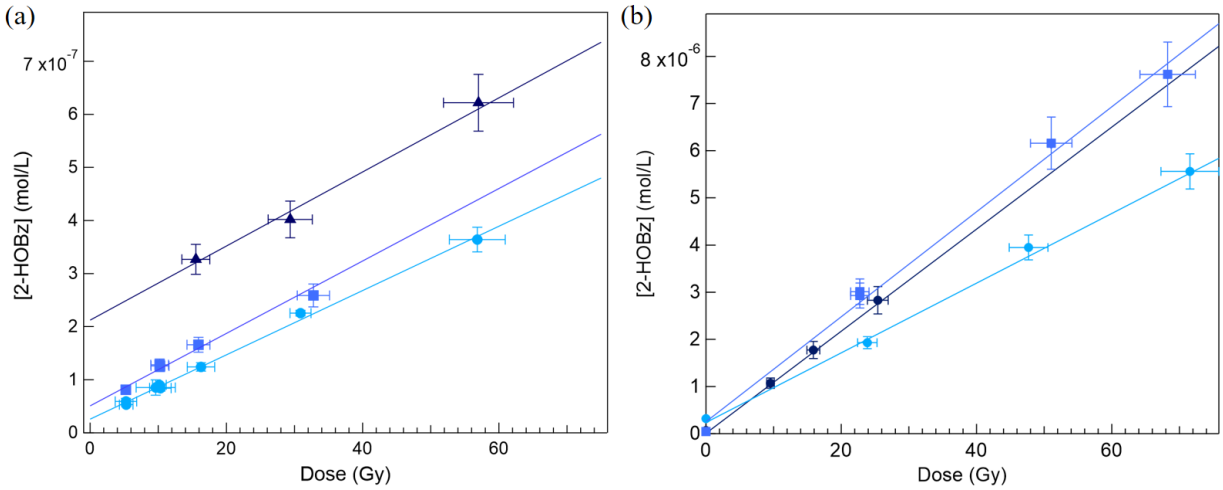

Figure IV-10: Quantification of the 2-HOBz formed upon irradiation in benzoate solutions of various concentrations (0.01, 0.1 and 1 M, from light blue to dark blue) (a) Results obtained with 1.28 keV X-rays using the microfluidic cell in dynamic conditions. (b) Gamma reference irradiations. Data are fitted with a linear curve in order to retrieve the production yield of hydroxyl radicals.

As shown in Table IV-2, production yields obtained during the two different beamtimes (2019 and 2020) are identical. The similarity of these results, recorded one year apart, attests to the robustness of the method. Moreover, these values are in good agreement with the production yield value reported by Vysin and co-workers ($G(HO^{\cdot})_{\text{terephtalic acid}}$ = 0.023±0.003 µmol/J), measured in the energy range of the water

window (284-543 eV). Finally, the constant value of the production yield over the wide concentration range tested is in entire agreement with the high LET behavior of SXs as observed in static studies [57], [70]. Finally, it can be noted that the time needed to collect and irradiate one sample at 30 Gy (flow rate ~5 µL/min) is approximately 1 hour, whereas it took almost three times as long to reach the same dose in the 1-cm thick static cell (see Table III-5 in Chapter III for more details). Therefore even if, to some extent, the error bars (~15%) can appear somewhat high, the number of samples collected and the reproducibility of the experiments demonstrate the robustness of the method.

IV.4. Probing K-shell threshold effects

IV.4.1. Solvated metallic ions K-shell

X-rays ionization cross-sections, for a given atom, are much more significant for K-shell electrons (core electrons) than those of outer-shell electrons (one order of magnitude higher)[59]. Therefore, in most cases, photoionization will lead to photo-electrons (PE) production and the emission of AE. Performing SX irradiations allow to access to K-shell photoionization energies. More precisely, it is possible to irradiate below and above the K-shell to probe threshold effects [71]. K-shell ionization experiments on biological samples at C, N, O, and P thresholds demonstrated an efficient inactivation following the irradiation[72]. In other works, bromine atoms were introduced in DNA samples to improve radiobiological efficiency [73]. Even if a minor element, it seems that Auger decay following Br K-shell photoionization, naturally present in cells, could have a significant impact[74], [75]. Following this logic, metallic ions are of main interest as they are vital elements in biological systems. Thanks to their redox properties, transition metals (Fe, Zn, Cu, Cd) and non-transition metal ions (Na, K, Mg, Ca) indeed play significant roles in living systems, such as in electron transport processes or catalytic reactions [76]. In such a context, scientists try to get deeper knowledge of organometallic biomolecules' physico-chemical properties. Many studies evidenced that radiation damages induced to metalloproteins were site-specific[77]–[79]. In particular, they demonstrated the fragility of the metallic center, which is often easily damaged[80]. It is becoming increasingly evident that radiation induces oxydo-reduction of the metallic center ions[81], [82]. This change in the metal's charge is thought to influence the active site's geometry, but it can also lead to a cascade of events. More recently, Cederbaum and his colleagues performed *ab initio* calculations to investigate the effect of core-ionizations at the solvated magnesium ions $Mg^{2+}(H_2O)_6$ K-edge, located at 1317 eV[83]. The emitted AE could interact with the system, causing secondary ionizations; resulting in significant damage to surrounding molecules[84]. This computational experiment showed that the core-ionization of the metallic ion would result in energy or charge transfers to the surrounding water molecules (through ICD and ETMD, see Chapter I section I.1.2.iii). The first solvation shell, thus ionized, would lead to the production of highly reactive species such as hydroxyl radicals

(in the case of single ionization, ICD or ETMD(2)) or superoxide radicals ($O_2^{\cdot-}$) (in the case of double ionization, ETMD(3))[85]. Using the benzoate system, as a direct probe of hydroxyl radical, and the newly developed microfluidic device, we therefore decided to irradiate aqueous samples containing metallic ions. More precisely, we dissolved magnesium and sodium sulfate salts (respectively $MgSO_4$ or Na_2SO_4 1 M) in benzoate solutions (10 mM). The choice of sulfate counter ions is motivated by the fact that no addition or oxidation reactions have ever been reported. It guarantees that the salts are not chemically involved and allows to focus on the photoionization of the metallic center.

Using the IRAD set-up on the METROLOGIE beamline, energies ranging from 1 keV to 1.4 keV are easily accessible and do not imply any modifications of the monochromator's gratings. The stability and high monochromaticity of the beamline provide the perfect environment to carry out experiments to investigate threshold effects. At ~8 µL/min, the average dose deposited in the sample ranges between 8 and 10 Gy, depending on the photon energy. Irradiations were conducted on a given solution at a fixed flow rate, varying the photon energy. Collected samples were weighted, and the experimental volume of liquid was compared to the one measured by the flowmeters. A perfect match was observed between the two measurement procedures during the three days of the experiment[53]. Several samples were collected for each photon energy to ensure the reproducibility of the experiment. When changing the solution, the entire microfluidic circuit was rinsed with water. Non-irradiated solutions were again collected and analyzed by fluorimetry as controls. Two batches of solutions were used at different times of the experiment to check the reproducibility. Data obtained for the two batches were averaged following the experiments conducted at photon energies below or above the K-edge (respectively, Na at 1070 eV and Mg at 1320 eV)[54]. The standard deviation of the results was used to calculate the error on each production yield. Results are displayed in Figure IV-11. Dose determination takes into account the absorption coefficient of the different solutions[86]. It must be noted that less than 10% of the photons are directly absorbed by the metallic ions (Na or Mg) above the K-edges.

[53] *It must be noted that the pressure was sligthly increasing during the experiment suggesting that the system was slowly clogging. However, the irradiations were conducted by monitoring the flowrate ensuring the stability of the system.*

[54] *For a given solution, no energy-dependence was indeed observed below (or above) the K-edges, given uncertainties*

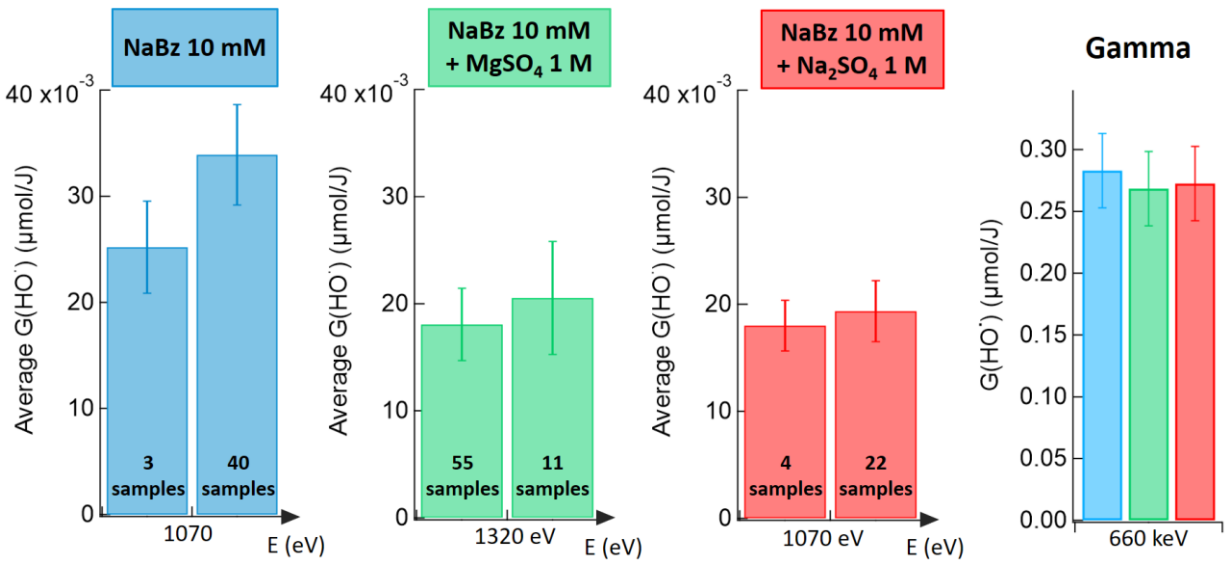

Figure IV-11: Production yield of hydroxyl radicals below and above metallic ions K-edge threshold (sodium or magnesium). Comparison with data obtained at 660 keV (Gamma-rays).

As observed in Figure IV-11, no threshold effect is observed around the Na or Mg K-edges. Good reproducibility of the results was observed, as shown by the error bars. However, we noted that the production yield of pure benzoate solutions (blue) remains two times higher than the production yield of sodium (red) or magnesium (green) solutions. However, this trend is not noticed for γ-rays irradiation, where the production yields are identical for the three solutions.

Ions are known to modify the structure and dynamics of water molecules in their first to third solvation shells[87]. Therefore, it is suggested that such modifications will impact water molecular properties (viscosity, hydrogens lability, charge distribution). However, the impact on the hydrogen bonding network is still highly discussed in the literature[88], [89]. It seems that the main question is the number of water molecules affected in the process. More precisely, hydrogen bonding is considered to change only in the ions solvation shell but not in the bulk. It could explain why ultra-fast spectroscopic methods (such as Nuclear Magnetic Resonance) did not evidence any salts effect on the hydrogen-bonding network[90]. In contrast, other studies have suggested that ions and counter-ions influence the orientation of the solvent[91].

Nevertheless, it is clear that the presence of ions will rigidify the water solvation shell[92]. Experimentally, we did notice a change in the dynamic viscosity of the different solutions.

Measurements were performed with an Oswald viscosimeter and are presented in Table IV-3. Experimental values were found in good agreement with the literature[93]. Therefore, the diffusion rates of the chemical species are decreased by a factor of nearly two in the highly concentrated salts solutions. However, the computational study of Cederbaum and co-workers suggest that hydroxyl production occurred through ICD and ETMD. Such processes are localized at the metallic center, and the diffusion processes should not highly impact surrounding molecules. Still, the high concentration of salts increases the ionic strength of the solution (values in Table IV-3), which could impact the electronic properties of the solution. Such modifications will modify the distribution of the ions in the solution and can affect ion pairing[89], [94]–[96].

Table IV-3: Molecular properties of the solutions tested.

		NaBz (10 mM)	Na_2SO_4 (1 M) + NaBz (10 mM)	$MgSO_4$ (1 M)+ NaBz (10 mM)
Density (kg/L)		≅1	1.12	1.16
Viscosity (cP= mPa · s)		1.04	1.64	1.94
Ionic strength		0.005	3.005	4.005
Fraction of photons absorbed in (%) **after the K-edge (1.08 and 1.32 keV respectively)**	Metallic ion (Na or Mg)	0,05% (Na, 1080eV)	8.8% (Na, 1080eV)	6.1% (Mg, 1320eV)
	In water	99.87% (1080eV)	83.5% (1080eV)	85.9% (1320eV)
	In SO_4^{2-}	none	7.7% (1080eV)	7.9% (1320eV)

The primary interrogation remains in the difference of behavior observed in SXs and γ-rays irradiations, where the production yield is equal for the three conditions. By investigating the hydroxyl radical production at a long time scale (~hundreds of ns)[55], we are looking at the final result of three steps:

a) The physical deposition process (core-ionization and subsequent PE and AE production) during which water and solute molecules are excited or ionized
b) The physicochemical step during which the radiolysis of previous ionized/excited molecules conducts to the production of initial molecular and radical species.

[55] *Scavenging time for a 10 mM benzoate solution.*

c) The heterogeneous chemical process during which the generated species diffuse from their initial position along the track and react with each other.

In order to evaluate how the high concentration of salt can affect the physical deposition process (a), we measured the total production of electrons under SXs exposure. This experiment was conducted using the XPS liquid jet set-up (see section II.2.1.iii for technical details). Measurements were performed on the three previous solutions, using a 1 keV photon beam (corresponding to the highest reachable photon energy on the PLEIADES beamline, where the experimental end-station was installed). A bias of 70 V was applied to the liquid jet to measure low kinetic energy electrons (until the secondary electron cut-off regions[56]). Recorded total spectra of emitted electrons are presented in Figure IV-12.

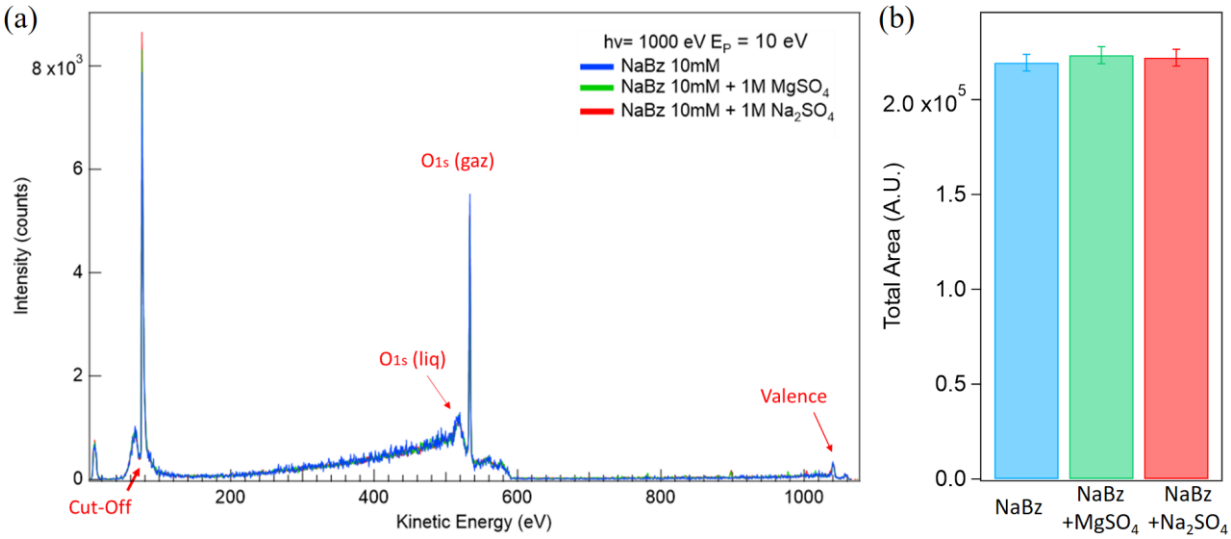

Figure IV-12: (a) Total XPS spectra of salts solutions recorded in the liquid micro-jet at 1 keV photon energy. A bias of +70 V was applied on the liquid jet to accelerate electrons from the cut-off (low kinetic energy electrons), (b) Comparison of the total area under the curves for the three solutions : NaBz 10mM (blue), NaBz 10mM+$MgSO_4$ 1M (green) and NaBz 10mM+Na_2SO_4 1M (red).

As observed from Figure IV-12, the PE spectra of the different solutions exposed to 1 keV photons are almost indistinguishable. Therefore, the difference in the hydroxyl production yield did not originate in an over-production of secondary electrons or differences in the spectrum of the emitted electrons.

[56] *As a reminder, the majority of secondary electrons undergo inelastic scattering events while going out of the liquid. Because of these inelastic collisions, these secondary electrons are ejected out of the material with reduced kinetic energy creating the "cut-off" region.*

Experimentally, it is impossible to decipher the effect of the presence of salts during the physicochemical step. Indeed, it is impossible to increase benzoate concentration, as previously done in section IV.2, to probe shorter time scales. The main reason is that the solution is already saturated with one mole of metallic sulfate salts. Adding more solute would therefore conduct to the formation of precipitates. However, using MC simulations, it is possible to have some hints[57] as to how the modification of the properties of the solution (presented in Table IV-3) will affect the production of $HO^{\cdot}$ radicals within the track. Calculations were performed by Jean-Philippe RENAULT, using the Geant4-DNA code [68]. The effect of density and viscosity were directly introduced by modifying the simulation's parameters. The effect of ionic strength (I) is usually introduced through the kinetic constant (k) through the relation of Bronsted-Bjerrum[97]:

$$\log_{10}\frac{k}{k^o} = 1.018 \cdot z_a \cdot z_b \cdot \left(\frac{\sqrt{I}}{1+\sqrt{I}} - 0.3 \cdot I\right) \quad \text{(IV-3)}$$

With

$$I = \frac{1}{2}\sum c_i \cdot z_i^2 \quad \text{(IV-4)}$$

Where c_i is the concentration and z_i the atomic charge (z_a *and* z_b for respective the reacting ions a and b).

The time evolution of G($HO^{\cdot}$) was simulated for particles of different LET, changing the solution's density, viscosity, and ionic strength (see Figure IV-13). The kinetic and diffusion constants are detailed in Appendix IV. MC simulations show that the only effect of increasing the density[58] is to reduce the final (primary) $HO^{\cdot}$ yield. In addition, this effect is higher for high LET particles (-10%) than for low LET particles (about -2%). The viscosity increase affects both initial and final yields. It is quite dramatic in this later case, as the primary yield decrease is about 45% for high LET particles and 35% for low LET. Changing the kinetic constants to take into account an increased ionic strength partially counteracts this strong depletion. Finally, if all these effects are taken into account, we find a 12% decrease at low LET (10 keV/µm) and a 30% decrease at high LET (500 keV/µm) for concentrated salts solutions, compared to pure liquid water. Thus, the

[57] It must be noted that even if MC calculations provide a very good representation of high energy electrons tracks (the theoretical G($HO^{\cdot}$) are very close to the measured one at 100 keV), theoretical results in the soft X-ray range remain far from the measured one. This was already shown in section IV.2, when comparing experimental G($HO^{\cdot}$) measured at ~1 keV.

[58] Each parameter was also varied separately (data not shown).

addition of the different effects during the chemical stage can most probably explain our observations.

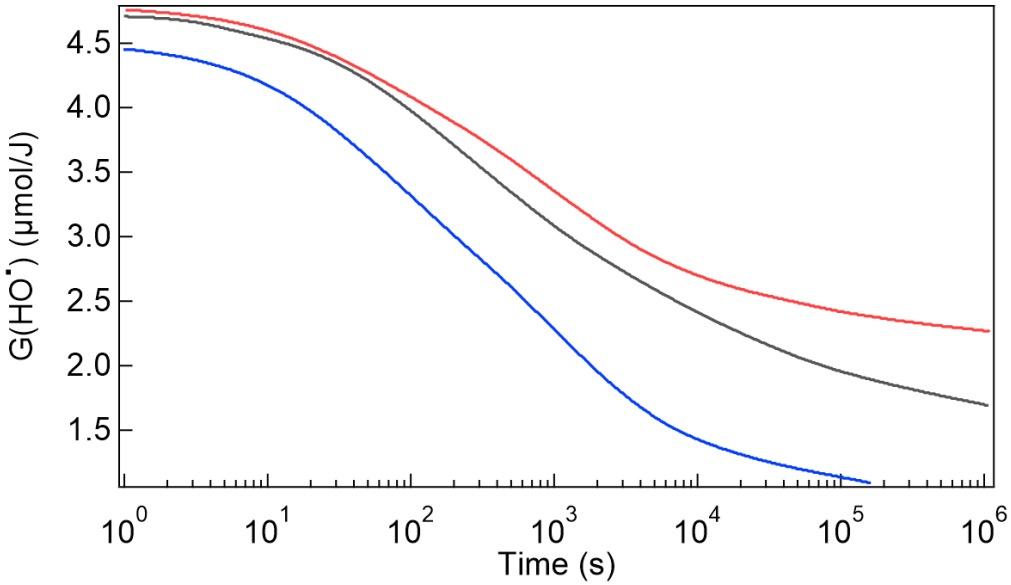

Figure IV-13: Time evolution of G($HO^{\bullet}$) yields. Monte-Carlo simulations were performed for 100 keV/µm (red), 10 keV/µm (black) and 500 eV/µm (blue) particles in a solution of 1.2 kg/L (reactions rates can be found in Appendix 4).

One last hypothesis that remains concerning the absence of variation at the K-shell thresholds can rely on the specificity of the probe used in the study. Indeed, it is known that for high LET particles, the yields of ROS species vary from the general scheme of water radiolysis. In particular, su**per**oxide radicals production seems to increase in the tracks of high LET particles[98]. A similar evolution is predicted for water molecules' multiple ionization[99]. Both of these particular events should also be produced when liquid water is exposed to SXs, above the O-K edge. Therefore, it could be interesting to vary the scavenging system to go a step further in describing the chemical processes induced by SXs irradiation.

IV.4.2. Towards the detection of superoxide radicals

IV.4.2.i. Superoxide radicals redox-based indirect assay

The superoxide radical ($O_2^{\bullet -}$), although a free radical, is not considered a particularly damaging species; unless it evolves and contributes to the production of more damaging

species[100]. For instance, several studies evidenced the crucial role of $O_2^{\cdot-}$ in aging processes and subsequent diseases, such as Parkinson's disease or cancer. Following these discoveries many direct or indirect methods were developed for the quantification of $O_2^{\cdot-}$ [101]. Most of these methods are scavenging methods. The detection technique, therefore, depends on the properties of the generated product. Among common scavengers of superoxide radicals, we focused our interest on the ferri-cytochrome c and tetrazolium salts[102]. Both scavenging reactions lead to the production of colored probes. The quantification of $O_2^{\cdot-}$ is thus performed using UV-Vis spectrophotometry. In order to validate the specificity of the reaction, irradiations were also carried out in the presence of superoxide dismutase (SOD). Naturally present in biological environments, this family of enzymes plays a crucial role in regulating oxidative stress[103]. This efficiency relies on their ability to catalyze the dismutation of $O_2^{\cdot-}$, as illustrated in the following equation:

$$2O_2^{\cdot-} + 2H^+ \xrightarrow{SOD} H_2O_2 + O_2 \qquad \text{(IV-5)}$$

$$\mathrm{k} = 4.93 \cdot 10^5\ M^{-1} \cdot s^{-1}\ (\text{at pH} \approx 7)$$

$$\mathrm{k}_{SOD} = 6.4 \cdot 10^9 M^{-1} \cdot s^{-1}\ (\text{at pH} \approx 7\ \text{for Cu} - \text{SOD})$$

The specificity and high efficiency of the reaction are ensured by the metallic center ion contained by these metalloproteins. SOD active centers can be either Fe, Zn, Ni, or Cu based, depending on the type of SOD[104][59]. As shown in Equation (IV-5), the dismutation reaction leads to molecular oxygen and hydrogen peroxide production. Superoxide production can therefore play a role in the re-oxidation of the environment.

- Superoxide scavenging using ferri-Cytochrome c

Cytochrome c (Cytc) is a soluble 12.5 kDa metallo-protein[105], well known in the detection of superoxide[106]–[108]. *In vivo,* this protein is involved in the mitochondrial respiratory chain, ensuring the transfer of electrons[109], [110]. The Cytc structure, Figure IV-14, contains a heme covalently bonded to the peptide chain by two cysteines. This heme c is a porphyrin macrocycle chelating an iron atom, ferrous (Fe^{2+}) or ferric (Fe^{3+}) state. Our solutions were prepared with ferri-cytochrome c. This oxidized form allows the protein to react with the superoxide anion radical to form the ferro-heme[111]–[113]:

$$O_2^{\cdot-} + [CytC]^{3+} \rightarrow O_2 + [CytC]^{2+} \qquad \text{(IV-6)}$$

[59] *The one used here contains two zinc atoms and two copper atoms.*

At room temperature (~20°C) and pH of 8.5, the rate constant has been estimated to be k ~ 1.5 $\cdot 10^5 M^{-1} \cdot s^{-1}$[114]. Spectroscopy in the visible allows access to the modifications of the heme's electronic transitions, which reflects the oxidation and ligation state of the heme[115].

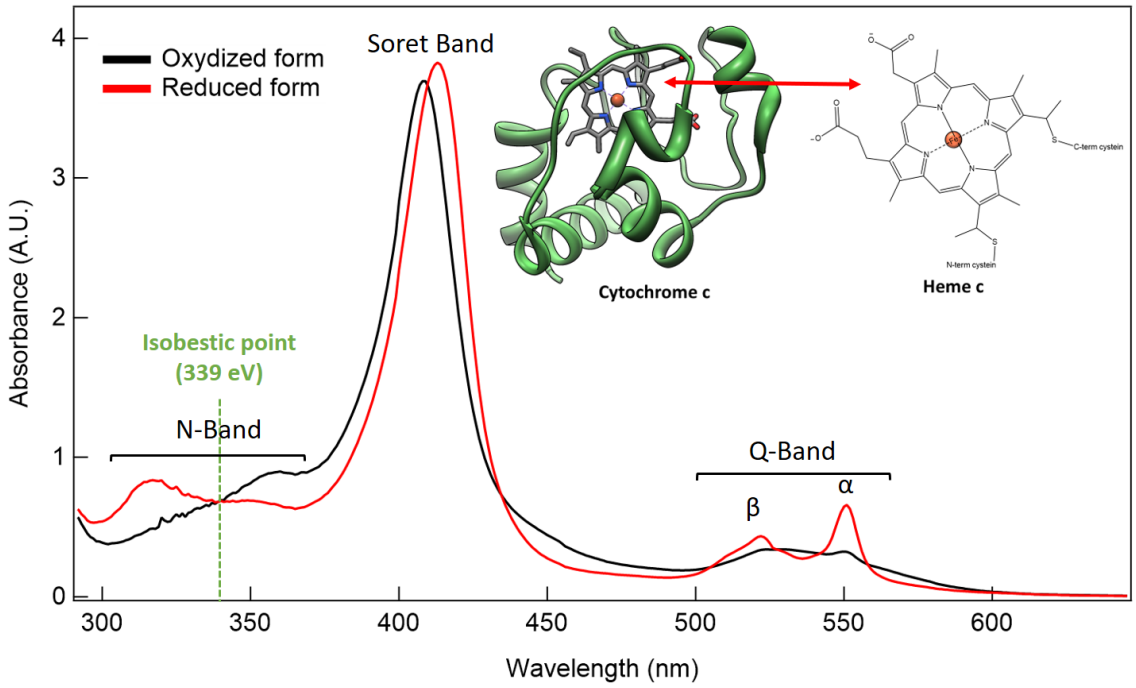

Figure IV-14: Measured absorption spectra of the oxidized and reduced form of the Cytc. Crystallographic structure of the horse Ferri-Cytc [147] *and chemical structure of heme c.*

The main characteristic of the spectrum of Cytc is the intense absorption band at 405–415 nm (B-band)s. This band, namely the Soret band, comes from a $\pi-\pi^*$ transition common in porphyrins[116]. At 500–550 nm is located the Q-band and at 310–370 nm is the N-band[60]. The Q band of the reduced form is split into two bands (α and β), as illustrated in Figure IV-14. The extinction coefficients were determined at 410 nm (absorption maximum of the Soret band of the oxidized form) and at 339 nm (isosbestic point) using a concentration range (15 to 500 µM, see Appendix V.1). Experimental measurements, $\varepsilon^{410nm}_{Ferri-Cytc}$= 103 800 ±200 $M^{-1} \cdot cm^{-1}$ and $\varepsilon^{339nm}_{Ferri-Cytc}$= 21 100 ±200 $M^{-1} \cdot cm^{-1}$, were found to be very closed to those of the literature[117].

[60] *Named after the Fischer-Stern and Platt-Gouterman nomenclature systems*

- Superoxide scavenging using tetrazolium salts

Colorimetric assays based on Tetrazolium salt compounds are well known for $O_2^{\cdot-}$ detection. Dyes such as NBT (Nitro-Blue Tetrazolium)[118], [119] or MTT (3-(4,5-Dimethylthiazol-2-Yl)-2,5-Diphenyltetrazolium Bromide)[120] are easily reduced by superoxide species. It leads to the generation of an indigo/purple-blue-colored diformazan form[120]. Although widely used in biological studies, these methods are limited by the low solubility of diformazan in water. Water-Soluble Tetrazolium salts (WST) have therefore been designed from the NBT structure to improve the solubility of such compounds [121]–[123]. More precisely, hydrophilic groups such as sulfonate groups were added to the phenyl ring of the tetrazolium salt. The WST-8, presented in Figure IV-15, reacts with $O_2^{\cdot-}$ and leads to an orange-colored formazan form (λ_{max}(formazan)= 460 nm)[120], [124].

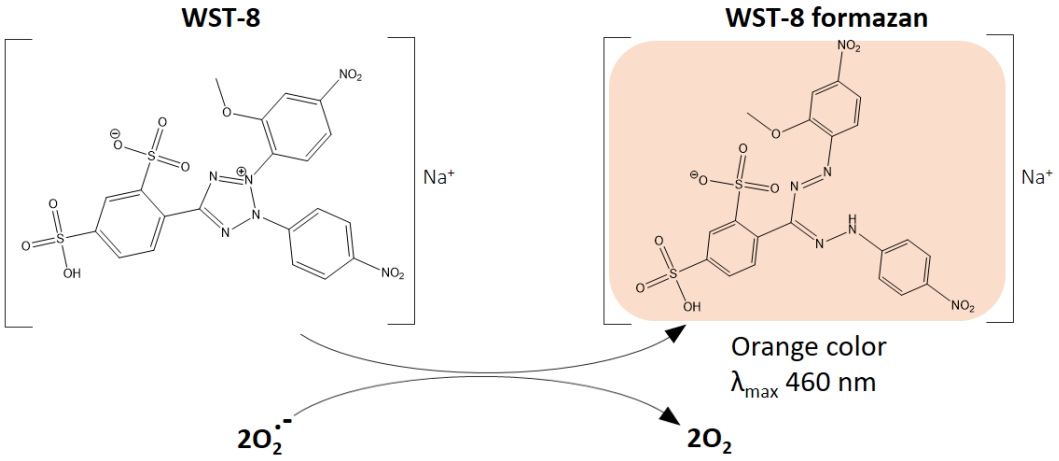

Figure IV-15: Superoxide radical scavenging reaction by Water Soluble Tetrazan-8.

This chemical probe presents a higher extinction coefficient for the formazan product ($\varepsilon_{460\ nm} = 3.07 \cdot 10^4\ M^{-1} \cdot cm^{-1}$) than cytochrome c[125]. Moreover, the initial tetrazan form does not absorb at 460 nm, which improves formazan detection's signal/noise ratio. Finally, this commercially available molecule has been widely used in enzymatic assays and NADPH detection[126]. It is well suited to our experiments as it presents a great sensitivity and efficiency at neutral pH[124].

IV.4.2.ii. Setting up assays performing γ-rays irradiation

- Cytochrome C

In order to investigate the behavior of the Cytc under irradiation, we first conducted γ-rays irradiation (Figure IV-16). Solutions of horse ferri-cytochrome c (45 µM) were prepared in phosphate buffer (20 mM) to maintain the pH at ~7.2 and irradiated with ^{137}Cs γ-rays, varying the exposure time. Solutions were also prepared, adding superoxide dismutase (SOD, 5 µM per sample) and irradiating under similar conditions to confirm superoxide production.

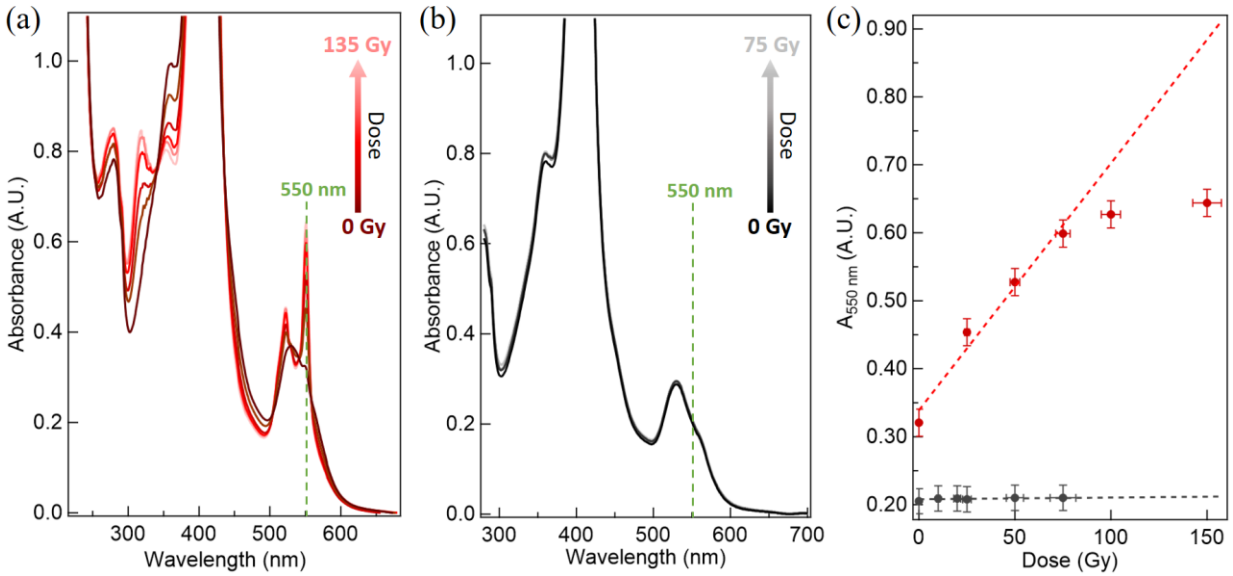

Figure IV-16: UV-Analysis of gamma irradiated solution of ferricytochrome c (45 µM in 20 mM phosphate buffer, pH =7.2) in aerated condition. Absorption spectra (a) without SOD (b) in presence of SOD (5 µM), (c) Optical density (OD) at 550 nm as function of the dose and fitted by a linear regression (y=a +bx). Fitting parameters were found to be a=0.339±0.006 and b=0.0036±0.0004 (OD/Gy). Vertical error bars indicate the standard error of the mean. Horizontal error bars correspond to the 6% random uncertainty on the dose.

The lack of change in the UV-spectral signature of Cytc in the presence SOD (Figure IV-16.(b)) ensures that the reduction of Fe^{3+} to Fe^{2+}, under γ-rays irradiation, is due to the production of superoxide. Indeed, without SOD (Figure IV-16.(a)), the characteristic signatures of the reduced form, the Q and N-bands, are observed. The profile of the Soret band (maximum at 410 nm) is presented in Appendix V.2. The optical density at 550 nm (α-band) increases linearly with the dose, up to ~80 Gy (Figure IV-16.(c)). In the literature, the difference of the extinction coefficient for the reduced and the oxidized form

of cytochrome c at 550 nm is known to be $2.1 \cdot 10^4\ mol^{-1} \cdot cm^{-1}$ and is independent of the pH[127], [128]. It is, therefore, possible to evaluate the production yield of superoxide radicals ($G(HO_2^{\cdot}/O_2^{\cdot-})$). A linear fit to the data allowed to estimate the $G(HO_2^{\cdot}/O_2^{\cdot-})$~ 0.17±0.01 µmol/J in aerated conditions. At higher doses, we noticed that the optical density reached a plateau suggesting that the protein is degraded.

- Water Soluble Tetrazolium probe (WST-8)

WST-8 samples (300 µM) were irradiated with γ-rays, with and without SOD (similarly to previous Cytc samples). The UV spectra are shown in Figure IV-17. The maximum absorbance at 460nm was used in Beer-Lambert's law to determine the concentration of formazan produced ($\varepsilon_{460\ nm} = 3.07 \cdot 10^4\ M^{-1} \cdot cm^{-1}$).

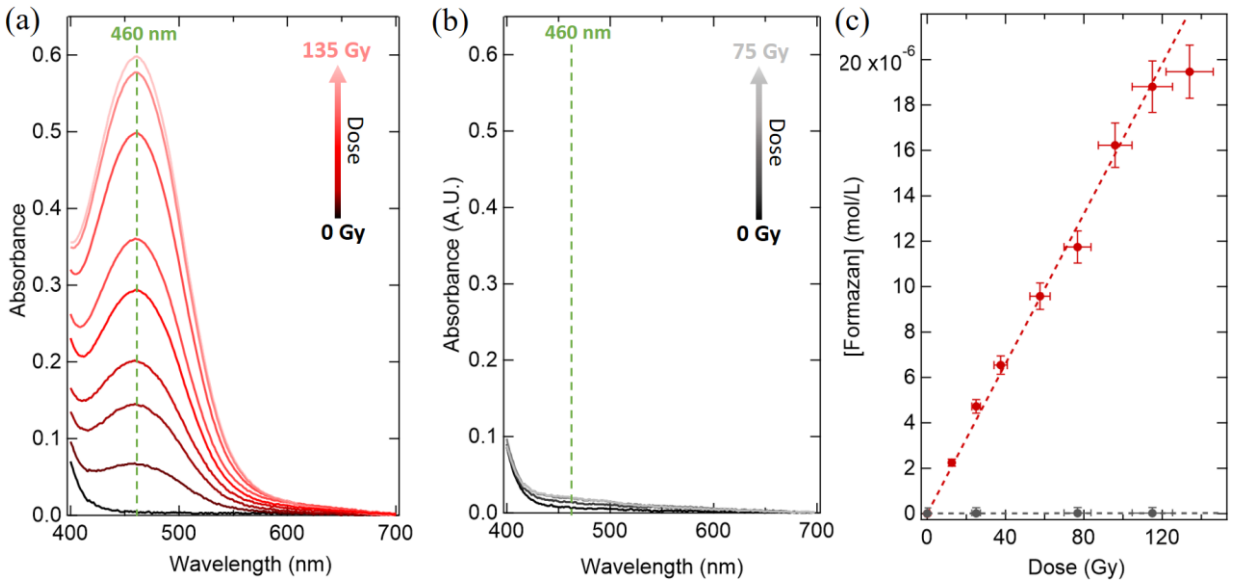

Figure IV-17: UV-analysis of 300 µM WST-8 aerated aqueous solutions, irradiated by gamma-rays. UV-spectra of solutions irradiated with increasing dose (a) without SOD and (b) adding 50µg/mL SOD ; (c) Evolution of the formazan concentration with the dose. Data (without SOD) are fitted to a linear curve (dotted line). The slope is equal to 0.165±0.003 µmol/J (r^2=0.997).

A linear increase in formazan concentration was observed, varying the dose deposited, as shown in Figure IV-17.(c). With the WST8 solution, the saturation was observed only for doses higher than 100 Gy. The superoxide production yield was found to be equal to $G(HO_2^{\cdot}/O_2^{\cdot-})$~ 0.165±0.003 µmol/J. This value is similar to the one measured previously with the Cytc, given uncertainties.

IV.4.2.iii. Irradiation by soft X-rays

When working on the synchrotron beamline using the microfluidic device, the WST8 probe was first selected, given its ease of use and high signal/noise ratio. In order to improve the detection process, an online UV-Vis detection cell was implemented (see Chapter III, section III.5.2.ii for more details). This setup allows measuring the absorption of the solution only 10 µL downstream the irradiation zone. Therefore, collecting the sample is no longer necessary. Moreover, closing the shutter allows having a direct comparison with non-irradiated samples. The signal/noise ratio was thus noticingly increased. For instance, the signal measured for samples exposed to a dose of 25 Gy is approximately two times higher than the signal of the non-irradiated sample in the case of Cytc solutions. In contrast, it is 50 times higher in the case of WST-8 solutions.

During "online" detection experiments, the WST-8 solutions were irradiated at different flow rates to vary the dose. Between each irradiation, the cell was displaced 0.7 mm along the x-axis. This misalignment allowed to measure the signal of the non-irradiated sample. This choice to move the cell instead of shutting the beam was motivated by the fact that the translation motors are computer-controlled. It can thus be synchronized with liquid injection programming. Hence, the WST-8 chemical probe solution was injected using a program controlling the hydrodynamic parameters (flow rate and inlet pressure). For a given flow rate, a total volume of 150 µL was irradiated to ensure that the solution reached the detection cell without dilution. Then the cell was automatically moved to the non-irradiating position. During this time, the inlet pressure was increased to 2 bar to rinse the cell with the non-irradiated sample. Figure IV-18 illustrates a series of irradiation performed at 1.1 keV photon energy.

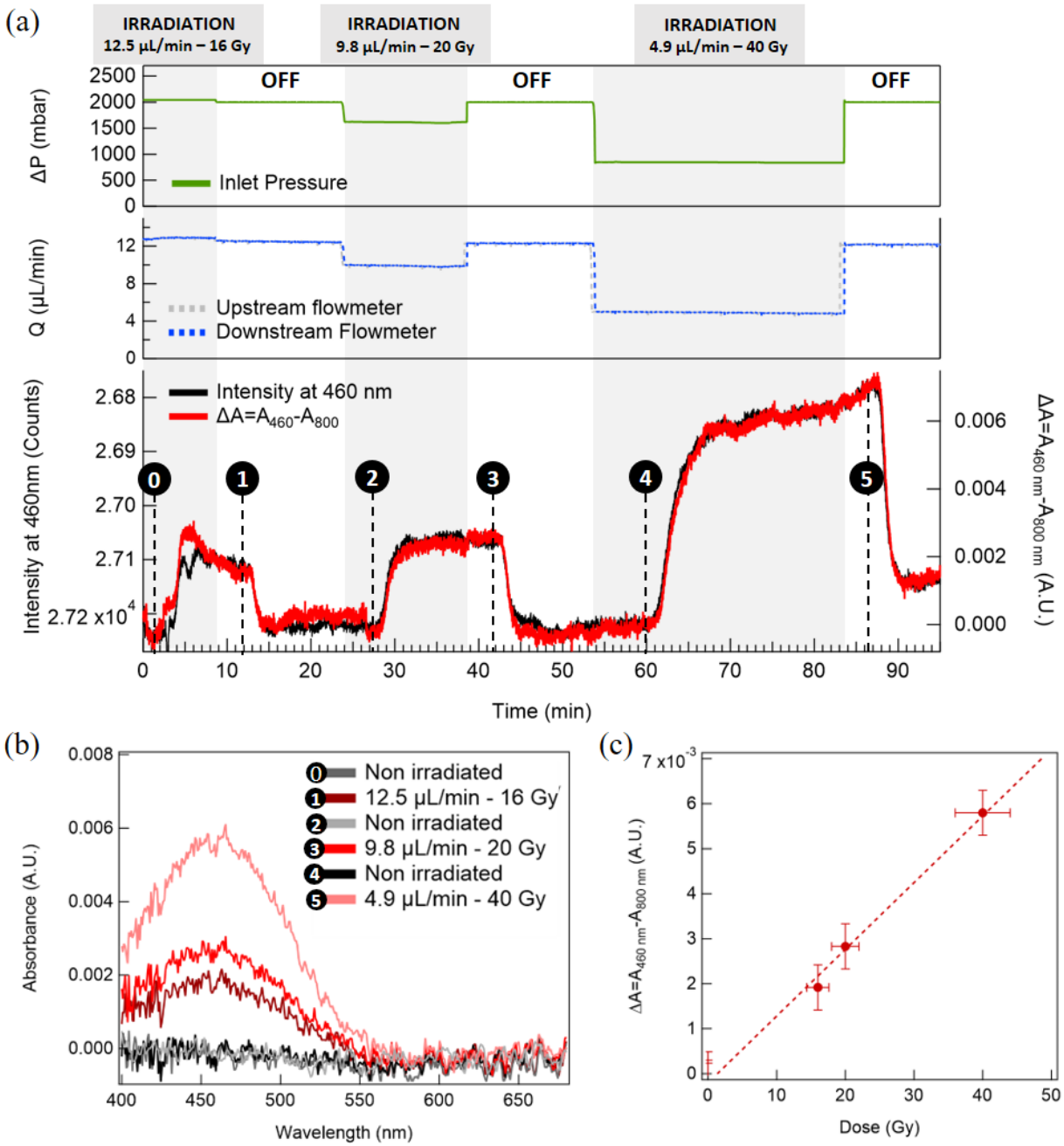

Figure IV-18: Online UV analysis using the detection cell (pathlength 2.5 mm) to measure the formazan produced by 1.1 keV soft X-rays irradiation of a 300 µM WST-8 solution. (a) Time evolution of the hydrodynamic parameters (inlet pressure and flowrates) monitored during the experiment and the intensity at 460 nm and absorbance. The x-position of the cell was synchronized with the flow monitoring to stop the irradiation (misalignment of the cell with respect to the beam). During this time, the pressure is increased to 2 bar to rinse the cell with the non-irradiated sample. This allows successive irradiations, without risk of mixing, and to repeat measurements on the non-irradiated sample. (b) Absorption spectra recorded at the times indicated by the numbers on the trendline (chosen when the trendline signal was stable). (c) Evolution of the absorption maximum (460 nm) as a function of the dose. The data were fitted to a linear regression. The slope is 0.000148±0.000007 (ΔA/Gy).

One can notice that three conditions were tested in only 90 minutes, with doses ranging from ~16 Gy to 40 Gy. It is much faster than when performing off-line analysis. Indeed, a collection volume of 150 µL is required for offline analysis. Moreover, it is necessary to discard all the liquid located downstream of the cell (contained in capillaries and fluidic devices) before beginning the collection. (~200 µL). Therefore the collection of three samples irradiated at the same flow rates (5, 10, and 13.5 µL/min) takes a minimum time of 2h20, and this does not include the collection of non-irradiated samples. During online analysis, the detection cell is located only ~12 µL downstream of the irradiation area. Therefore at 10 µL/min, the signal should be detected after approximately 1-2 minutes. However, as observed in Figure IV-18.(a) (bottom black and red curves), the signal gradually increases before reaching its maximum. This stabilization time depends on the injection rate. Indeed, due to the pressure difference between the injection and collection tubes, a Poiseuille profile appears in the capillaries (see Figure IV-19)[129].

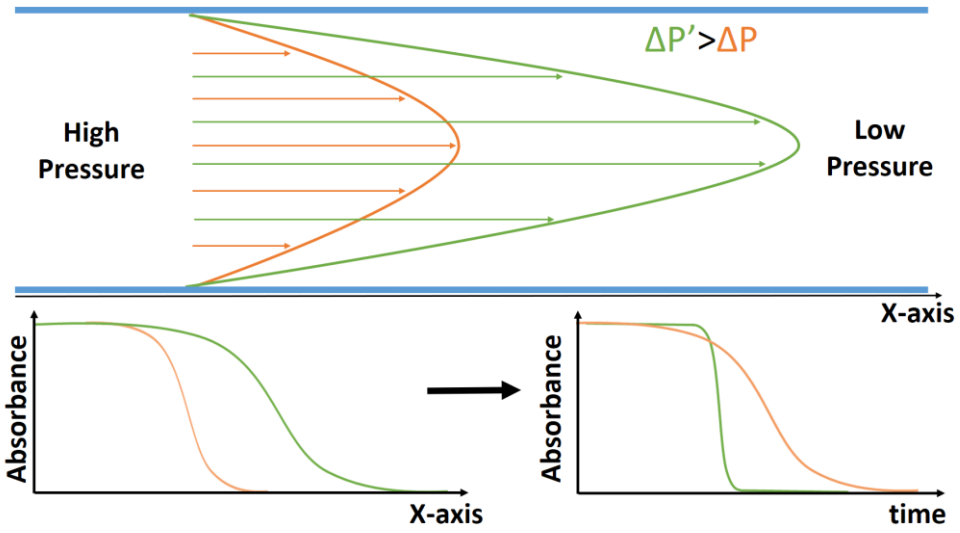

Figure IV-19: (Top) Scheme of the Poiseuille profile of the flowing liquid in a capillary. (Bottom) Scheme of the absorbance measured for different inlet pressures (different flowrates) plotted versus the horizontal (x-axis) position along the capillary (at a fixed time) and versus the time of analysis (at a fixed x position).

Consequently, the irradiated sample (or respectively the non-irradiated one depending on the conditions) is diluted with the non-irradiated (respectively irradiated) sample present upstream in the capillary. The Poiseuille distribution is less critical at a low flow rate than at a high flow rate, where the pressure is higher. However, the fluid is also slower when passing in front of the detection zone. The final time evolution is thus slower than

the one observed at a high flow rate, where the fluid is quickly renewed. It is well illustrated in Figure IV-18.(a) (bottom black and red curves), where the signal of the irradiated sample takes longer to reach its steady-state value than the signal of the non-irradiated sample, which is continuously injected at 2 bar. We notice that the intensity undergoes long-term fluctuations during the analysis. It was associated with possible electronic noise from the UV lamp.

Nevertheless, as the signal of the non-irradiated sample is measured directly after each irradiation, a correction was applied by calculating the relative absorbance (subtraction of the value at a non-absorbed wavelength: $\Delta A = A_{460\ nm} - A_{800nm}$). The baseline fluctuation ($\Delta A_{460} \sim 0.001$) was considered as the statistical error. The absorption maxima of each UV spectrum were plotted as a function of the deposited dose (Figure IV-18.(c)). A linear evolution was observed. The production yield $G(HO_2^{\cdot}/O_2^{\cdot-})$ was calculated using the extinction coefficient of the formazan form and the 2.5 mm pathlength of the detection cell, resulting in $G(HO_2^{\cdot}/O_2^{\cdot-})$=0.019 ±0.001 µmol/J at 1.1 keVphoton energy.

Measurements were performed at different photon energies between 1.1 and 1.8 keV by automating the irradiation cycle and the photon energy change. More precisely, the sample was injected following an irradiation program, as previously described, to measure five samples signals at different doses (corresponding to 5, 10, 13.5, 10, and 5 µL/min flow rates). This procedure, consisting in increasing and then decreasing the dose, allows controlling the reproducibility of the measurements. As explained before, the system is rinsed by the non-irradiated solution between each irradiation step to recover the signal of the non-irradiated sample. At the end of each sequence, the photon energy is automatically changed. Thanks to the environment provided by the microfluidic circuit, it is possible to work in anoxic conditions. Such conditions are performed by injecting deoxygenated solutions (bubbling argon overnight into the solution) and connecting the gas inlet (pressure controller) to an argon bottle instead of compressed air. In deaerated conditions, the initially dissolved molecular oxygen is eliminated from the sample. It will automatically reduce the yield of superoxide radicals, as it will decrease the reaction rate of oxygen and hydrated electrons:

$$e_{aq}^{-} + O_2 \rightarrow O_2^{\cdot-} \qquad \text{(IV-5)}$$
$$k = 2 \cdot 10^{10}\ M^{-1} \cdot s^{-1}$$

Therefore anoxic samples irradiation allows evaluating the direct production of superoxide as no molecular oxygen is initially dissolved in the solution (see Table IV-4). Moreover, by adding SOD in excess in the solution, we can completely scavenge superoxide radicals to evaluate the direct reaction rate of solvated electrons with WST8.

The different conditions tested and their expected impact on the production yield of formazan is summed up in Table IV-4.

Table IV-4: Sources of $O_2^{\cdot-}$ production in the different conditions tested.

Conditions	**O_2**	**Anoxic**	**Anoxic +SOD**
Yield measured	$O_2^{\cdot-}$directly produced (intrinsic reactions) + generation through reaction (IV-5)	$O_2^{\cdot-}$directly produced (intrinsic reactions) + Solvated electron remaining on a µs timescale	Solvated electron remaining on a µs timescale

Experimental results obtained in the different conditions are presented in Figure IV-20 for the different photon energies studied (1.1-1.8 keV soft Xrays and 660 keV γ-rays).

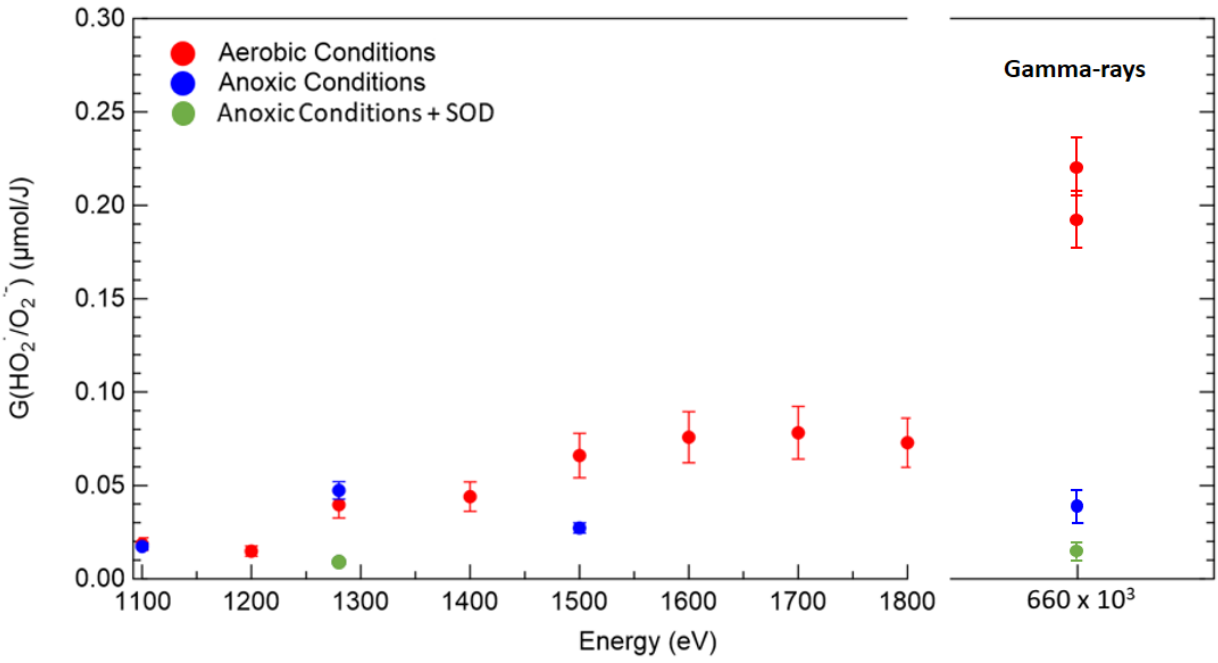

Figure IV-20: Evolution of the superoxide production yield measured using the WST8 chemical probe (300 µM). Series of irradiations were conducted at different flowrate in order to retrieve the G-value from the linear fit using the absorption signal of the formazan (460 nm). Results are presented varying the photon energy for aerated conditions (red), anoxic conditions (blue) and anoxic conditions in presence of SOD (green). Data at 660 keV were obtained usig gamma-rays.

As shown in Figure IV-20, water-soluble tetrazolium salt such as the WST-8 probe is perfectly specific to superoxide radicals quantification. It does not react with aqueous electrons, as the yield obtained with SOD in anoxic conditions (green) is nearly zero. The yield of superoxide radicals, formed *via* water molecules oxygen K-shell ionization (see Chapter I), is expected to increase as the photon energy decrease. Indeed, as the energy becomes closer to the energy of the oxygen K-edge (~543 eV), the yield of K-shell ionization increases (approximately one per photon absorbed). Such phenomena are known to promote the production of superoxide radicals[54], [130]. This observation is reminiscent of the MC simulations of B. Gervais (see Figure IV-4). What we observe here, with great precision, is how the change in track structure affects the electron yield. In order to probe the actual superoxide production yield, it may be necessary to scavenge other radicals produced in the track. Indeed, the dense production of ROS, particularly hydroxyl radicals, could affect the measured yield of superoxide, as intra-track recombination can occur with superoxide radicals. Therefore, a main prospect is to add specific scavengers of different radical species to disentangle the effect of each species.

IV.5. Conducting K-shell irradiation at high dose-rate

IV.5.1. Behavior of the benzoate dosimeter

With the IRAD setup, the energies accessible using the microfluidic cell were restricted to the 1-1.8 keV range. Indeed, absorption in air and through the exit window of the setup limits the maximum accessible doses, which would have been <1 Gy at 1 µL/min for energies <1 keV on the METROLOGIE beamline. Studies under static conditions (Q=0) in the microfluidic cell, on the other hand, gave non-reproducible results as presented in section IV.3.1. Therefore, a solution was to perform experiments on the PLEIADES beamline, where the photon flux is two orders of magnitude higher than on METROLOGIE. However, it must be noted that no filtering device of higher harmonics is available on PLEIADES to date. The contribution of higher orders must therefore be taken into account for some energies. Finally, considering the PLEIADES beam's high flux (~10^{13} ph/s), we decided to implement the microfluidic cell, as the sample can be renewed and the cell can be installed in a vacuum chamber (see Chapter III for more details). Considering that only the absorption in the silicon nitride window of the microfluidic cell remains, K-shells of carbon (284 eV), oxygen (543 eV), and nitrogen (410 eV) are now accessible. The deposited dose ranges from 400 Gy (25 µL/min) to 1.2 kGy (9 µL/min) at 220 eV. It was, therefore, crucial to investigate the effect of such a high dose on water radiolysis. This was investigated by following the production of 2-HOBz in benzoate solutions, as it is directly related to the production of hydroxyl radicals.

On PLEIADES, three user-modifiable parameters allow varying the dose deposited in the sample without changing the photon energy. The first one is the flow rate, which directly impacts the exposure time (but none on the dose rate in the irradiated area). Higher flow rate injection allows a faster renewal of the probe, limiting the over-consumption effect. The second parameter is the beam geometry. Indeed, by decreasing the horizontal exit slits of the monochromator, it is possible to decrease the photon flux (ph/s) without changing the fluence (ph/cm²). More precisely, it decreases the size of the irradiated area (without changing the dose rate in the irradiated area). It, therefore, leads to a more inhomogeneous dose deposition. Finally, we can detune the undulator gap (see Chapter II, section II.1.2). Detuning the undulator (without changing the photon energy

selection of the monochromator) allows modifying the beam's fluence (ph/cm2). The dose rate in the irradiated zone will thus decrease, but the exposure time will remain constant. By varying one of these three parameters, while the two others remain constant, it is possible to perform irradiation at different doses. Three series of experiments were therefore conducted using 0.1 M benzoate solutions. Irradiations were performed at 350 eV to compare with the data obtained at the C K-edge using the static cell[57]. Conditions and results are shown in Figure IV-21. The error on the dose is estimated to be 10% (see Chapter III, section III.4.3) and to 8% for the 2-HOBz concentration (according to calibration curves of 0.1 M benzoate solutions).

Parameter	(a) Undulator detuning	(b) Exit slits	(c) Flow rate
Modification of	Beam fluence	Beam geometry	Irradiation time of exposure
Impact on	Local dose rate	Homogeneity of irradiation field	Solution renewal
G(2-HOBz) (µmol·J^{-1})	0.0015±0.0001	0.0013±0.0002	0.0012±0.0002

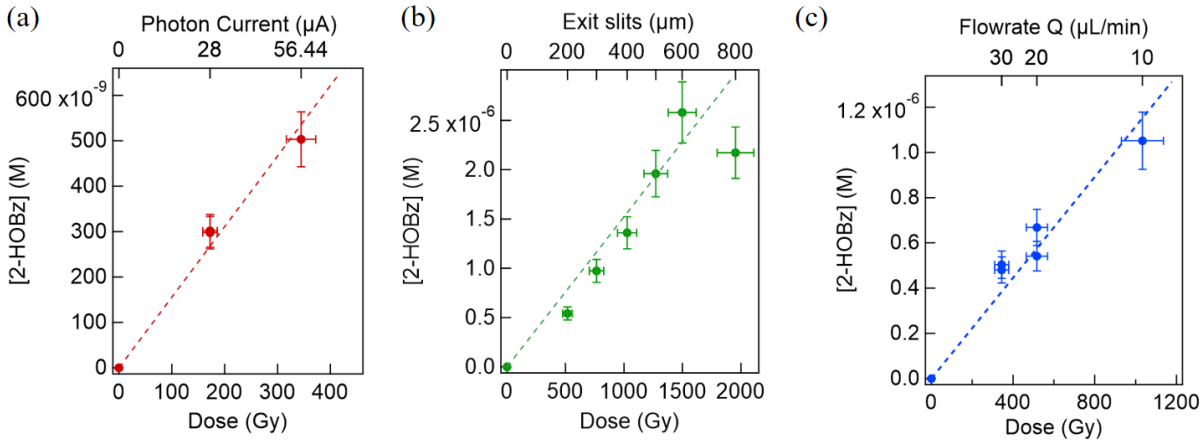

Figure IV-21: Quantification of the 2-HOBz produced in irradiated benzoate solution by varying the dose deposited (a) detuning the undulator, (b) varying the vertical slits of the monochromator, (c) modifying the flowrate of injection in the microfluidic cell. Experiments were conducted on PLEIADES beamline at 350 eV photon energy.

Regardless of the parameter, we varied, we observed that the production of the 2-HOBz was proportional to the dose deposited. The G-value was similar for the three experiments, leading to an average $G_{350\ eV}$(2-HOBz)= 0.0014 ±0.0002 µmol/J at 350 eV. This value is more than one order of magnitude below the one measured using the static cell at the same photon energy ($G_{350\ eV}$(2-HOBz)= 0.026 ±0.0002 µmol/J). One explanation could be

the overconsumption of oxygen in the sample due to the high dose rate achieved on the PLEIADES beamline. Indeed, this would directly impact the hydroxylation rate. It was, for example, evidenced by Fang *et al.* that the hydroxylation rate of terephthalate drops by a factor of 15 in a deaerated environment[131]. Similarly, a decrease of a factor of 3 can be observed for the coumarin dosimeter[132]. Concerning the benzoate, different reasons could explain the decrease of the G(2-HOBz). At first, the ortho-hydroxylation reactions may not have the same ratio. It could have been evidenced by mass spectrometry on irradiated samples. Another explanation could be the production of intermediate products. In particular, the concentration of dissolved oxygen in the sample influences the reaction rate between benzoate and solvated electrons. Indeed, beyond a few hundred nanoseconds, the benzoate or adduct is not protected and can react directly with solvated electrons to form an e^--adduct ($Bz^{2\cdot-}$)[133]. At high benzoate concentrations (>1 mM), the rate of reaction between e^-_{aq} and benzoate anion is k~ $3.2 \cdot 10^9$ $M^{-1} \cdot s^{-1}$[50]. Therefore, it directly competes with the hydroxylation reaction (k_s~$5.9 \cdot 10^9$ $M^{-1} \cdot s^{-1}$). In aqueous solution, $Bz^{2\cdot-}$ protonates to form $HBz^{\cdot-}$. Under low average dose rate irradiation conditions, when samples are irradiated at air, $HBz^{\cdot-}$ disappears on tens of µs time scale in a first-order process by electron release to water[133]. However, in deaerated conditions, e^--adduct can highly contribute to decrease the production yield of hydroxyl radicals. This competition was widely studied by O'Donnell *et al.*[134]. In order to disentangle the contamination of the e^--adduct, they performed reactions in deaerated conditions using N_2O to scavenge solvated electrons. They noticed that when ~1 of e^-_{aq} do not react with N_2O, the hydroxylation rate decreased from $5.9 \cdot 10^9$ $M^{-1} \cdot s^{-1}$ to $4.13 \cdot 10^9$ $M^{-1} \cdot s^{-1}$. It can therefore be hypothesized that e^-_{aq}have a high kinetic contribution in our case. This could be further investigated using scavenger of electrons or hydroxyl radicals.

IV.5.2. Looking for radio-induced damage on biological samples

The metallic atoms thresholds, investigated in section IV.4.1, represent less than 10% of the beam absorption. On the other hand, carbon, nitrogen, and oxygen thresholds are expected to have a more dramatic biological effect considering their higher atomic percentage[135]–[138]. The aim of this experiment was, therefore, to investigate threshold effects following core-ionization on biomolecules. For these experiments, we decided to inject a solution of Cytochrome C[139]. As for experiments conducted on METROLOGIE, the solutions were irradiated in the microfluidic cell at different flow rates. Photon energies were 350 eV and 800 eV in order to probe the C and O K-edges. Experiments were carried out in oxygenated and anoxic conditions to investigate the effect of oxygen. Irradiated samples were collected and analyzed by UV-Vis spectrophotometry. Results are presented in Figure IV-22.

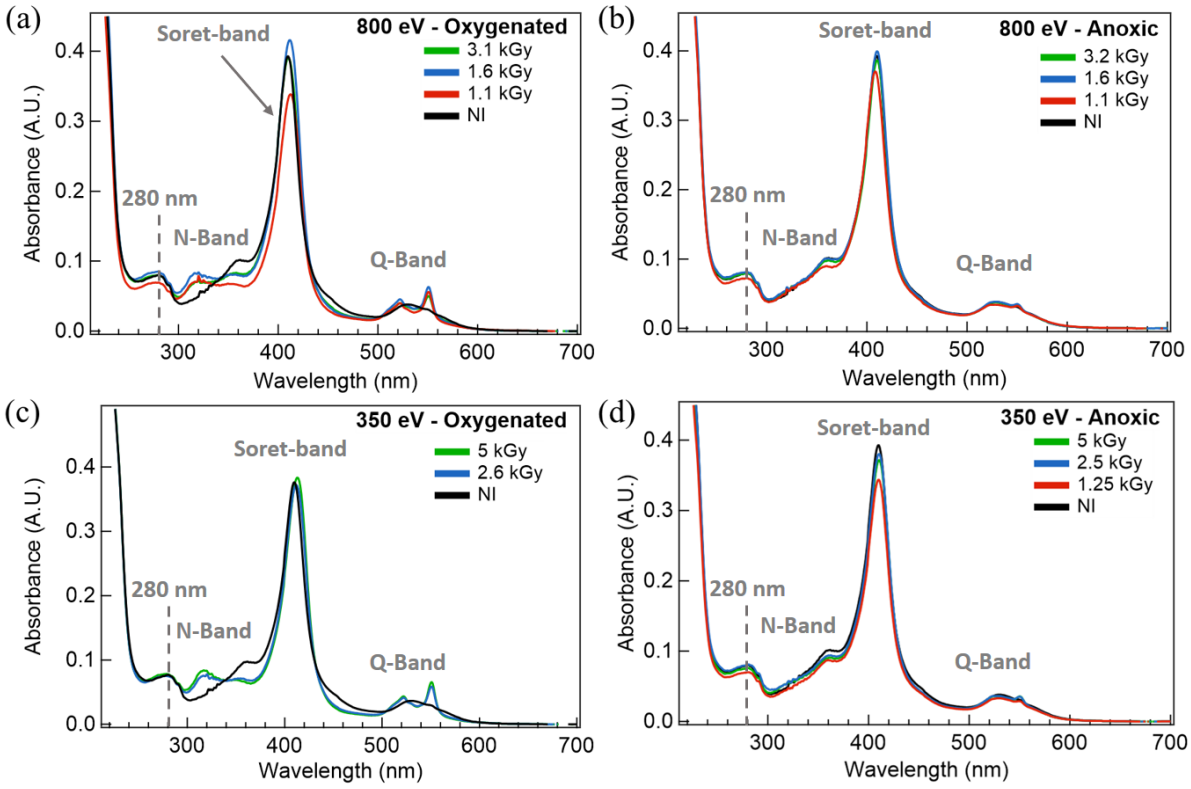

Figure IV-22: UV analysis of cytc aqueous samples (45 µM in phosphate buffer 20 mM) irradiated under soft X-rays (a)-(b) & (c)-(d) correspond to respective spectra reccorded in anoxic and aerated conditions at 350 eV and 800 eV photon energy.

The general evolution of the UV-Vis spectrum is a good indicator of tertiary structural changes of the protein. More precisely, the signal at 280 nm arises because of the aromatic side chains of amino acids (Tyrosine, Tryptophan residues) present in the protein sequence[140]. Any change in signal intensity reflects environmental modification around these specific amino acids. Similarly, the Soret band reflects the heme interactions. Finally, the different positions of the N-band and Q-band in the two redox forms reflect the oxidation state of the metallic ion (Fe).

As shown in Figure IV-22, the samples irradiated in oxygenated conditions exhibit more changes than in anoxic conditions. It suggests that the molecular oxygen presence increases biological modifications. This result is in good agreement with the fact that the presence of oxygen can increase not only ROS production but also fix radical damages [141]. The second observation is that the N-band (310-370 nm) and the Soret-band (or B-band) are particularly affected. However, there was no clear dose-response relationship, suggesting that results are not reproducible. At such a high dose (>100 Gy), we did not expect to observe any linear response of the cytochrome c oxidation for the Q-band. Indeed, as previously shown with γ-rays irradiation, the signal at 550 nm reaches a plateau for doses higher than ~70 Gy (see section IV.4.2.ii).

It should be mentioned that the flow rate in the microfluidic circuit decreased rapidly during the beamtime (28 µL/min to 10 µL/min in one day). We have already observed flow rates decrease of this order, but rather on a week-scale (presence of dust inside the capillaries, which progressively increase the hydrodynamic resistance). In the present situation, this could suggest the formation of protein aggregates in the circuit. It is indeed known that hemoproteins can aggregate[142]. In addition, the silicon nitride window broke twice, which never happened when irradiation was conducted at air. Given the non-reproducibility, we assumed that the microfluidic cell was fouled with protein samples. Therefore, the collected Cytc samples were analyzed using gel electrophoresis to further investigate the Cytc degradation at 800 eV and 350 eV.

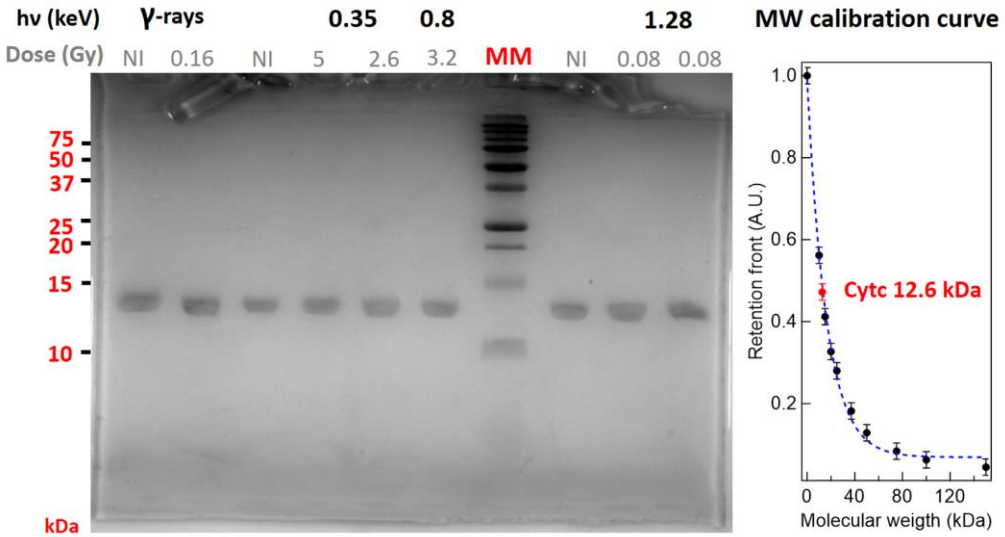

Figure IV-23: SDS-Page gel electrophoresis in non reduced conditions (2.8 µg of sample deposited per well), Molecular marker (MM) was loaded in order to identify bands.

The gel analysis was performed after 6 months of storage at -18 °C[61]. Irradiated samples stored after the METROLOGIE (1.28 keV) and PLEIADES (350 and 800 eV) beamtimes were compared to freshly γ-irradiated samples (^{137}Cs 660 keV) (see Figure IV-23). Measurements were performed in denaturant conditions (see Chapter II, section II.3.6 for more details). Another gel electrophoresis was conducted in reduced conditions (presence of beta-mercapto ethanol) to fully denature the proteins and over-see scission products (see Appendix V.3). No fragments were detected for both conditions. Considering the detection limit of this technique, which is ~20 ng, results suggest that less than 1% of the fragment is formed. Due to lack of time, it was not possible to perform more analysis on the samples. For instance, it would have been interesting to use other characterization techniques (circular dichroism, IR) to highlight the changes in the tertiary structure.

Finally, the results indicate minimal effects of ionization at the K threshold in the condensed phase. However, comparing UV-analysis, it seems that SXs irradiations lead mainly to the reduction of Cytc, compared to the γ-rays where more changes are observed. The irradiation protocol must now be optimized to complete these interesting preliminary results in the future.

[61] *UV-vis analysis was conducted on the samples and compared to data obtained on unfrozen samples. It demonstrates that the storage did not impact the spectral signature of the protein.*

IV.6. Conclusion on Chapter IV

Thanks to the combination of a highly sensitive scavenging probe of hydroxyl radicals and dedicated irradiation setups, we succeeded in investigating the track structure of SXs. More precisely, SXs (0.2–2 keV) were first used to probe the physical and physico-chemical effects of sub-keV electrons on liquid water. The G($HO^{\cdot}$) quantification, performed for an extensive range of photon energies, allowed to determine a production minimum at ~1 keV. Experiments performed at different scavenging times (from 170 ns to 170 ps) evidenced that the G-values were relatively independent of the benzoate concentration around this energy. These results provide evidence that sub-keV electrons behave as high linear energy transfer particles since they can deposit hundreds of electronvolts in nanometric volumes.

Regarding the microfluidic device, the micrometer-sized thickness of the channel provides a high precision on the dose deposition process along the beam axis. Moreover, continuous flow conditions for the irradiation prevent an over-irradiation of the dosimeter by continuously renewing the sample under the beam. Over-irradiation, which can affect all chemical dosimeters[143], leads to inconsistent measurements and is, therefore, a significant concern in dosimetry. With synchrotron radiation, a strong over-irradiation of the dosimeter can occur due to the high incident photon flux. Of course, the dose deposited depends on the effective fraction of the beam absorbed and therefore varies upon the photon energy. In this project, the development of the cell was dedicated to a low penetration beam.

More specifically, it is clear that the analysis of the sample, at long term after the dose deposition, does not allow to describe the whole process of the irradiation. In order to fully understand the consequences observed, it is necessary to look at events occurring at shorter times (femtosecond range). Recently, liquid environments have been developed for XPS analysis[144], which could also be a possible development for the cell. Indeed, electron spectroscopy remains a tool of choice for the analysis of K-shell photoionizations.

Bibliography Chapter IV

[1] W. Wang, D. Becker, and M. D. Sevilla, "The influence of hydration on the absolute yields of primary ionic free radicals in gamma-irradiated DNA at 77 K. I. Total radical yields.," *Radiat. Res.*, vol. 135, no. 2, pp. 146–54, Aug. 1993.

[2] N. Mroczka and W. A. Bernhard, "Hydration Effects on Free Radical Yields in DNA X-Irradiated at 4 K," *Radiat. Res.*, vol. 135, no. 2, p. 155, Aug. 1993.

[3] S. G. Swarts, M. D. Sevilla, D. Becker, C. J. Tokar, and K. T. Wheeler, "Radiation-induced DNA damage as a function of hydration. I. Release of unaltered bases.," *Radiat. Res.*, vol. 129, no. 3, pp. 333–44, Mar. 1992.

[4] P. O'neill, "Pulse Radiolysis of DNA—Effects of Environment," *Free Radic. Res. Commun.*, vol. 6, no. 2–3, pp. 153–154, Jan. 1989.

[5] S. Gregoli, M. Olast, and A. Bertinchamps, "Radiolytic pathways in γ-irradiated DNA: Influence of chemical and conformational factors," *Radiat. Res.*, vol. 89, no. 2, pp. 238–254, 1982.

[6] M. Wolter, M. Elstner, and T. Kubař, "Charge transport in desolvated DNA," *J. Chem. Phys.*, vol. 139, no. 12, 2013.

[7] J. B. MacNaughton *et al.*, "Dependence of DNA Electronic Structure on Environmental and Structural Variations," *J. Phys. Chem. B*, vol. 110, no. 32, pp. 15742–15748, Aug. 2006.

[8] H. Hayashi, "Charged Particle and Photon Interactions with Matter Recent Advances , Applications ," no. January 2010, 2014.

[9] B. Halliwell, "Biochemistry of oxidative stress," *Biochem. Soc. Trans.*, vol. 35, no. 5, pp. 1147–1150, Nov. 2007.

[10] W. G. Burns and H. E. Sims, "Effect of radiation type in water radiolysis," *J. Chem. Soc. Faraday Trans. 1 Phys. Chem. Condens. Phases*, vol. 77, no. 11, pp. 2803–2813, 1981.

[11] S. M. Pimblott, J. A. Laverne, D. M. Barteis, and C. D. Jonah, "Reconciliation of transient absorption and chemically scavenged yields of the hydrated electron in radiolysis," *J. Phys. Chem.*, vol. 100, no. 22, pp. 9412–9415, 1996.

[12] H. Fricke and E. J. Hart, "The Oxidation of Fe ++ to Fe +++ by the Irradiation with X-Rays of Solutions of Ferrous Sulfate in Sulfuric Acid," *J. Chem. Phys.*, vol. 3, no. 1, pp. 60–61, Jan. 1935.

[13] R. M. Lazo, H. A. Dewhurst, and M. Burton, "The Ferrous Sulfate Radiation Dosimeter: A Calorimetric Calibration with Gamma Rays," *J. Chem. Phys.*, vol. 22, no. 8, pp. 1370–1375, 1954.

[14] R. Watanabe, N. Usami, and K. Kobayashi, "Oxidation yield of the ferrous ion in a fricke solution irradiated with monochromatic synchrotron soft x-rays in the 1.8-10 kev region," *Int. J. Radiat. Biol.*, vol. 68, no. 2, pp. 113–120, 1995.

[15] M. Hoshi *et al.*, "Iron(II) sulphate (fricke solution) oxidation yields for 8.9 and 13.6kev x-rays from synchrotron radiation," *Int. J. Radiat. Biol.*, vol. 61, no. 1, pp. 21–27, 1992.

[16] J. A. LaVerne and R. H. Schuler, "Radiation chemical studies with heavy ions: Oxidation of ferrous ion in the Fricke dosimeter," *J. Phys. Chem.*, vol. 91, no. 22, pp. 5770–5776, 1987.

[17] C. K. Ross and N. V. Klassen, "Water calorimetry for radiation dosimetry," *Phys. Med. Biol.*, vol. 41, no. 1, pp. 1–29, 1996.

[18] J. Cadet *et al.*, "Hydroxyl radicals and DNA base damage," *Mutat. Res. - Fundam. Mol. Mech. Mutagen.*, vol. 424, no. 1–2, pp. 9–21, 1999.

[19] J. M. Burns *et al.*, "Methods for reactive oxygen species (ROS) detection in aqueous environments," *Aquat. Sci.*, vol. 74, no. 4, pp. 683–734, 2012.

[20] A. Gomes, E. Fernandes, and J. L. F. C. Lima, "Fluorescence probes used for detection of reactive oxygen species," *J. Biochem. Biophys. Methods*, vol. 65, no. 2–3, pp. 45–80, 2005.

[21] A. Mozumder, "Structure of Charged Particle Tracks in Condensed Media," *Fundam. Radiat. Chem.*, pp. 41–69, 1999.

[22] S. C. Ashawa, U. R. Kini, and U. Madhvanath, "The aqueous coumarin system as a low range chemical dosimeter," *Int. J. Appl. Radiat. Isot.*, vol. 30, no. 1, pp. 7–10, 1979.

[23] A. R. Anderson and E. J. Hart, "Molecular Product and Free Radical Yields in the Decomposition of Water by Protons, Deuterons, and Helium Ions," *Radiat. Res.*, vol. 14, no. 6, p. 689, Jun. 1961.

[24] J. Fulford, P. Bonner, D. T. Goodhead, M. A. Hill, and P. O'Neill, "Experimental determination of the dependence of OH radical yield on photon energy: A comparison with theoretical simulations," *J. Phys. Chem. A*, vol. 103, no. 51, pp. 11345–11349, 1999.

[25] L. Vyšín *et al.*, "Chemical Dosimetry in the 'Water Window': Ferric Ions and Hydroxyl Radicals Produced by Intense Soft X Rays.," *Radiat. Res.*, vol. 000, 2020.

[26] J. A. La Verne, "Radical and molecular yields in the radiolysis of water with carbon ions," *Int. J. Radiat. Appl. Instrumentation. Part C. Radiat. Phys. Chem.*, vol. 34, no. 1, pp. 135–143, Jan. 1989.

[27] J. A. Laverne and S. M. Pimblott, "Scavenger and time dependences of radicals and molecular products in the electron radiolysis of water: Examination of experiments and models," *J. Phys. Chem.*, vol. 95, no. 8, pp. 3196–3206, 1991.

[28] C. Ferradini and J.-P. Jay-Gerin, "La radiolyse de l'eau et des solutions aqueuses : historique et actualité," *Can. J. Chem.*, vol. 77, no. 9, pp. 1542–1575, 1999.

[29] S. M. Pimblott and J. A. LaVerne, "Diffusion-kinetic theories for LET effects on the radiolysis of water," *J. Phys. Chem.*, vol. 98, no. 24, pp. 6136–6143, 1994.

[30] H. Yamaguchi, Y. Uchihori, N. Yasuda, M. Takada, and H. Kitamura, "Estimation of Yields of OH Radicals in Water Irradiated by Ionizing Radiation," *J. Radiat. Res.*, vol. 46, no. 3, pp. 333–341, 2005.

[31] J. L. Magee and A. Chatterjee, "Theory of the chemical effects of high-energy electrons," *J. Phys. Chem.*, vol. 82, no. 20, pp. 2219–2226, Oct. 1978.

[32] H. Yamaguchi, "A spur diffusion model applied to estimate yields of species in water irradiated by monoenergetic photons of 50 eV-2 MeV," *Int. J. Radiat. Appl. Instrumentation. Part*, vol. 34, no. 5, pp. 801–807, 1989.

[33] M. A. Hill and F. A. Smith, "Is the response of the Fricke dosimeter constant for high energy electrons and photons?," *Radiat. Phys. Chem.*, vol. 47, no. 4, pp. 637–647, 1996.

[34] J. S. Francesc Salvat, José M. Fernández-Varea, *PENELOPE -2006 : A Code System for Monte Carlo Simulation of Electron and Photon Transport*. 2006.

[35] P. Hovington, D. Drouin, and R. Gauvin, "CASINO: A new monte carlo code in C language for electron beam interaction -part I: Description of the program," *Scanning*, vol. 19, no. 1, pp. 1–14, Dec. 2006.

[36] H. Nikjoo, D. Emfietzoglou, T. Liamsuwan, R. Taleei, D. Liljequist, and S. Uehara, "Radiation track, DNA damage and response - A review," *Reports Prog. Phys.*, vol. 79, no. 11, 2016.

[37] Y. Itikawa and N. Mason, "Cross sections for electron collisions with water molecules," *J. Phys. Chem. Ref. Data*, vol. 34, no. 1, pp. 1–22, 2005.

[38] S. Uehara, H. Nikjoo, and D. T. Goodhead, "Comparison and assessment of electron cross sections for Monte Carlo track structure codes," *Radiat. Res.*, vol. 152, no. 2, pp. 202–213, Aug. 1999.

[39] C. Bousis, D. Emfietzoglou, P. Hadjidoukas, H. Nikjoo, and A. Pathak, "Electron ionization cross-section calculations for liquid water at high impact energies," *Nucl. Instruments Methods Phys. Res. Sect. B Beam Interact. with Mater. Atoms*, vol. 266, no. 8, pp. 1185–1192, 2008.

[40] J. E. Turner, J. L. Magee, and H. A. Wright, "Physical and chemical development of electron tracks in liquid water," *Radiat. Res.*, vol. 96, no. 3, pp. 437–449, 1983.

[41] Y. Gao, Y. Zheng, and L. Sanche, "Low-energy electron damage to condensed-phase DNA and its constituents," *Int. J. Mol. Sci.*, vol. 22, no. 15, 2021.

[42] C. Champion, "Electron impact ionization of liquid and gaseous water: A single-center partial-wave approach," *Phys. Med. Biol.*, vol. 55, no. 1, pp. 11–32, 2010.

[43] J. P. Freyer, M. E. Schillaci, and M. R. Raju, "Measurement of the g-value for $1 \cdot 5$ kev x-rays," *Int. J. Radiat. Biol.*, vol. 56, no. 6, pp. 885–892, 1989.

[44] W. A. Armstrong, B. A. Black, and D. W. Grant, "The radiolysis of aqueous calcium benzoate and benzoic acid solutions," *J. Phys. Chem.*, vol. 64, no. 10, pp. 1415–1419, Oct. 1960.

[45] W. A. Armstrong and D. W. Grant, "A Highly Sensitive Chemical Dosimeter for Ionizing Radiation," *Nature*, vol. 182, no. 4637, pp. 747–747, Sep. 1958.

[46] W. A. Armstrong and D. W. Grant, "The Aqueous Benzoate System as a Sensitive Dosimeter for Ionizing Radiations," *Can. J. Chem.*, vol. 38, no. 6, pp. 845–850, 1960.

[47] R. Musat, S. Moreau, F. Poidevin, M. H. Mathon, S. Pommeret, and J. P. Renault, "Radiolysis of water in nanoporous gold," *Phys. Chem. Chem. Phys.*, vol. 12, no. 39, pp. 12868–12874, 2010.

[48] G. Huang, J. Si, C. Qian, W. Wang, S. Mei, and C. Wang, "Ultrasensitive Fluorescence Detection of Peroxymonosulfate Based on a Sulfate Radical-Mediated Aromatic Hydroxylation," *Anal. Chem.*, vol. 90, pp. 14439–14446, 2018.

[49] G. Albarran, M. Esparza, and E. Mendoza, "Oxidation of hydroxybenzoic acids by {bullet operator}OH radical produced radiolytically," *Radiat. Phys. Chem.*, vol. 107, pp. 109–114, 2015.

[50] G. V. Buxton, C. L. Greenstock, W. P. Helman, and A. B. Ross, "Critical Review of rate constants for reactions of hydrated electrons, hydrogen atoms and hydroxyl radicals (·OH/·O− in Aqueous Solution," *J. Phys. Chem. Ref. Data*, vol. 17, no. 2, pp. 513–886, 1988.

[51] I. Loeff and A. J. Swallow, "On the Radiation Chemistry of Concentrated Aqueous Solutions of Sodium Benzoate," *J. Phys. Chem.*, vol. 68, no. 9, pp. 2470–2475, Sep. 1964.

[52] Y. Manevich, K. D. Held, and J. E. Biaglow, "Coumarin-3-Carboxylic Acid as a Detector for Hydroxyl Radicals Generated Chemically and by Gamma Radiation," *Radiat. Res.*, vol. 148, no. 6, p. 580, Dec. 1997.

[53] M. Kim, S. K. Ko, H. Kim, I. Shin, and J. Tae, "Rhodamine cyclic hydrazide as a fluorescent probe for the detection of hydroxyl radicals," *Chem. Commun.*, vol. 49, no. 72, pp. 7959–7961, 2013.

[54] B. Gervais, M. Beuve, G. H. Olivera, and M. E. Galassi, "Numerical simulation of multiple ionization and high LET effects in liquid water radiolysis," *Radiat. Phys. Chem.*, vol. 75, no. 4, pp. 493–513, Apr. 2006.

[55] V. Cobut, Y. Frongillo, J. P. Patau, T. Goulet, M. J. Fraser, and J. P. Jay-Gerin, "Monte Carlo simulation of fast electron and proton tracks in liquid water - I. Physical and physicochemical aspects," *Radiat. Phys. Chem.*, vol. 51, no. 3, pp. 229–243, 1998.

[56] M. Anbar, M. Bambenek, and A. B. Ross, "Selected specific rates of reactions of transients

from water in aqueous solution. 1. Hydrated electron," *Nsrds-Nbs-43*. 1973.

[57] L. Huart *et al.*, "Soft X-ray Radiation and Monte Carlo Simulations: Good Tools to Describe the Radiation Chemistry of Sub-keV Electrons," *J. Phys. Chem. A*, vol. 124, no. 10, pp. 1896–1902, 2020.

[58] J.-J. YEH, *Atomic calculation of photoionization cross-sections and asymmetry parameters*. Gordon and Breach, 1993.

[59] J. H. Scofield, "Theoretical Photoionization Cross Sections From 1 To 1500 keV," *Livermore, Calif.*, pp. 5–6, 1973.

[60] R. Sankari *et al.*, "Vibrationally resolved O1s photoelectron spectrum of water," *Chem. Phys. Lett.*, vol. 380, no. 5–6, pp. 647–653, 2003.

[61] K. Wiklund, J. M. Fernndez-Varea, and B. K. Lind, "A Monte Carlo program for the analysis of low-energy electron tracks in liquid water," *Phys. Med. Biol.*, vol. 56, no. 7, pp. 1985–2003, 2011.

[62] D. Emfietzoglou, G. Papamichael, and H. Nikjoo, "Monte Carlo Electron Track Structure Calculations in Liquid Water Using a New Model Dielectric Response Function," *Radiat. Res.*, vol. 188, no. 3, pp. 355–368, 2017.

[63] J. Meesungnoen, J. P. Jay-Gerin, A. Filali-Mouhim, and S. Mankhetkorn, "Low-energy electron penetration range in liquid water," *Radiat. Res.*, vol. 158, no. 5, pp. 657–660, 2002.

[64] G. Baldacchino *et al.*, "Determination of the time-dependent OH-yield by using a fluorescent probe. Application to heavy ion irradiation," *Chem. Phys. Lett.*, vol. 468, no. 4–6, pp. 275–279, 2009.

[65] A. I. Kassis, "The amazing world of Auger electrons," *Int. J. Radiat. Biol.*, vol. 80, no. 11–12, pp. 789–803, 2004.

[66] D. Emfietzoglou and H. Nikjoo, "Accurate Electron Inelastic Cross Sections and Stopping Powers for Liquid Water over the 0.1-10 keV Range Based on an Improved Dielectric Description of the Bethe Surface," *Radiat. Res.*, vol. 167, no. 1, pp. 110–120, 2007.

[67] J. Schuemann *et al.*, "TOPAS-nBio: An Extension to the TOPAS Simulation Toolkit for Cellular and Sub-cellular Radiobiology," *Radiat. Res.*, vol. 191, no. 2, p. 125, 2019.

[68] W. G. Shin *et al.*, "Evaluation of the influence of physical and chemical parameters on water radiolysis simulations under MeV electron irradiation using Geant4-DNA," *J. Appl. Phys.*, vol. 126, no. 11, 2019.

[69] M. P. Gaigeot *et al.*, "A multi-scale ab initio theoretical study of the production of free radicals in swift ion tracks in liquid water," *J. Phys. B At. Mol. Opt. Phys.*, vol. 40, no. 1, pp. 1–12, Jan. 2007.

[70] D. T. Goodhead, "Energy deposition stochastics and track structure: What about the target?," *Radiat. Prot. Dosimetry*, vol. 122, no. 1–4, pp. 3–15, 2006.

[71] R. W. Howell, V. R. Narra, K. Sastry, and D. Rao, *Biophysical Aspects of Auger Processes*, First Edit. 1992.

[72] M. A. Hervé Du Penhoat *et al.*, "Double-strand break induction and repair in V79-4 hamster cells: The role of core ionisations, as probed by ultrasoft X-rays," *Int. J. Radiat. Biol.*, vol. 86, no. 3, pp. 205–219, 2010.

[73] Y. Furusawa, H. Maezawa, and K. Suzuki, "Enhanced Killing Effect on 5-Bromodeoxyuridine Labelled Bacteriophage T1 by Monoenergetic Synchrotron X-Ray at the Energy of Bromine K-shell Absorption Edge.," *J. Radiat. Res.*, vol. 32, no. 1, pp. 1–12, Jan. 1991.

[74] H. Menke, W. Köhnlein, S. Joksch, and A. Halpern, "Strand Breaks in Plasmid DNA, Natural and Brominated, by Low-energy X-rays," *Int. J. Radiat. Biol.*, vol. 59, no. 1, pp.

85–96, Jan. 1991.

[75] A. Yokoya, K. Takakura, R. Watanabe, K. Akamatsu, and T. Ito, "EPR studies of 5-bromouracil crystal after irradiation with X rays in the bromine K-edge region," *Radiat. Res.*, vol. 162, no. 4, pp. 469–473, 2004.

[76] I. Bertini, H. B. Gray, E. I. Stiefel, and J. S. Valentine, *Biological inorganic chemistry: structure and reactivity*, vol. 44, no. 11. 2007.

[77] O. Carugo and K. D. Carugo, "When X-rays modify the protein structure: Radiation damage at work," *Trends Biochem. Sci.*, vol. 30, no. 4, pp. 213–219, 2005.

[78] J. E. Penner-Hahn, M. Murata, K. O. Hodgson, and H. C. Freeman, "Low-temperature X-ray absorption spectroscopy of plastocyanin: Evidence for copper-site photoreduction at cryogenic temperatures," *Inorg. Chem.*, vol. 28, no. 10, pp. 1826–1832, 1989.

[79] R. H. G. Baxter, B. L. Seagle, N. Ponomarenko, and J. R. Norris, "Specific radiation damage illustrates light-induced structural changes in the photosynthetic reaction center," *J. Am. Chem. Soc.*, vol. 126, no. 51, pp. 16728–16729, 2004.

[80] J. Yano *et al.*, "X-ray damage to the Mn4Ca complex in single crystals of photosystem II: A case study for metalloprotein crystallography," *Proc. Natl. Acad. Sci.*, vol. 102, no. 34, pp. 12047–12052, Aug. 2005.

[81] S. V. Antonyuk and M. A. Hough, "Monitoring and validating active site redox states in protein crystals," *Biochim. Biophys. Acta - Proteins Proteomics*, vol. 1814, no. 6, pp. 778–784, 2011.

[82] H. P. Hersleth and K. K. Andersson, "How different oxidation states of crystalline myoglobin are influenced by X-rays," *Biochim. Biophys. Acta - Proteins Proteomics*, vol. 1814, no. 6, pp. 785–796, 2011.

[83] V. Stumpf, K. Gokhberg, and L. S. Cederbaum, "The role of metal ions in X-ray induced photochemistry," *Nat. Chem.*, vol. 8, no. 3, pp. 237–241, May 2015.

[84] R. W. Howell, "Auger processes in the 21st century," *Int. J. Radiat. Biol.*, vol. 84, no. 12, pp. 959–975, 2008.

[85] I. Tavernelli, M. P. Gaigeot, R. Vuilleumier, C. Stia, M. A. H. Du Penhoat, and M. F. Politis, "Time-dependent density functional theory molecular dynamics simulations of liquid water radiolysis," *ChemPhysChem*, vol. 9, no. 14, pp. 2099–2103, 2008.

[86] B. L. Henke, E. M. Gullikson, and J. C. Davis, "X-Ray Interactions: Photoabsorption, Scattering, Transmission, and Reflection at E = 50-30,000 eV, Z = 1-92," *At. Data Nucl. Data Tables*, vol. 54, no. 2, pp. 181–342, Jul. 1993.

[87] Y. Marcus, "Effect of ions on the structure of water," *Pure Appl. Chem.*, vol. 82, no. 10, pp. 1889–1899, 2010.

[88] G. Stirnemann, E. Wernersson, P. Jungwirth, and D. Laage, "Mechanisms of acceleration and retardation of water dynamics by ions," *J. Am. Chem. Soc.*, vol. 135, no. 32, pp. 11824–11831, 2013.

[89] Y. Yao, Y. Kanai, and M. L. Berkowitz, "Role of charge transfer in water diffusivity in aqueous ionic solutions," *J. Phys. Chem. Lett.*, vol. 5, no. 15, pp. 2711–2716, 2014.

[90] A. W. Omta, "Negligible Effect of Ions on the Hydrogen-Bond Structure in Liquid Water," *Science (80-.).*, vol. 301, no. 5631, pp. 347–349, Jul. 2003.

[91] K. J. Tielrooij, N. Garcia-Araez, M. Bonn, and H. J. Bakker, "Cooperativity in Ion Hydration," *Science (80-.).*, vol. 328, no. 5981, pp. 1006–1009, May 2010.

[92] R. Mancinelli, A. Botti, F. Bruni, M. A. Ricci, and A. K. Soper, "Perturbation of water structure due to monovalent ions in solution," *Phys. Chem. Chem. Phys.*, vol. 9, no. 23, pp. 2959–2967, 2007.

[93] A. Korosi and B. M. Fabuss, "Viscosities of Binary Aqueous Solutions of NaCl, KCl, Na2SO4, and MgSO4 at Concentrations and Temperatures of Interest in Desalination Processes," *J. Chem. Eng. Data*, vol. 13, no. 4, pp. 548–552, 1968.

[94] N. Gavish and K. Promislow, "Dependence of the dielectric constant of electrolyte solutions on ionic concentration: A microfield approach," *Phys. Rev. E*, vol. 94, no. 1, pp. 1–7, 2016.

[95] J. Mähler and I. Persson, "A study of the hydration of the alkali metal ions in aqueous solution," *Inorg. Chem.*, vol. 51, no. 1, pp. 425–438, 2012.

[96] S. I. Mamatkulov, K. F. Rinne, R. Buchner, R. R. Netz, and D. J. Bonthuis, "Water-separated ion pairs cause the slow dielectric mode of magnesium sulfate solutions," *J. Chem. Phys.*, vol. 148, no. 22, 2018.

[97] P. Debye, "Reaction Rates in Ionic Solutions," *Trans. Electrochem. Soc.*, vol. 82, no. 1, p. 265, 1942.

[98] J. Meesungnoen and J.-P. Jay-Gerin, "High-LET Radiolysis of Liquid Water with 1 H + , 4 He 2+ , 12 C 6+ , and 20 Ne 9+ Ions: Effects of Multiple Ionization," *J. Phys. Chem. A*, vol. 109, no. 29, pp. 6406–6419, Jul. 2005.

[99] B. Gervais, M. Beuve, G. H. Olivera, M. E. Galassi, and R. D. Rivarola, "Production of HO2 and O2 by multiple ionization in water radiolysis by swift carbon ions," *Chem. Phys. Lett.*, vol. 410, no. 4–6, pp. 330–334, 2005.

[100] M. Valko, C. J. Rhodes, J. Moncol, M. Izakovic, and M. Mazur, "Free radicals, metals and antioxidants in oxidative stress-induced cancer," *Chem. Biol. Interact.*, vol. 160, no. 1, pp. 1–40, 2006.

[101] M. Hayyan, M. A. Hashim, and I. M. Alnashef, "Superoxide Ion: Generation and Chemical Implications," *Chem. Rev.*, vol. 116, no. 5, pp. 3029–3085, 2016.

[102] A. Okado-Matsumoto and I. Fridovich, "Assay of superoxide dismutase: Cautions relevant to the use of cytochrome c, a sulfonated tetrazolium, and cyanide," *Anal. Biochem.*, vol. 298, no. 2, pp. 337–342, 2001.

[103] I. Fridovich, "Superoxide Anion Radical ($O^{\cdot-}2$), Superoxide Dismutases, and Related Matters," *J. Biol. Chem.*, vol. 272, no. 30, pp. 18515–18517, Jul. 1997.

[104] L. Flohé and F. Ötting, "[10] Superoxide dismutase assays," in *Methods*, vol. 105, no. 1975, 1984, pp. 93–104.

[105] E. Margoliash and E. L. Smith, "Amino-Acid Sequence of Horse Heart Cytochrome C : Peptides released by Digestion with Chymotrypsin," *Nature*, vol. 192, no. 4808, pp. 1121–1123, Dec. 1961.

[106] B. M. Babior, R. S. Kipnes, and J. T. Curnutte, "Biological Defense Mechanisms. The production by leukocytes of superoxide, a potential bactericidal agent," *J. Clin. Invest.*, vol. 52, no. 3, pp. 741–744, Mar. 1973.

[107] C. Garrido, L. Galluzzi, M. Brunet, P. E. Puig, C. Didelot, and G. Kroemer, "Mechanisms of cytochrome c release from mitochondria," *Cell Death Differ.*, vol. 13, no. 9, pp. 1423–1433, 2006.

[108] J. C. Reed, "Cytochrome c: Can't live with it - Can't live without it," *Cell*, vol. 91, no. 5, pp. 559–562, 1997.

[109] L. Banci *et al.*, "Effects of extrinsic imidazole ligation on the molecular and electronic structure of cytochrome c," *J. Biol. Inorg. Chem.*, vol. 6, no. 5–6, pp. 628–637, 2001.

[110] E. Racker, "Mechanisms of Energy Transformations," *Annu. Rev. Biochem.*, vol. 46, no. 1, pp. 1006–1014, Jun. 1977.

[111] J. Butler, G. G. Jayson, and A. J. Swallow, "The reaction between the superoxide anion radical and cytochrome c," *Biochim. Biophys. Acta - Bioenerg.*, vol. 408, no. 3, pp. 215–

222, Dec. 1975.

[112] J. M. McCord and I. Fridovich, "The reduction of cytochrome c by milk xanthine oxidase.," *J. Biol. Chem.*, vol. 243, no. 21, pp. 5753–5760, 1968.

[113] W. H. Koppenol, K. J. H. Van Buuren, J. Butler, and R. Braams, "The kinetics of the reduction of cytochrome c by the superoxide anion radical," *Biochim. Biophys. Acta - Bioenerg.*, vol. 449, no. 2, pp. 157–168, Nov. 1976.

[114] M. M. Tarpey, D. A. Wink, and M. B. Grisham, "Methods for detection of reactive metabolites of oxygen and nitrogen: In vitro and in vivo considerations," *Am. J. Physiol. - Regul. Integr. Comp. Physiol.*, vol. 286, no. 3 55-3, 2004.

[115] M. Dixon, R. Hill, and David Keilin, "The Absorption Spectrum of the Component c of Cytochrome," *Proc. R. Soc. London. Ser. B, Contain. Pap. a Biol. Character*, vol. 109, no. 760, pp. 29–34, Sep. 1931.

[116] M. Gouterman, "Spectra of porphyrins," *J. Mol. Spectrosc.*, vol. 6, no. 4, pp. 138–163, Jan. 1961.

[117] W. D. Butt and D. Keilin, "Absorption spectra and some other properties of cytochrome c and of its compounds with ligands," *Proc. R. Soc. London. Ser. B. Biol. Sci.*, vol. 156, no. 965, pp. 429–458, Nov. 1962.

[118] B. H. J. Bielski, G. G. Shiue, and S. Bajuk, "Reduction of nitro blue tetrazolium by CO2- and O2- Radicals," *J. Phys. Chem.*, vol. 84, no. 8, pp. 830–833, 1980.

[119] Y. Liu *et al.*, " In vitro measurement of superoxide dismutase-like nanozyme activity: a comparative study ," *Analyst*, 2021.

[120] M. W. Sutherland and B. A. Learmonth, "The tetrazolium dyes MTS and XTT provide new quantitative assays for superoxide and superoxide dismutase," *Free Radic. Res.*, vol. 27, no. 3, pp. 283–289, 1997.

[121] H. Tominaga *et al.*, "A water-soluble tetrazolium salt useful for colorimetric cell viability assay," *Anal. Commun.*, vol. 36, no. 2, pp. 47–50, 1999.

[122] M. Ishiyama, M. Shiga, K. Sasamoto, M. Mizoguchi, and P. He, "A New Sulfonated Tetrazolium Salt That Produces a Highly Water-Soluble Formazan Dye," *Chem. Pharm. Bull.*, vol. 41, no. 6, pp. 1118–1122, 1993.

[123] K. Hamasaki, K. Kogure, and K. Ohwada, "A biological method for the quantitative measurement of tetrodotoxin (TTX): Tissue culture bioassay in combination with a water-soluble tetrazolium salt," *Toxicon*, vol. 34, no. 4, pp. 490–495, 1996.

[124] M. Ishiyama, Y. Miyazono, K. Sasamoto, Y. Ohkura, and K. Ueno, "A highly water-soluble disulfonated tetrazolium salt as a chromogenic indicator for NADH as well as cell viability," *Talanta*, vol. 44, no. 7, pp. 1299–1305, 1997.

[125] H. Ukeda, T. Shimamura, M. Tsubouchi, Y. Harada, Y. Nakai, and M. Sawamura, "Spectrophotometric assay of superoxide anion formed in Maillard reaction based on highly water-soluble tetrazolium salt," *Anal. Sci.*, vol. 18, no. 10, pp. 1151–1154, 2002.

[126] K. Chamchoy, D. Pakotiprapha, P. Pumirat, U. Leartsakulpanich, and U. Boonyuen, "Application of WST-8 based colorimetric NAD(P)H detection for quantitative dehydrogenase assays," *BMC Biochem.*, vol. 20, no. 1, pp. 1–14, 2019.

[127] R. M. Zabinski-Snopko and G. H. Czerlinski, "Spectrophotometric titrations of ferricytochrome C with ferrohexacyanide in the pH range 5 to 7," *J. Biol. Phys.*, vol. 9, no. 3, pp. 155–167, Sep. 1981.

[128] V. Massey, "The microestimation of succinate and the extinction coefficient of cytochrome c," *Biochim. Biophys. Acta*, vol. 34, no. I954, pp. 255–256, 1959.

[129] F. M.White, "Viscous Fluid Flow." p. 629, 2006.

[130] G. Baldacchino *et al.*, "Importance of radiolytic reactions during high-LET irradiation modalities: LET effect, role of O2 and radiosensitization by nanoparticles," *Cancer Nanotechnol.*, vol. 10, no. 1, 2019.

[131] X. Fang, G. Mark, and C. von Sonntag, "OH radical formation by ultrasound in aqueous solutions Part I: the chemistry underlying the terephthalate dosimeter," *Ultrason. Sonochem.*, vol. 3, no. 1, pp. 57–63, Feb. 1996.

[132] G. Louit, S. Foley, J. Cabillic, A. Valleix, J. P. Renault, and S. Pin, "The reaction of coumarin with the OH radical revisited : hydroxylation product analysis determined by fluorescence and chromatography," vol. 72, pp. 119–124, 2005.

[133] M. Simic and M. Z. Hoffman, "Acid-base properties of the radicals produced in the pulse radiolysis of aqueous solutions of benzoic acid," *J. Phys. Chem.*, vol. 76, no. 10, pp. 1398–1404, 1972.

[134] D. M. O'Donnell, "Short-Lived Aqueous Benzoate Redox States Examined by Time-Resolved Resonance Raman Spectroscopy," 2010.

[135] K. Fujii, Y. Fukuda, and A. Yokoya, "Observation of cleavage in DNA and nucleotides following oxygen K-shell ionization by measuring X-ray absorption near edge structure," *Int. J. Radiat. Biol.*, vol. 88, no. 12, pp. 888–894, 2012.

[136] K. Fujii *et al.*, "Roles of Hydration for Inducing Decomposition of 2-Deoxy-d-ribose by Ionization of Oxygen K-Shell Electrons," *Radiat. Res.*, vol. 189, no. 3, pp. 264–272, Mar. 2018.

[137] M. A. Herve Du Penhoat *et al.*, "Lethal effect of carbon K-shell photoionizations in Chinese hamster V79 cell nuclei: Experimental method and theoretical analysis," *Radiat. Res.*, vol. 151, no. 6, pp. 649–658, 1999.

[138] B. Fayard *et al.*, "Cell Inactivation and Double-Strand Breaks: The Role of Core Ionizations, as Probed by Ultrasoft X Rays," *Radiat. Res.*, vol. 157, no. 2, pp. 128–140, 2002.

[139] H. S. Wang, "Development of fluorescent and luminescent probes for reactive oxygen species," *TrAC - Trends Anal. Chem.*, vol. 85, pp. 181–202, 2016.

[140] J. M. Antosiewicz and D. Shugar, "UV–Vis spectroscopy of tyrosine side-groups in studies of protein structure. Part 1: basic principles and properties of tyrosine chromophore," *Biophys. Rev.*, vol. 8, no. 2, pp. 151–161, Jun. 2016.

[141] G. V. Buxton, *Radiation Chemistry - Present Status and Future Trends*, vol. 4, no. 3. 2001.

[142] K. S. Ambe, U. S. Kumta, and A. L. Tappel, "Radiation Damage to Cytochrome c and Hemoglobin," vol. 15, no. 6, pp. 709–719, 1961.

[143] A. K. Pikaev, "Chemical Dosimetry of Pulsed Electronic Radiation," *Russ. Chem. Rev.*, vol. 41, no. 9, pp. 786–794, 1972.

[144] R. Endo, D. Watanabe, M. Shimomura, and T. Masuda, "In situ X-ray photoelectron spectroscopy using a conventional Al-Kα source and an environmental cell for liquid samples and solid-liquid interfaces," *Appl. Phys. Lett.*, vol. 114, no. 17, p. 173702, Apr. 2019.

[145] J. M. C. Gutteridge, "Ferrous-salt-promoted damage to deoxyribose and benzoate. The increased effectiveness of hydroxyl-radical scavengers in the presence of EDTA," *Biochem. J.*, vol. 243, no. 3, pp. 709–714, May 1987.

[146] C. Gosse, S. Stanescu, J. Frederick, and S. Lefrançois, "A flow cell for soft X-ray spectromicroscopy in liquid media Charlie," *J. Mater. Chem. B*, vol. 6, no. 35, pp. 7634–7639, 2020.

[147] G. W. Bushnell, G. V. Louie, and G. D. Brayer, "High-resolution three-dimensional structure of horse heart cytochrome c," *J. Mol. Biol.*, vol. 214, no. 2, pp. 585–595, 1990.

Chapter V. Early time analysis

Contents Chapter V

Chapter V. Early time analysis

The role of the water molecules surrounding biomolecules remains of primary interest while studying radio-chemistry. In addition to the indirect role of the ROS previously depicted in chapter IV, it is also clear that the hydration level can impact the early processes of light-matter interaction such as excitations, ionizations, and subsequent deexcitation pathways. In order to study and understand the effect of the aqueous solvent at very short times (femto-second), we performed electron spectroscopy measurements. Soft X-rays are particularly suitable for studying the chemical environment and investigating the early processes occurring through photoionization. Using synchrotron radiation to examine the electronic structure with soft X-ray absorption and emission (XPS, AES) spectroscopy provides valuable information about the different states that electrons can occupy. More precisely, this can help determine the density of states (DOS), i.e., the number of electronic states per unit volume per unit energy. Such information is essential to describe the electronic structure of the solvated molecules and to interpret charge transfer processes[1]. The development of an under-vacuum liquid micro-jet, introduced by Faubel and co-workers, offered the perfect environment for liquid XPS studies. A similar installation has been successfully implemented on the PLEIADES beamline in recent years. However, some concerns about the general performance of the liquid jet sensitivity, stability of the biomolecule during the liquid retrieving process, liquid-vapor interfaces behavior, need to be investigated prior to applying these measurements to biomolecules irradiation. This chapter is therefore dedicated to the description of how spectroscopy helps to understand energy deposition processes. Proof of concept will be illustrated on small molecules (~ tens of atoms) to fully characterize the liquid jet environment and investigate the effect of the solvent during the photoionization process. In order to elucidate the fundamental mechanisms of the interaction, a magnetic bottle type time-of-flight electronic spectrometer (MB-TOF) was implemented for the first time with the PLEIADES liquid micro-jet. This spectrometer, specifically optimized to study multi-electronic processes, could bring information on the electronic states leading to the emission of AE. Finally, we will present our first results on proteins to highlight the advantages and drawbacks of liquid XPS measurements on such complex systems.

V.1. Proof of concept with benzoate salt

Electron spectroscopy provides information on the photoionization process. Therefore, it gives key elements on the influence of the solvent on the electronic structure of solvated molecules. Even if under-vacuum liquid jets are more and more frequent at synchrotrons centers, several questions remain unsolved concerning the repartition of the molecules inside the jet and their interaction with the solvent in the bulk and at the interface[2].

As illustrated in the previous chapters of this manuscript, benzoate is the molecule at the center of our water radiolysis studies. This aromatic carboxylic compound, previously used as a hydroxyl radicals scavenger, is highly soluble (up to 2 M), readily available, and harmless. It seemed obvious to us to study it by XPS with a liquid jet to oversee the effect of the solvent on its electronic structure and eventual irradiation damage during the measurement. Before studying more complex systems of biological interest, we decided to conduct a complete spectroscopic study of benzoate aqueous solutions. At first, we decided to measure the eventual effect of irradiation during the XPS measurements. Thus, an aqueous solution of benzoate (one liter at a concentration of 0.5 M) was injected through the liquid micro-jet. The solution underwent several successive XPS analyses (seven irradiations at 400 eV) and was collected for further fluorescence analysis to probe hydroxylation. No fluorescence could be measured, suggesting that no 2-HOBz was formed, or at least in enough quantity to be detected via fluorescence[62].

Similarly, no change in the XPS spectra was observed. In order to evaluate the sensitivity of the XPS signal, a solution of benzoate (0.5 M) was exposed to 1 kGy using γ-rays. This solution, containing $3 \cdot 10^{23}$ molecules/L, was then injected in the under-vacuum liquid micro-jet for XPS analysis. Again, no difference was observed in the XPS spectra of irradiated and non-irradiated samples. Such experiments evidenced that the actual liquid jet environment could not be used as an irradiation setup. The number of molecules exposed to the synchrotron beam that could undergo modifications is indeed too small to be detected via analytical methods after solution retrieval. However, these experiments validated that XPS offers a suitable environment for the study of small molecules as the experimental conditions do not damage them. Now, several questions

[62] *Other hydroxybenzoate were not quantified. See chapter II for more details about 2-HOBz fluorescence.*

remain when studying solvated molecules using XPS: How does the aqueous solvent affect the XPS signal? Does the solvation sphere of the molecules in solution impact the signal of the core level? How does it impact the signal of valence electrons?

V.1.1. Investigation of molecular repartition

V.1.1.i. Sensitivity of liquid XPS

A significant challenge when using an under-vacuum liquid micro-jet is first to understand the behavior of the molecules at the liquid/air interface. Given the surface sensitivity of XPS measurements, detailed in Chapter I, the depth distribution of the molecules inside the jet can influence the results (spectral shifts, peak intensities). The repartition of the molecules inside the jet is not expected to be homogeneous, either in terms of orientation or concentration. Indeed, liquid-gas interfaces studies evidenced that the physico-chemical properties of the aqueous solvent can be significantly different at the surface and in the bulk of the solution[3].

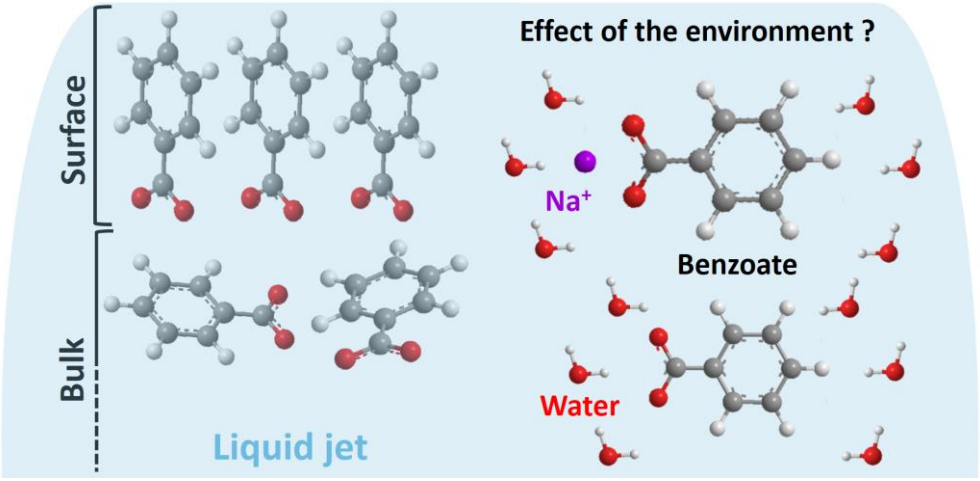

Figure V-1: Schematic illustration of the repartition of benzoate molecules at the interface, and in the bulk of a solutions. Presentation of the benzoate chemical environment in solution.

A classic example is the case of surfactant molecules, which modify the surface tension of an aqueous solution[4]. The behavior of amphiphilic molecules, including benzoate, was simulated at the air/water interface to understand the origin of surface tension changes[5]. This computational study evidenced that hydrotrope molecules, which contain an aromatic ring as a carbon chain, tend to orientate themselves at the solution's surface (see illustration in Figure V-1). On the contrary, the solute molecules tend to be randomly

oriented in the bulk, where the water molecules are present in a more homogeneous way. The surface sensitivity of XPS is ideally suited to study such spatial organization at interfaces. More specifically, at low photon energy, such as 400 eV, the resulting PE from the carbon atoms has kinetic energies in the 105-110 eV range (C-Kedge ~284 eV). The IMFP of electrons in liquid water is approximately 1 nm[6] (see Chapter I, Figure I-11). Therefore at low photon energy, the signal originates from an outermost molecular layer of the liquid jet. It was also shown that XPS is sensitive enough to describe the molecule's orientation for quite large molecules, such as the benzoate, by analyzing the relative areas of different core level signals linked to specific chemical functions. For instance, the liquid XPS study of a large fatty acid surfactant (decanoic acid) demonstrated that the carbon chains were oriented towards the surface of the liquid jet [7].

Similarly, experimental and theoretical calculations on benzoate showed that the hydrophobic aromatic carbon chain is repelled from the bulk of the jet[8]. The study even evidenced modification of molecules' orientation depending on the protonation of the molecule. As illustrated in Figure V-2, the signal of sodium benzoate at the carbon K-edge presents two contributions.

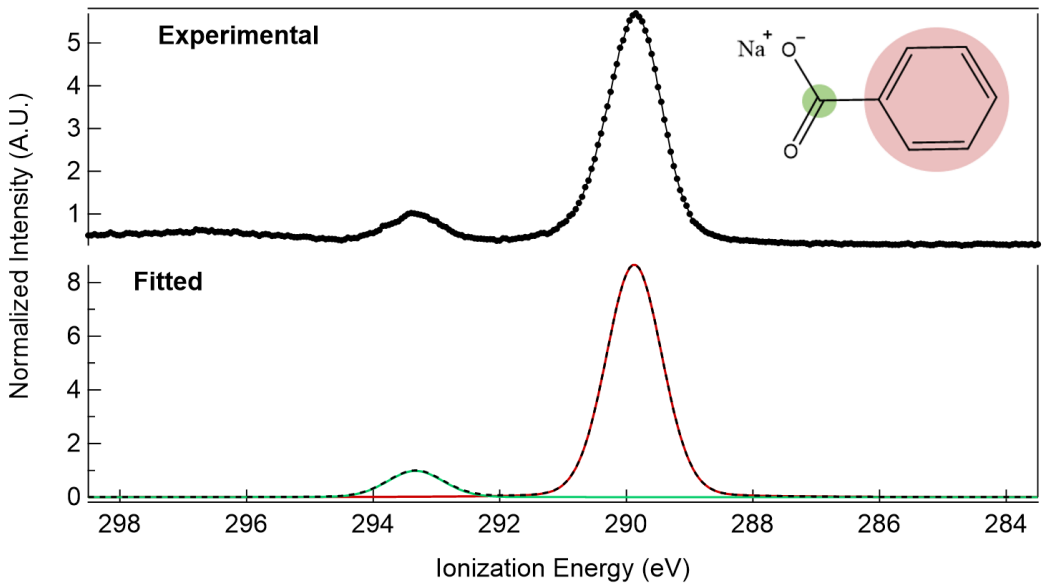

Figure V-2: XPS C1s signal of a 0.5 M benzoate solution analyzed at 400 eV photon energy (50 eV pass energy, polarization linear vertical (LV)). Experimental spectrum (black symbol) was calibrated according to the vacuum level. Signal was fitted by two contributions corresponding respectively to the aromatic ring (red) and the carboxylic function (green). The resulting envelope is plotted with a Tougaard background substracted (black dotted curve) and normalized to the signal of the carboxylic function.

The data presented in Figure V-2 were obtained at the SOLEIL synchrotron using the liquid micro-jet and the HDA of the PLEIADES beamline. The spectrum was recorded at 400 eV, with a pass energy of 50 eV. The synchrotron light polarization was linear vertical (LV), which corresponds to the light polarization parallel to the spectrometer axis for the PLEIADES setup. The total resolution for the measured energy is 0.13 eV. Data were calibrated on the O1s liquid phase signal (at 538.1 eV[9]). XPS signal is normalized to the signal of the carboxylic function. Data are then fitted by SGL(30) functions adding an asymmetric parameter to fit the experimental signal perfectly[10] (see section II.2.1 in Chapter II). The envelope and the two contributions are plotted after subtracting a Tougaard background[11]. The signal of the aromatic ring (red) is centered at ~290 eV ionization energy. The carboxylic function (green) is attributed to the signal at higher ionization energy according to the chemical shift –induced by the bonding with the oxygens (depletion of the electron density on the carbon).

More than the absolute ionization energies of the C core levels, this chemical shift is of particular interest as it will bring information about the benzoate chemical environment. As mentioned above in this section, the peak area also provides interesting information on the orientation of the molecules. In order to probe the sample at various depths, we recorded XPS spectra of 0.5 M benzoate solutions at different photon energies, between 400 and 4300 eV. Experiments were conducted on several beamlines (see Figure V-3). On the PLEIADES beamline (400 and 1000 eV), spectra were recorded using a LV polarization and a pass energy of 50 eV leading to a total resolution of 0.13 eV. On the GALAXIE beamline (2300 eV and 4300 eV), spectra were recorded in LH polarization (the light polarization parallel to the spectrometer axis), using a pass energy of 200 eV, reaching a total resolution of 0.1 eV for both photon energies. On the LUCIA beamline (2700 eV), the polarization was LH (the light polarization perpendicular to the spectrometer axis), the pass energy 100 eV, reaching a total resolution of approximately 1 eV.

From XPS spectra analysis, it was observed that the ratio between the two carbon core-levels signals varies with the photon energy. The area ratio ($C_{Benzene}$:$C_{Carboxyl}$) tends to decrease as the photon energy increases, taking into account the uncertainties. For the low-energy photons (400 eV), the ratio is found close to 10 (see Table V-1). This value, similar to one found in the study of Ottosson *et al.* at 360 eV[8], can be explained by the

orientation of the benzoate molecules with the benzene ring perpendicular to the surface (see Figure V-1). More precisely, the electrons ejected from the aromatic ring, being emitted closer to the surface, contribute more efficiently to the XPS signal than the PE emitted from the carboxylic function located deeper in the liquid jet (the distance between these two parts of the molecules is 0.425 nm).

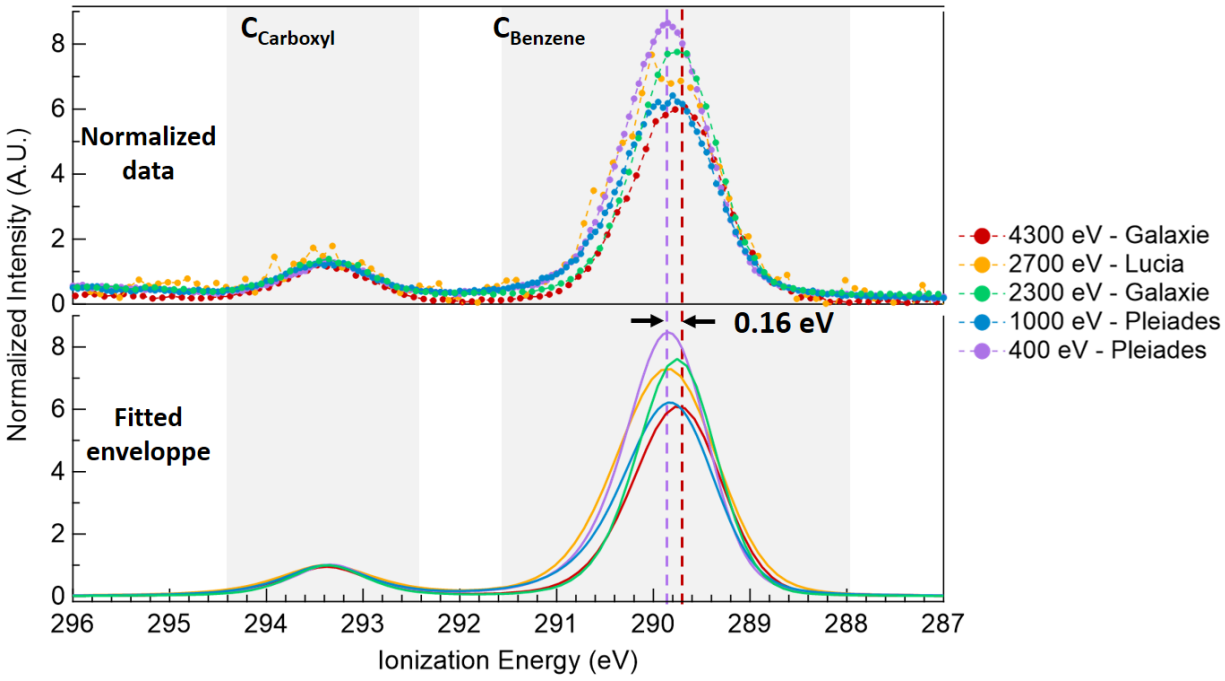

Figure V-3: XPS spectra of 0.5 M NaBz aqueous solutions. Experiments were conducted at different photon energies, using the liquid jet set-up on different SOLEIL synchrotron beamlines. Raw data were normalized to the $C_{carboxyl}$ signal. Fitting envelope spectra were obtained by subtracting a Tougaard background and using voigt functions. An assymetric tail was added for the $C_{Benzene}$ signal.

For photon energies above 1 keV, the ratio is close to the stoichiometric one (6:1). This value suggests that molecules are randomly oriented in the bulk of the liquid jet. It must be noted that the measured ratio can also be affected by the elastic scattering of the outgoing PE. Such effect may explain the variation observed at higher photon energies, 2300 eV, for instance, where the ratio is different from the stoichiometric ratio expected[12] (even if relatively far from the threshold).

As illustrated in Figure V-3 and Table V-1, a variation of the $C_{Benzene}$ chemical shift is observed for spectra recorded at 400 eV and 4300 eV. The energy difference between $C_{Benzene}$ and $C_{Carboxyl}$, referred to as ΔE_Cindeed varies from 3.64 ±0.02 eV to 3.82 ±0.02 eV respectively (see Table V-1). The error on ΔE_C is directly related to the uncertainty of the

fit. Indeed, for the same photon energy, the total experimental resolution, which results mainly in peak broadening, does not influence the energy difference measured

Table V-1: Summary of the data retrieved from XPS spectra of NaBz aqueous solutions (0.5 M) analyzed in the liquid jet setup at various photon energy, on different beamlines

Energy (eV)		**360 (Ottosson 2012)**		**400**	**1000**	**2300**	**2700***	**4300**
		BzCOOH	**$BzCOO^-$**	PLEIADES		GALAXIE	LUCIA	GALAXIE
PE IMFP (nm)		~1 nm		1 nm	3 nm	7 nm	8 nm	~10 nm
Area Ratio $C_{Benzene}$:$C_{Carboxyl}$		7.86	10.01	9.6 ±0.7	5.9 ±0.7	7.5 ±0.5	6.3 ±2	6.3 ±0.5
FWHM		Not mentioned		0.97	1.06	0.97	1.13	1.05
Position (eV)	$C_{Benzene}$	290	289.7	289.74 ±0.13	289.71 ±0.13	289.66 ±0.10	289.74 ±1.00	289.57 ±0.10
	$C_{Carboxy\ 1}$	294.2	293.1	293.34 ±0.13	293.38 ±0.13	293.37 ±0.10	293.43 ±1.00	293.39 ±0.10
ΔE_C (eV)		4.2	3.4	3.64 ±0.02	3.67 ±0.02	3.71 ±0.02	3.69 ±0.07	3.82 ±0.02

Comparing our experimental values to those obtained by Ottosson *et al.*[8], one could think that the variations of ΔE_C could be due to the protonation of the benzoate. However, the pH of the solution remained unchanged during our experiments. The benzoic acid proportion inside the 0.5 M benzoate solution thus remains negligible and should not influence the XPS spectra. Indeed, the eventual presence of additional peaks at 294.2 eV and 290 eV (for protonated benzoate) would have increased both the width of the carboxylic and benzene peaks

.

V.1.1.ii. Theoretical influence of the environment

Prof. Nobuhiro Kosugi performed simulations from The graduate University for Advanced Studies/SOKENDAI - Institute for Molecular Science in Japan. He performed *ab initio* self-consistent-field (SCF) calculations for the ground and core-ionized states based on a relaxed core-hole state using the GSCF3 program package[13]. The theoretical details of the method are presented in a recent paper[14], and further details are given in Appendix VI.1. The aim was first to evaluate the effect of water molecules around the

benzoate. The XPS signal of benzoate can be theoretically described with five contributions. The first one corresponds to the carboxyl group and the four other ones correspond to the benzene ring (see the full description of atomic numbering in Figure V-4). Because of the symmetry of the molecule, carbons $C_{(3\ \&\ 4)}$ and $C_{(5\ \&\ 6)}$ are respectively equivalent. The exact theoretical values are presented in Appendix VI.1.i).

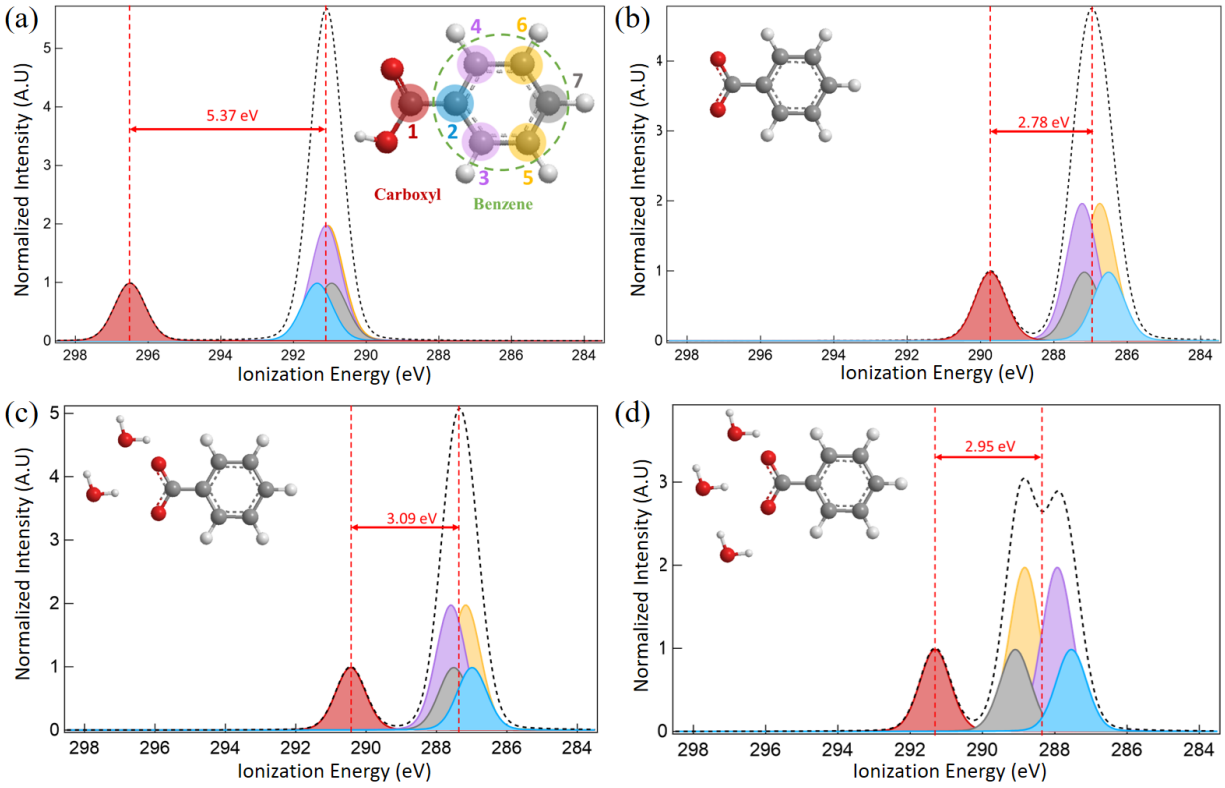

Figure V-4: Reconstructed XPS spectra obtained from computational approach structures: (a) benzoic acid, (b) benzoate, (c)-(d) benzoate with respectively two or three water molecules in its vicinity.

The theoretical results shown in Figure V-4 indicate that the protonation of the benzoate highly increases the energy difference between the two peaks (more than 2 eV). This observation is consistent with the experimental observation of Ottosson *et al.*, even if the calculated energy difference is two times higher than their experimental one (see Table V-1). Adding water molecules in the vicinity of the carboxyl group led to a slight increase of ΔEC. One can also note that, without considering the Na^+ counter ion, the calculated ΔE_C values remain inferior to the one found experimentally. The effect of interactions between carboxylate ions and water clusters in the presence of a sodium ion (Na^+) was then also evaluated.

Table V-2: Theoretical ionization energies obtained for benzoate molecules in the presence of Na^+, with or without water molecules.

Position	no water	2 H_2O	3 H_2O	5 H_2O
$C_{Carboxyl}$ (eV)	293.844	294.038	293.83	293.962
$C_{Benzene}$ (eV)	290.017	290.135	289.987	290.337
ΔE_C (eV)	3.827	3.903	3.843	3.625
Distance $C_{Carboxyl}$-Na^+	3.0 Å	3.0 Å	2.6 Å	4.2 Å
Structure	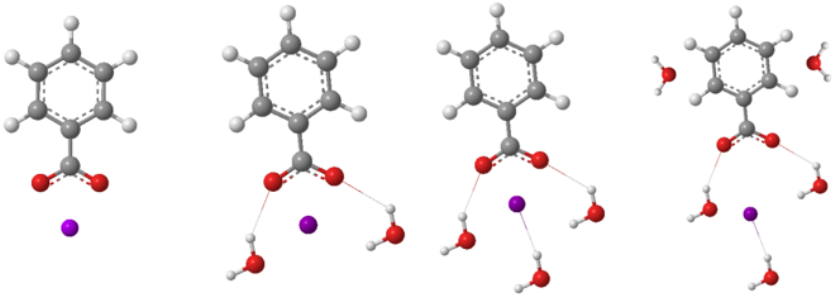			

Table V-2 presents the theoretical ionization energies calculated for sodium benzoate (NaBz), adding an increasing number of water molecules[15]. One can note that as soon as the sodium ion is taken into account, calculated positions (absolute ionization energies) are found similar to the ones obtained experimentally (Table V-1). In order to look over the values of the dry benzoate molecule (no water), solid XPS analyses were conducted using a conventional XPS laboratory. Experimental spectra are presented in Appendix VI.2. The difference in energy ΔE_C was found equal to 3.8± 0.02 eV, which perfectly agrees with the theoretical value (3.827 eV, see Table V-2)[63].

From the theoretical values, it is observed that the ΔE_C stays approximately the same when either the sodium or the carboxyl group is solvated (up to three water molecules), and thus they are not so much influenced by the solvation. However, ΔE_C decreases when two other water molecules are added in the vicinity of the benzoate ion (5 water molecules in total), passing from 3.843 to 3.625 eV. Thus, a desolvation around the benzene ring should increase the ΔE_C. The experimental values obtained for ΔE_C however increase with the photon energy. It is difficult to believe that in the bulk, the benzoate ions will be less solvated. The value of 3.64 eV, already found at 400 eV, seems to indicate that with a concentration of 0.5 M, there are already water molecules all around the benzoate ion,

[63] *Absolute position are also in good agreement as the $C_{Benzene}$ was found at 289.2 ±0.35 eV with respect to the gold Fermi level, corresponding to an ionization energy of ~290.4 eV (Gold ionization energy threshold at -5.5 eV).*

even if at the surface. However, adding water molecules also impacts the distance the carboxylate and the sodium ion (increase from 3 Å to 4.2 Å as the number of water molecule increases from 2 to 5, as illustrated in the structures presented in Table V-2). In order to further investigate this parameter, theoretical ionization energies were calculated varying the distance $C_{Carboxyl}$-Na^+ in the absence of water (see Appendix VI.1.iii). Results evidenced that by decreasing the distance from 3.0 Å to 2.5 Å, the ΔE_C value increases from 3.5 to 3.8 eV.

It thus seems that the change in the value of ΔE_C captures the variation of the distance $C_{Carboxyl}$-Na^+, which could be longer by 0.2-0.3 Å at the surface than in the bulk. Nevertheless, solvation of the benzoate molecule could also impact the repartition (orientation and concentration) of the molecules inside the jet, and thus the ratio of the two carbon XPS signals.

V.1.1.iii. Probing solvation shell

As previously described, benzoate molecules tend to orient themselves at the interface. However, at high concentrations, close to the solubility limit, the proximity of the solutes molecules may impact this order. To probe the differences in the solvation shell in the bulk or at the surface of the jet, we injected benzoate of increasing concentrations (0.5 M, 1 M, and 2 M). Solutions were analyzed by XPS measurements performed at different photon energies to probe the surface and the bulk. XPS spectra are presented in Figure V-5 without normalization on the raw data (top graphs). Fitting was achieved as previously described in section V.1.1. Fitted envelopes are, for the same photon energy, normalized to the $C_{carboxyl}$, to facilitate the interpretation of the ratios of the peak. For all photon energies, it is clear that the overall carbon signal increases with the increase in solution concentration (see the number of counts/s on the left axis), taking into account that for each photon energy, the beamline and the spectrometer parameters were kept constant.

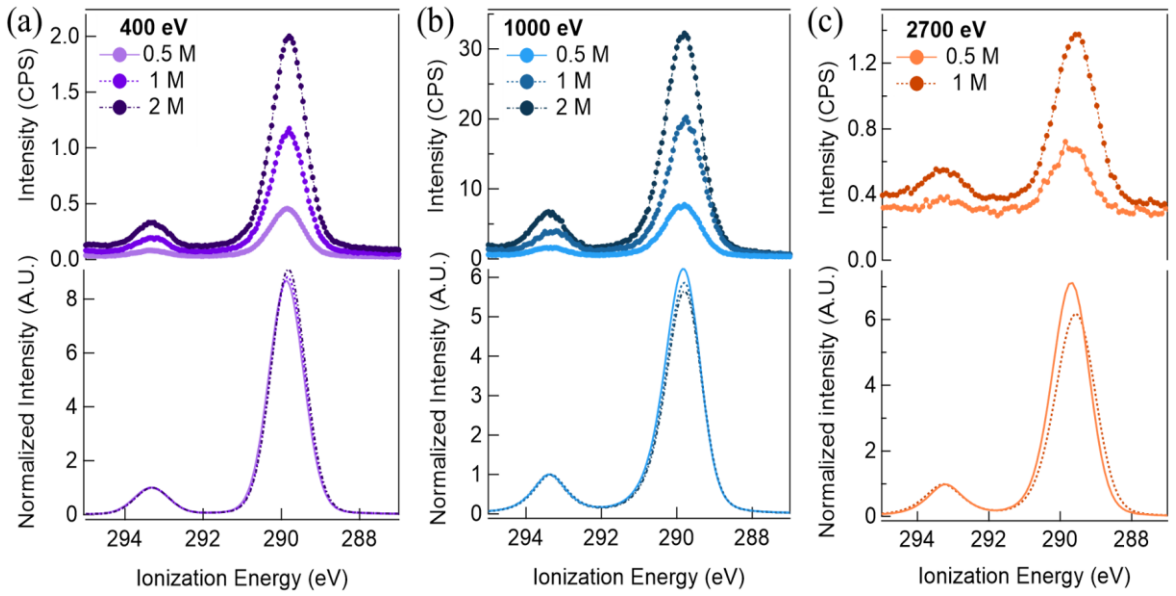

Figure V-5: Experimental spectra of sodium benzoate aqueous solutions of various concentrations measured on the PLEIADES (400 eV and 1000eV) and LUCIA (2700 eV) beamlines, with the same electron spectrometer. On the top graph, experimental raw data (in count/s) are represented (round markers) for the various concentration tested. On the bottom graph, fitted envelopes were normalized to the $C_{Carboxyl}$ signal and a Tougaard background was substracted to ease the comparison between the different solutions.

In order to have a closer look, the evolution of peaks areas with the concentration was evaluated for 400 eV, 1000 eV, and 2700 eV photon energies (see Figure V-6). Data presented in Figure V-6 are normalized to the area of the 1 M solution.

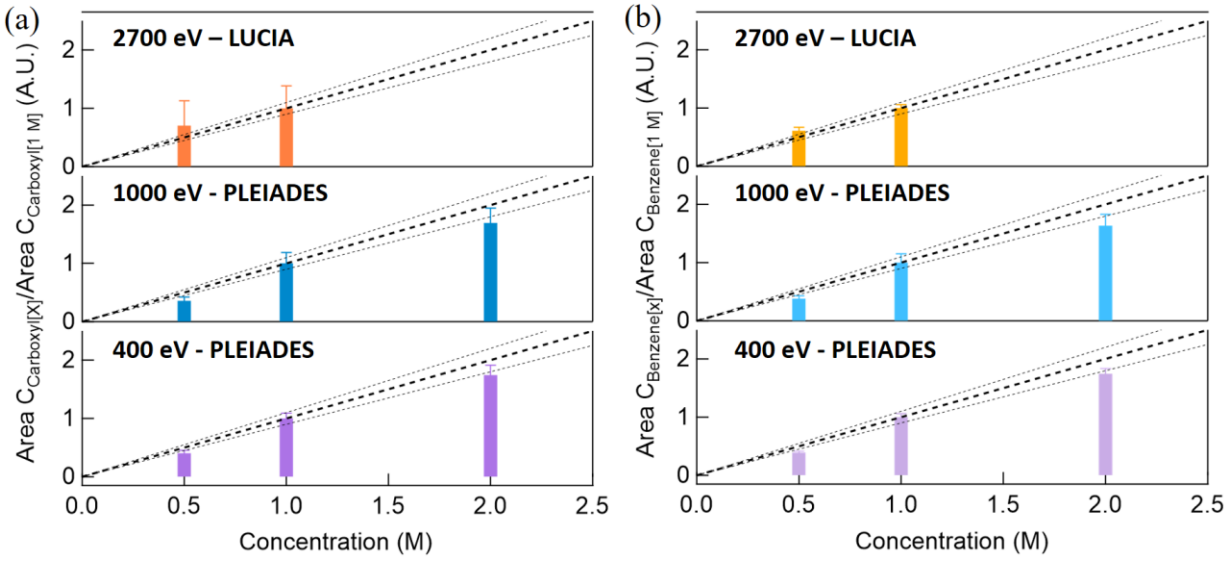

Figure V-6: Evolution of the XPS signal area varying the concentration. Respective area of the (a) $C_{carboxyl}$ and (b) $C_{Benzene}$ peaks were normalized to the area of the corresponding peak for the 1 M solution. Data are presented for different photon energies. The black dotted lines is the curve y=x (thick line) with 10% confidence.

The XPS signal is expected to be proportional to the concentration of the solute, if the scattering of the outgoing electrons can be neglected. Therefore, the normalized area should evolve following the curve y=x. As shown in Figure V-6, minor discrepancies are observed for results recorded at high concentrations but remain in the 10% confidence band range. These results suggest that the orientation of the molecules at the surface is therefore spontaneous and not due to the packing (interaction between solute molecules) and support the assumption that even at the surface, benzoate ions are still surrounded by water molecules even at a concentration of 2 M. Moreover, the area ratio $C_{Benzene}$:$C_{Carboxyl}$ remains constant for the three concentrations tested at 400 eV (see Table V-3).

Table V-3: Experimental values of XPS spectra measured at 400 eV (PLEIADES), 1000 eV (PLEIADES) and 2700 eV (LUCIA) for various concentration

		400 eV			1000 eV			2700 eV	
Concentration (M)		0.5	1	2	0.5	1	2	0.5	1
Area Ratio $C_{Benzene}$:$C_{Carboxyl}$ uncertainty		9.6 ±0.7	9.8 ±0.5	9.9 ±0.5	6.6 ±0.7	6.3 ±0.7	6 ±0.4	6.3 ±2	6.7 ±1
FWHM		0.95	0.95	0.94	1.06	1.06	1.06	1.13	1.29
Position (eV)	$C_{Benzene}$	289.74 ±0.13	289.7± 0.13	289.64 ±0.13	289.71 ±0.13	289.63 ±0.13	289.67 ±0.13	289.74 ±1.00	289.66 ±1.00
	$C_{Carboxyl}$	293.34 ±0.13	293.31 ±0.13	293.26 ±0.13	293.38 ±0.13	293.28 ±0.13	293.40 ±0.13	293.43 ±1.00	293.44 ±1.00
ΔE_C (eV)		3.64 ±0.02	3.60 ±0.02	3.67 ±0.02	3.67 ±0.02	3.65 ±0.02	3.73 ±0.02	3.69 ±0.07	3.78 ±0.05

Similar results are observed for higher photon energies, indicating that the molecules remain randomly organized in the bulk (ratio close to 6), even for highly concentrated solutions. Concerning the solvation of the benzoate, no variation was observed on the ΔE_C varying the concentration, taking into account the uncertainties. Therefore as expected, the concentration increase does not affect the solvation shell of the molecules. It would have been interesting to investigate further the effect of the sodium ion on the ΔE_C. However, other benzoate salts, such as magnesium salt, for instance, remain poorly soluble in water (<1 g/L). Such liquid XPS experiments would therefore require very long acquisition times to reach a high resolution.

Finally, we can conclude that the XPS study of core-level electrons brought crucial information on the repartition of the molecules inside the liquid jet. Similarly, the binding energies of the electrons in the valence orbitals of solvated molecules can also bring important information. Especially as it gives direct information on the position of the molecule's highest occupied molecular orbital (HOMO), and therefore could help, for example, to understand the chemical reactions in an aqueous solution[16].

V.1.2. Studying the valence band of solutes

We present here the XPS valence band spectra of a 1 M sodium benzoate aqueous solution measured at 100 eV photon energy. The binding energy calibration of the valence band was performed using the well-established $1b_1$ gas-phase energy at 12.60 eV[17]. Figure V-7 shows the PE spectrum of liquid water, including the gas-phase contribution (red spectrum). The blue spectrum represents the water gas-phase contribution with almost no contribution from the liquid phase (integration of the XPS signal away from the liquid jet, see Chapter II, section II.2.1.iii for more details).

The labels in the figure refer to the three valence molecular orbitals $1b_1$, $3a_1$, and $1b_2$ of the water molecules. The gas and liquid phase contributions to the photoemission spectra are indicated by the respective subscripts (e.g., $(1b_1)_{gas}$ and $(1b_1)_{liq}$. The $(1b_1)_{liq}$ band for a 1 M sodium benzoate solution is obtained at 11.09 eV. The difference in energy of 1.51 eV between the liquid-gas $1b_1$ signal is in agreement with the literature ($\Delta E((1b_1)_{gas}$-$(1b_1)_{liq}) = 1.45$ eV measured by Winter *et al.* [18]). The photoionization threshold of liquid water (with 1M of sodium benzoate) was found equal to 9.74 ±0.15 eV, obtained by extrapolating the slope of the $(1b_1)_{liq}$ signal. This value is close to the ones previously reported in the literature for neat liquid water (9.9 eV[18] and 10.06 eV[19]). The similarity of these results implies that adding a non-negligible concentration of salt only slightly modifies the main contribution of the water electronic states. The lower value of the onset could be due to the presence of hidden electronic states of the sodium benzoate under the $(1b_1)_{liq}$. Zooming on the low-energy part of the spectrum (Figure V-7.(b)), allows the

determination of the ionization threshold of solvated sodium benzoate at 7.96 ±0.15 eV. To the best of our knowledge, this value has not yet been reported in the literature.

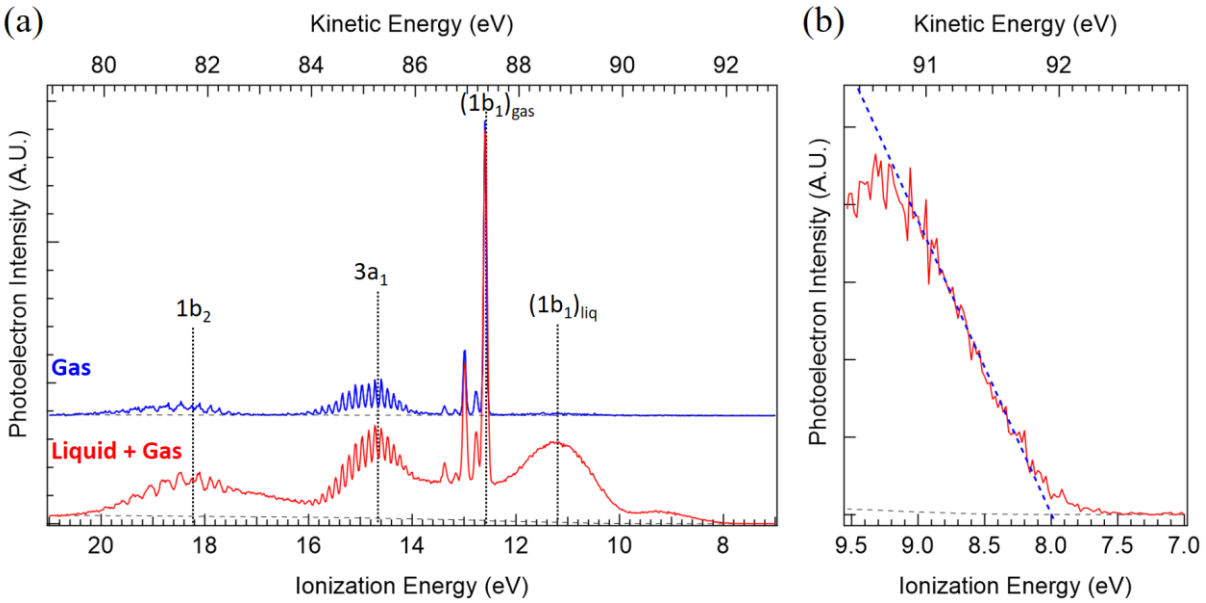

Figure V-7: Valence band spectra of a sodium benzoate aqueous solution (1 M) measured in a liquid jet. The experiment was conducted at 100 eV photon with a pass energy of 20 eV. (a) Total spectra of the aqueous benzoate (red). The spectrum of the solution shows a contribution of the water gas phase due to evaporation. The spectrum of the gas-phase (blue) can be evaluated by intergrating the image of the detector far from the jet (see text for more details). Molecular orbitals of the liquid and gas water phases are labeled with respective subscript l or g for liquid and gas. (b) Contribution of the solvated benzoate and determination of the photoionization threshold by linear extrapolation.

In the liquid micro-jet, the liquid water contributions may hide contributions of the NaBz below them. For this reason, similar valence band measurements were conducted in the solid phase, using XPS laboratory instrumentation. Binding energy was calibrated with respect to the gold Fermi level (see Chapter II, section II.2.1.ii for experimental details). UPS's valence spectrum of the solid phase brings information on the electron density of states hidden below the water bands. As presented in Figure V-8, the electronic structure of sodium benzoate presents different contributions labeled from I to IX. The ionization threshold of sodium benzoate (or valence band maximum) was found equal to IET_{NaBz}^{solid}= 3.4±0.35 eV (linear extrapolation of the band I). The difference observed with the IET_{NaBz}^{liquid} can be assimilated to the work function of the solution. The resulting value of $\varphi_{solution}$= 4.56±0.50 eV is in agreement with the one reported in the literature for

water, which is around 4.7 eV[43,62]. Theoretical calculations are needed in order to decipher the different characters of chemical bonding associated with these orbitals. However, ionization energies of the inner valence shell of aromatic hydrocarbons (benzene derivatives) were extensively studied[20]–[22]. The solid benzene UPS spectrum measured by Riga *et al.* is presented in Figure V-8 to bring information on the character of benzoate molecular orbitals[23].

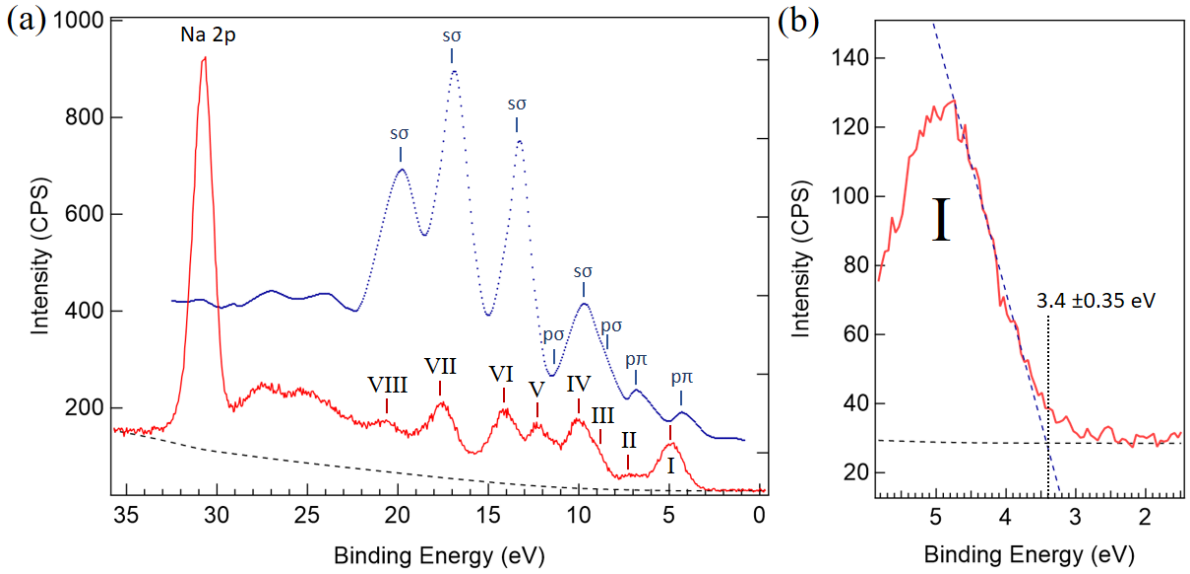

Figure V-8: Valence band spectrum of NaBz measured in the solid phase using Al K-α X-rays (pass energy 20 eV). (a) Total UPS spectrum of benzoate (red) and benzene from the litterature (blue)[23], (b) Photoionization threshold determination by a linear extrapolation of the band I. The value for solid benzoate was 3.4±0.35 eV with respect to the gold Fermi level.

Attribution is presented in Table V-4. Other peaks at higher bending energies are in general due to transitions between π orbitals.

Table V-4: UPS analysis of sodium benzoate dry crystals.

Band	**I**	**II**	**III**	**IV**	**V**	**VI**	**VII**	**VIII**
Energy level (eV)	4.9	7.2	8.9	10.1	12.3	14.2	17.6	20.8
Character	pπ	pπ	pσ	sσ	pσ	sσ	sσ	sσ

The determination of electronic structures, particularly the ionization thresholds of a solvated molecule, can help investigate the impact of irradiation. Indeed, knowing the

solvated molecule's electrical properties allows us to understand better the deexcitation pathways of secondary electrons emitted during the photoionization. Nevertheless, emission spectroscopy probes only core holes formed by photoionization. In order to retrieve more information about the electronic structure, absorption spectroscopy should also be considered.

V.1.3. Study of interatomic Auger transitions

Above the carbon K-edge threshold, core-ionization and following deexcitation processes (normal Auger decay, ICD, ETMD) can occur and constitute the aim of XPS analysis. On the contrary, the core-excitation is more probable below the K-edge threshold: a core electron is excited to an initially unoccupied valence level (LUMO). It forms the basis of XAS and XAFS, which are used to study the unoccupied electronic states of the targeted molecule.

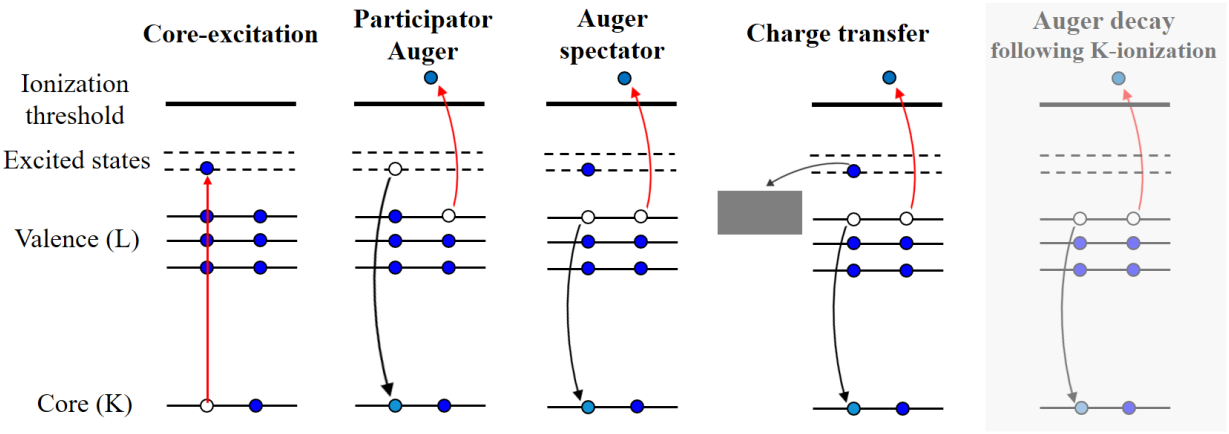

Figure V-9: Scheme of the non radiant processes that could occur arround and above K-edge resonances. See the text for more details. (Image adapted from [24])

As for core-ionization, the core excitation of a molecule can lead to various deexcitation processes that can be either radiative or non-radiative (emission or not of photons)[24]. Both are good tools to probe the unoccupied electronic structure of a sample but, in the context of electron spectroscopy, we will focus on non-radiative processes. Core-excited states undergo Auger decay in the femtosecond regime[25]. This deexcitation process is usually referred to as auto-ionization or resonant Auger effect. Contrary to the normal Auger process, the resonant Auger effect cannot be decomposed in two steps because the

excitation and the decay cannot be disentangled. Gel'mukhanov and co-workers developed in the theory of X-ray Raman Scattering to interpret this resonant process[26]. The excited electron can either participate in the decay process (participator Auger) or not be involved in the decay process (spectator Auger), leading to different final states of the singly charged ion. Indeed, the participator decay will lead to single-hole final state configurations. In contrast, the spectator decay will lead to two-hole configurations lying higher in energy than the previous ones (see Figure V-9).

In the liquid phase, charge transfer processes may also occur as excited molecules interact efficiently with their neighbors[24]. The resulting final state configuration of the initially excited molecule contains two holes. Figure V-9 also presents the normal Auger decay, the main relaxation channel in organic matter (see Chapter I, section I.1.2). One can observe that normal Auger decay and core-excitation deexcitation through charge transfer via the solvent lead to similar final states. Such similarity suggests that it would be possible to observe charge transfer processes in the region of kinetic energies belonging to the normal Auger decay.

First, it is essential to identify (in terms of photon energy) the different resonances, which could occur below the C1s ionization threshold. To do this, we plotted the partial electrons yield[64] as a function of the photon energy for a sodium benzoate aqueous solution (NaBz 0.5 M). Data were obtained using the HDA of the PLEIADES beamline set at a pass energy of 200 eV and an entrance slit of 50 µm.

[64] *We are speaking about partial electron yield as only electrons linked to the first valence states are detected.*

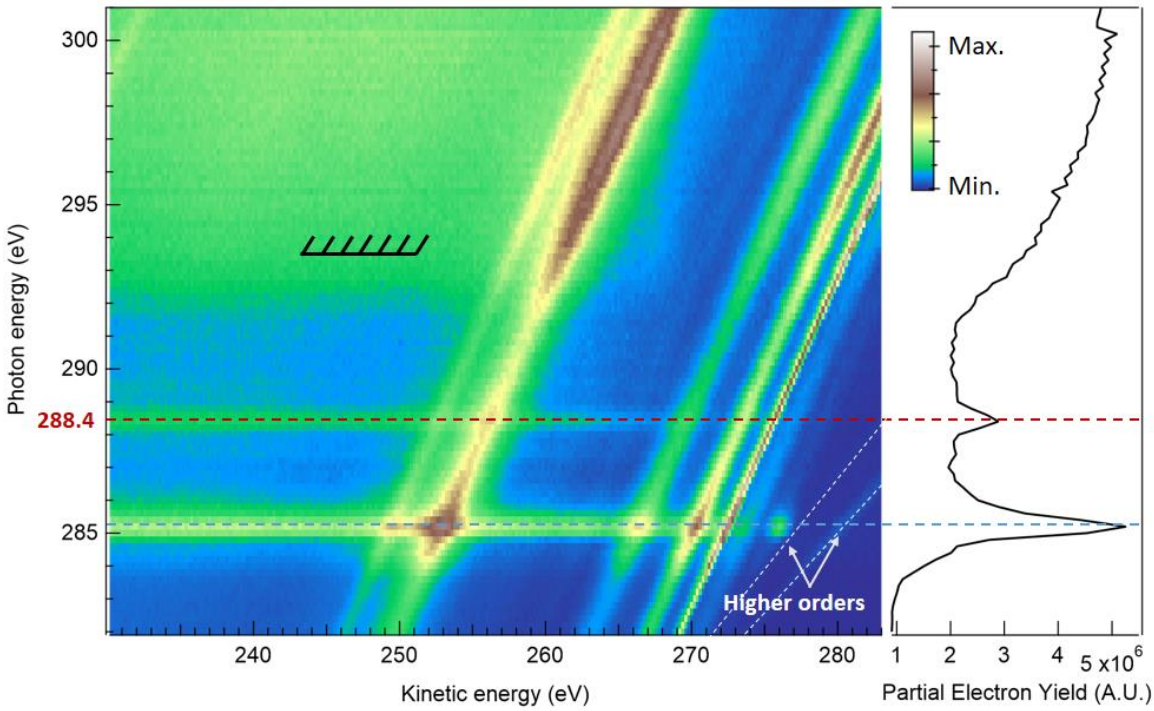

Figure V-10: Resonant Auger spectroscopy of liquid aqueous solutions of sodium benzoate (NaBz 0.5 M): 2D map showing the kinetic energy of the electrons emitted around the C K-edge (step 0.2 eV) vs the photon energy (step 0.2 eV). Intensities were normalized by the photon flux. White dotted lines indicate the production of 2nd order C1s PE. The black curve represents the experimental partial electron yield spectrum of solvated NaBz obtained after integrating the total number of electrons at each photon energy.

Figure V-10 presents a 2D map (normalized by the photon flux) of the resonant Auger spectra (RAS) recorded with photon energies varying, with a step of 0.2 eV, around the C K-edge resonance. The diagonal lines correspond to the PE signal. Indeed, as we are looking at PE, the lines disperse linearly (with a slope of 1) as a function of the photon energy. PE generated from higher orders light will disperse faster, as it can be seen in the bottom right of the 2D map. At each photon energy, the integration of the total electron signal leads to a partial electron yield spectrum represented by the black curve (Figure V-10).

We observe an increase of the partial electron yield towards ~292 eV corresponding to the ionization threshold of the C K-edge in the liquid phase. In addition, two structures are observed at respectively 285.2 eV and 288.4 eV. Figure V-11 presents the RAS spectra recorded at these respective photon energies, where resonant structures are observed (highest intensity), as well as an" off-resonance" spectrum taken at 282 eV (grey curve).

Theoretical calculations are still ongoing in order to identify which electronic states are involved in these resonances. However, the spectra presented in Figure V-11 show that the first resonance (hν= 285.2 eV) populates lower energy final electronic states than the second one (see increasing signals (i) to (iii)). It indicates that participator decays prevail during the excitation at 285.2 eV, contrary to the second resonance that does not populate the lowest valence states, and thus spectator decays probably happen. For example, the benzoate state (i) and (iii) are quasi non-resonant at 288.4 eV.

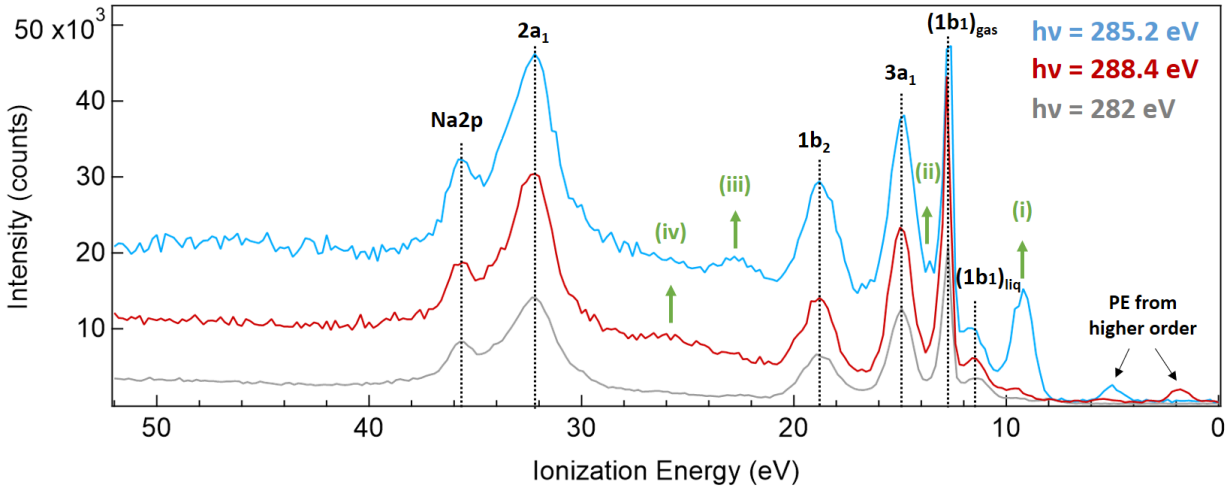

Figure V-11: Resonant Auger spectra of sodium benzoate in an aqueous solution (0.5 M). Data are extracted at various photon energies from the previous 2D-map presented in Figure V-10.

Another interesting point is the increase of the secondary electrons at the two resonant energies. On the 2D-map (Figure V-10), it is characterized by the two high intensity horizontal lines. In addition, the horizontal line at 288.4 eV starts only after the $1b_2$ states, compared to the one at 285.2 eV that extends until the lowest electronic final state. It confirms the predominance of the spectator decays for the second resonance. The production of these secondary electrons is also of particular interest as they can further induce ionization or excitation of the molecules present in the solution. Above the threshold, their emissions are significant due to the core-ionization.

Looking at the 2D map, it seems that the different water valence states are also significantly populated by the resonant effect. It might appear strange, as it is the carbon electrons of the benzoate that are excited. Moreover, in this region, the direct ionization cross-section for water should decrease monotonously. However, as shown in Figure V-12, many electronic states of the benzoate are lying" under" the predominant water bands.

Also, it is necessary to compare them with the electronic structures of the valence spectrum of the benzoate measured in the solid-state.

For the solid-state, the calibration was performed using the gold signal. The Na2p signal was found at 30.8±0.35 eV, which is in good agreement with the literature (30.4 eV[27]). In order to compare the two spectra, , data for the liquid phase was calibrated to the signal of Na2p at 30.9 eV[28], [29][65]. Figure V-12 shows that many electronic states of the benzoate have identical binding energy as the $1b_1$, $3a_1$, $1b_2$, and $2a_1$ states of liquid water (bands V, III, and II, for instance). Also, it is probably these different states of benzoate, which are populated during the core-excitation, and their increased intensities raise "artificially" the signal of the different water bands. In between the different water bands, resonant electronic states of benzoate can also be seen, especially for the first resonance. Comparing solid and liquid states analysis, one can also note that all the valence states of the benzoate are not resonant. Indeed, the solid valence spectrum also presents features that are not present in liquid RAS spectra (see the bands VIII).

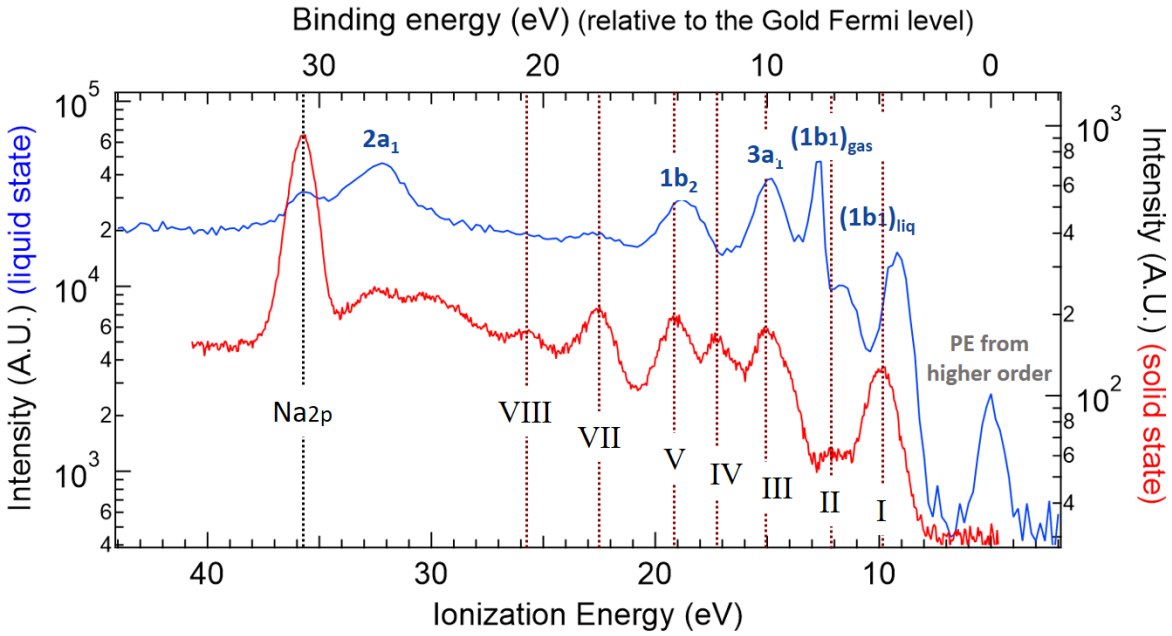

Figure V-12: Investigation of charge transfer fingerprints in the region of kinetic energies belonging to the normal Auger decay of C K-edge for solvated sodium benzoate. Blue spectrum corresponds to the XPS spectra recorded in liquid phase at 285.2 eV. Red spectrum is the valence spectra of solid NaBz. Data were calibrated with respect to the Fermi level using the signal of Na2p for the liquid phase and Au4d for the solid spectrum.

[65] *One must note that the shift in energy was equal to the previous determined value of the work function (4.6 eV).*

Due to the high contribution of the water gas-phase signal, it was not possible to perform this study at the oxygen edge. Indeed, the liquid phase resonances were drowned under the gas phase ones. The creation of a core-hole implies the complex reorganization of the electronic structure of the targeted system. Normal AE emitted in the deexcitation process can be used as a sensitive probe to study electron-electron correlations in molecules. To disentangle the different normal Auger spectra and thus better understand the eventual effects of the environment during the decay processes of the initial core hole, it is necessary to use a dedicated setup. Indeed, HDA not only limits the number of electrons collected but, in addition, does not allow to correlate the emission of AE with the PE. We will extend our study of benzoate solution using coincidence measurement, coupling a Magnetic Bottle Time-Of-Flight (MB-TOF) spectrometer to the liquid micro-jet. This setup developed by SOLEIL and LCPMR partners for the HighEneCh project was used and tested during my PhD for the first time.

V.2. Investigation of the Auger processes

V.2.1. Filtration of liquid and gas O1s signals

Even if the first coincidence experiments, using standard electrostatic spectrometers, were conducted on solid metallic samples [30], the large majority of the subsequent studies focused on isolated molecules (gas phase)[31]. It can be easily understood given the difficulty of performing these measurements in the condensed phase (many events, electron scattering). However, if used on a liquid sample, electron-electron coincidence measurements, or APECS, could help theoretical simulations as it brings information on the populated final states. Indeed, APECS measurements allow to retrieve the different structures of the Auger spectra. It thus brings crucial information on deexcitation processes to fill the hole created. To that aim, a MB-TOF was coupled with the liquid jet on the PLEIADES beamline for the first time. Only one similar setup was mounted by the team of U. Hergenhahn[32]. This implementation is far from being trivial given the specific geometry of the PLEIADES liquid jet, which is enclosed inside a compact differential box, increasing, even more, the challenge to get a good alignment between the SR beam, the liquid jet, the magnet, and the entrance of the spectrometer. The basic principle of the setup is presented in Chapter II, section II.2.2.

As a reminder, the diameter of the liquid micro-jet (Ø40 µm) is smaller than the one of the beam. Given the low penetration of soft X-rays, only electrons from the illuminated part of the liquid micro-jet surface can be detected. Consequently, a significant contribution of electrons can arise from the surrounding vapor phase (evaporation of the liquid water), ionized all along the synchrotron beam. As a first example of the possibilities of coincidence measurements on organic molecules in the liquid phase, we tried to determine if it would be possible to filter the events originating from the liquid from those of the vapor phase. For this, we decided to inject a benzoate salts solution as it was previously studied in non-coincidental XPS. The experimental total electron spectrum (photon energy 580 eV, ~40 eV above the O1s ionization threshold) is presented in Figure V-13. We decelerated the electrons by 20 eV to reduce the low-energy electrons

background. It also helps to improve the resolution since ΔE/E is about 2% of the kinetic energy in the MB-TOF spectrometer.

Several atomic contributions can be identified from the total electron spectra (Figure V-13), here presented as a function of both kinetic and ionization energies. The O1s PE are observed at ~20 eV kinetic energy (~540 eV IE) and C1s PE at ~270 eV (~290 eV IE). Finally, structures from AE and the valence band are identified at higher kinetic energy. AE are easily identified by changing the photon energy, as their kinetic energies are independent of photon energy (contrary to PE). Some structures around 60 eV and a broader contribution between 150 to 220 eV have not been identified yet, but seem to come from an artifact of the experimental setup, probably due to false coincidences.

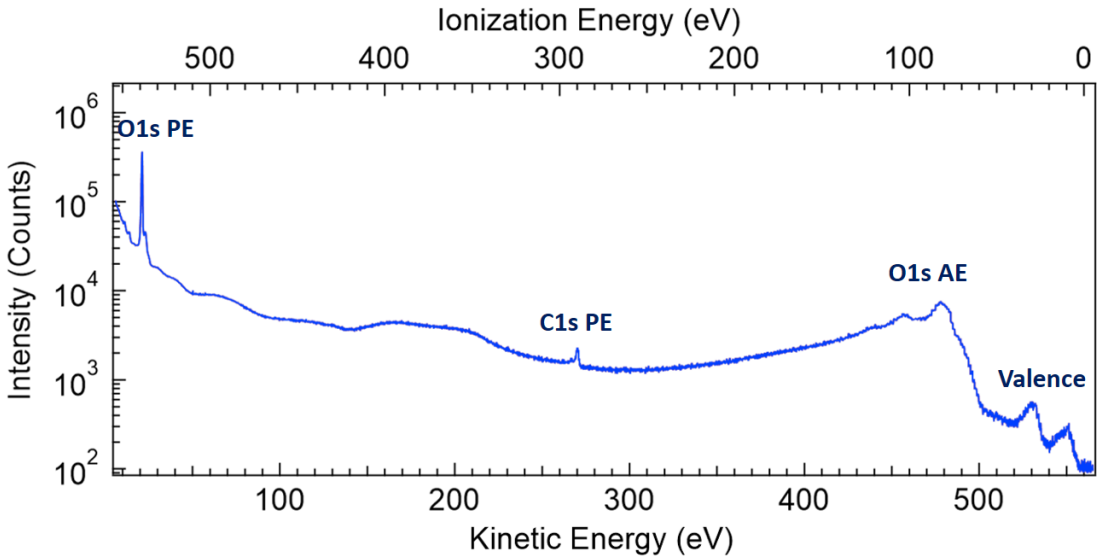

Figure V-13: Total electron spectra measured on a 1 M benzoate solution after one hour of acquisition (count rate in logarithmic scale). Conditions of acquisition were hν=580 eV, (deceleration of 20 eV); AE energy step 1 eV, PE energy step 0.1 eV, 13k-17k e⁻/s ~1h acquisition, Energy calibration was performed on the O1s gas signal and Ar2p resonances.

In order to see the different correlations between PE and AE, data are represented in a two-dimensional map, as illustrated in Figure V-14, with PE kinetic energy (y-axis) versus the AE kinetic energy (x-axis). Projections, either on the y- or x-axis, allow retrieving XPS (red curve) or AES spectra (black curve), respectively. This representation highlights coincidence events by the presence of more intense areas. In the XPS spectrum, we can identify three contributions corresponding to the water gas-phase (highlighted in

blue), centered at 19 eV KE, the water liquid-phase (highlighted in red), centered at 22 eV, and the solvated benzoate (highlighted in green), centered at 24 eV.

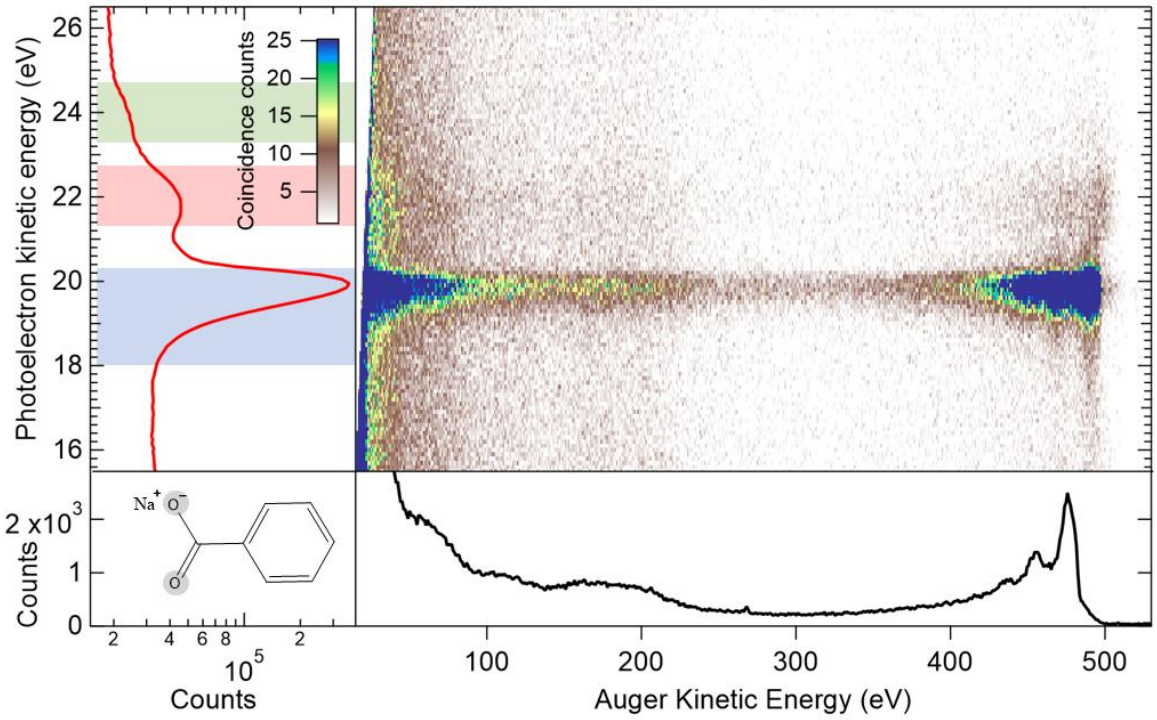

Figure V-14: O1s coincidence measurement on 1M benzoate solution (a) Coincidence map in energy: Data projection along the y-axis and x-axis represent the XPS spectra (red curve) and AES spectra (black curve) respectively.

The Auger spectra of O1s in coincidence with the three different contributions of the XPS spectrum can be obtained by filtering the data first according to the kinetic energies of the PE in the selected contribution and then by projection on the x-axis. Typical results are presented in Figure V-15 for the three contributions previously highlighted. We noticed that the position of the jet with respect to the entrance of the magnetic bottle as well as the magnet had a high impact on the general appearance of the backgrounds signal.

As illustrated in Figure V-15, the spectrum from the water vapor phase (blue spectra) is found similar to the one of the literature[33]–[35] except for a shift of ~20 eV, which is due to the global deceleration of the electrons. For the liquid phase spectrum, a decrease in the structures resolution is observed. It can be due to the fact that electrons undergo a high number of collisions with molecules before reaching the spectrometer entrance[36].

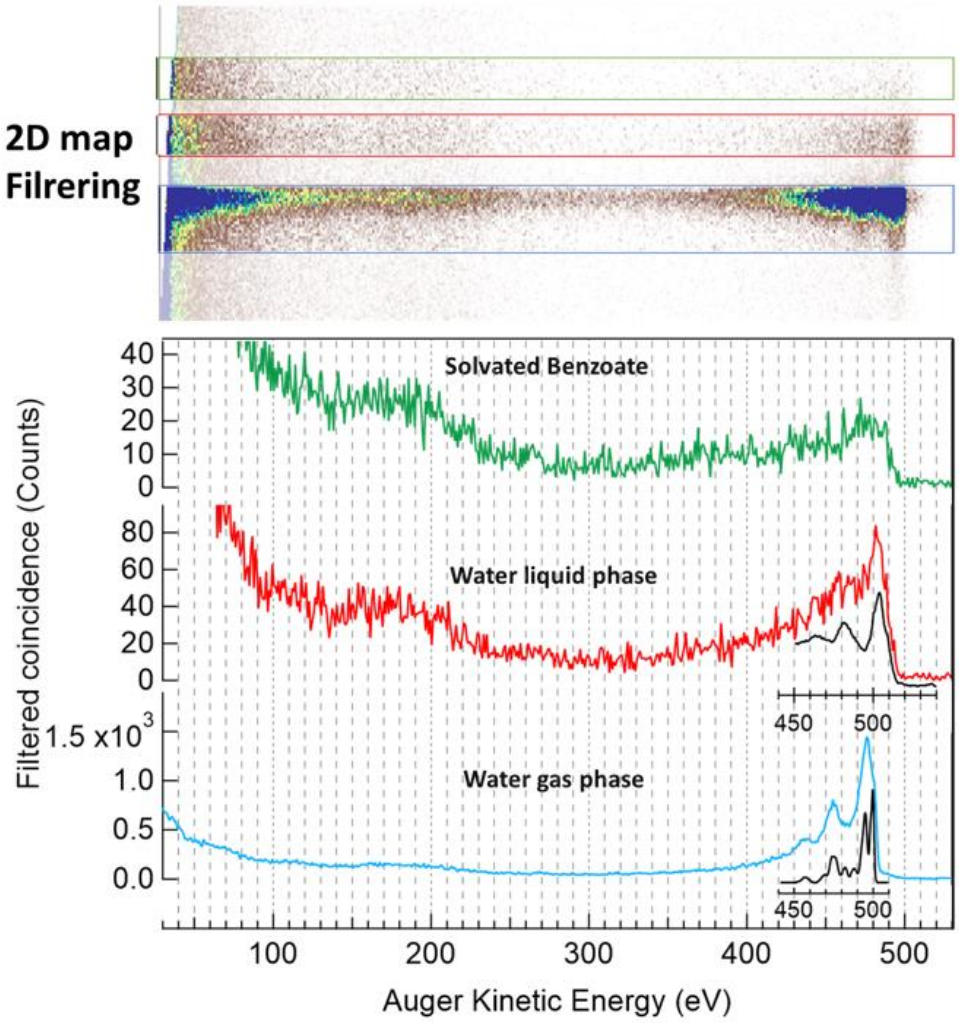

Figure V-15: Filtering of the O1s coincidence map of an aqueous benzoate solution (1 M). Filtered projections corresponding to gas-phase water (blue), liquid water (red) and solvated benzoate (green). Conditions of acquisition were hv=580 eV, applied bias -20V, AE energy step 1 eV, PE energy step 0.1 eV, 13k-17k e⁻/s. Energy calibration was performed on the O1s gas signal and Ar2p resonances. Data are compared with spectra from the litterature for the water gas and liquid phases [38]. The shift observed between kinetic energies of the theoretical results and experimental one is of 20 eV, which is coherent whith the deceleration bias applied on the MB-TOF.

Two studies by Winter and co-workers[37], [38] present the Auger electron spectrum of the water liquid phase. This latter was obtained in a liquid jet, using a non-coincidental setup. The AES spectrum was obtained by subtracting the gas-phase signal from the total AES measured (liquid+gas phase). As in our measurements, Winter *et al.* evidenced significant similarities in spectra from both phases, considering the loss of resolution. The resemblance in the Auger signals in the gas-phase (isolated molecules) and liquid phase spectra indicates that the excited states of water molecules in the liquid phase are probably in a broken hydrogen bond configuration[38]. In another study conducted by Öhrwall and

co-workers[39], the contribution of hydrogen bonding was further investigated by comparing AE spectra from isolated water molecules and water clusters. Results indicate a high-energy structure in the cluster spectra. More precisely, they observed an extension of ~12 eV from the maximum of the molecular spectrum. Such observation correlates with the shoulder observed in the liquid (see the broadening of the red spectrum in Figure V-15), which is also about ten eV from the prominent peak of the gas phase.

The benzoate molecule's results obtained at the oxygen K-edge (green spectrum in Figure V-15) suffer the measurement statistic (27 counts maximum). During the experiment, the recording time was indeed evaluated according to the total number of events. The latter is thus dominated mainly by the water O1s signal, which was very intense compared to the solvated benzoate molecule signal.

The structure at 150-200 eV does not seem to be an intrinsic contribution from the liquid. Indeed, its maximum intensity (~40 cps / 1 eV PE kinetic energy integration) remains identical in all three spectra. Moreover, this structure was observed in all liquid spectra recorded during this experiment (beamtime in 2019) but not in the following experiments (2020 & 2021). The filtering of the data, using the coincidence 2D-map, ensures a sufficient distinction between the different contributions of the XPS spectra. Therefore, this method is perfectly adapted to study the electronic structure of the solvated molecule, provided that its signal does not overlap too much with the water contributions (gas and liquid). We retrieved three different Auger spectra demonstrating that, even with a dense medium as a liquid jet, we achieved measurements conditions where false coincidences are not dominant[66].

V.2.1.i. First results at the carbon K-edge

Studies on the carbon K-edge were conducted at a photon energy of 335 eV with an applied bias of -20V on the solenoids. As for the O K-edge, a 2D-map was recorded (see Figure V-16). It also presents the PE (red curve) and the AE (black curve) spectra. On the C1s XPS spectrum, we can identify the contribution of the aromatic ring at ~26 eV KE (289 eV IE) and the one of the carboxylic function at ~23 eV KE (292 eV IE). These

[66] *In our data treatment, events were filtered in two electrons events but the false coincidences were not subtracted. These fortuitous events can lead to some "false" structures in the AE spectrum. Different strategies are under evaluation.*

values are very similar to the measurement with the HDA presented before (see V.1.1.i). We can also observe, above 20 eV in kinetic energy, an overall structure from satellites peaks due to π-π* shake-up.

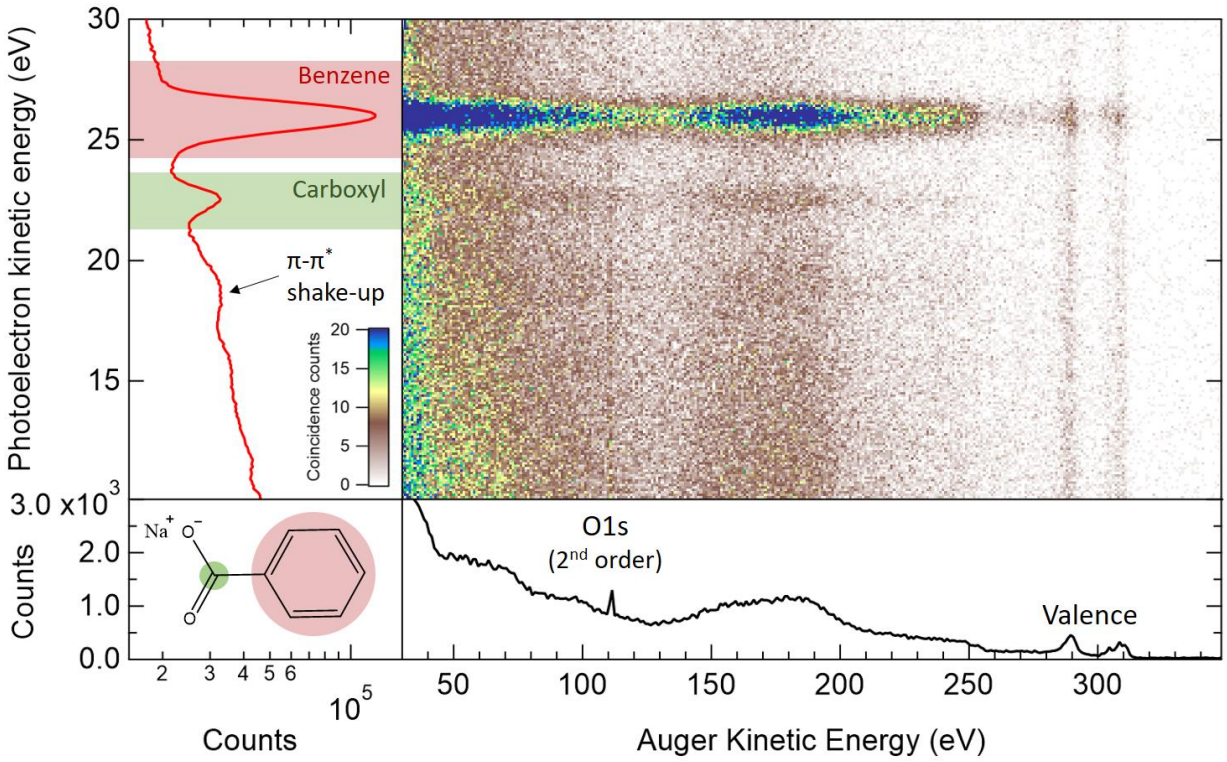

Figure V-16: C1s coincidence 2D-map of 1M benzoate solution flowing through the liquid jet: Data projections along the y-axis and x-axis represent the XPS spectra (red curve) and AES spectra (black curve) respectively. Conditions of acquisition were hν=335 eV, applied bias -20V, step Auger energy 1 eV, step PE energy 0.1 eV, 13k-17k e⁻/s. Results correspond to a total acquisition time of 40 min. Energy calibration was performed on O1s gas signal and Ar2p resonances.

On the total AE spectra (black curve in Figure V-16), we also noticed a contribution of O1s PE originating from the 2nd order of light from the monochromator. This signal is sufficiently intense to be detected, given the high density of water in the medium. Another feature observed is the band's presence at 150-200 eV, similar to the previous O1s analysis (hν=560 eV). It is thus very likely that it is a parasitic peak of the background noise induced by the experimental setup (field lines disturbance due to a bad alignment or false coincidences). Moreover, although we have filtered the data on "two-electrons" events, we observe a relatively intense valence band contribution (at 300 eV kinetic energy). The signal was thus attributed to a consequent amount of false coincidences.

Auger spectra in coincidence with the two different contributions of benzoate were extracted and are presented in Figure V-17. The signal of the O1s PE (2nd order) was normalized to the valence signal in order to compare the two spectra. We can notice a difference, with a plateau shape around ~240 eV kinetic energy for the signal of the aromatic ring compared to the one of the carboxyl.

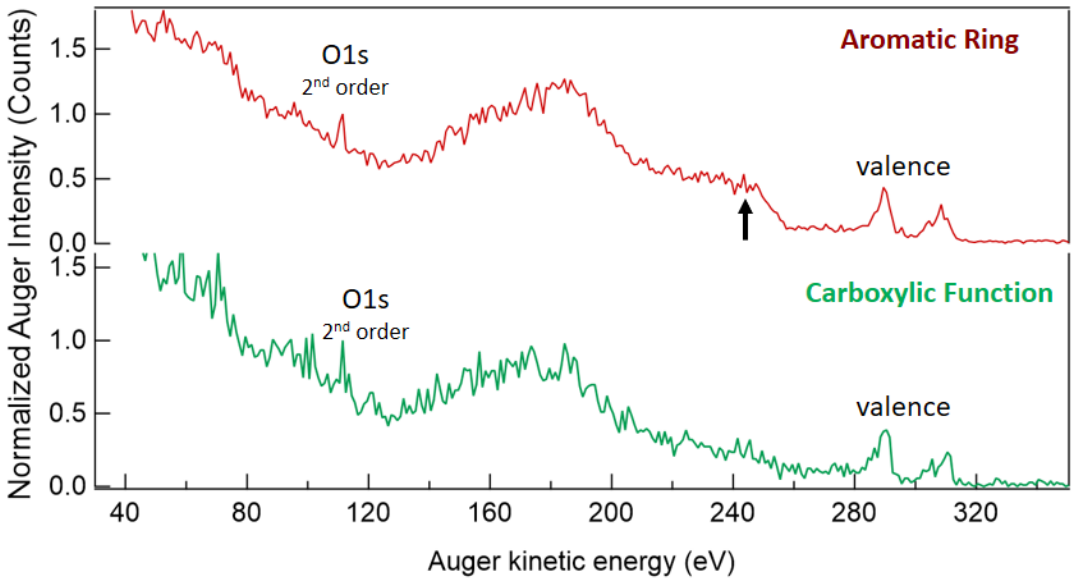

Figure V-17: Filtered projection of the 2D map presented in Figure V-16: Auger spectra correlated to PE from the aromatic ring (red curve) and the carboxyl function (green curve). Data were normalized to the O1s signal.

In order to further investigate the changes observed on Auger spectra depending on the chemical environment of carbon atoms, we decided to inject various aromatic components: sodium 2-hydroxy-benzoate (2-HOBz), sodium benzoate (NaBz), and benzoic acid (Bz) with a concentration of ~1 M[67]. At the C K-edge, spectra suffer no contamination from the solvent signal. Moreover, as for the HDA study, the solute molecules do not evaporate, so all signals came from the liquid phase. Data were acquired at 335 eV, with an applied bias of 20 V, reaching an overall resolution of ~0.5 eV. Electron collection was performed to reach an average of 1 billion events for each measurement. The analysis of the XPS spectra, illustrated in Figure V-18.(a), allows us to differentiate the different contributions of carbon atoms depending on their chemical environment.

[67] *For benzoic acid, the concentration was limited to the solubility limit 25 mM.*

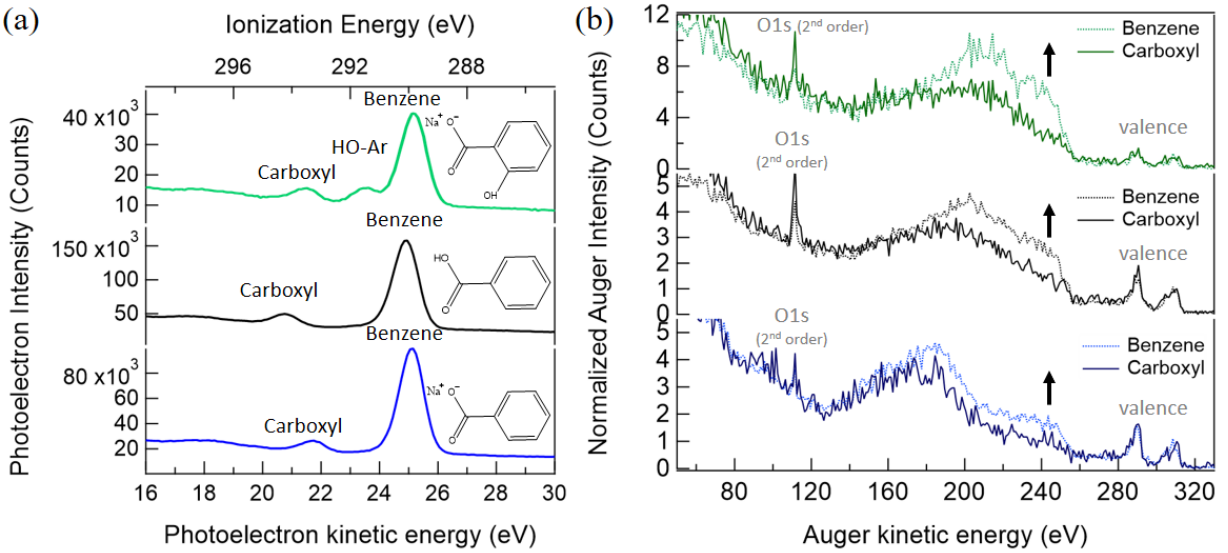

Figure V-18: MB-TOF analysis of aqueous solution of 2-hydroxy-benzoate (green), benzoic acid (black), and benzoate (blue): (a) XPS spectra, (b) Filtered AES spectra for the different PE contributions: benzene ring (dotted line) and carboxyl function (solid line). Data were normalized to the valence signal.

The aromatic ring leads to a signal centered at 290 eV IE. The signal of the carboxylic function is observed at ~294 eV IE with small shifts observed depending on the protonation (chemical shift of ΔE~1eV). Finally, the HO-$C_{aromatic}$ of the hydroxyl-benzoate is observed at 291 eV. Looking closer at sodium benzoate and sodium 2-HOBz, we can also notice that the relative areas of the peaks are found around ~9-10, suggesting that molecules are oriented perpendicular to the surface[7] (see the fitting parameter in Appendix VI.3).

After generating the coincidence 2D maps for each sample studied (presented in Appendix VI.3), we filtered the Auger signal correlated to PEs relative to the benzene ring and the carboxyl. In order to compare the spectra, data were normalized to the valence signal (see Figure V-18.(b)). We observed a contribution of the Auger spectra around 240 eV KE for all three aromatic compounds, correlated to the aromatic ring PE signal. By comparing the benzoic acid and benzoate spectra (resp. black and blue spectra in Figure V-18), it seems that the protonation of the benzoate anion tends to displace the barycenter of the Auger band towards lower kinetic energies. Specific attribution is impossible without a solid theoretical support. We can only assume that the final states of the dications populated after C1s ionization are different for an ionization on the benzene or the carboxylic carbons. Coincidence spectroscopy can bring some clue on the populated final states following an Auger decay. Therefore, it can help us understand the energy deposit,

bringing key information for computational simulations investigating post-Auger dissociation processes. These proofs of concept on simple molecules such as benzoate suggest promising results for the study of molecules of biological interest, whose electronic structure is generally particularly sensitive to solvation processes. It could also give needed inputs for the computational approaches that try to understand the influence of the Auger processes. With theoretical support, it could permit to determine the final electronic states linked to a specific PE. Nevertheless, even in more complex systems, in which it starts to be challenging to calculate the final states, the measurement will still permit determining the range of kinetic energies of the Augers electrons linked to a specific PE.

The measurements display very broad Auger structures, but it could still be interesting to compare the normal Auger spectra obtained in coincidence with spectra obtained via resonant Auger, in the same kinetic energy range to try hunting charge transfer processes.

V.3. Study of large biomolecule

V.3.1.i. Compatibility between proteins and the vacuum liquid jet

Thanks to the development of liquid jets and near-ambient pressure XPS (NAP-XPS), the determination of the electronic and geometric structure of biological samples is no longer limited to solid-state ultra-high vacuum analysis[40], [41], but can be performed in the native liquid state. The XPS study of biomolecules in an aqueous environment can significantly advance the knowledge of specific biological processes, such as protein-ligand interactions[42], cofactor properties[43], and more specifically, charge transfer in biosystems. Indeed, large biomolecules, and proteins, in particular, are highly sensitive to the electronic changes that take place due to the surrounding water molecules. Moreover, the highly labile hydrogen bonds play a crucial role in the structure of proteins and influence their biological function. However, to date, liquid XPS studies have been focused on the study of small amino acids[44], [45]. The liquid jet offers the perfect environment to study the electronic structure of biomolecules (proteins, sugars, DNA), as the liquid environment will help preserve the protein structure. The Bovine Serum Albumin (BSA) is a compound of choice for the proof of concept for this XPS study. Indeed, the BSA properties are well known because of its numerous biochemical applications (biochemical assays, cell cultures)[46]. This protein presents a high solubility in water (up to 40 g/L) and high stability in various environments (pH, temperature, pressure).

Moreover, compared to the Cytc protein previously used in Chapter IV, it is highly affordable, as it comes from purified bovine blood, which is a by-product of the cattle industry. Several solid phase studies have been reported on BSA[47]–[50], for all these reasons. Unfortunately, these studies do not allow the description of the protein's electronic properties in its natural state, i.e., in an aqueous medium. Only one single core-level XPS study of a protein in an aqueous solution, the BSA, has been reported to date in a NAP-XPS study, but with very low resolution and statistics[47]. The study of such a high and complex structure could demonstrate the great potential of liquid jet measurements. However, it is first essential to validate that the passage through the liquid micro-jet does not denature the protein sample. It can be easily achieved using the PLEIADES setup as the solution injected can be retrieved at the end of the experiment.

Solutions were prepared at high concentrations (0.5 mM – 36 g/L). In such conditions, the aqueous solution is self-buffered (pH = 7.2). The protonation of the protein at this concentration should thus be sufficient to avoid charging problems. Therefore, no salts were added to the protein solution. The prepared solution was dialyzed for one day to eliminate small molecular fragments[48]. Once irradiated with the synchrotron light, the protein solution was retrieved and analyzed by UV-visible absorption, UV circular dichroism, and electrophoresis. All the results are summarized in Figure V-19.

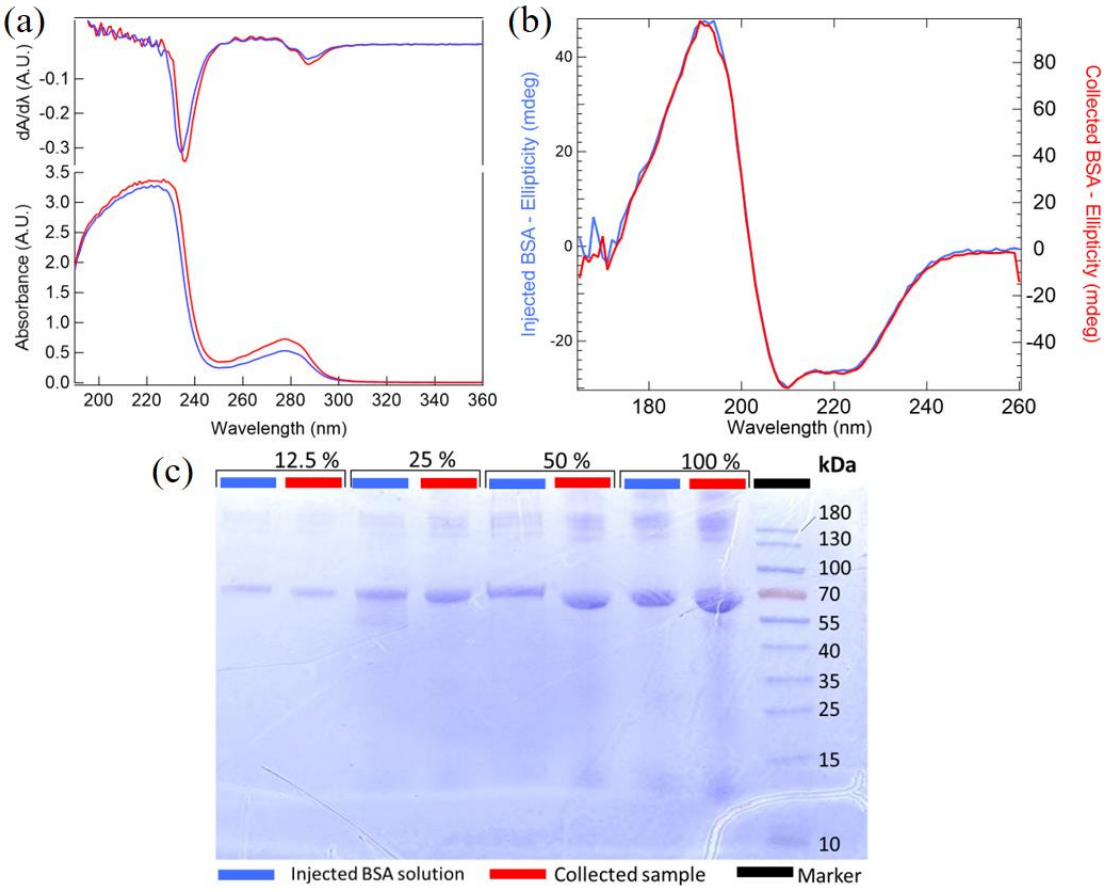

Figure V-19: Comparison of the solution before (blue) and after (red) its passage through the liquid microjet. (a) UV-vis absorption spectra and first derivative conducted on a solution diluted by a factor of 40 (band at 200 nm is still saturated), (b) SRCD spectra of the two solutions, (c) Gel electrophoresis with various concentrations.

In the case of proteins, far UV absorption (180-260 nm) contains information about peptidic bonds. The near UV region (250-330 nm) provides information about the environment of aromatic amino acids[49], [50]. UV-analysis of the collected solution reveals that it became more concentrated as it passed through the liquid jet (passage and storage in the collection bottle)(see Figure V-19.(a)). The evolution of the absorbance signal

evidenced a concentration increase of ~36% after the passage through the liquid micro-jet. The absence of significant change in the derivative of the signals indicates that the peptidic bonds remain intact and that the absorbance change is only due to water evaporation[68]. This phenomenon is classically observed for any aqueous sample injected into the vacuum liquid jet. Moreover, before being analyzed, the BSA solution stays hours in the pumped recycling bottle (during all the XPS, UPS measurements). In order to fully describe the secondary structure (α-helices, β-sheets, turns, and disordered structures), Synchrotron Radiation Circular Dichroism (SRCD) experiments were conducted by Frank Wien on a dedicated end station[51] of the DISCO beamline at SOLEIL Synchrotron (Saint-Aubin, France).

SRCD spectra were recorded from 170 to 260 nm (see Figure V-19.(b)). The path length was measured by light interference of the cell filled with pure water on a spectrophotometer in the visible domain. Spectra were averaged, baseline subtracted, and normalized at 190 nm using the CDtoolX software[52]. The respective amount of the different conformations was estimated using the online server BeStSel[53], [54] and is presented in Table V-5. SRCD allows working at a high concentration, such as the one used here. At pH = 7.2, a stable folding and homogeneous distribution of the protein in the solution is expected[55]. However, if any damage should occur, a change in the folding should be detected. Comparison of obtained SRCD spectra does not show significant differences in terms of structure. The high content of the helix structure (~70%) is in good agreement with the reported structure of the BSA in the literature[56], [57]. Therefore, no modification of the protein could be evidenced[58].

Table V-5: Secondary structural content of BSA assessed by deconvolution of far-UV (165-260nm) SRCD spectra using the BeStSel web server.

Treatment	α-helix	β-elements	Others
Before Injection	72.4	8	19.7
After Collection	73.5	8.1	18.5

Finally, we examined protein fragmentation using SDS PAGE gel electrophoresis (see Figure V-19.(c)). Each sample was deposited by increasing the amount of protein per well

[68] *The band at 200 nm is saturated at the concentration of study (~1 g/L).*

(dilution ratio 1:8, 1:4, 1:2, and 1). In addition to the expected monomeric form of the BSA (~66 kDa), we observe multimeric forms (>130 kDa) and some fragments (<15 kDa) for the low dilution ratio. Their presence in both injected and collected samples suggests that they are not damages or aggregations inherent to the experiment but rather to the preparation of the samples. The sensitivity of the fragment detection on the gel analysis is ~10ng (corresponding to 1 mg/L in our case). In order to investigate more precisely, the fragmentation of the protein LC-MS analysis could be envisaged. We tried to measure XPS spectra on solutions of various BSA concentrations in a 50mM NaCl solution (0.5 g/L, 2g/L, and 5 g/L). This range of concentration allows us to investigate the limit of detection of the protein. These measurements revealed that the study of the protein for concentrations lower than 0.5 g/L was not possible considering the accumulation time necessary for acquiring XPS measurements with a good signal-to-noise ratio. Thus, a concentration of fragments of 1 mg/L in a 36g/L BSA solution would not influence the XPS spectrum measured with the liquid jet.

A last important part is the stability of the protein solution under vacuum. Indeed, we encountered some difficulties during the injection of the protein solution under vacuum. On several occasions, the jet froze during the passage of the protein. After varying different parameters (nozzle size, catcher temperature, flow rate, and catcher/nozzle distance), we highlighted the crucial importance of the catcher's position relative to the jet. Indeed, it is evident that the jet must be centered on the center of the catcher in order to collect the fluid.

Nevertheless, a certain flexibility of the jet's position is usually accepted (possibility to approach to within ~20 µm of the catcher's edge). However, with the protein solution, the setting of the jet is crucial. Possibly, the high protein concentration (36 g of BSA per liter), leading to a higher viscosity, could modify the physical properties of the liquid jet expansion, which tends to make it quite unstable. On the contrary, the study at lower concentrations, 5 g/L, for example, did not raise any particular problems. Of course, working with lower concentrations implies a longer accumulation time since the amount of solute is directly related to the intensity of the XPS signal (decrease of the number of counts/unit of time). Therefore, the passage of biomolecules solutions under vacuum must be tested prior to conducting XPS measurements to ensure the vacuum jet's stability.

V.3.1.ii. Limits of core-level spectroscopy

We succeeded in recording the BSA's core-level spectra in the under-vacuum liquid jet for the first time. As previously mentioned, these data have been frequently reported in the solid-state. Some values retrieved from the literature are presented in Appendix VII. Some discrepancies were observed in the attributions. Indeed, the number of contributions attributed to a given signal (C1s, N1s) varies depending on the studies, even if experimental setup resolutions are similar. In our case, we decided to record the XPS spectrum in the solid and liquid states (pH = 7.2) to investigate the aqueous solvent's effect. As shown in Figure V-20, no significant differences were observed for solid and liquid at the C K-edge, taking into account the uncertainties of measurements. On synchrotrons, experimental spectra are recorded with a total resolution of 0.13 eV at 400 eV. However, the signal of the XPS peak is broader than the expected resolution due to the high number of initial states, due to the numerous slight differences in the chemical environment. For solid-state experiments conducted in the laboratory, the resolutions are only 0.35 to 0.5 eV (depending on the pass energy chosen).

The resulting values and fitting parameters are presented in Table V-6[69] and compared to those obtained by Jain *et al.* in NAP-XPS[47]. The difference in the energy scales in Figure V-20 is due to the reference signal used for calibration during the two experiments. Indeed, in solid analysis and for the NAP-XPS, binding energies are given with respect to the Gold Fermi level sample. For the liquid micro-jet, the spectra are referenced with respect to the vacuum level (see calibration details in Chapter II, section II.2.1). The energy difference between the two levels can be seen as the work function of the solution, neglecting the dipolar contribution of the surface potential energy [59]. It was found to be equal to $\Phi_{solution}$= 4.9 (±0.2) eV. This value is in good agreement with the one reported in the literature for water, which is around 4.7 eV[43,62], and the one previously measured for sodium benzoate (4.56±0.35 eV see V.1.2).

[69] *For the solid analysis, data are presented for the samples deposited on gold plate as they were recorded with a pass energy E_p= 20 eV (resolution of 0.35 eV) instead of those on copper recorded with E_p = 40 eV (0.5 eV resolution).*

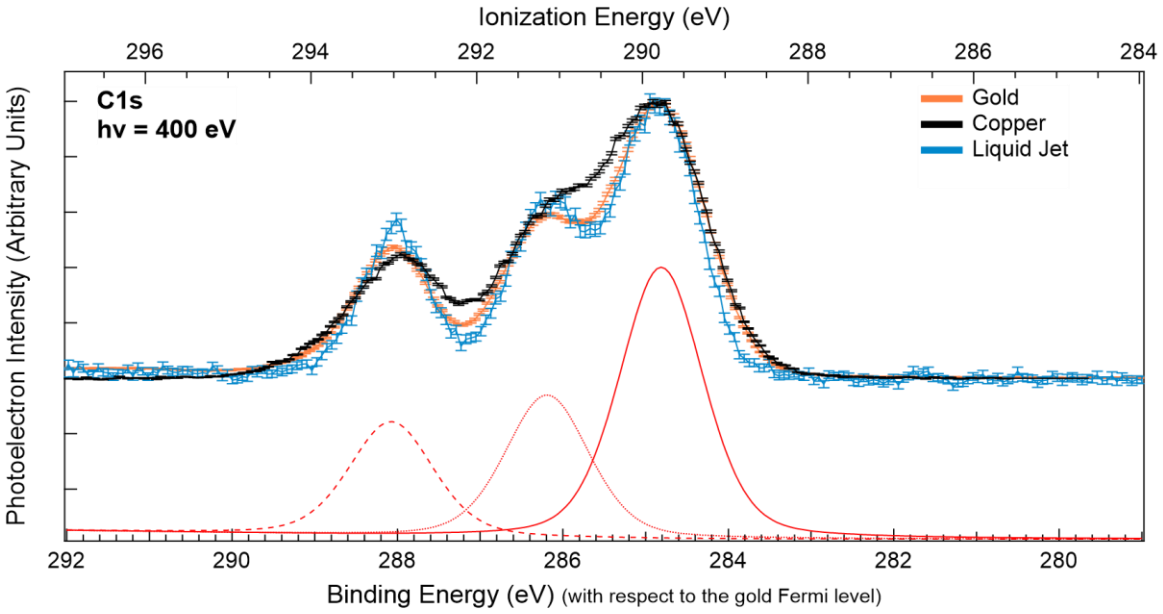

Figure V-20: Comparison of C1s XPS spectra measured on dry samples deposited either on copper scotch (black), a gold plate (orange) or in the liquid phase (blue). Contribution (red). The energy difference between the binding energy and the ionization energy of XPS signal is attributed to the work function of the aqueous solution (Φ_{water}~4.9 ±0.2 eV).

According to these results, three contributions were assigned to the C1s spectra. The peak around 284.9 eV (BE referenced with respect to the gold Fermi level) was attributed to carbon bonded to carbon or hydrogen. The peak for carbon singly bonded to oxygen or nitrogen was found at 286.2 eV. Carbonyl and/or amide carbon and carboxyl carbon are regrouped in the peak centered at288.0 eV.

Table V-6: Comparison of spectral features measured in solid (dry) and liquid state (solvated by water molecules).

Solid State (this study)			**Liquid State (this study)**			**Liquid State (NAP-XPS[10])**		**C1s And%At** [60]	
Position (±0.35 eV)	**%At**	**FWHM**	**Position** (±0.13 eV)	**%At**	**FWHM**	**Position** (±1.7 eV)	**FWHM**		
284.9	**47**	1.18	289.8	**52.5**	0.93	285	1.47	C-C/C-H	**46**
286.2	**29**	1.18	291.1	**26**	0.93	286.2	1.47	C-O/C-N	**28**
288.0	**24**	1.18	293.0	**21.5**	0.93	287.4	1.47	N-C=O	**24**
						288.6	1.47	O-C=O	**2**

Experimental values are in good agreement with the values from the literature (see literature values reported in Appendix VI). In the work of Jain and co-workers, which was also performed in the liquid state, a fourth contribution between the C(C-O/C-N) and the

C(N-C=O) peaks is added. Our high-resolution spectrum rejects the presence of this fourth component, at least with the intensity proposed by Jain and co-workers.

In order to determine the contributions of the different carbon types present in the protein, computational methods were applied to retrieve the theoretical binding energies. These calculations were performed by Jean-Philippe Renault (CEA-Saclay). Considering the most abundant types of carbon in a protein, we expect three major bands: C_{alpha} (583 over 3181 carbon atoms), C_{beta} (567/3181), and $C_{peptidic}$ (583/3181). The $C_{aliphatic}$ (coming from the valine, leucine, and isoleucine side chains) is the fourth most abundant population (302/3181), followed by additional minor bands for $C_{carboxylate}$ (40+59), $C_{alcohol}$ (34+28), for instance.

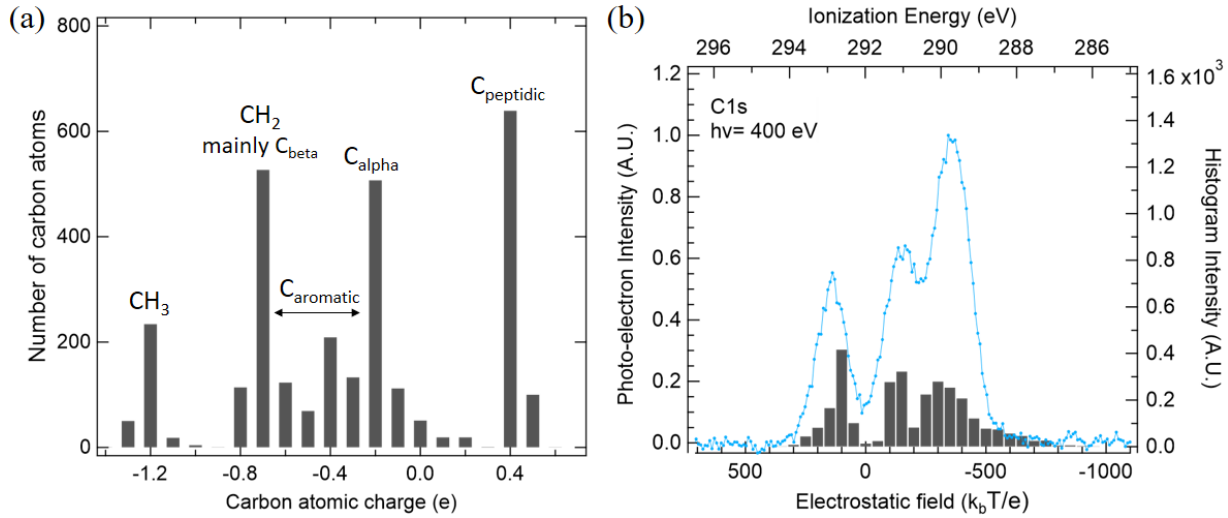

Figure V-21: BSA liquid C1s XPS spectra attribution (a) Distribution of atomic charges calculated in the BSA structure with a 3 Å water layer on its surface. (b) BSA experimental XPS signal (blue) recorded at 400 eV photon energy in the liquid state. Comparison with the distribution of atomic charges calculated in BSA structure with a 3 Å water layer on its surface.

The binding energy, E_{prot}, of the different atom's type, is related to the binding energy E_{vac}^{∞} of an isolated atom of the same electronic state in vacuum by [61]:

$$E_{prot} = E_{vac}^{\infty} + \varepsilon Q + V + E_{pol} \quad \text{(V-1)}$$

Where Q is the charge of the considered atom, ε a core-frontier coupling constant; V is the potential energy of the electron to be photo-ionized in the electrostatic field generated by the distribution of charges in the molecule (sometimes designated as the Madelung constant); and E_{pol} is the polarization energy of the system, when a core hole is formed after photoemission. Therefore, Q and V are initial state effects, whereas E_{pol} is a

final state effect. Q depends on the chemical environment of the atom. It is the main contribution to the chemical shift in organic molecules and can be obtained from *ab initio* calculations on the initial state. V depends on the atom's localization within the protein, as the electrostatic potential is not homogeneous. However, we can assume that within each amino acid, all atom types will feel the same potential, and thus that V will have the same enlargement effect on all types of atoms.

The dependence of E_{pol} on the atom types/atom location has been explored by *ab initio* calculations on the core ionized final state[62]. In our case, relaxation effects cannot be explored systematically by calculation on a macromolecule, as there are as many final states as carbon atoms in the protein. Nevertheless, we must keep in mind that the intramolecular relaxation energy term is nearly constant for most atom types in organic compounds and that initial state effects dominate the C1s binding energy shifts[63], [64]. Therefore, we tried to analyze the shape and position of the XPS signal using only information on the Q and V distributions.

The atomic charges Q of a BSA structure with a 3 Å water layer on its surface (BSA_{wat}) were calculated using Density Functional Theory (DFT). In such a system, the number of atoms coming from the protein and the added layer is equivalent. The Hirschfeld description of charges was used here as it seems more relevant in the XPS context[65], [66]. The distribution of carbon charges can be defined with four major populations: peptidic carbons (0.4±0.1 e), alpha carbons (-0.2±0.4 e), aromatic (-0.4±0.2 e), and aliphatic carbons (CH_2 & CH_3, -1.2±0.5 e) as illustrated in Figure V-21.(a). The atomic percentage (%At.) of each C type can be compared to the experimental one (presented in Table V-6). More precisely, the C-C/C-H contribution can be calculated from CH_3, CH_2, and $C_{aromatic}$ contribution and is 51% theoretically. For C-O and C-N, corresponding to C_{alpha}, we can calculate a percentage of 24%, and finally, the $C_{peptidic}$ corresponds to 25%. These three values are similar to the experimental%At measured by fitting the XPS spectra and to the expected ones[60]. Thus, the hydration leads to minimal changes in the charges. It is also evident that this description level is incomplete and that both the number of bands and their widths are not adequately represented. The sole information we get is that we cannot attribute a significant component solely to carboxylate. Therefore, an additional term from Equation (V-2) was used to consider the effect of V in addition

to Q. To approach it, we used standard electrostatic calculations for proteins in solution[67]. All Q charges were used for this calculation. The electrostatic field (expressed in k_bT/e) was then calculated at the different atomic position, allowing to take into account both local (Q) and global contribution (V). This combination captures the main features of the carbon spectra with only three prominent bands, as presented in Figure V-21.(b). The two first can be attributed respectively to $C_{peptidic}$ and $C_{alpha,}$ but the third one comes from both C_{beta} and $C_{aliphatic}$ carbons. The aromatic amino acids see their carbons distributed underneath these two peaks.

Finally, we also performed XPS analysis at the N and O K-edges. Results obtained on solid and liquid samples are presented in Figure V-22.

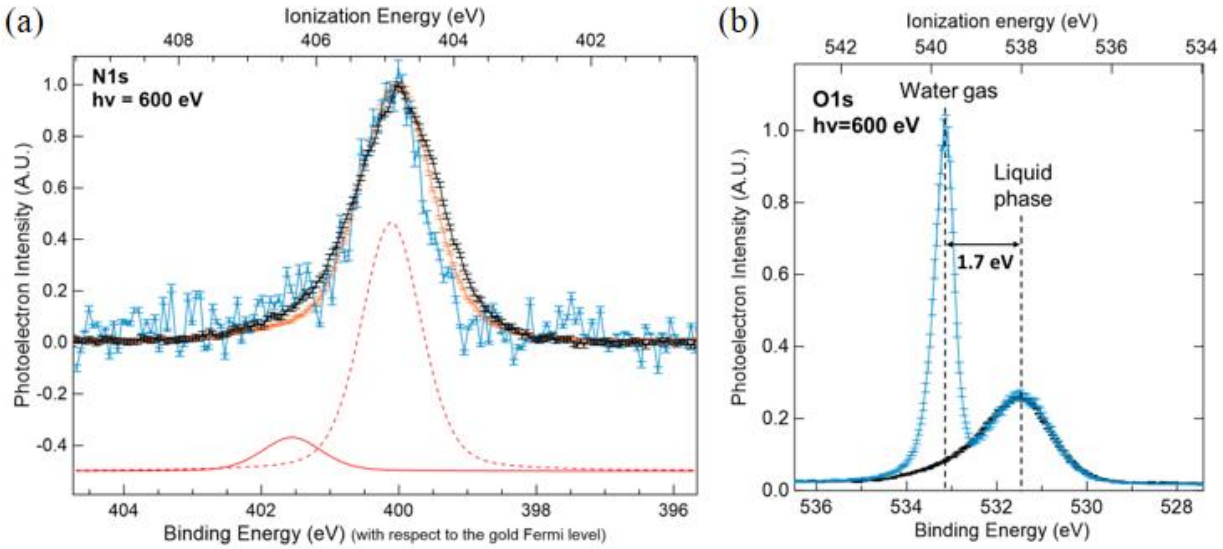

Figure V-22: XPS spectra of BSA (a) N1s and (b) O1s. Comparison of photoelectron data measured on dry samples deposited either on copper scotch (black), a gold plate (orange) or in the liquid phase (blue). Different contributions (red). The energy difference between the binding energy and the ionization energy of XPS signal is attributed to the work function of the aqueous solution (Φwater~4.9 ±0.2 eV)

The N1s signal (Figure V-22.(a)) was fitted with two contributions. The peak at 400 eV BE constitutes the main component (>90%) and is mainly attributed to the amide signal. The second peak at 401 eV BE is usually attributed to the protonated amine[68]. Its absence/presence can vary with respect to the pH (the pH of the solution before the drying in the case of a solid sample)[68]. It can be surprising that, despite the complex structure of the protein, only two contributions are finally observed on the N 1s signal.

For the O1s spectra, the contribution of the solvated protein is entirely masked by the contribution of the liquid water (see Figure V-22.(b)). However, even in the solid-state study, no resolved contribution can be attributed.

As stated earlier, these results highlight that the interpretation of XPS spectra of such macromolecular systems needs theoretical supports to disentangle the different eventual contributions. It also highlights the risk of over-interpretation of XPS spectra in the case of such complex systems. It is also surprising that the solvation does not strongly influence XPS structures, as the solid-state spectra are identical to those obtained with the liquid jet.

V.3.2. Water influence on the electronic structure

V.3.2.i. Characterization of the valence band

Several electron transfer mechanisms (electron hopping, super-exchange) have been proposed since the pioneering studies of Vault & Chance and Gray & Winckler[69], [70]. These models involve an electron tunneling, where the energy barrier will be defined either by the valence (hole transfer) or conduction (electron transfer) bands energy. These barrier values are critical to calculate tunneling efficiencies and, up to now, have been either based on crude assumptions, on gas-phase spectroscopic measurement, or electronic calculations on simple compounds[71]. Among the different experimental techniques, photoemission spectroscopy provides unique information on the band structure. The value of the valence band edge was measured here for the first time for a protein in solution (see Figure V-23). The water component (band III) dominates the valence band signal, corresponding to the $1b_1$ molecular orbital, with a maximum at 11.4±0.1 eV (fitted with a Gaussian function). The photoionization threshold is extrapolated at 10.0±0.1 eV (see linear fit on Figure V-23.(a)). These determined values are almost similar to those of the literature[18], [72]. Therefore, the protein has a minimal effect on water's electronic structure and work function, even at this high concentration. However, additional bands can be attributed to the protein. Indeed, a two steps structure is located below the $1b_1$ band of water (bands I and II, on Figure V-23.(b)-(c)). Two thresholds can be determined by extrapolating the slopes of the steps. The first threshold is located at 5.7±0.3 eV and the second one at 7.4±0.1 eV.

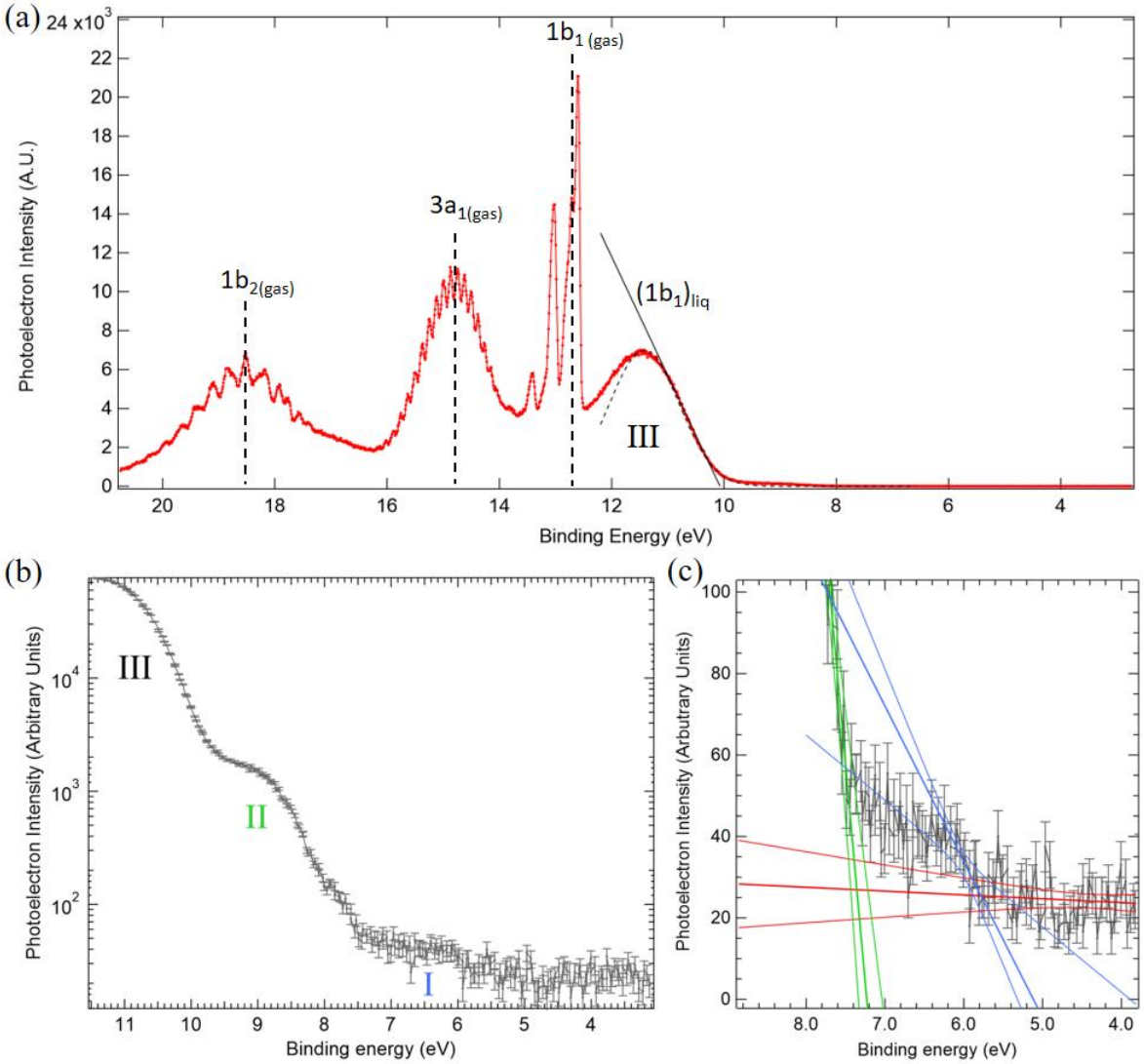

Figure V-23: (a) Valence photoelectron of the BSA aqueous solution (36 g/L) measured at 100 eV photon energy. Emissions due to ionization of three orbitals of water gas phase are labeled. The liquid water contribution of $1b_1$ was fitted by a Gaussian function (black dotted curve), (b) Logarithmic scale graphic of valence band to clearly distinguish the three bands structure (identified with roman numbers), (c) Determination of thresholds by fitting valence signal with linear fit (solid lines) with confidence interval of 99% (dotted line): background (red), band I (blue) and band II (green). Error bars correspond to the statistical error.

In the literature, valence bands of peptides are usually located at 7 eV[73], [74] (considering that the ionization threshold is the opposite of the energy of the Highest Occupied Molecular Orbital (HOMO)). Even the more readily oxidable species (tryptophan or tyrosine) also have HOMO energies in the -8 eV range [71], [75]. Therefore the value of the HOMO measured here (-5.7 eV) is significantly higher. Different origins for this upper part of the BSA valence band can be envisioned. At first, the secondary structure of the protein can influence electron transport. Alpha helixes, for instance, which are the main structural motifs in BSA, can increase the HOMO energy up to 2.5 eV[75].

Secondly, HOMO energies of various types of cysteinates have been measured in the -5.5 eV range[76], [77]. However, we have only one free cysteine in BSA[78], and we do not expect to be so sensitive in our measurements. Finally, electrostatic effects can also be envisioned[79].

In order to decipher the orbital nature of the upper part of the valence band, DFT calculations were performed by Jean-Philippe Renault to calculate the projected density of states (PDOS) for different atoms of the hydrated BSA (using the previous structure with a 3 Å water added layer). In order to compare with the experimental signal, the $1b_1$ signal of liquid water was subtracted[70]. Results are presented in Figure V-24

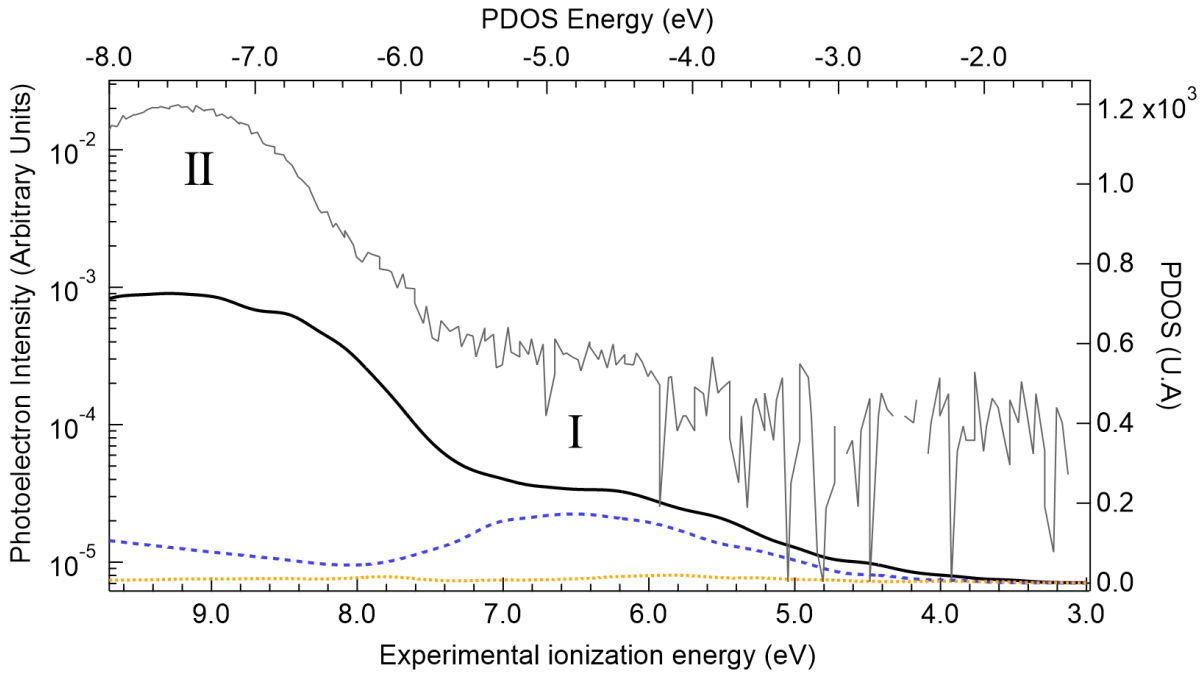

Figure V-24: Projected density of states of carbon (black solid line), nitrogen (blue dotted line), and sulfur (yellow dashed line) atoms calculated from electronic structure of the hydrated BSA structure. Comparison with experimental data from valence spectra of the BSA aqueous with substraction of the Gaussian contribution of the $1b_1$ ionization band of liquid water from NaCl 0.05 M.

We can directly observe that the sulfur PDOS is barely visible, with a small maximum around -4.2 eV. It indicates that the cysteine of the proteins, even if it can be part of, is not the main component of the protein HOMO. The carbon, which is the highest contributor to the density of states, shows two major peaks at -4.7 eV and -7.6 eV. These

[70] *The gaussian contribution of the 1b1(liq) was determined reccording a spectra of liquid neat water (NaCl 0.05 M)*

seem to contribute respectively to the bands I and II. The band I of the valence spectra is also found in the nitrogen PDOS (around -5 eV). It suggests that the orbitals in this energies region significantly contribute from carbon/nitrogen functional groups, either peptide bonds or aromatic amino acids like histidine or tryptophan. Band II would therefore arise mainly from CH_x functions.

In order to confirm the underlying contribution of the carbon PDOS, three additional projections were conducted, one on the C_{beta} of alanine (46 occurrences in BSA distributed all over the protein), one over the $C_{peptidic}$ of alanines, and one on the C_{delta} of aromatic amino acids (see Figure V-25).

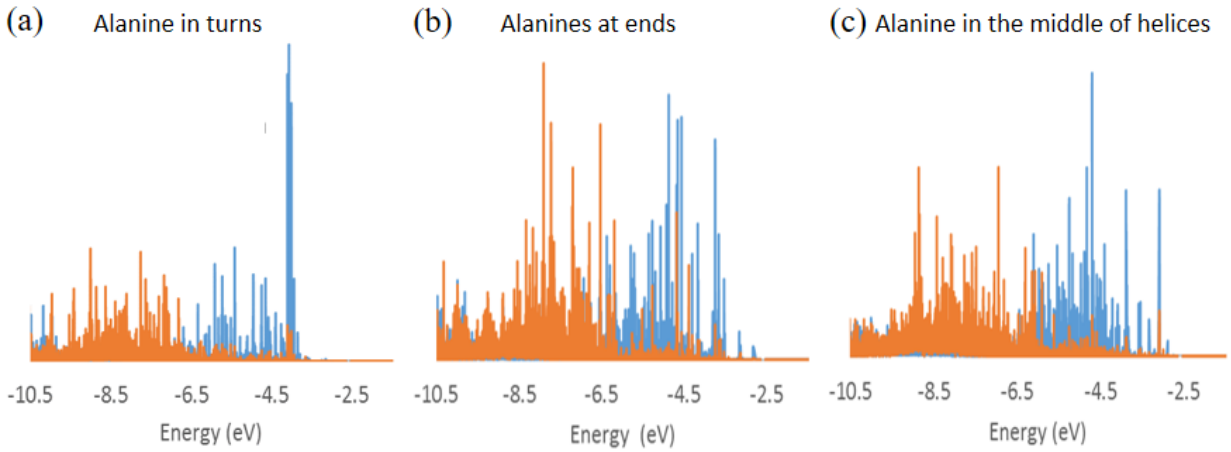

Figure V-25: Local density of states for peptidic (blue) and beta (orange) carbons of alanines, in various secondary structures.

Noticingly, irrespective of the secondary structure they belong to (in turns, at the end of alpha helixes or in the middle of them), $C_{peptidic}$ DOS contributes in the -5 eV range. The alpha helix structure motif does not impose a dramatic shift in the considered DOS but rather a widening that suggests some delocalization of the orbitals. Even though the energy distribution of the PDOS seems to agree with the calculation, it is not the case for the intensity of the respective bands. Considering only the carbon contribution, the ratio between the C_{II} and the C_I bands is around 3. For the experimental valence spectra, the ratio is around ~50. PE data may not correspond to the total density of states for three reasons: (1) signal broadening, (2) difference in ionization cross-section, and (3) PE inelastic scattering.

In the Gelius interpretation[64], [80], [81], a difference of molecular cross-section goes back to the atomic cross-sections. C, O, and N cross-sections are not so different at the considered energy. Furthermore, a difference of cross-section of the atomic subshell (s,p) components cannot either be an explanation, as, in the considered photon energy region (100 eV), the photoionization cross-section of the different types of atomic orbitals are very close[82], [83]. A different PE scattering between saturated and unsaturated bands may at first seem to be a more appropriate explanation. One can imagine that peptide bonds, especially in alpha helixes, may be deeper in the protein than the amino acid side chains surrounding them, and thus that their PE are more scattered. However, the distance from the surface of various types of carbons (Table V-7[84]) was calculated[71], and no significant difference between them was evidenced.

Table V-7: Distance of various carbons with respect to the protein surface. The distances were calculated using Biopython and MSMS*[84]*

Carbon Type	**$C_{peptidic}$**	**C_{beta}**	**C_{gamma}**	**C_{delta}**
Average distance from the surface (Å)	2.58	2.5	2.52	2.51

To go further, and as spectral broadening may be sensitive to solvation (the so-called inhomogeneous broadening), we measured the valence band spectrum of dry BSA in a vacuum. As the contribution of water no more masks the signal, we can distinguish six features/bands that are more salient (see Figure V-26). As previously discussed, the absolute values of the valence band energy between the liquid and solid phase are associated with the solution's work function ($\Phi_{solution}$= 4.9±0.2 eV). Even if it is difficult to evaluate the influence of the substrate on the deposited dried BSA, we can attribute the band at -3 eV to the band I and the one at -7 eV to the band II by comparison with density of state calculations performed on a dry protein. The band I was fitted by a Gaussian function centered at 4.3±0.35 eV and the ionization threshold was extrapolated from the valence spectra giving a value of 2.5±0.35 eV.

[71] *Calculations performed by Jean-Philippe RENAULT*

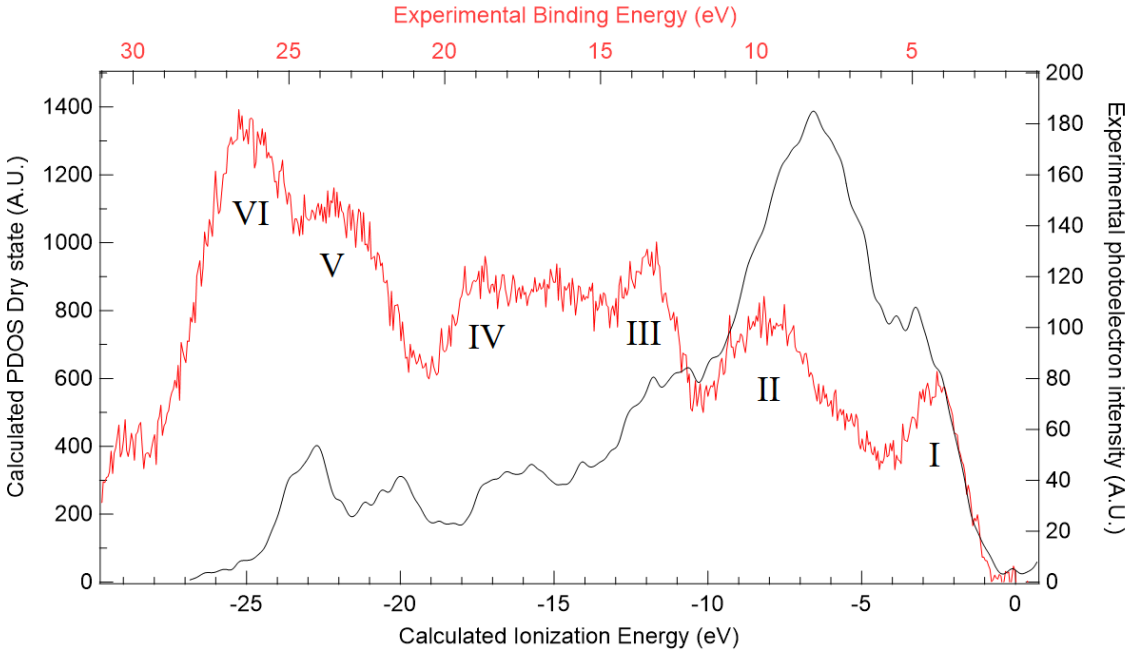

Figure V-26: Total PDOS of the hydrated protein (grey) compared to the experimental valence band recorded on protein crystals (red line).

Dehydration of the protein seems to make only the unsaturated band more apparent. Moreover, the ratio of the two bands from the experimental valence spectra is around 1.4. This value is closer to the one expected from the DOS calculations, of around 1.7. For the moment, we have no explanation for the low intensity of the unsaturated band in the hydrated protein. One hypothesis remains that water influences the spatial extension of valence–electron holes in liquids through its H-bond network[85], [86].

V.3.2.ii. Determination of the bandgap

Now that we have a better understanding of the valence band structure, it is possible to have a complete description of the band diagrams of the protein. According to obtained data from the liquid jet, the ionization energy threshold (IET) of the band I of the BSA with respect to the vacuum level is equal to $IET_{vac,Band\ I(Liquid)}$ =5.7 ±0.3 eV. This value, combined with the evaluated BSA solution work function ($\Phi_{solution}$~4.9 ±0.2 eV), gives an energy difference between the Fermi level and the HOMO of the BSA of 1.0 ±0.36 eV. Thanks to the UV-vis analysis of the BSA[72], it is possible to retrieve the optical band gap value using the Tauc representation[87], as given in Equation (V-3):

$$(F(R)h\nu)^{\frac{1}{\gamma}} = B\left(h\nu - E_g\right) \qquad (V\text{-}3)$$

With h the Planck constant, ν the frequency of the photons, E_g the value of the energy of the bandgap and B a constant. γ is equal to ½ for a direct bandgap transition.

For the liquid protein sample spectrum (Figure V-27, red curve), the linear region extrapolated to the energy axis leads to the optical band gap value of 4.25±0.07 eV. For the solid-state (Figure V-27, green curve), Tauc treatment led to a similar optical band gap value of 4.15±0.08 eV. These values allow a complete description of the band structure of the protein in a dry and hydrated state (see Figure V-28).

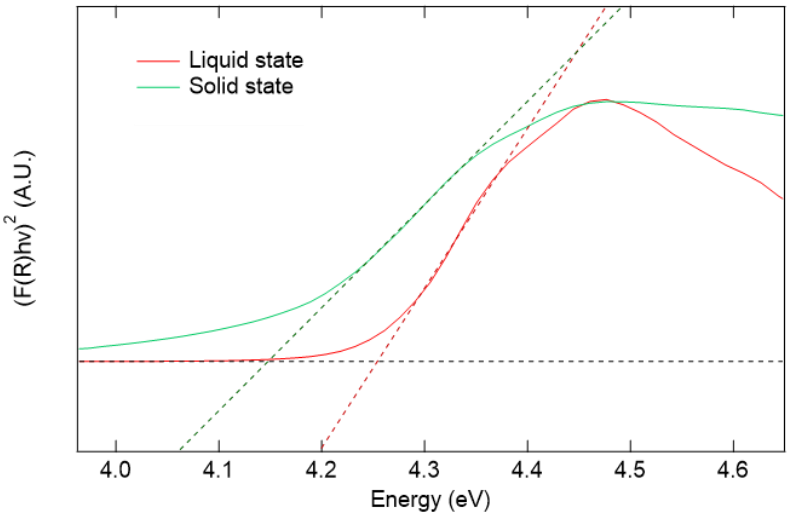

Figure V-27: Band gap energy determination from the Tauc plot with the linear region extrapolated to the energy axis for hydrated (red curve) and dried state (green curve) of the BSA solution (1 g/L)

[72] *To record the band gap in solid states, samples were dried on a quartz plate to measure transmitted light.*

For a bandgap of 4 eV, the HOMO is expected to be 2 eV below the Fermi level. In the solid case, the HOMO, located at -2.5±0.35 eV, is in good agreement with the expected band diagram. However, in the case of the solvated protein, the value of 1 eV seems to indicate an electron depletion.

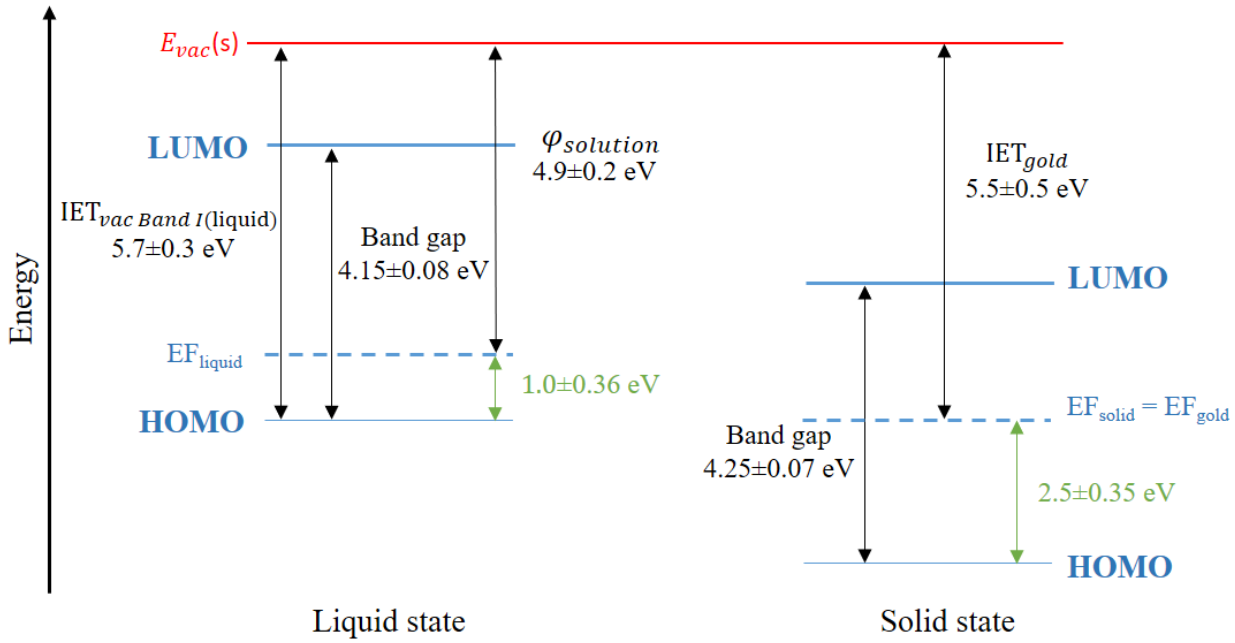

Figure V-28: Description of the BSA band structure in solid and liquid phase.

Our result, therefore, sheds new light on the role of water in protein conduction. It has indeed been known for a long time that water favors protein conductivity[71]. This effect was described as the opening of protonic conduction pathways by the water[72,73]. Even if early articles identified in parallel an electronic pathway activated by water[71], our results suggest that these electronic components of the protein conductivity occur through-hole transport, as previously suggested by pulse radiolysis studies[74]. Along with the change in band shape observed upon hydration on the valence band, our observation points towards a specific role of water in hole delocalization in proteins.

V.4. Conclusions on Chapter V

The XPS measurements performed in this thesis focused at first on studying a small chemical: Sodium benzoate. These experiments allowed us to characterize the under-vacuum liquid jet environment and oversee this technique's potential for describing the electronic structure of solvated molecules. Measurements performed in both liquid and solid states evidenced that core levels can be affected by the solvation shell. However, in light of our study on a large system, such as the BSA protein, it was shown that, taking into account the system's complexity, it became too challenging to make such observation on the core levels. More precisely, no significant differences were observed between the results in both states.

Nevertheless, the UPS study on the valence band highlighted changes in the band structure. Such results can be of great importance in understanding more complex experiments on the protein electronic structure, such as resonant Auger and core hole clock spectroscopies[88] and, more specifically, how water modulates this structure.

In the context of the ANR project, I got the opportunity to participate in experiments coupling the liquid micro-jet and a magnetic bottle. This setup is of primary interest as it allows to characterize all the emitted electrons following core-ionization. Such experiments, however, require close collaboration with theoreticians to fully understand the results. In the future, XPS measurement coupling the HDA and the magnetic bottle could bring further the understanding of photoionization processes in liquids as it would allow the complete detection of the events (MB-TOF) with a good resolution (HDA).

Bibliography Chapter V

[1] E. F. Aziz, "The solvation of ions and molecules probed via soft X-ray spectroscopies," *J. Electron Spectros. Relat. Phenomena*, vol. 177, no. 2–3, pp. 168–180, 2010.

[2] R. Dupuy, C. Richter, B. Winter, G. Meijer, R. Schlögl, and H. Bluhm, "Core level photoelectron spectroscopy of heterogeneous reactions at liquid–vapor interfaces: Current status, challenges, and prospects," *J. Chem. Phys.*, vol. 154, no. 6, p. 060901, 2021.

[3] Y. S. Blanco, Ö. Topel, É. G. Bajnóczi, J. Werner, O. Björneholm, and I. Persson, "Chemical equilibria of aqueous ammonium-carboxylate systems in aqueous bulk, close to and at the water-air interface," *Phys. Chem. Chem. Phys.*, vol. 21, no. 23, pp. 12434–12445, 2019.

[4] M. Hopkins Hatzopoulos, J. Eastoe, P. J. Dowding, S. E. Rogers, R. Heenan, and R. Dyer, "Are Hydrotropes Distinct from Surfactants?," *Langmuir*, vol. 27, no. 20, pp. 12346–12353, Oct. 2011.

[5] B. Minofar, P. Jungwirth, M. R. Das, W. Kunz, and S. Mahiuddin, "Propensity of formate, acetate, benzoate, and phenolate for the aqueous solution/vapor interface: Surface tension measurements and molecular dynamics simulations," *J. Phys. Chem. C*, vol. 111, no. 23, pp. 8242–8247, 2007.

[6] D. Emfietzoglou, I. Kyriakou, R. Garcia-Molina, and I. Abril, "Inelastic mean free path of low-energy electrons in condensed media: beyond the standard models," *Surf. Interface Anal.*, vol. 49, no. 1, pp. 4–10, Jan. 2015.

[7] N. L. Prisle, N. Ottosson, G. Öhrwall, J. Söderström, M. Dal Maso, and O. Björneholm, "Surface/bulk partitioning and acid/base speciation of aqueous decanoate: Direct observations and atmospheric implications," *Atmos. Chem. Phys.*, vol. 12, no. 24, pp. 12227–12242, 2012.

[8] N. Ottosson, A. O. Romanova, J. Söderström, O. Björneholm, G. Öhrwall, and M. V. Fedorov, "Molecular sinkers: X-ray photoemission and atomistic simulations of benzoic acid and benzoate at the aqueous solution/vapor interface," *J. Phys. Chem. B*, vol. 116, no. 43, pp. 13017–13023, 2012.

[9] B. Winter, E. F. Aziz, U. Hergenhahn, M. Faubel, and I. V. Hertel, "Hydrogen bonds in liquid water studied by photoelectron spectroscopy," *J. Chem. Phys.*, vol. 126, no. 12, pp. 0–6, 2007.

[10] V. Jain, M. C. Biesinger, and M. R. Linford, "The Gaussian-Lorentzian Sum, Product, and Convolution (Voigt) functions in the context of peak fitting X-ray photoelectron spectroscopy (XPS) narrow scans," *Appl. Surf. Sci.*, vol. 447, pp. 548–553, 2018.

[11] M. P. Seah, "Background subtraction," *Surf. Sci.*, vol. 420, no. 2–3, pp. 285–294, Jan. 1999.

[12] J. Söderström *et al.*, "Nonstoichiometric Intensities in Core Photoelectron Spectroscopy," *Phys. Rev. Lett.*, vol. 108, no. 19, p. 193005, May 2012.

[13] N. Kosugi and H. Kuroda, "Efficient methods for solving the open-shell scf problem and for obtaining an initial guess. The 'one-hamiltonian' and the 'partial scf' methods," *Chem. Phys. Lett.*, vol. 74, no. 3, pp. 490–493, Sep. 1980.

[14] D. Céolin, H. Yuzawa, and T. Saisopa, "Substituent effects in aqueous solutions of carboxylate salts studied by x-ray absorption spectroscopy at the oxygen K- edge Substituent effects in aqueous solutions of carboxylate salts studied by x-ray absorption spectroscopy at the oxygen K-edge," *J. Chem. Phys*, vol. 155, p. 014306-1, 2021.

[15] N. Kosugi, E. Shigemasa, and A. Yagishita, "High-resolution and symmetry-resolved oxygen

K-edge spectra of O2," *Chem. Phys. Lett.*, vol. 190, no. 5, pp. 481–488, 1992.

[16] R. Seidel, B. Winter, and S. E. Bradforth, "Valence Electronic Structure of Aqueous Solutions: Insights from Photoelectron Spectroscopy," *Annu. Rev. Phys. Chem.*, vol. 67, no. 1, pp. 283–305, 2016.

[17] M. S. Banna, B. H. McQuaide, R. Malutzki, and V. Schmidt, "The photoelectron spectrum of water in the 30-140 eV photon energy range," *J. Chem. Phys.*, vol. 84, no. 9, pp. 4739–4744, 1986.

[18] B. Winter, R. Weber, W. Widdra, M. Dittmar, M. Faubel, and I. V. Hertel, "Full Valence Band Photoemission from Liquid Water Using EUV Synchrotron Radiation," *J. Phys. Chem. A*, vol. 108, no. 14, pp. 2625–2632, 2004.

[19] P. Delahay and K. Von Burg, "Photoelectron emission spectroscopy of liquid water," *Chem. Phys. Lett.*, vol. 83, no. 2, pp. 250–254, Oct. 1981.

[20] G. Bieri, F. Burger, E. Heilbronner, and J. P. Maier, "Valence Ionization Energies of Hydrocarbons," *Helv. Chim. Acta*, vol. 60, no. 7, pp. 2213–2233, Nov. 1977.

[21] D. Menzel *et al.*, "Core excitation, decay, and fragmentation in solid benzene as studied by x-ray absorption, resonant Auger, and photon stimulated desorption," *J. Chem. Phys.*, vol. 96, no. 3, pp. 1724–1734, Feb. 1992.

[22] Y. Ishiguro, Y. Yamakita, and N. Hayashi, "Penning ionization electron spectroscopy of anisole, thioanisole, and selenoanisole by collision with He*(23S): Conjugation effects and conformational stability," *Chem. Phys. Lett.*, vol. 754, no. June, p. 137653, Sep. 2020.

[23] J. Riga, J.-J. Pireaux, and J. J. Verbist, "An ESCA study of the electronic structure of solid benzene.," *Mol. Phys.*, vol. 34, no. 1, pp. 131–143, Jul. 1977.

[24] F. O. L. Johansson *et al.*, "Femtosecond and Attosecond Electron-Transfer Dynamics in PCPDTBT:PCBM Bulk Heterojunctions," *J. Phys. Chem. C*, vol. 122, no. 24, pp. 12605–12614, 2018.

[25] D. Céolin *et al.*, "Ultrafast Charge Transfer Processes Accompanying KLL Auger Decay in Aqueous KCl Solution," *Phys. Rev. Lett.*, vol. 119, no. 26, p. 263003, Dec. 2017.

[26] F. Gel'mukhanov and H. Ågren, "Resonant X-ray Raman scattering," *Phys. Rep.*, vol. 312, no. 3–6, pp. 87–330, May 1999.

[27] J. C. Fuggle and N. Mårtensson, "Core-level binding energies in metals," *J. Electron Spectros. Relat. Phenomena*, vol. 21, no. 3, pp. 275–281, 1980.

[28] G. Indlekofer and P. Oelhafen, "Electronic structure of liquid lithium and sodium from electron spectroscopy," *J. Non. Cryst. Solids*, vol. 117–118, pp. 340–343, Feb. 1990.

[29] H. Tissot *et al.*, "Cation Depth-Distribution at Alkali Halide Aqueous Solution Surfaces," *J. Phys. Chem. C*, vol. 119, no. 17, pp. 9253–9259, 2015.

[30] H. W. Haak, G. A. Sawatzky, and T. D. Thomas, "Auger-Photoelectron Coincidence Measurements in Copper," *Phys. Rev. Lett.*, vol. 41, no. 26, pp. 1825–1827, Dec. 1978.

[31] T. Arion and U. Hergenhahn, "Coincidence spectroscopy: Past, present and perspectives," *J. Electron Spectros. Relat. Phenomena*, vol. 200, pp. 222–231, Apr. 2015.

[32] M. N. Pohl *et al.*, "Sensitivity of Electron Transfer Mediated Decay to Ion Pairing," *J. Phys. Chem. B*, vol. 121, no. 32, pp. 7709–7714, Aug. 2017.

[33] H. Fellner-Feldegg, H. Siegbahn, L. Asplund, P. Kelfve, and K. Siegbahn, "ESCA applied to liquids IV. A wire system for ESCA measurements on liquids," *J. Electron Spectros. Relat. Phenomena*, vol. 7, no. 5, pp. 421–428, 1975.

[34] L. Inhester, C. F. Burmeister, G. Groenhof, and H. Grubmüller, "Auger spectrum of a water molecule after single and double core ionization," *J. Chem. Phys.*, vol. 136, no. 14, p. 144304, Apr. 2012.

[35] W. E. Moddeman, T. A. Carlson, M. O. Krause, B. P. Pullen, W. E. Bull, and G. K. Schweitzer, "Determination of the K—LL Auger Spectra of N 2 , O 2 , CO, NO, H 2 O, and CO 2," *J. Chem. Phys.*, vol. 55, no. 5, pp. 2317–2336, Sep. 1971.

[36] H. Shinotsuka, B. Da, S. Tanuma, H. Yoshikawa, C. J. Powell, and D. R. Penn, "Calculations of electron inelastic mean free paths . XI . Data for liquid water for energies from 50eV to 30keV," no. July 2016, pp. 238–252, 2017.

[37] B. Winter, U. Hergenhahn, M. Faubel, O. Björneholm, and I. V. Hertel, "Hydrogen bonding in liquid water probed by resonant Auger-electron spectroscopy," *J. Chem. Phys.*, vol. 127, no. 9, p. 094501, Sep. 2007.

[38] M. A. Brown, M. Faubel, and B. Winter, "X-Ray photo- and resonant Auger-electron spectroscopy studies of liquid water and aqueous solutions," *Annu. Reports Sect. "C" (Physical Chem.*, vol. 105, p. 174, 2009.

[39] G. Öhrwall *et al.*, "The electronic structure of free water clusters probed by Auger electron spectroscopy," *J. Chem. Phys.*, vol. 123, no. 5, p. 054310, Aug. 2005.

[40] P. G. Rouxhet, N. Mozes, P. B. Dengis, Y. F. Dufrêne, P. A. Gerin, and M. J. Genet, "Application of X-ray photoelectron spectroscopy to microorganisms," *Colloids Surfaces B Biointerfaces*, vol. 2, no. 1–3, pp. 347–369, 1994.

[41] Y. F. Dufrêne, T. G. Marchal, and P. G. Rouxhet, "Probing the organization of adsorbed protein layers: Complementarity of atomic force microscopy, X-ray photoelectron spectroscopy and radiolabeling," *Appl. Surf. Sci.*, vol. 144–145, pp. 638–643, 1999.

[42] N. Sylvetsky, "Toward Simple, Predictive Understanding of Protein-Ligand Interactions: Electronic Structure Calculations on Torpedo Californica Acetylcholinesterase Join Forces with the Chemist's Intuition," *Sci. Rep.*, vol. 10, no. 1, pp. 1–12, 2020.

[43] V. Gogonea, J. M. Shy, and P. K. Biswas, "Electronic structure, ionization potential, and electron affinity of the enzyme cofactor (6R)-5,6,7,8-Tetrahydrobiopterin in the gas phase, solution, and protein environments," *J. Phys. Chem. B*, vol. 110, no. 45, pp. 22861–22871, 2006.

[44] D. Nolting, E. F. Aziz, N. Ottosson, M. Faubel, I. V. Hertel, and B. Winter, "pH-induced protonation of lysine in aqueous solution causes chemical shifts in X-ray photoelectron spectroscopy," *J. Am. Chem. Soc.*, vol. 129, no. 45, pp. 14068–14073, 2007.

[45] N. Ottosson *et al.*, "On the Origins of Core−Electron Chemical Shifts of Small Biomolecules in Aqueous Solution: Insights from Photoemission and *ab Initio* Calculations of Glycine $_{aq}$," *J. Am. Chem. Soc.*, vol. 133, no. 9, pp. 3120–3130, Mar. 2011.

[46] T. Peters, *All About Albumin*. Elsevier, 1995.

[47] V. Jain *et al.*, "Bovine serum albumin, aqueous solution, by near-ambient pressure XPS," *Surf. Sci. Spectra*, vol. 26, no. 1, p. 014027, 2019.

[48] J. Luo, C. Wu, T. Xu, and Y. Wu, "Diffusion dialysis-concept, principle and applications," *J. Memb. Sci.*, vol. 366, no. 1–2, pp. 1–16, Jan. 2011.

[49] J. M. Antosiewicz and D. Shugar, "UV–Vis spectroscopy of tyrosine side-groups in studies of protein structure. Part 1: basic principles and properties of tyrosine chromophore," *Biophys. Rev.*, vol. 8, no. 2, pp. 151–161, Jun. 2016.

[50] A. R. Goldfarb, L. Saidel, and E. Mosovich, "The ultraviolet absorption spectra of proteins," *J. Biol. Chem.*, vol. 193, no. 1, pp. 397–404, Nov. 1951.

[51] M. Réfrégiers *et al.*, "DISCO synchrotron-radiation circular-dichroism endstation at SOLEIL," *J. Synchrotron Radiat.*, vol. 19, no. 5, pp. 831–835, 2012.

[52] A. J. Miles and B. A. Wallace, "CDtoolX, a downloadable software package for processing and analyses of circular dichroism spectroscopic data," *Protein Sci.*, vol. 27, no. 9, pp. 1717–

1722, 2018.

[53] A. Micsonai *et al.*, "Accurate secondary structure prediction and fold recognition for circular dichroism spectroscopy," *Proc. Natl. Acad. Sci. U. S. A.*, vol. 112, no. 24, pp. E3095–E3103, 2015.

[54] A. Micsonai *et al.*, "BeStSel: A web server for accurate protein secondary structure prediction and fold recognition from the circular dichroism spectra," *Nucleic Acids Res.*, vol. 46, no. W1, pp. W315–W322, 2018.

[55] Y. Li *et al.*, "Salting up of Proteins at the Air/Water Interface," *Langmuir*, vol. 35, no. 43, pp. 13815–13820, 2019.

[56] R. C. Feldhoff and T. Peters, "Fragments of Bovine Serum Albumin Produced by Limited Proteolysis. Isolation and Characterization of Peptic Fragments," *Biochemistry*, vol. 14, no. 20, pp. 4508–4514, 1975.

[57] I. Gülseren, D. Güzey, B. D. Bruce, and J. Weiss, "Structural and functional changes in ultrasonicated bovine serum albumin solutions," *Ultrason. Sonochem.*, vol. 14, no. 2, pp. 173–183, 2007.

[58] C. Leggio, L. Galantini, and N. V. Pavel, "About the albumin structure in solution: Cigar expanded form versus heart normal shape," *Phys. Chem. Chem. Phys.*, vol. 10, no. 45, pp. 6741–6750, 2008.

[59] G. Olivieri, A. Goel, and A. Kleibert, "Quantitative ionization energies and work," *Phys. Chem. Chem. Phys.*, no. 42, vol. 18, pp. 29506-29515, 2016.

[60] C. M. Pradier and F. Ka, "Adsorption of Bovine Serum Albumin on Chromium and Molybdenum Surfaces Investigated by Fourier-Transform Infrared Reflection - Absorption Spectroscopy (FT-IRRAS) and X-ray Photoelectron Spectroscopy," pp. 6766–6773, 2003.

[61] I. Lindgren, "Chemical shifts in X-ray and photo-electron spectroscopy: a historical review," *J. Electron Spectros. Relat. Phenomena*, vol. 137–140, no. SPEC. ISS., pp. 59–71, Jul. 2004.

[62] W. Müller, J. Flesch, and W. Meyer, "Treatment of intershell correlation effects in ab initio calculations by use of core polarization potentials. Method and application to alkali and alkaline earth atoms," *J. Chem. Phys.*, vol. 80, no. 7, pp. 3297–3310, Apr. 1984.

[63] R. W. Paynter and H. Benalia, "A time- and angle-resolved X-ray photoelectron spectroscopy study of polystyrene exposed to a nitrogen plasma," *J. Electron Spectros. Relat. Phenomena*, vol. 136, no. 3, pp. 209–220, 2004.

[64] U. Gelius and K. Siegbahn, "ESCA studies of molecular core and valence levels in the gas phase," *Gen. Discuss. Faraday Soc.*, vol. 54, pp. 257–268, 1972.

[65] A. Hernandez-Laguna, J. Maruani, R. McWeeny, and S. Wilson, *Quantum Systems in Chemistry and Physics*, vol. 2, Kluwer Academic Publishers, Dordrecht, 2002.

[66] A. J. Stasyuk, M. Solà, and A. A. Voityuk, "Reliable charge assessment on encapsulated fragment for endohedral systems," *Sci. Rep.*, vol. 8, no. 1, pp. 1–8, 2018.

[67] E. Jurrus *et al.*, "Improvements to the APBS biomolecular solvation software suite," *arXiv*, 2017.

[68] K. P. Fears, "Measuring the pK/pI of biomolecules using X-ray photoelectron spectroscopy," *Anal. Chem.*, vol. 86, no. 17, pp. 8526–8529, 2014.

[69] H. B. Gray and J. R. Winkler, "Electron tunneling through proteins," *Q. Rev. Biophys.*, vol. 36, no. 3, pp. 341–372, 2003.

[70] D. De Vault and B. Chance, "Studies of Photosynthesis Using a Pulsed Laser: I. Temperature Dependence of Cytochrome Oxidation Rate in Chromatium. Evidence for Tunneling," *Biophys. J.*, vol. 6, no. 6, pp. 825–847, 1966.

[71] J. R. Winkler and H. B. Gray, "Long-range electron tunneling," *J. Am. Chem. Soc.*, vol.

136, no. 8, pp. 2930–2939, 2014.

[72] S. Thürmer *et al.*, "Accurate Vertical Ionization Energy and Work Function Determinations of Liquid Water and Aqueous Solutions," no. 31, vol. 12., pp. 10558-10582, 2021.

[73] M. A. Wolak *et al.*, "Electronic structure of self-assembled peptide nucleic acid thin films," *J. Phys. Chem. C*, vol. 115, no. 34, pp. 17123–17135, 2011.

[74] L. Sepunaru *et al.*, "Electronic transport via homopeptides: The role of side chains and secondary structure," *J. Am. Chem. Soc.*, vol. 137, no. 30, pp. 9617-9626, 2015.

[75] L. Sepunaru *et al.*, "Electronic transport via homopeptides: The role of side chains and secondary structure," *J. Am. Chem. Soc.*, vol. 137, no. 30, pp. 9617-9626, 2015.

[76] P. C. Chang *et al.*, "Molecular Basis of the Antioxidant Capability of Glutathione Unraveled via Aerosol VUV Photoelectron Spectroscopy," *J. Phys. Chem. B*, vol. 120, no. 39, pp. 10181–10191, 2016.

[77] M. Baghbanzadeh *et al.*, "Charge Tunneling along Short Oligoglycine Chains," *Angew. Chemie*, vol. 127, no. 49, pp. 14956–14960, 2015.

[78] S. Ariyasu, H. Hayashi, B. Xing, and S. Chiba, "Site-Specific Dual Functionalization of Cysteine Residue in Peptides and Proteins with 2-Azidoacrylates," *Bioconjug. Chem.*, vol. 28, no. 4, pp. 897–902, 2017.

[79] E. A. Kraut, R. W. Grant, J. R. Waldrop, and S. P. Kowalczyk, "Precise Determination of the Valence-Band Edge in X Ray Photoemission Spectra," *Phys. Rev. Lett.*, vol. 44, no. 24, p. 1620, 1980.

[80] C. J. Allan, U. Gelius, D. A. Allison, G. Johansson, H. Siegbahn, and K. Siegbahn, "ESCA studies of CO2, CS2 and COS," *J. Electron Spectros. Relat. Phenomena*, vol. 1, no. 2, pp. 131–151, 1972.

[81] J. C. Green and P. Decleva, "Photoionization cross-sections: A guide to electronic structure," *Coord. Chem. Rev.*, vol. 249, no. 1–2, pp. 209–228, 2005.

[82] J.-J. Yeh, *Atomic calculation of photoionization cross-sections and asymmetry parameters*. Gordon and Breach, Langhorne PA, ISBN 2-88124-585-4, 1993.

[83] J. J. Yeh and I. Lindau, "Atomic calculation of photoionization cross-sections and asymmetry parameters," *Atomic Data Nuclear Data Tables*, vol. 32, no. l, pp. 1–155, 1985.

[84] M. F. Sanner, A. J. Olson, and J. C. Spehner, "Reduced surface: An efficient way to compute molecular surfaces," *Biopolymers*, vol. 38, no. 3, pp. 305–320, 1996.

[85] C. D. Wanger, W. M. Riggs, L. E. Davis, J. F. Moulder, and G. E.Muilenberg, "Handbook of X-ray Photoelectron Spectroscopy," in *Surface and Interface Analysis*, U. Eden Prairie, Minnesota, Ed. 1981.

[86] S. Chandra, I. N. Ansari, G. Dixit, F. Lepine, and A. Bhattacharya, "Experimental Evidence of Sensitivity of the High Harmonic Generation to Hydrogen Bonding," *J. Phys. Chem. A*, vol. 123, no. 24, pp. 5144–5149, 2019.

[87] J. Tauc, R. Grigorovici, and A. Vancu, "Optical Properties and Electronic Structure of Amorphous Germanium," *Phys. status solidi*, vol. 15, no. 2, pp. 627–637, Sep. 1966.

Conclusion & Perspectives

Conclusion & Perspectives

The understanding of biological damage induced by ionizing radiation is an all-time story. Following the evolution of synchrotron experiments to characterize biological systems, such as microscopy or crystallography, more and more powerful light sources were developed. More specifically, there is an obvious interest in developing techniques on liquid for the analysis of biological systems. Unfortunately, the advantages offered by synchrotron radiation may become limited in terms of efficiency if the biological target suffers radiation damage, especially in the presence of water with the ROS produced during radiolysis. For instance, several studies highlighted sample degradation during protein solutions analysis (aggregation, fragmentation)[1], [2]. In this context, this PhD tried to bring more information on the damage mechanisms induced by core-ionization on biomolecules in liquid samples. Experiments conducted with SXs aimed at deciphering the roles of PE and AE, picturing the fate of multi-ionized molecules, and investigating energy and electron transfer (ICD, ETMD) in the case of solvated molecules.

The first challenge of this thesis was to develop technical setups to overcome the high attenuation of SXs in the condensed phase, especially for low photon energy (C, O, and N K-edges).

It all began with the IRAD setup, which was coupled to the METROLOGIE beamline at the SOLEIL synchrotron facility. The IRAD setup offers significant advantages in terms of experimental settings since it leaves the sample at atmospheric pressure. It is thus ideally suited for cells irradiation, for instance[3]. Thanks to the computer-controlled translation tables and new holders installation, it became possible to automate the irradiations. The implementation of the microfluidic cell led us to improve alignment processes (photodiode, scintillator), resulting in a better characterization of the beam and improving the reproducibility of the irradiations. In parallel, a vacuum chamber has been built to facilitate access to lower photon energies. The development of this experimental endstation drastically improved liquid samples irradiations at the C K-edge. Nevertheless, this vacuum setup is still under development with two main points still to improve. The first one is to access ultra-high vacuum (around 10^{-10} mbar) to avoid carbon deposits. The

second one is to integrate filters and attenuator assemblies to control the synchrotron beam intensity and monochromaticity (higher orders suppression). Given the current developments, we can only envisage new experiments on more extensive energy ranges to probe further the K-shell ionization effects or even probe the L-shell of heavier atoms (Mg, P, and Br). Finally, these setups are now perfectly suitable for being installed on other synchrotron facilities or low-energy particle sources, known to be challenging due to their low penetration.

Working with liquid samples and low penetration beams led us to adapt a microfluidic cell[73] to optimize the irradiation process. Actually, the microfluidic cell implementation offers several advantages in terms of automatization (time and sample saving, accuracy), alignment reliability (in ambient or under-vacuum conditions), dose deposition homogeneity, and chemical environment (control of dissolved gases). On top of that, many online detection couplings can be considered to optimize the physicochemical characterization of the irradiated samples. In addition to the UV-vis absorption method presented in chapter III, online mass spectrometry detection is currently under development for near-future experiments. As a perspective, new *in-situ* techniques can be explored, such as X-ray light detection (absorption or emission), by optimizing the use of the SiPM.

A promising future is also to be expected for the vacuum liquid micro-jet device developed for XPS measurements. Indeed, the recovery of the sample remains a great advantage since it also allows us to study the radiation-induced damage. Our experiments on more and more challenging solutions (from small molecules to complex biological systems) allowed us to understand and optimize the stability of the jet (catcher position and temperature). If, for the moment, no irradiation effect was evidenced, from an XPS point of view, it offers a great interest for the study of biomolecules in an aqueous medium. As for the microfluidic cell, it can be envisaged to couple the micro-jet with *in situ* detection techniques. In particular, detecting photon emission through the fluorescence of generated excited states could allow probing more deeply the liquid jet (compared to the previous XPS experiments focusing on emitted electrons with low IMFP)[5]. Finally, the

[73] *The microfluidic device was first developed for STXM experiments by Gosse et al. (see [4]).*

main limitation for biomolecules study using the micro-jet is the amount of solution needed for experiments. Therefore, it might be a good idea to consider the implementation of a closed-loop for sample recycling; while keeping in mind the problem of volatile samples evaporation under vacuum leading to concentration increases.

Finally, we are extremely proud of the MB-TOF and liquid micro-jet favorable outcome. Although data analysis is still a crucial point to be improved, the success of the challenging technical development needs to be underlined. One must keep in mind the long acquisition times needed for these experiments. However, the contribution of retrieved data seems very promising for understanding the multi-ionization processes in the liquid state and highlighted the essential role of the theoretical support.

The second aim of this thesis was to bring a better description of the radiochemical processes occurring in liquid samples under SXs exposure.

Firstly, it has been shown that the $HO^{\cdot}$ production yields quantification well describes sub keV electrons tracks. Results exhibited a minimum production yield at around 1 keV photon energy, which was independent of the scavenging time (beyond 200 ps). These experimental results highlighted that sub keV electrons behave as high LET particles (LET of ~100 keV/µm), with a more pronounced tendency than those depicted by Monte Carlo simulation predictions. This difference could originate from the simultaneous emission of electrons (PE and AE) or the accuracy of MC calculations (low energy electrons cross-section values scarcity for liquid-state). The microfluidic cell allowed us to validate these results and rule out the hypothesis of a probe or oxygen overconsumption, which could have distorted the results. A remaining question is the fate of the ionization products from $HO^{\cdot}$ recombination reactions. For this, it would be necessary to probe faster dynamics (<100 ps) by doing experiments on pulsed X-ray sources, or to probe a possible overproduction of H_2O_2 or the $HO^{\cdot}/e^{-}$ recombination (*via* fluorescence emission due to the creation of excited states).

Secondly, $HO^{\cdot}$ quantification experiments were conducted on highly concentrated metallic salts solutions to probe the effect of ICD and ETMD processes following a core-ionization. No K-edge threshold effect was evidenced from the $HO^{\cdot}$ quantification results. However, the probe was maybe not ideally suited for this experiment as the high density

of $HO^{\cdot}$ produced through ICD and ETMD may be hidden in the track of secondary electrons emitted. In addition, there may be some viscosity and ionic strength effects that need to be further investigated. In fact, such experiments would need to find a probe that reacts differently to $HO^{\cdot}$ and stripping electrons. It could also be interesting to probe another ionization threshold, where the ETMD precesses are more probable[6].

Lastly, undergoing experiments try to investigate the fate of multi-ionized species, mainly through the development of superoxide radical quantification methods. In light of the Cytc irradiation studies, it can appear surprising that no protein fragmentation was evidenced on the collected samples, considering the high dose deposited. However, these results should be considered cautiously as solid pieces of evidence (SEM analysis and flow rate decrease) suggest that an aggregation of the protein solution occurred in the microfluidic cell. In conclusion, it must be admitted that the Cytc system was too complicated given the novelty of the experimental setup coupling the microfluidic cell and the vacuum chamber. For the future, it seems more reasonable to work on smaller biomolecules (amino acids, nucleotides).

Finally, a strategy was to use spectroscopic techniques to investigate the production of PE and AE electron emission, emphasizing their role in the core-ionization processes of solvated molecules.

The high-resolution spectroscopic studies on organic molecules allowed us to extract information on the solvation effect at the C K-edge. In the context of the NaBz molecule, experimental analyses, supported by theoretical calculations, indeed suggested that the distance between the sodium and the benzoate ions can impact the XPS signal. Furthermore, it was also shown that XPS is an excellent tool to probe the specific orientation of the molecules at the surface, which is of great interest for studying the behavior of vacuum/water interfaces[7]. It would be interesting to complete these data by investigating results at more photon energies to probe a possible elastic/inelastic scattering of the PE[8].

In light of the BSA protein study, it is interesting to note that XPS measurements of solvated or solid samples give almost identical spectra.

More generally, it seems that the spectroscopy of the valence bands of a solute (if not masked by the ones of water) allows determining its electronic structure. Moreover, the comparison with similar measurements in the solid phase allows us to suggest significant solvation effects.

At the end of this thesis, I set up all the tools which can allow an exhaustive study of the main target of irradiation experiments: the DNA molecule. We can thus conduct step-by-step experiments, working on the elementary bricks (nucleoside, nucleotides), on oligo-nucleotides (molecular beacon with online detection), up to plasmids in an aqueous medium. In particular, a project was mounted with the Pr. Akinari Yokoya (from the National Institutes for Quantum and Radiological Science and Technology, Tokai, Ibaraki, Japan) to irradiate DNA molecules in the presence of bromide atoms in an aqueous medium. Indeed, they recently published a spectroscopic study depicting electronic properties changes in DNA samples containing Br atoms[14]. The liquid environment, provided by the microfluidic cell, should bring very new and innovative results on solvent influence. Indeed, it will allow investigating how brominated DNA electronic states are affected by the hydrogen bonding of the water. It, therefore, may help to decipher the link between cell inactivation and core-ionization cross-sections in solvated states. This project is planned to take place on February-March 2022 at the photon factory, thanks to a JSPS fellowship[74]. In parallel, we have already started spectroscopic and irradiation studies on a phosphated sugar (glucose-phosphate), which can be considered as a molecular brick, mimicking the DNA backbone, and on urea solutions (data not shown).

One of the difficulties of my thesis is the still persistent separation between the spectroscopic and irradiation approaches (complete change of sample environment). Indeed, with the current state of the liquid micro-jet geometry and SR focusing, it has not been possible to perform simultaneous XPS and radiation damage analyses. It was suggested that the actual low deposited dose (subsequent to the liquid flow rate and beam

[74] *Summer program Fellowship from the Japan Society for the Promotion of Sciences (JSPS) obtained in 2020 (postponed due to the Covid-19 pandemic).*

size) does not lead to significant damage (below the detection limit). However, this point could be improved by developing a liquid micro-jet dedicated to irradiation studies, for example, by decreasing the diameter and flow rate of the jet. Similarly, we can envision the development of a microfluidic cell for XPS measurements, using graphene membranes as windows, for instance[11].

Bibliography Conclusion & Perspectives

[1] S. Kuwamoto, S. Akiyama, and T. Fujisawa, "Radiation damage to a protein solution, detected by synchrotron X-ray small-angle scattering: dose-related considerations and suppression by cryoprotectants," *J. Synchrotron Radiat.*, vol. 11, no. 6, pp. 462–468, Nov. 2004.

[2] R. F. Fischetti, D. J. Rodi, A. Mirza, T. C. Irving, E. Kondrashkina, and L. Makowski, "High-resolution wide-angle X-ray scattering of protein solutions: Effect of beam dose on protein integrity," *J. Synchrotron Radiat.*, vol. 10, no. 5, pp. 398–404, 2003.

[3] B. Fayard *et al.*, "Cell Inactivation and Double-Strand Breaks: The Role of Core Ionizations, as Probed by Ultrasoft X Rays," *Radiat. Res.*, vol. 157, no. 2, pp. 128–140, 2002.

[4] C. Gosse, S. Stanescu, J. Frederick, and S. Lefrançois, "A flow cell for soft X-ray spectromicroscopy in liquid media Charlie," *J. Mater. Chem. B*, vol. 6, no. 35, pp. 7634–7639, 2020.

[5] A. Hans *et al.*, "Efficient Fluorescence Quenching by Distant Production of a Free Electron," *J. Phys. Chem. Lett.*, vol. 10, no. 5, pp. 1078–1082, Mar. 2019.

[6] C. Richter, "Specific probing of the hydrogen bonding network in aqueous mixtures of glycerol and dimethyl sulfoxide," Uppsala University.

[7] R. Dupuy, C. Richter, B. Winter, G. Meijer, R. Schlögl, and H. Bluhm, "Core level photoelectron spectroscopy of heterogeneous reactions at liquid–vapor interfaces: Current status, challenges, and prospects," *J. Chem. Phys.*, vol. 154, no. 6, p. 060901, 2021.

[8] J. Söderström *et al.*, "Nonstoichiometric Intensities in Core Photoelectron Spectroscopy," *Phys. Rev. Lett.*, vol. 108, no. 19, p. 193005, May 2012.

[9] L. Huart *et al.*, "Soft X-ray Radiation and Monte Carlo Simulations: Good Tools to Describe the Radiation Chemistry of Sub-keV Electrons," *J. Phys. Chem. A*, vol. 124, no. 10, pp. 1896–1902, 2020.

[10] L. Huart *et al.*, "A microfluidic dosimetry cell to irradiate solutions with poorly penetrating radiations: a step towards online dosimetry for synchrotron beamlines," *J. Synchrotron Radiat.*, vol. 28, no. 3, pp. 778–789, 2021.

[11] R. Endo, D. Watanabe, M. Shimomura, and T. Masuda, "In situ X-ray photoelectron spectroscopy using a conventional Al-Kα source and an environmental cell for liquid samples and solid-liquid interfaces," *Appl. Phys. Lett.*, vol. 114, no. 17, p. 173702, Apr. 2019.

[12] K. M. Lange and E. F. Aziz, "Electronic structure of ions and molecules in solution: A view from modern soft X-ray spectroscopies," *Chem. Soc. Rev.*, vol. 42, no. 16, pp. 6840–6859, 2013.

[13] C. Gosse *et al.*, "A pressure-actuated flow cell for soft X-ray spectromicroscopy in liquid media," *Lab Chip*, 2020.

[14] M. Hirato, M. Onizawa, Y. Baba, Y. Haga, K. Fujii, S. Wada, A. Yokoya, *Int. J. Radiat. Biol.* **2020**, 1–7.

Appendices

Contents Appendices

Appendix I. Silicon Photomultiplier

SiPM are composed of a matrix of micro-cells or pixels connected in parallel to a standard reading channel. Their principle is based on Geiger discharge processes.

Figure A-1: SiPM devices: ① SiPM chip, ② Lecture card, ③ Pre-amplifier, ④ Bias source.

Briefly, photon absorption in silicon will induce electron-hole creation. When a pair is created, the electric field accelerates the charges and produces new charges by ionization. These new charges will, in turn, be accelerated, and the multiplication of these charges will create an avalanche. When the applied voltage (V_{Bias}) is higher than the breakdown voltage, the silicon becomes conductive and effectively amplifies the original electron-hole pair into a macroscopic current flow. The statistical probability that an incident photon interacts with a microcell to produce a Geiger avalanche is defined as the Photon Detection Efficiency:

$$PDE(\lambda, V) = \eta(\lambda) + \varepsilon(V) \cdot F$$

Where $\eta(\lambda)$ is the quantum efficiency of silicon, $\varepsilon(V)$ is the avalanche initiation probability and F is the fill factor of the device.

$\varepsilon(V)$ is mainly defined by the gain, which is the amount of charge created for each detected photon. It is therefore proportional to the applied overvoltage $\Delta V = V_{Bias} - V_{Breakdown}$ and the microcell capacitance. According to the commercial parameters, the gain of SiPM is scaling linearly with the applied overvoltage. Nevertheless, the gain also depends on the temperature. Indeed, when the temperature increases, the vibrations of the network will make the ionization more complicated and thus limit the avalanche. The

MPPC must be placed in an environment where the temperature is kept constant to have a stable signal. One must know that the gain decrease is also linear.

The F parameter refers to the geometrical efficiency and indicates the proportion of the active surface of a SiPM and decreases with the number of pixels. Indeed, for the same total surface of SiPM, the higher the number of pixels, the lower the active surface will be, as a larger surface will be used for the connections (wires, resistors). One must note that the signal emitted by a pixel does not depend on the number of photons that trigger the pixel. Consequently, when the number of photons arriving on the SiPM is high, the probability that two electrons arrive simultaneously on the same pixel is high. Then a saturation effect breaks the proportionality relationship between the number of triggered pixels and the number of incident photons. Therefore, it is necessary to have a maximum number of pixels for high brightness detection (intense photon flux). On the other hand, the filling coefficient will be less good than for SiPM with larger pixels.

Appendix II. Microfluidic cell's additional information

Appendix II.1. Hydrodynamic theoretical parameters

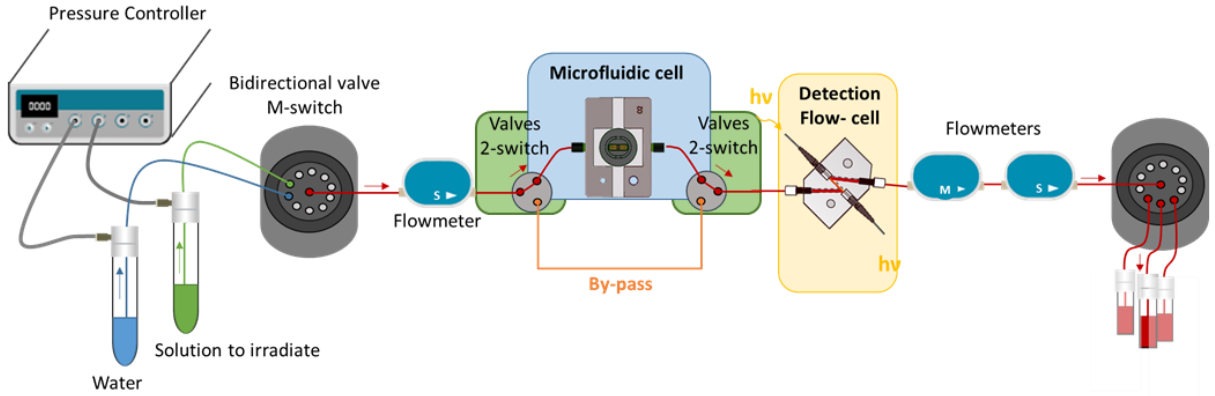

#	Item	Characteristics (internal volume, sizes)		
		Length (mm)	Internal volume (µL)	Hydrodynamic Resistance (Pa.s)
- 1 -	**Fluiwell-1C 15mL**		**0.00**	**0.00E+00**
	F-120 fitting			
- 2 -	**FEP tubing 1/16"OD 0.01" ID1**		**0.00**	**0.00E+00**
- 5 -	**Upchurch adapter 1/16"–1/32" OD**	0.00	**0.00**	**0.00E+00**
	ref P-881 - true zero dead volume (ZDV) connection			
- 6 -	**PEEK blue tubing 1/32"OD 0.01" ID1**	98.00	**4.97**	**9.59E+11**
- 7 -	**Flowmeter S**	**85.00**	**1.50**	**6.84E+12**
- 8 -	**PEEK blue tubing 1/32"OD 0.01" ID1**	172.00	**8.72**	**1.68E+12**
-9-	**Upchurch adapter 1/16"–1/32" OD**	0.00	**0.00**	**0.00E+00**
	ref P-881 - true zero dead volume (ZDV) connection			
- 10 -	**FEP tubing 1/16"OD 0.01" ID1**	820.00	**41.55**	**8.03E+12**
-11-	**2-switch (1)**		**4.00**	
- 12" -	**By-Pass FEP tubing 1/16"OD 0.01" ID1**	255.00	**12.92**	**2.50E+12**
- 12a-	**FEP tubing 1/16"OD 0.01" ID1**	150.00	**7.60**	**1.47E+12**
- 12b -	**LQ-cell** length = 5 mm width = 1.0 mm thickness = 5.3µm	5.00 1.20 0.0053	**0.032**	**3.35848E+14**
	Teflon piece canal	19.20	**3.770**	**1.25E-02**
- 12c -	**FEP tubing 1/16" OD 0.01" ID1**	150.00	**7.60**	**1.47E+12**
- 13 -	**2-switch (2)**		**4.00**	
- 14 -	**FEP tubing 1/16"OD 0.01" ID1**	180.00	**9.12**	**1.76E+12**
- 15 -	**Detection Flow Cell**	8.00	**2.00**	**3.21E-03**
- 16 -	**FEP tubing 1/16"OD 0.01" ID1**	120.00	**6.08**	**1.17E+12**
- 17 -	**Upchurch adapter 1/16"–1/32" OD**	0.00	**0.00**	**0.00E+00**
	ref P-881 - true zero dead volume (ZDV) connection			
- 18 -	**PEEK blue tubing 1/32"OD 0.01" ID1**	150.00	**7.60**	**1.47E+12**
- 19 -	**Flowmeter M**	**35.12**	**5.10**	**0.00E+00**
- 20 -	**PEEK blue tubing 1/32"OD 0.01" ID1**	80.00	**4.05**	**7.83E+11**
- 21 -	**Flowmeter S**	**85.00**	**1.50**	**6.84E+12**
- 22 -	**PEEK blue tubing 1/32"OD 0.01" ID1**	200.00	**10.13**	**1.96E+12**
- 23 -	**Upchurch adapter 1/16"–1/32" OD**	0.00	**0.00**	**0.00E+00**
	ref P-881 - true zero dead volume (ZDV) connection			
- 24 -	**FEP tubing 1/16"OD 0.01" ID1**	150.00	**7.60**	**1.47E+12**
- 25 -	**M-switch**		**?**	
- 26 -	**FEP tubing 1/16"OD 0.01" ID1**	150.00	**7.60**	**1.47E+12**

Appendix II.2. Microfluidic-tool program for the sample collection

- Programming on "automation tool" software

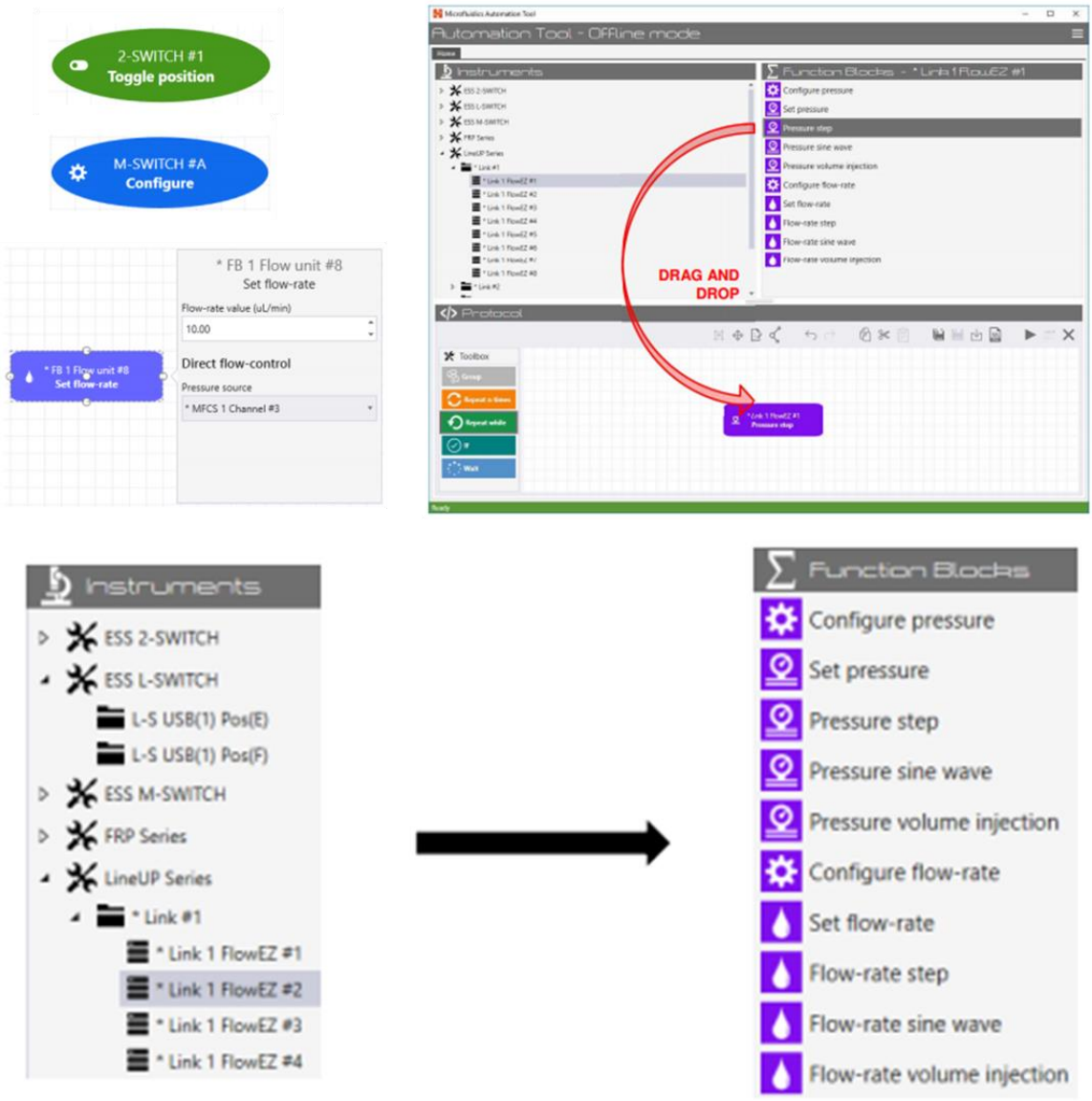

- Example of a program for irradiations

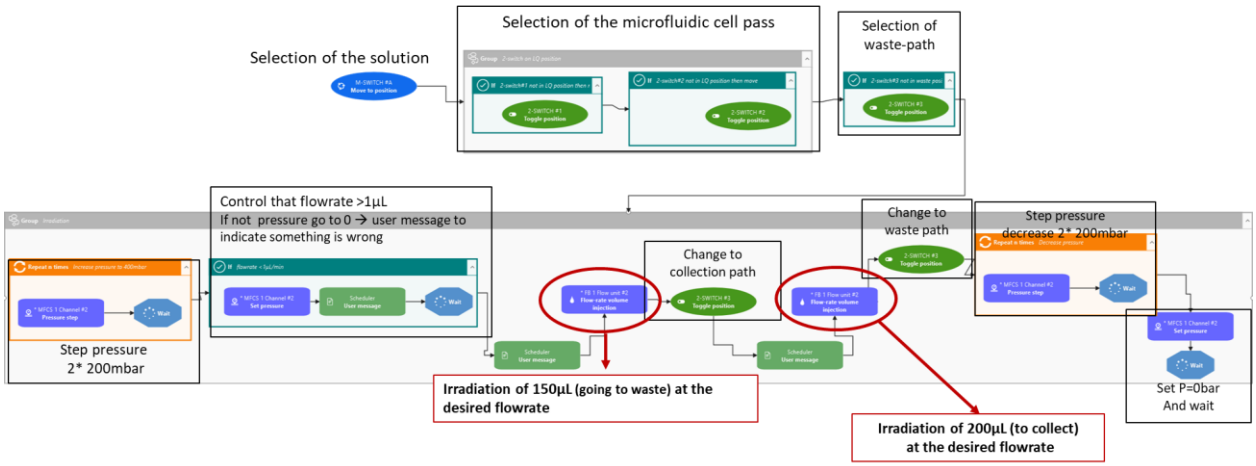

Appendix II.3. Python program for online analysis

```
#Loading python package
    import os
    from os import listdir
    from os.path import isfile, join
    import matplotlib.pyplot as plt
    import numpy as np
    import pandas as pd
    def split(lst,n):
      return [lst[i::n] for i in range(n)]
    n=1043
#Loading data
DATA_PATH=r".\DATA_PATH\"
    #Creation of a dedicated folder for formatted data to avoid deleting the raw data.
    FORMAT_PATH=r".\FORMAT_PATH\ "
    #Creation of a path for saving the extracted evolution spectra
    WRITE_PATH=r".\WRITE_PATH\OnlineDetection\OD_550nmCytC\4"
    pathfname = DATA_PATH
    pathformat = FORMAT_PATH
    #All spectra are recorded in different files: we are loading all the files in a list
    fnamelist = [f for f in listdir(pathfname) if isfile(join(pathfname,f))]
    #Each file is called and modified to replace coma per dot
    for fname in fnamelist :
      with open(os.path.join(pathfname,fname)) as fin,
open(os.path.join(pathformat,fname), 'w') as fout:
        for line in fin:
          fout.write(line.replace(',', '.'))
    #Change fname_format : ODX_WST8, needed otherwise the program skip some data
    #We define 3 Parameters (a,b,c) in order to treat all the files (depend of the name
format given while recording data)
    fname_format = r"OD4_abs_Absorbance___{un:01}___{deux:05}.txt"
    a=0
    b=7387
    c=(0-a)
    fnamelist = [fname_format.format(un = i,deux = i+c) for i in range(a,b)]
    #Creation of an emptu list which will be filled with the extracted data (for exemple
data at 460 nm)
    evolution=[]
    time=[]
    i=0
    # "Ocean Optics time series file" is loaded in 1045 array composed of all the numbers
(x) contained in each column (y)
```

```
    #skiprows=14 removes the header of Ocean Opticsfiles
    #np.arange(2,n,1) allows to load by removing the first columns which are corresponding to the date
    for fname in fnamelist :
      i=i+1
      data = np.loadtxt(os.path.join(pathformat,fname), skiprows = 14)
      data = data[data[:,0].argsort()]
    #Calculate the relative absorbance (optional)
      y=data[479,1]-data[1029,1]
      evolution.append(y)
      time=range (0,len(evolution))
      time.append(i)
    #Ploting the results
    plt.plot(time,evolution, label='evolution at 550nm')
    plt.xlabel(r"time (min)")
    plt.ylabel(r"Delta Absorbance 550nm(u.a.)")
    plt.legend()
    plt.tight_layout()
    plt.figure()
    plt.show()
    #Saving the spectra in excel format in two columns with headers: time and evolution
    txt_to_write = [time, evolution]
    d = dict(time=list(time), evolution=list(evolution))
    df = pd.DataFrame.from_dict(d, orient='index').transpose().fillna('')
df.to_excel(os.path.join(WRITE_PATH,fname + '.xls'), index=False, header="Time \t Evolution "
```

Appendix III. Analysis of the Benzoate Dosimeter

Appendix III.1. Hydroxylation rate

In this study, hydroxyl radical yield is calculated by measuring 2-HOBz concentration. A hydroxylation rate of 30% was taken into account to evaluate the hydroxyl radical yield according to values of the literature measured in aerated conditions[4], [5]. Under irradiations, these results have shown that hydroxylation occurs mainly in ortho positions[6]. Indeed, the production yield of 2-HOBz is at least 2 times higher than other hydroxylated products in calcium benzoate solutions[6]. In order to verify that the products are produced in the same ratio with soft X-ray, samples irradiated at 1.28 keV in the microfluidic cell were analyzed using LC-MS. Chromatograms are presented in **Erreur ! Source du renvoi introuvable.**.

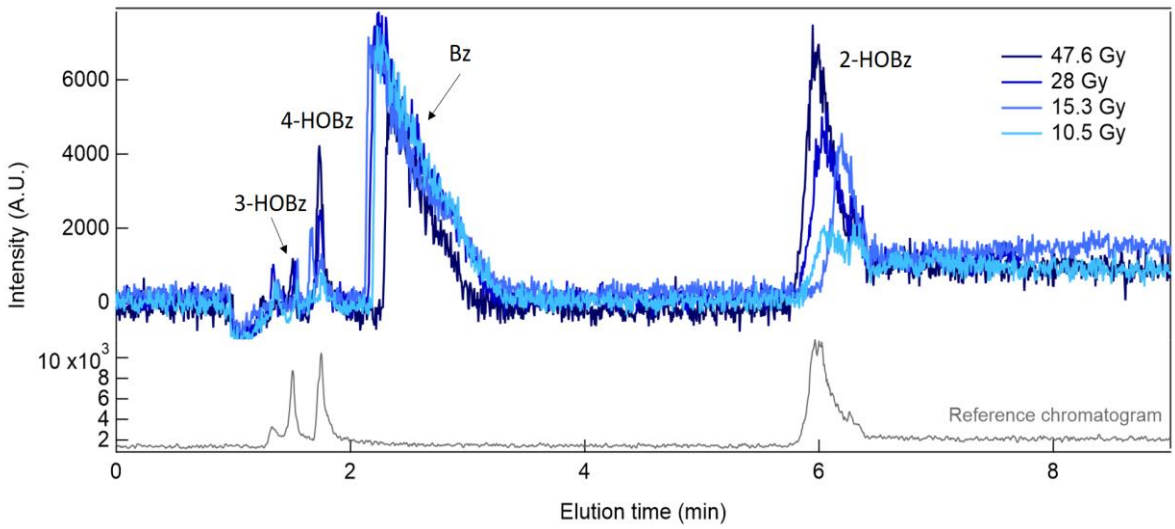

Figure A-2: LC-MS analysis of NaBz 10 mM solutions irradiated using the microfluidic cell on Metrology beamline (1.28 keV). Extracted chromatogram (m/z = 137) are presented for the different samples irradiated at 10.5, 15.3, 28 and 47.6 Gy (from lightest to darkest blue), corresponding flowrates are respectively 8, 5, 2.5 and 1.3 µL/min. A reference chromatogram for the hydroxylated products is presented to facilitate peak identification.

The different isomers were separated using a C18 reversed-phase HPLC column packed with silica gel grafted by carbon chains (18 carbon atoms)[7]. Such functionalization of silanol groups (Si-OH) helps separate compounds by making the stationary phase more apolar. This technique is based on the separation of molecules based on hydrophobic interactions between solute molecules in the mobile phase and ligands attached to the stationary phase. In such conditions, hydrophobic compounds are retained mainly by the stationary phase (higher elution time). Injected commercial solutions identify

hydroxylated derivatives of Benzoate. Following the chromatograms presented in **Erreur ! Source du renvoi introuvable.**, we observe that the 2-HOBz is effectively more retained. However, the meta- and para-products (namely 3-HOBz, 4-HOBz) are less retained than Benzoate. These results indicate that the orientation of the 3-HOBz and 4-HOBz molecules does not allow interaction between the hydroxyl function and the stationary phase. Once products are identified, major products (4-HOBz and 2-HOBz) are quantified by analyzing the chromatograms. Relative areas of 2-HOBz and 4-HOBz are plotted according to the dose calculated as presented in section II.3. The precision evaluates error bars in determining the peak area in the chromatogram.

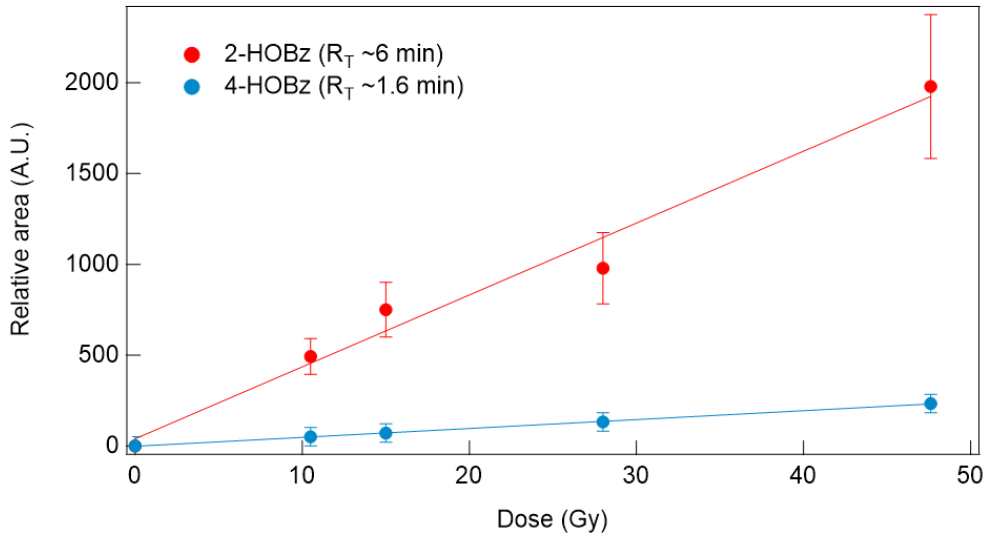

Figure A-3 : Quantification of the major hydroxylated products detected in irradiated benzoate samples. Data are represented plotting the relative area of 2-HOBz and 4-HOBz varying the dose. Data are fitted by a linear curve. Error bars represents the uncertainties on the peaks area.

Linear evolution is observed as expected by fluorescence results previously conducted in static conditions. Obtained results illustrate that the 2-HOBz is effectively the primary product with a production yield at least three times higher than 4-HOBz. These measurements support our quantification of the hydroxyl radical by tracking the fluorescence of 2-HOBz produced during irradiation. These measurements suggest that quantification of the hydroxyl radical by monitoring 2-HOBz fluorescence is the most relevant. The exact hydroxylation rate was not determined as the signal of NaBz was saturated at 10 mM.

Appendix III.2. Reference γ-rays Irradiation

In order to check the behavior of the benzoate dosimeter, reference irradiations were conducted by γ-rays irradiation. Samples were irradiated using the protocol previously described with the GammaCell®. A series of irradiation was conducted for each solution studied, varying the dose (time of exposure inside the GammaCell®). Benzoate solutions were then analyzed by fluorescence measurement. Classical results obtained for 10 mM benzoate solutions are presented in Figure A-4.(a). The maximum intensity (406 nm) is converted to 2-HOBz concentration ([2-HOBz]) using calibration curves[75]. By studying the evolution of [2-HOBz] varying the dose, a linear evolution is observed in Figure A-4.(b).

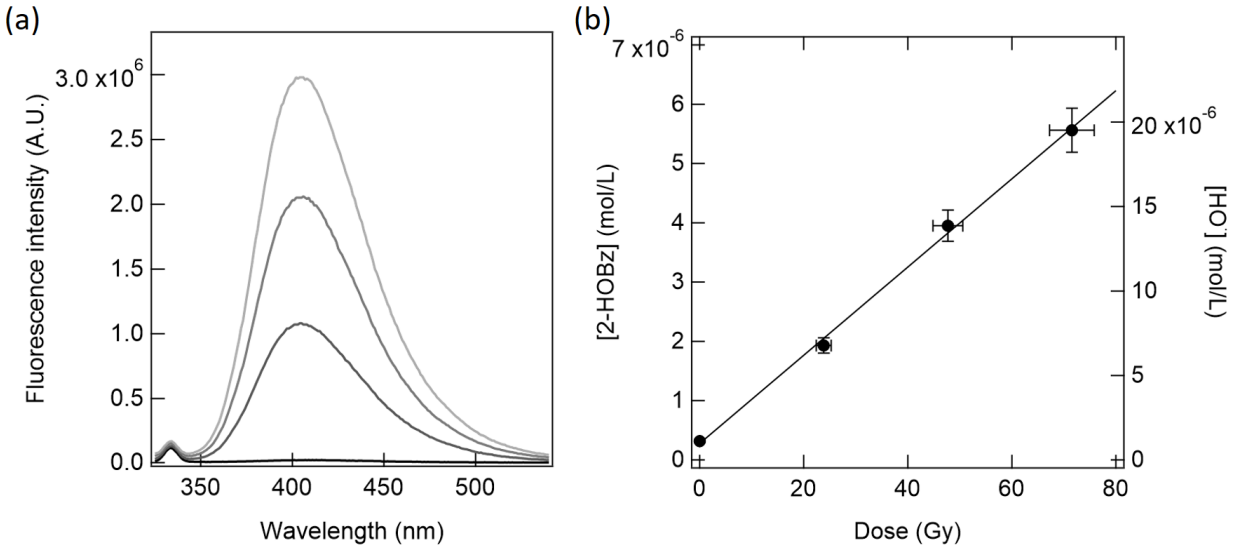

Figure A-4: Determination of the hydroxyl radical yield for gamma irradiation. Presented data were obtained on NaBz 10 mM aerated solutions: (a) Fluorescence signal curves obtained for increasing time of exposure, (b) Deduced hydroxyl radical concentration in fonction of a dose. The hydroxyl concentration was deduced from calibration curves obtained on the same fluorimeter with same solution varying concentration of 2-HOBz.

[75] *Each time, calibration solutions were freshly prepared and analyzed under the same conditions.*

Appendix IV. Salts effect Monte-Carlo input parameters

Kinetic constants 10^{10} M^{-1} s^{-1}

	Initial	Modified
e^-_{aq} + e^-_{aq} -> H_2 + 2 HO^-	0.636	63
e^-_{aq} + $H^\bullet$ -> H_2 + HO^-	2.5	2.5
e^-_{aq} + $HO^\bullet$ -> HO^-	2.95	2.95
e^-_{aq} + H_3O^+ -> $H^\bullet$	2.11	0.02
e^-_{aq} + H_2O_2 -> HO^- + $H^\bullet$	1.1	1.1
$HO^\bullet$ + $HO^\bullet$ -> H_2O_2	0.55	0.55
$HO^\bullet$ + $H^\bullet$ -> H_2O	1.55	1.55
$H^\bullet$ + $H^\bullet$ -> H_2	0.503	0.503
HO^- + H_3O^+ -> H_2O	11.3	0.113

Diffusivities 10^{-9} m^2 s^{-1}

	Initial	Modified
e^-_{aq}	0.636	63
$H^\bullet$	2.5	2.5
$HO^\bullet$ -> HO^-	2.95	2.95
H_3O^+	2.11	0.02
H_2O_2	1.1	1.1

Appendix V.Analysis of the Ferri-Cytochrome c

Appendix V.1. Concentration curves

Solutions of ferri-cytochrome c, prepared in different phosphate buffer concentrations (20 mM), were analyzed by UV-vis analysis using the nanodrop 2000 to retrieve the epsilon values. Results are presented in Figure A-5. The fitting parameters of the linear curve A = f(concentration) are compared to epsilon values found in the literature (Table A-).

Table A-1: : Extinction coefficient of ferri-cytochrome C (horse) from previous experimental data and literature values.

Position	**Measured epsilon values**	**Epsilon values from** [8]
410 nm (Maxima)	103770 $L \cdot mol^{-1} \cdot cm^{-1}$	106100 $L \cdot mol^{-1} \cdot cm^{-1}$
339 nm (Isobestic point)	21069 $L \cdot mol^{-1} \cdot cm^{-1}$	20900 $L \cdot mol^{-1} \cdot cm^{-1}$

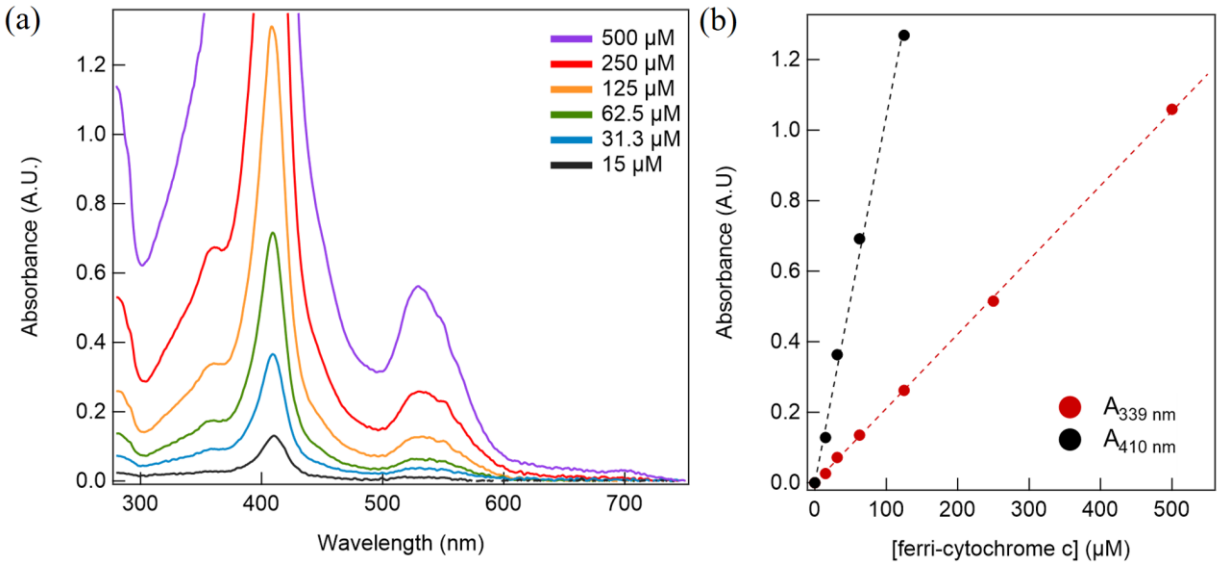

Figure A-5: UV-Vis analysis of the ferricytochrome C using the nanodrop (pathlength 1 mm): (a) Abosrption spectra of ferricytochrome c solutions of various concentrations, (b) Evolution of the absorption signal at 410 nm and 339 nm varying the concentration. Linear fit were applied (dotted lines) in order to determine the epsilon values.

Appendix V.2.γ-rays irradiation of Cytochrome C solutions

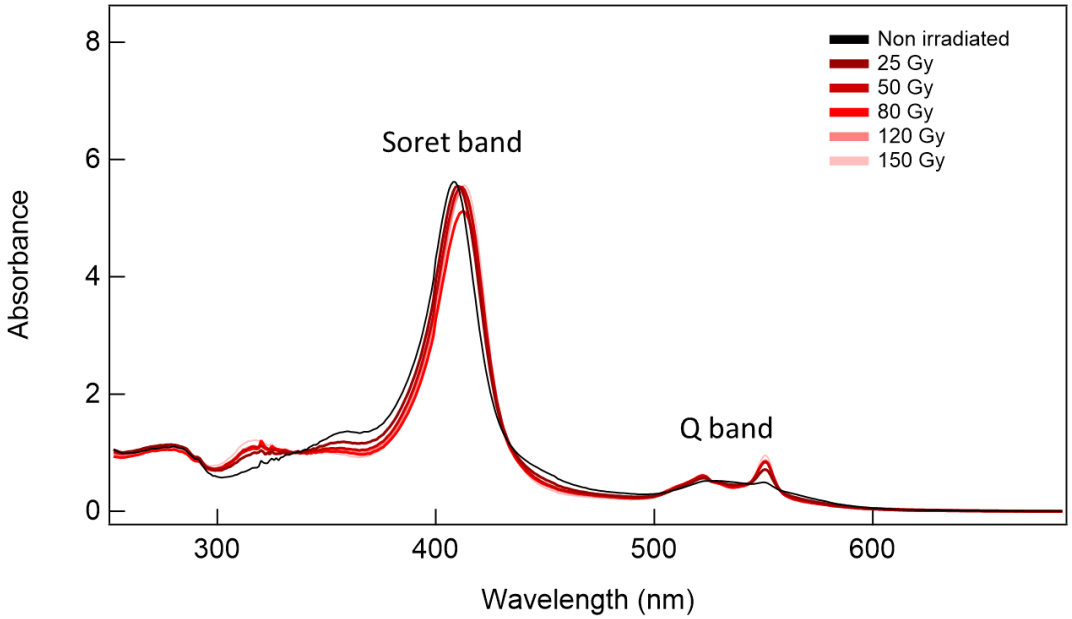

Figure A-6118: UV-Vis analysis of irradiated sample 45 µM FerriCytochrome c solutions prepared in phosphate buffer (20 mM). Analysis was performed on ten times diluted samples using the JASCO spectrophotometer with HELLMA cell (pathlengh 1 cm). Spectra were renormalized to the signal measured at 335 nm. No linear evolution was observed on the Soret band.

Appendix.V.3.Gel electrophoresis in reducing conditions

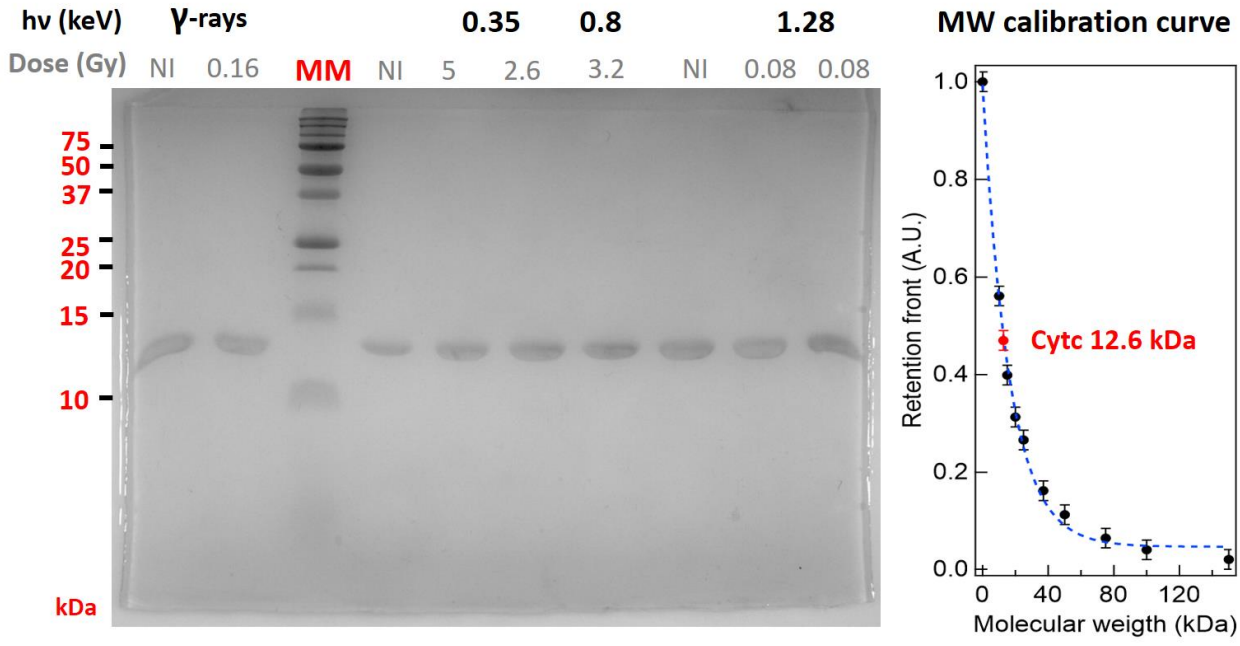

Figure A-7119: SDS-Page gel electrophoresis analysis of irradiated solutions of cytc (45 µM) in reduced conditions.

Appendix VI. Sodium Benzoate Spectroscopic study

Appendix VI.1.Theoretical analysis

Prof. Nobuhiro Kosugi performed simulations from the graduate University for Advanced Studies/SOKENDAI - Institute for Molecular Science in Japan. He performed ab initio self-consistent-field (SCF) calculations for the ground state and core-ionized states based on a relaxed core-hole state using the GSCF3 program package[9] and obtained ΔSCF ionization energies for different model structures with and without water solvent effects. Isolated carboxylate ions carboxylic acid and water clusters with a sodium ion were separately optimized within the second-order Møller-Plesset perturbation theory using the 6-311G* basis set as recently published[10]. Interacting geometries between carboxylate ions and water clusters with a sodium ion were partly optimized before reaching fully optimized geometries. According to their established method[11], core-ionized states of these molecules were obtained by SCF calculations of their single-core hole states with an extended plus polarization basis set (3111121/4111/1*) for carbon atoms with a core hole, double/triple zeta plus polarization basis sets (721/412/1*) for oxygen (carboxyl and carboxylate) and carbon atoms, double/triple zeta basis sets (52121/41), (721/412) and (411) for Na^+, oxygen (water) and hydrogen atoms, respectively[12].

Appendix VI.1.i. Effect of water without sodium ion

Table A-2: Theoretical position of C1s peaks for different water protonation numbers without considering the sodium contribution (Na^+ ions).

Position (eV)	BzCOOH	$BzCOO^-$	$BzCOO^- + 2\ H_2O$	$BzCOO^- + 3\ H_2O$
$C_1 = C_{Carboxyl}$	296.47	289.73	290.44	291.32
C_2	291.38	286.51	286.99	287.53
$C_{(3\ \&\ 4)}$	291.12	287.23	287.59	287.92
$C_{(5\ \&\ 6)}$	291.09	286.75	287.17	288.83
C_7	290.97	287.17	287.51	289.09
$C_{Benzene}$	291.1	286.95	287.35	288.37
FWHM	0.99	1.82	1.28	Not equal
$\Delta E_C\ (eV)$	5.37	2.78	3.09	2.95

Theoretical spectra were retrieved from the C1s peak positions considering that each carbon atom contributes for $1/7^{th}$ of the total area of the XPS signal. The signal due to $C_{(3\ \&\ 4)}$ and $C_{(5\ \&\ 6)}$ thus contribute for $2/7^{th}$ each. Each XPS signal was simulated using a Voigt function (SGL(30))[13] with a constraint of equal FWHM.

Appendix VI.1.ii. Effect of water environment on sodium benzoate

Theoretical spectra for Benzoate in the presence of a sodium ion were simulated using two Voigt functions with similar FWHM and the maximum taken at the theoretical binding energies (Table A-2), with an area ratio of 6:1 (stoichiometric ratio of $C_{Benzene}$:$C_{Carboxyl}$). Optimized geometries are presented in Figure, with simulated XPS spectra: without water (black), with two water molecules on the carboxylate (blue), with a third water molecule on Na^+ (green), and finally with two additional water molecules close to the benzene ring (red).

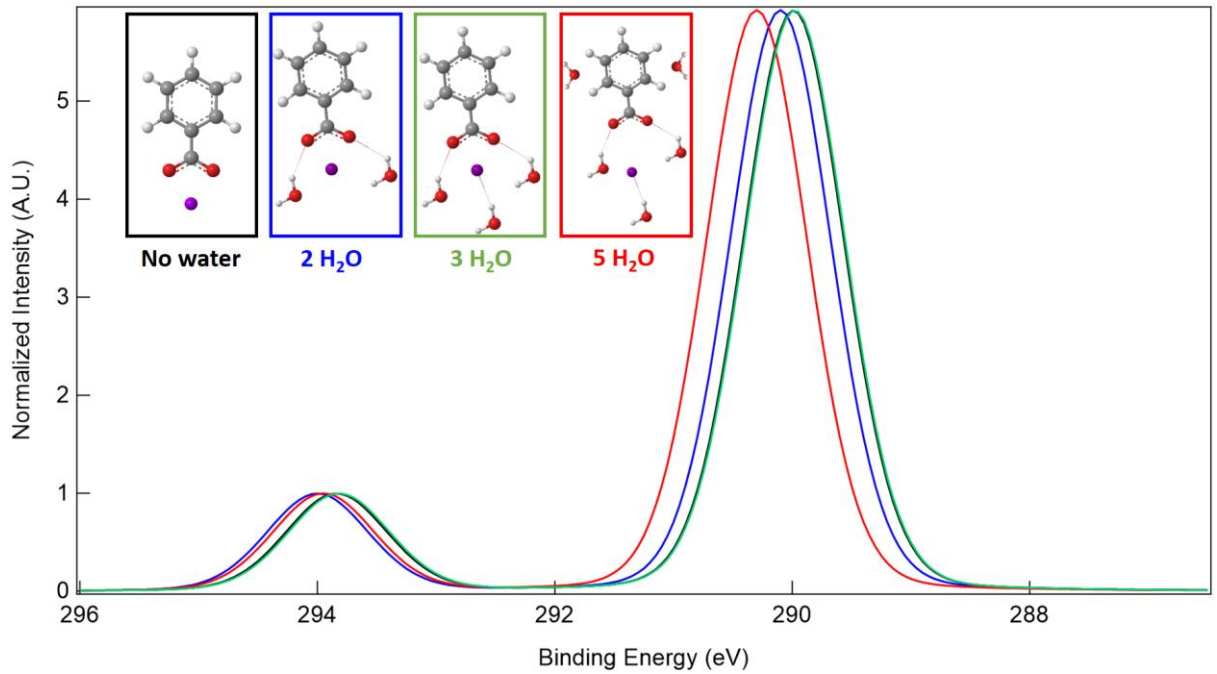

Figure A-8: Theoretical spectra obtained for optimized geometry with Na^+ ion are presented for the different conditions: absence of water (black), or presence of respectively two (blue), three (green) or 5 (red) water molecules.

Appendix VI.1.iii. Investigation of the sodium effect

Table A-3: Dependence of two C1s peak energies on the distance between carboxylate carbon and Na^+ ion in the case of no water structure.

Distance $C_{Carboxyl}$-Na^+	**$C_{Carboxyl}$ (eV)**	**$C_{Benzene}$ (eV)**	ΔE_C
2.50 Å	293.84	290.01	3.83 eV
2.80 Å	293.5	289.87	3.63 eV
3.00 Å	293.26	289.76	3.50 eV

Appendix VI.2. Solid-State XPS analysis of the Sodium Benzoate

The solid-state XPS spectrum of NaBz at the C-K edge was recorded by depositing the sample on carbon scotch. No contamination of adventitious carbon was detected. Data were calibrated by referencing the signal $C_{Benzene}$ at 284.9 eV with respect to the gold Fermi level.

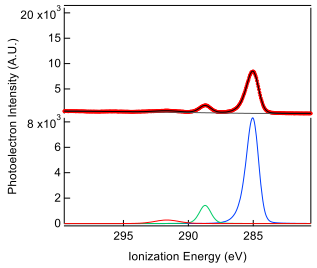

Figure A-9: XPS spectra of solid NaBz: Top spectrum represents the raw data (red markers) and the fitted envelope. Bottom spectrum represents the three contributions: $C_{Benzene}$ (blue), $C_{Carboxyl}$ (green) and the shake-up ($\pi \rightarrow \pi^*$ transition) (red).

		Dry Benzoate XPS analysis
Ratio $C_{Benzene}$:$C_{carboxyl}$		6.2 ±0.5
FWHM		0.95
Position (eV)	$C_{Benzene}$	284.9 ±0.35
	$C_{Carboxyl}$	288.7 ±0.35
ΔE_C (eV)		3.80 ±0.02

Table A-4: XPS features of solid NaBz given with respect to the gold Fermi Level (Ionization energy = E_B + 5.3 eV)

Appendix VI.3. APECS: Comparison with benzoate derivatives

All coincidence measurements were acquired using the liquid micro-jet coupled with a MB-TOF. Results correspond to a total acquisition time of 40 min. Conditions of acquisition were hv=335 eV, applied bias -20V, step Auger energy 1 eV, step PE energy 0.1 eV, 13k-17k e-/s. Energy calibration was performed on O1s gas signal and Ar2p resonances.

Appendix VI.3.i. 2D map results

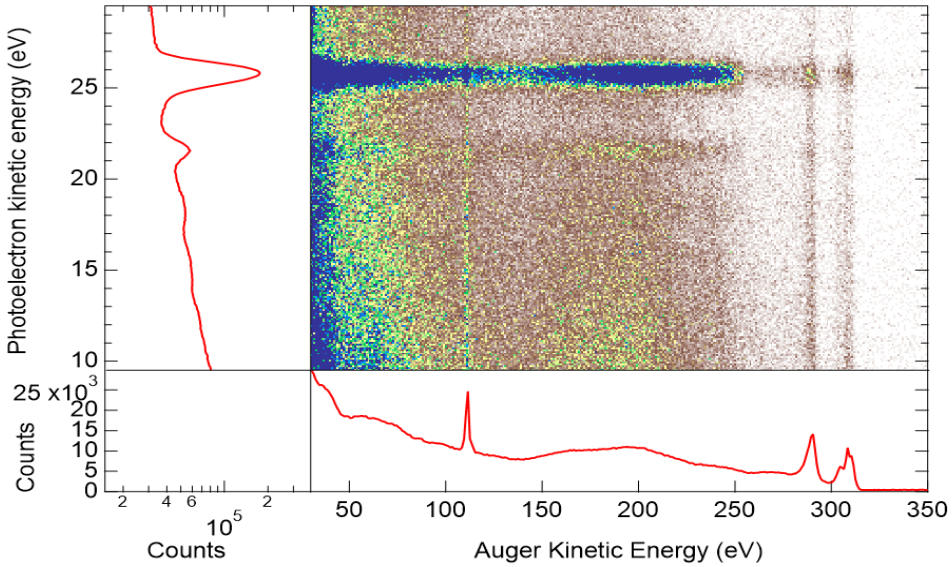

Figure A-10: Coincidence map of benzoic acid aqueous solution (~0.05 M).

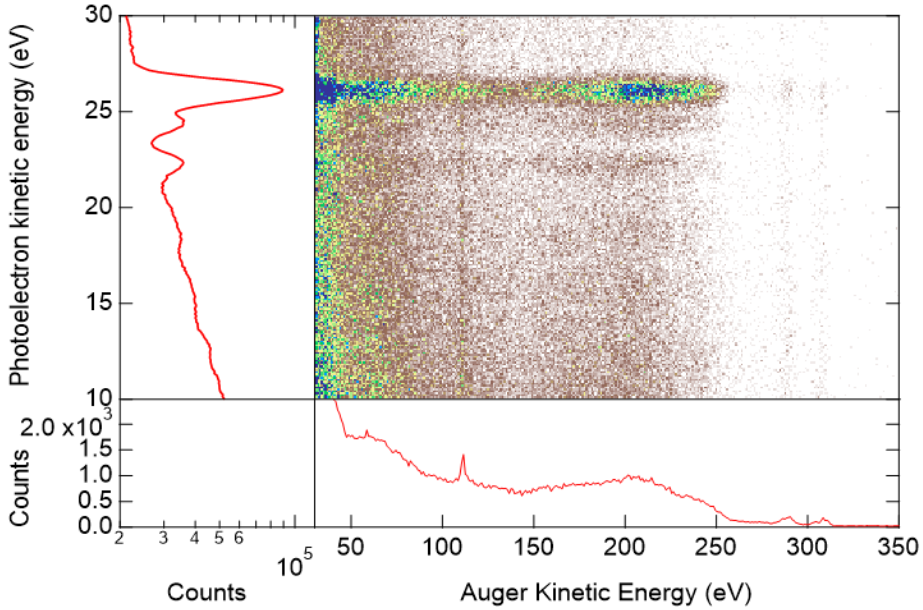

Figure A-11: Coincidence map of 2-hydroxybenzoate aqueous solution (1 M).

Appendix VI.3.ii. Extracted XPS spectrum

XPS spectrum was recorded using the liquid micro-jet coupled with the MB-TOF.

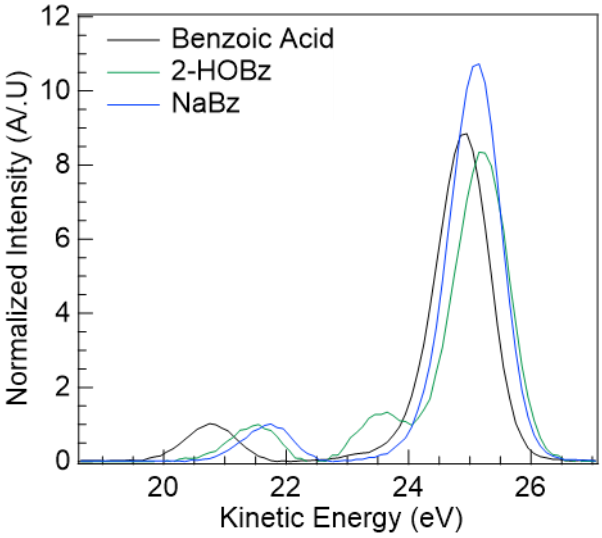

Figure A-12: XPS spectra of benzoate derivatives recorded with a MB-TOF

	Benzoic Acid	**NaBz**	**2-HOBz**
$\mathbf{C_{carboxyk}}$	294.2±0.5	293.3±0.5	293.5±0.5
$\mathbf{C_{Benzene}}$	290±0.5	289.9±0.5	289.8±0.5
$\mathbf{C_{HO\text{-}Ar}}$	-	-	291.5
ΔEC	4.2±0.2	3.4±0.2	3.7±0.2
Area Ratio	~9±1	10±1	~8±1

Table A-5: Fitted parameter of the XPS spectra recorded with the MB-TOF

Appendix VII. XPS analysis of the BSA from the literature

Table 8: BSA XPS parameters from the literature

Ref.	C1s contributions positions (in eV)				N1s contribution positions (in eV)		Calibration
	C-C/C-H	C-O C-N	C=N C=C O-C-O	OC=O N-C=O	N1s		
[14]	285	286.6		288.4	400 (organic)		C-H at 285 eV
[15]	286.5	287.4		289.4	401.3		Ag $3d_{5/2}$
[16]	285	286.2	287.5	288.3	400		C-H at 285 eV
[17]	284.6	285.8		287.6	400		C-H at 285 eV
[18]	284.8	286.1		288.2	400.2		C-H at 284.8 eV
[19]	285	286.4		288.3	400.2		C-H 285 eV
[20]			287.9	289	NH 400.0	NH_3^+ 401.4	Au4$f_{7/2}$, Cu2$p_{3/2}$, and Ag3$d_{5/2}$ *
[21]	285.4	286.5	287.8	288.8	400.9		Au4$f_{7/2}$, Cu2$p_{3/2}$*
[22]	285	286.6		288.4	NH 399	NH_3^+ 401	C-H at 285 eV
[23]	285.4	286.7	287.9	288.7	400.8		Au4$f_{7/2}$, Cu2$p_{3/2}$*
[24]	284.7	286	287.7		C=N 397.5	C- N 400	C-H at 285 eV

* referred with standard reference values[25]

Appendix VIII. List of Publications

Published:

- **A Microfluidic Dosimetry Cell to Irradiate Solutions with Poorly Penetrating Radiations : A Step towards Online Dosimetry for Synchrotron Beamline.** L. Huart, C. Nicolas, M.-A. Hervé du Penhoat, J.-M. Guigner, C. Gosse, J. Palaudoux, S. Lefrançois, P. Mercere, P. Dasilva, J.-P. Renault, C. Chevallard, *J. Synchrotron Radiat.* **2021**, *28*, 778–789.

- **Soft X-Ray Radiation and Monte Carlo Simulations: Good Tools to Describe the Radiation Chemistry of Sub-keV Electrons.**

L. Huart, C. Nicolas, J. A. Kaddissy, J. M. Guigner, A. Touati, M. F. Politis, P. Mercere, B. Gervais, J. P. Renault, M. A. Hervé Du Penhoat, *J. Phys. Chem. A* **2020**, *124*, 1896–1902.

- **XPS measurement of the curvature induced intra-wall polarization in inorganic nanotubes: importance for photocatalytic applications**,

M-C. Pignié, S. Patra, L. Huart, A.R. Milosavljevic, J-P. Renault, J. Leroy, C. Nicolas, O. Sublemontier, S. Le Caër and A. Thill, *Nanoscale* **2021**, 46, 19650-19662.

To be submitted soon:

- **Non-destructive XPS study of protein electronic structure in aqueous media,**

J.-P. Renault, L. Huart, M.-A. Hervé Du Penhoat, A. Milosavljević, J. Bozek, J. Palaudoux, J.-M. Guigner, C. Chevallard, L. Marichal, J. Leroy, F. Wien, C. Nicolas

- **First electron coincidences measurements on solvated sodium benzoate in water (in liquid micro-jet device),**

J. Palaudoux, L. Huart, B. Lutet-Toti, R. Dupuy, R. Vacheresse, M. Reinhardt, D. Cubaynes, D. Céolin, M.A. Hervé du Penhoat, J.P. Renault, J.-M. Guigner, A. Kumar, J. Bozek, U. Ergenhahn, I. Ismail, P. Lablanquie, F. Penent and C. Nicolas

- **A new liquid microjet setup for X-ray photoelectron spectroscopy of liquid solution over wide range of photon energy,**

A. Kumar, L. Huart, A. Milosavljević, J. Bozek, N. Kosugi, C. Nicolas

Writing in progress:

- **Results on probing Solvated metallic ions K-shell**

References Appendices

[1] A. Hemel, "Propriétés mécaniques de membranes d ' épaisseur nanométriques : construction et mise au point d ' un essai de gonflement To cite this version : HAL Id : tel-01748891 soutenance et mis à disposition de l ' ensemble de la Contact : ddoc-theses-contact@univ," 2018.

[2] M. Sekimoto, H. Yoshihara, and T. Ohkubo, "Silicon Nitride Single-Layer X-Ray Mask.," *J. Vac. Sci. Technol.*, vol. 21, no. 4, pp. 1017–1021, 1982.

[3] O. Tabata, K. Kawahata, S. Sugiyama, and I. Igarashi, "Mechanical property measurements of thin films using load-deflection of composite rectangular membrane," *Micromechanics MEMS Class. Semin. Pap. to 1990*, vol. 20, pp. 667–671, 1997.

[4] I. Loeff and A. J. Swallow, "On the Radiation Chemistry of Concentrated Aqueous Solutions of Sodium Benzoate," *J. Phys. Chem.*, vol. 68, no. 9, pp. 2470–2475, Sep. 1964.

[5] W. A. Armstrong and D. W. Grant, "The Aqueous Benzoate System as a Sensitive Dosimeter for Ionizing Radiations," *Can. J. Chem.*, vol. 38, no. 6, pp. 845–850, 1960.

[6] W. A. Armstrong, B. A. Black, and D. W. Grant, "The radiolysis of aqueous calcium benzoate and benzoic acid solutions," *J. Phys. Chem.*, vol. 64, no. 10, pp. 1415–1419, Oct. 1960.

[7] H. Engelhardt, B. Dreyer, and H. Schmidt, "Properties and diversity of C18 bonded phases," *Chromatographia*, vol. 16, no. 1, pp. 11–17, 1982.

[8] W. D. Butt and D. Keilin, "Absorption spectra and some other properties of cytochrome c and of its compounds with ligands," *Proc. R. Soc. London. Ser. B. Biol. Sci.*, vol. 156, no. 965, pp. 429–458, Nov. 1962.

[9] N. Kosugi and H. Kuroda, "Efficient methods for solving the open-shell scf problem and for obtaining an initial guess. The 'one-hamiltonian' and the 'partial scf' methods," *Chem. Phys. Lett.*, vol. 74, no. 3, pp. 490–493, Sep. 1980.

[10] D. Céolin, H. Yuzawa, and T. Saisopa, "Substituent effects in aqueous solutions of carboxylate salts studied by x-ray absorption spectroscopy at the oxygen K- edge Substituent effects in aqueous solutions of carboxylate salts studied by x-ray absorption spectroscopy at the oxygen K-edge," *J. Chem. Phys*, vol. 014306, 2021.

[11] N. Kosugi, E. Shigemasa, and A. Yagishita, "High-resolution and symmetry-resolved oxygen K-edge spectra of O2," *Chem. Phys. Lett.*, vol. 190, no. 5, pp. 481–488, 1992.

[12] S. Huzinaga, J. Andzelm, M. Klobukowski, E. Radzio-Andzelm, Y. Sasaki, and H. Tatewaki, *Gaussian Basis Sets for Molecular Calculations*. Amsterdam: Elsevier, 1984.

[13] V. Jain, M. C. Biesinger, and M. R. Linford, "The Gaussian-Lorentzian Sum, Product, and Convolution (Voigt) functions in the context of peak fitting X-ray photoelectron spectroscopy (XPS) narrow scans," *Appl. Surf. Sci.*, vol. 447, pp. 548–553, 2018.

[14] A. I. Muñoz and S. Mischler, "Electrochimica Acta Electrochemical Quartz Crystal Microbalance and X-Ray Photoelectron Spectroscopy study of cathodic reactions in

Bovine Serum Albumin containing solutions on a Physical Vapour Deposition-CoCrMo biomedical alloy," *Electrochim. Acta*, vol. 180, pp. 96–103, 2015.

[15] Y. Zhou, X. Hu, C. Dou, H. Liu, S. Wang, and P. Shen, "Structural studies on metal-serum albumin. IV. The interaction of Zn(II), Cd(II) and Hg(II) with HSA and BSA.," *Biophys. Chem.*, vol. 42, no. 2, pp. 201–11, 1992.

[16] C. Debiemme-chouvy, S. Haskouri, and H. Cachet, "Study by XPS of the chlorination of proteins aggregated onto tin dioxide during electrochemical production of hypochlorous acid," vol. 253, pp. 5506–5510, 2007.

[17] W. Chen, X. Wu, and R. Car, "X-Ray Absorption Signatures of the Molecular Environment in Water and Ice," vol. 017802, no. July, pp. 1–4, 2010.

[18] C. J. P. P. Boonaert *et al.*, "Adhesion of Lactococcus lactis to model substrata: Direct study of the interface," *Colloids Surfaces B Biointerfaces*, vol. 22, no. 3, pp. 171–182, 2001.

[19] B. E. Torres Bautista *et al.*, "Effect of protein adsorption on the corrosion behavior of 70Cu-30Ni alloy in artificial seawater," *Bioelectrochemistry*, vol. 97, pp. 34–42, 2014.

[20] K. P. Fears, "Measuring the pK/pI of biomolecules using X-ray photoelectron spectroscopy," *Anal. Chem.*, vol. 86, no. 17, pp. 8526–8529, 2014.

[21] C. M. Pradier and F. Ka, "Adsorption of Bovine Serum Albumin on Chromium and Molybdenum Surfaces Investigated by Fourier-Transform Infrared Reflection - Absorption Spectroscopy (FT-IRRAS) and X-ray Photoelectron Spectroscopy," pp. 6766–6773, 2003.

[22] C. Valero-Vidal, A. Igual-Muñoz, C.-O. A. Olsson, and S. Mischler, "Adsorption of BSA on Passivated CoCrMo PVD Alloy: An EQCM and XPS Investigation," *J. Electrochem. Soc.*, vol. 161, no. 6, pp. C294–C301, 2014.

[23] I. Frateur, L. Lartundo-Rojas, C. Méthivier, A. Galtayries, and P. Marcus, "Influence of bovine serum albumin in sulphuric acid aqueous solution on the corrosion and the passivation of an iron-chromium alloy," *Electrochim. Acta*, vol. 51, no. 8–9, pp. 1550–1557, 2006.

[24] A. Swaidan *et al.*, "A facile preparation of CuS-BSA nanocomposite as enzyme mimics: Application for selective and sensitive sensing of Cr(VI) ions," *Sensors Actuators, B Chem.*, vol. 294, no. May, pp. 253–262, 2019.

[25] M. P. Seah, I. S. Gilmore, and G. Beamson, "XPS: Binding energy calibration of electron spectrometers 5 - Re-evaluation of the reference energies," *Surf. Interface Anal.*, vol. 26, no. 9, pp. 642–649, 1998.

List of Figures

List of Tables

List of abbreviations

Abbreviation	Meaning
2-HOBz	2-Hydroxy Benzoate
AE	Auger Electron
AES	Auger Electron Spectroscopy
APECS	Auger Photo-Electron Coincidence Spectroscopy
BSA	Bovine Serum Albumin (protein)
CCD	Charge-Coupled Device
CEA	Centre des Energies Atomiques et des Energies Alternatives
CXRO	Center for X-ray Optics
Cytc	Cytochrome c
DFT	Density Functional Theory
DNA	Deoxyribose Nucleic Acid
DSB	Double-Strand Break
EDX	Energy-Dispersive X-ray Spectroscopy
ENS	Ecole Normale Supérieure
ESCA	Electron Spectroscopy for Chemical Analysis
ESI	ElectroSpray Ionization
ETMD	Electron Transfer Mediated Decay
EXAFS	Extended X-ray Absorption Fine Structure
FEP	Fluorinated Ethylene-Propylene
FWHM	Full Width Half-Maximum
HDA	Hemispherical Deflection Analyzer
HOMO	Highest Occupied Molecular Orbital
ICD	Interatomic/Intermolecular Coulombic Decay
IE	Ionization Energy
IET	Ionization Energy Threshold
IMPMC	Institut de Minéralogie, de Physique des Matériaux et de Cosmochimie
IUPAC	International Union of Pure and Applied Chemistry
KE	Kinetic Energy
LC-MS	Liquid-Chromatography coupled to Mass Spectrometry
LCPMR	Laboratoire de Chimie Physique-Matière et Rayonnement
LET	Linear Energy Transfer
LINAC	LInear ACcelerator
LUMO	Lowest Unoccupied Molecular Orbital
LV	Linear Vertical (polarization)
MB-TOF	Magnetic Bottle Time-Of-Flight
MC	Monte-Carlo
MCP	MicroChannel Plate
MED	Mean Escape Depth

MTT	3-(4,5-Dimethylthiazol-2-Yl)-2,5-Diphenyltetrazolium Bromide
NaBz	Sodium Benzoate
NAP-XPS	Near-Ambient Pressure X-ray Photo-electron Spectroscopy
NBT	Nitro-Blue Tetrazolium
NEXAFS / XANES	Near-Edge X-ray Absorption Fine Structure
NEXAMS	Near-edge X-ray absorption mass spectrometry
NIST	National Institute of Standards and Technology
OD	Optical Density
PCB	Printed Circuit Board
PDMS	Poly-Di-Methyl-Siloxane
PDOS / DOS	(Partial) Density Of States
PE	Photo-Electron
PEEK	PolyEtherEtherKetone
PEPICO	Photo-Electron Photo-Ion coincidence
PIPICO	Photo-Ion Photo-Ion coincidence
PMMA	Poly(Methyl MethAcrylate)
PTFE	PolyTetraFluoroEthylene
RAS	Resonant Auger Spectroscopy
ROS	Reactive Oxygen Species
RT	Retention Time
SCF	Self-Consistent-Field
SEM	Scanning Electron Microscope
SGL	Sum Gaussian-Lorentzian
SiPM	Silicon PhotoMultiplier
SOD	SuperOxide Dismutase
SR	Synchrotron Radiation
SRCD	Synchrotron Radiation Circular Dichroism
SSB	Single-Strand Break
SST	Stainless Steel
STM	Scanning Tunneling Microscopy
STXM / TXM	(Scanning) Transmission X-ray Microscopy
SX	Soft X-ray
TEM	Transmission Electron Microscopy
TIC	Total Ion Current
UPS	UV Photo-electron Spectroscopy
UV-Vis	Ultra-Violet Visible light
VUV	Vacuum Ultra-Violet light
WST	Water-Soluble Tetrazolium
XAS	X-ray Absorption Spectroscopy
XFEL	X-ray Free Electron Laser
XPS	X-ray Photo-electron Spectroscopy
YAG:Ce	Yttrium Aluminium Garnet (Cerium)